University of Southampton

Faculty of Engineering and Physical Sciences

School of Chemistry

Metal-Organic Framework Composites for Nuclear Waste Clean-Up

by

Tom S. Crickmore MChem AMRSC

ORCID ID 0000-0001-7564-2700

Thesis for the degree of Doctor of Philosophy

November 2022

For my parents, Simon and Fiona, whose belief allowed me to pursue this journey, and whose unconditional love and support helped me to complete it.

“Research is what I’m doing when I don’t know what I’m doing.” – ***Wernher von Braun***

University of Southampton

Abstract

Faculty of Engineering and Physical Sciences

School of Chemistry

Doctor of Philosophy

Metal-Organic Framework Composites for Nuclear Waste Clean-Up

by

Tom S. Crickmore MChem AMRSC

Radioactive pertechnetate (TcO_4^-) has been proven a troublesome fission product from the spent fuel of nuclear reactors. Current reprocessing is not effective at removing TcO_4^- from effluent resulting in discharges of the anion into watercourses through both authorised and accidental incidents. Metal-organic frameworks (MOFs) have been proposed as candidate adsorbents for TcO_4^- as a result of their high porosity and the ability to fine tune their properties towards particular applications. The processing of these materials into application specific configurations, such as composites, can enhance the physical properties and aid in recycling of the adsorbent. This project will involve the synthesis of both novel and existing MOFs followed by the processing of these materials into composites that can selectively adsorb TcO_4^-. We opt wherever possible to use benign reagents, and environmentally sustainable techniques for the synthesis of these materials. As such, we close this thesis by presenting our work in sustainable MOF syntheses.

Chapter one introduces the key areas of this project. We discuss the nuclear industry and the need for nuclear waste remediating materials. Metal-organic frameworks and their composites are discussed as well as key literature. We close this chapter by highlighting current materials for pertechnetate remediation and lay out the project aims.

In chapter two we present our work into ReO_4^- remediation, a nonradioactive surrogate of pertechnetate, with the MOF UiO-66-NH_2 ($[Zr_6O_4(OH)_4(BDC\text{-}NH_2)_6]$) (BDC-$NH_2$ = aminoterephthalic acid). The MOF undergoes post-synthetic modification (PSM) with excess ethyl isocyanate to generate the MOF UiO-66-$(NH_2)_{1.8}(NHC(O)NHC_2H_5)_{4.2}$. UiO-66-$NH_2$ is configured into two bio-composites, alginate hydrogel beads and cellulose filter papers. The effectiveness of the PSM material and the bio-composites for perrhenate remediation is assessed.

We turn our attention to crystal engineering of coordination polymers and MOFs in chapter three. Crystal engineering is applied to investigate the effect that structural isomerism of the organic linker N,N'-bis(pyridylmethyl)urea and the counter anion present in silver cationic coordination polymers plays on the resulting crystal structure and topology. Initial studies suggested that the ortho structural isomer could selectively crystallise ReO_4^- over competing anions such as nitrate and sulphate however this was ultimately found to not be the case. Silver coordination polymer stability in the presence of application concentration levels of chloride was found to be not sufficient to warrant ReO_4^- remediation studies. Three new zinc-based materials

are also synthesised and characterised in chapter three. The urea-based organic linkers 4,4'-(carbonylbis(azanediyl))dibenzoic acid and N,N´-bis(4-pyridylmethyl)urea are used in these materials, two of which are mixed linker systems. This chapter presents a total of 14 crystal structures, 11 of which have not been previously reported.

In chapter four we investigate sustainable syntheses of calcium-based MOFs. Recycled chicken eggshells as well as polyethylene terephthalate (PET) bottles are used as sustainable sources of calcium and terephthalic acid respectively, for a one-pot synthesis of $[Ca(BDC)(H_2O)_3]$. Furthermore, eggshells were used to synthesise the MOFs $[Ca(SQ)(H_2O)]$ and $[Ca(FU)(H_2O)_3]$. Mechanochemistry is applied to provided largely solventless and sustainable syntheses for the three listed MOFs.

Table of Contents

List of Accompanying Materials vi

Research Thesis: Declaration of Authorship vii

Contributing Author Declaration viii

Acknowledgements ix

Abbreviations xi

Chapter One – Introduction 21

1.1 The need for Nuclear Waste Clean-Up 23

1.1.1 Iodine-131 24

1.1.2 Strontium-90 25

1.1.3 Caesium Isotopes 25

1.1.4 Technetium-99 25

1.2 An Introduction to Metal-Organic Frameworks 28

1.2.1 Metal-Organic Framework Design 30

1.2.2 Synthetic Methods of Metal-Organic Frameworks 43

1.2.3 Metal-Organic Framework Applications 46

1.3 Existing Materials for Pertechnetate Remediation 51

1.4 Metal-Organic Framework Composites 59

1.5 Experimental Methods 63

1.6 Project Aims 48

1.7 References 69

Chapter Two – UiO-66-NH_2: PSM and Green Approaches to its Composites 77

2.1 Introduction 77

2.1.1 UiO-66-NH_2 Post-Synthetic Modifications 79

2.1.2 MOF@Biopolymer Composites 81

2.2 Chapter Outlook 86

2.3 Results and Discussion 88

2.3.1 PSM Reactions to Generate Urea Moieties in UiO-66-NH_2 88

2.3.2 UiO-66-NH_2@FFP Composites 101

2.2.3 UiO-66-NH_2@Alginate Composites 111

2.4 Conclusion and Further Work 120
2.5 Experimental 123
2.6 References 126
Chapter Three – Crystal Engineering of Urea-Containing Coordination Polymers and MOFs 131
3.1 Introduction 131
3.1.1 Urea-Based MOF Crystal Engineering 133
3.1.2 Selective Crystallisation of Anions 136
3.2 Chapter Outlook 138
3.3 Results and Discussion of Crystal Engineering of Silver-Based CPs 140
3.3.1 Synthesis and Characterisation of Urea-Based Organic Linkers 140
3.3.2 Synthesis and Characterisation of Silver N,N'-bis(2-pyridylmethyl)urea CPs 141
3.3.3 Synthesis and Characterisation of Silver N,N'-bis(3-pyridylmethyl)urea CPs 148
3.3.4 Synthesis and Characterisation of Silver N,N'-bis(4-pyridylmethyl)urea CPs 154
3.3.5 Discussion 163
3.4 Results and Discussion of Mixed-Linker Urea-Based MOFs and LMOFs Using Zinc Salts . 167
3.4.1 Zn-MOF-1 ($Zn_2(OBA)_2$(4-MeUR-N) 4.5·DMF) 167
3.4.2 Zn-LMOF-2 (Zn(IP)(4-MeUR-N) 0.7·DMF) 174
3.4.3 Zn-LMOF-3 ($Zn(UR\text{-}CO_2H)(H_2O)_2$) 179
3.4.4 Discussion 186
3.5 Conclusion 190
3.6 Experimental 193
3.7 References 198
Chapter Four – Calcium-Based MOFs from Biomineralised $CaCO_3$ Sources 201
4.1 Introduction 201
4.2 Chapter Outlook 205
4.3 Results and Discussion 206
4.3.1 Characterisation of Recycled Precursors 206
4.3.2 Calcium Terephthalate Trihydrate ($[Ca(BDC)(H_2O)_3]$) 209
4.3.3 Calcium Squarate Hydrate ($[Ca(SQ)(H_2O)]$) 218
4.3.4 Calcium Fumarate Trihydrate ($[Ca(FU)(H_2O)_3]$) 221
4.3.5 Ca-MOF-1 ($Ca(UR\text{-}CO_2H)(H_2O)_4$) 229

4.4 Conclusion and Further Work 240

4.5 Experimental 242

4.6 References 245

Chapter Five – Conclusion & Future Work 249

Appendix 251

List of Accompanying Materials

All related data can be found *via* the University of Southampton data repository service and is open access following the necessary embargo period. Once available, this can be accessed through this link: https://doi.org/10.5258/SOTON/D2004.

Research Thesis: Declaration of Authorship

Print name: Tom Simon Crickmore

Title of thesis: Metal-Organic Framework Composites for Nuclear Waste Clean-Up

I declare that this thesis and the work presented in it are my own and has been generated by me as the result of my own original research.

I confirm that:

1) This work was done wholly or mainly while in candidature for a research degree at this University;
2) Where any part of this thesis has previously been submitted for a degree or any other qualification at this University or any other institution, this has been clearly stated;
3) Where I have consulted the published work of others, this is always clearly attributed;
4) Where I have quoted from the work of others, the source is always given. With the exception of such quotations, this thesis is entirely my own work;
5) I have acknowledged all main sources of help;
6) Where the thesis is based on work done by myself jointly with others, I have made clear exactly what was done by others and what I have contributed myself;
7) Parts of this work have been published as:
    a) 'Toward Sustainable Syntheses of Ca-MOFs', T. S. Crickmore, H. B. Sana, H. Mitchell, M. Clark & D. Bradshaw, *Chem. Commun.*, 2021, **57**, 10592.

Signature: ..... Date:.....

Contributing Author Declaration

The author declares the following contributions made by supporting researchers and thanks them for their invaluable input.

N_2 gas adsorption data in chapter two was collected by Alice Oakley. BET fitting was completed by the author. Due to equipment failure, a small number of SEM images throughout the thesis were collected by Aran Amin. ICP-MS samples were processed by the GAU-Radioanalytical group at the National Oceanography Centre Southampton.

Rui Xu, an MSci research student, synthesised Zn-LMOF-3 presented in chapter three. The author supported this work through experiment design, student supervision, data collection and data interpretation.

In chapter four, Haamidah Begum Sana & Molly Clark conducted the calcium MOF experiments utilising eggshells as the calcium source for [Ca(SQ)(H_2O)] and room temperature synthesis of [Ca(SQ)(H_2O)] respectively. Further work was initiated by Hannah Mitchell to combine this work with organic linkers derived from PET plastic. The author supervised HM by providing aid in experimental design, data collection and support in data interpretation. All single-crystal structures in chapter four were collected and solved by the author. All analysis in this chapter was solely carried out by the author although the data may have originated from one of the three listed student researchers. Rob Clowes from the University of Liverpool completed the CO_2 adsorption experiments.

Acknowledgements

From day one of this adventure, I have thought about what I would be writing in the acknowledgements section of my thesis; reflecting on the path that it has taken and thanking the ones that got me to the end.

I owe so many thanks to Dr Darren Bradshaw, my primary supervisor and fellow ale enthusiast. Thank you for the support, the care, and the laughs you brought to the office and lab. I truly appreciate the insight you have given me into both the MOF and academia fields and the motivation you have provided right up until the very end. I look forward to my return to Southampton in the future for a pint or two. Thank you also to the past and present members of the Bradshaw group that I have had the pleasure of sharing my journey with. In particular; Dr Smaragda Lymperopoulou, Dr Marion Specht, and Dr Maria Gonzalez who made the lab such a fun and supportive place to be. I have had the opportunity to support many undergraduate students with their studies in the Bradshaw lab. Thanks to them for helping me grow as both a researcher and mentor.

Thanks also go to Professors Andy Cundy and Phil Warwick from GAU at the National Oceanography Centre Southampton for their assistance and expertise in the application testing of my work. I would like to extend my appreciation to the facility managers and technicians across the university, in particular those within the Characterisation and Analytics group in the department of Chemistry and the National Crystallography Service, who have provided training and support with many of the techniques that are integral to the results within this thesis. Cheers to the Reid, Raja, and Kanaras groups who have been invaluable in providing advice, equipment, and the regular pub trip. Being able to burst into your labs, always uninvited, with queries and requests made a lot of the following work easier to complete.

Cheers to Dan (possibly the only person that wants an after-work pint as much as I do) and Iona (you've tolerated Dan and I unwaveringly) for being such great friends over the past four years. Our chaotic chats and your good humour always kept me going, even on the hardest of days. Thank you to Mol for being an all-round joy. I will miss our conversations across the lab bench, our Pret trips, and you managing to somehow dye everything you can get your hands on with rhodamine B. Thanks to all my fab friends that I have been fortunate enough to meet during my time at Bath, many of whom I continue to share good times and make memories with. There are far too many of you to list here, but you all know who you are, and I cannot thank you enough for sticking by me over all these years. You are all incredible people who are changing the World, for the better, in your own, unique ways. Keep showing me how it's done.

Acknowledgements

To my family, without whose love and support this whole thing would have never got off the ground. Mum, Dad, Beth, Laura, Tracey, Dee, Phil, and my grandparents; what a lucky man I am to have you all. Knowing you are there for me, and always will be, is all I need. Thank you for the smiles, the laughs and, most importantly, the sweet tooth.

To my XC. You are a glowing light that has effortlessly shone during the darkest and hardest stage of my PhD. Your love, strength, and selflessness will not easily be forgotten, and I cannot thank you enough for your patience over the last year. I look forward to more sunsets, more star gazing, and more exploring with you and Maeve, by my side.

And finally, to my little girl. Success can be measured in a million and one ways - academic success is just one of them. I cannot wait to see what you excel at and what makes you tick. Whether it is art, reading, sports, or helping others. I hope it fills you with as much joy as science has for me. I like to make sense of the World around me, and I can't wait to help you do the same.

Cheers.

Abbreviations

H_2BDC ..... Benzene-1,4-dicarboxylic acid (Terephthalic acid)

$H_2BDC\text{-}NH_2$ ..... 2-Aminobenzene-1,4-dicarboxylic acid (Aminoterephthalic acid)

BHET ..... Bis(hydroxyethyl) terephthalate

BPY ..... Bipyridine

H_3BTC ..... Benzene-1,3,5-tricarboxylic acid (Trimesic acid)

H_4BTEC ..... Benzene-1,2,4,5-tetracarboxylic acid

$[Ca(BDC)(H_2O)_3]$ ..... Calcium terephthalate trihydrate

$[Ca(FU)(H_2O)_3]$ ..... Calcium fumarate trihydrate

Ca-MOF ..... Calcium-based metal-organic framework

$[Ca(SQ)(H_2O)]$ ..... Calcium squarate hydrate

CSD ..... Cambridge structural database

DABCO ..... 1,4-diazabicyclo[2.2.2]octane

DMF ..... N,N'-Dimethylformamide

FFP ..... Functionalised filter paper

FP ..... Filter paper

FTIR ..... Fourier transform infrared spectroscopy

H_2FU ..... *trans*-Butenedioic acid (Fumaric acid)

HKUST ..... Hong Kong University of Science and Technology

ICP-MS ..... Inductively coupled plasma mass spectrometry

IM ..... Imidazolate

HINA ..... Isonicotinic acid

H_2IP ..... 1,3-Benzenedicarboxylic acid (Isophthalic acid)

IRMOF ..... Isoreticular metal-organic framework

IUPAC ..... International Union of Pure and Applied Chemistry

L ..... Linker

LMOF ..... Layered metal-organic framework

LSC ..... Liquid scintillation counting

MeUR-N ..... N,N'-Bis(pyridylmethyl)urea

Abbreviations

MIL..... Matériaux de l'Institut Lavoisier

2-MIM..... 2-Methylimidazole

MOF..... Metal-organic framework

MOFAC..... Metal-organic framework aerogel composite

MON..... Metal-organic nanosheet

NMR..... Nuclear magnetic resonance

H_2OBA..... 4,4'-Oxybis(benzoic acid)

PBU..... Primary building unit

PET..... Poly(ethylene) terephthalate

PSLE..... Post-synthetic ligand exchange

PSM..... Post-synthetic modification

PXRD..... Powder X-ray diffraction

SBU..... Secondary building unit

SCSC..... Single-crystal to single-crystal

SCXRD..... Single crystal X-ray diffraction

SEM..... Scanning electron microscopy

H_2SQ..... Squaric acid

TGA..... Thermogravimetric analysis

THF..... Tetrahydrofuran

TIB..... 1,2,4,5-tetra(1H-imidazol-1-yl)benzene

TIPM..... Tetrakis[4-(1-imidazolyl)phenyl]methane

TJNU..... Tianjin Normal University

UiO..... Universitetet i Oslo

UR-CO_2H..... 4,4'-(Carbonylbis(azanediyl))dibenzoic acid

ZIF..... Zeolitic imidazolate framework

Chapter 1 Introduction

Nuclear energy in the UK was first utilised for electricity generation in 1956 when Calder Hall, the world's first industrial scale nuclear power plant, was commissioned. Since then, 25 more nuclear power reactors in the UK, and over 600 worldwide, have been constructed and generated electricity for public use.[1] Nine of those UK reactors, spread across five different sites, are still in operation and are responsible for around 20% of the electricity produced in the country.[2,3] Nuclear power has reliably provided a baseload to the national grid for well over 50 years.

The nuclear fuel cycle produces radioactive waste at each and every stage, in particular the mining and recovery as well as the reprocessing of spent fuel.[4] The first stage of the fuel cycle involves obtaining uranium from uranium ores through mining and milling (figure 1.1). Leading countries in this process include Australia, Canada, Kazakhstan, Russia, Namibia, and Niger who in 2009 collectively produced over 50,000 tonnes of uranium ore.[5] The ore is processed through several chemical reactions to yield a material that contains 65-70% uranium and is referred to as the infamous 'yellowcake', or U_3O_8. The natural isotopic abundance of uranium is 0.055%, 0.711%, and 99.28% of the isotopes U-234, U-235 and U-238 respectively.[6] Modern reactors require enriched fuel, which contains between 3-5% U-235. Thus, the yellowcake must be processed to improve the U-235 content *via* centrifugation or gas diffusion through porous membranes.[7] Once enriched, U_3O_8 is converted to UF_3. This UF_3 is further reacted to UO_3, reduced to UO_2 ceramic, and pressed into hollow pellets. UO_2 is the uranium-based compound that is used in nuclear reactors within the UK.

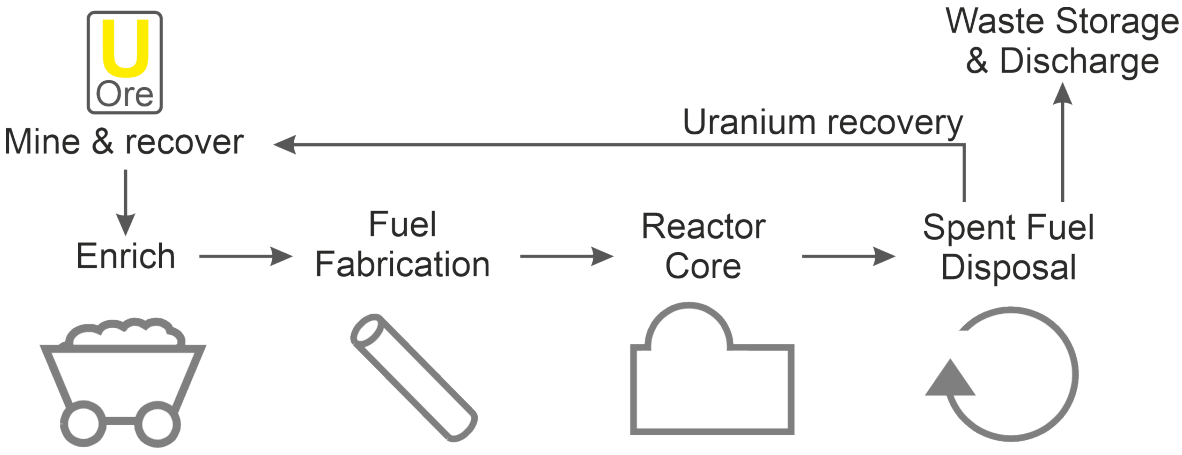

Figure 1.1. The nuclear fuel cycle starting at the mining of uranium ore and finishing with the storage, discharge, and recycling of fissile material.

The UO_2 pellets are loaded into zirconium or stainless-steel tubes to form fuel rods that are combined into fuel assemblies for easy insertion into the reactor core. Within the reactor U-235 undergoes nuclear fission through the adsorption of a neutron (equation 1.1). The fission event

causes the release of energy, in the form of heat, three additional neutrons and the fission by-products Ba-139 and Kr-94. The neutrons are released with sufficient energy to cause three further fission events, hence the term 'chain reaction' used to describe fission reactions. The thermal energy released is transferred to coolant which in turn heats water in the reactor boilers, turning it to steam. It is this steam which drives the turbines, generating electricity. After 3-4 years the fuel's activity will decrease to a point where it is regarded as 'spent'. The fuel is then transferred to a fuel pond, where it sits in water for an extended period. The fuel ponds carry many benefits including the allowing of: fuel cooling, the decay of short lived isotopes in a controlled environment and the containment of radiation.[8]

$$^{235}_{92}U + {}^{1}_{0}n \rightarrow {}^{139}_{56}Ba + {}^{94}_{36}Kr + 3\,{}^{1}_{0}n$$ **Equation 1.1**

By 2035 it is anticipated that all currently operational UK reactors will have ceased operation and the process of decommissioning will have begun.[9] This will involve the dismantling of all conventional equipment such as the turbines and generators as well as the removal of all spent nuclear fuel from the reactor cores and fuel ponds. The majority of this fuel will remain untouched for a long period of time; however, it will eventually require permanent storage in a geological disposal facility. Until 2018, fuel from the UK's AGR (Advanced Gas-Cooled Reactors) and Magnox reactors was sent for reprocessing to facilities such as Sellafield in Cumbria. Sellafield was responsible for the reprocessing of spent nuclear fuel from UK reactors since the beginning of the country's nuclear energy program. Here the removal of the stainless-steel fuel cladding of the fuel rods took place in order for the radioactive contents to undergo reprocessing. Reprocessing involved the dissolution of the spent fuel pellets in 4M nitric acid. Uranium and plutonium were separated from the fission products through the addition of kerosene and tributyl phosphate to the acidic mixture. The radionuclides concentrate in the organic phase allowing for easy extraction.[10] Uranium and plutonium are either then refined and recycled or sent for long-term storage as waste.

The remaining fission products undergo heating in a calciner followed by the addition of borosilicate granules to form a glass, in a process known as vitrification.[11] More volatile components of the remaining fission products are unable to be vitrified due to the high temperatures necessary to melt the borosilicate glass.[12] These components, such as technetium complexes, are difficult to isolate and consequently effluent-containing technetium is discharged into the sea as a last resort.[13]

As the reprocessing operations at Sellafield start to wind down there is now a requirement to undertake post-operation clean out of facilities, and to continue to process the waste products that have been temporarily stored on site. It is believed that it will take around 120 years to clean up 17 of the earliest nuclear sites within the UK and will cost between £99 and £232 billion.[14]

1.1 The Need for Nuclear Waste Clean-Up

The release of radioactive matter into local environments occurs *via* two pathways: (**1**) authorised discharge into water courses and (**2**) accidental release *via* leakage or mishap. While the reprocessing of nuclear fuel at sites such as Sellafield and Hanford (USA) is mostly completed without issue, spillages of radionuclide-contaminated water and solvent does occur. Underlying soil and groundwater at these sites have therefore been exposed to different radioactive isotopes that have been produced from the nuclear fission of uranium and plutonium. Accidental radioactive releases such as that seen at Chernobyl in 1986 resulted in severe soil, atmosphere, and water contamination in areas surrounding the reactor. Ever since this area has been unhabitable.[15] Airborne radionuclides such as iodine-131 were detected as far as Sweden within a week of the incident. Similar effects were also felt in 2011 when the Fukushima Daiichi power plant in Japan was hit by a tsunami.[16] This resulted in the disabling of reactor cooling to three of the stations units, the melt down of these reactors and as well as the generation and pressurisation of hydrogen gas, which ultimately detonated. Efforts to contain both these disasters resulted in the contamination of groundwater with radionuclides due to the leakage of contaminated water from the reactor systems. Figure 1.2 summarises the key pathways in which radionuclides are dispersed into local environments from nuclear sites.

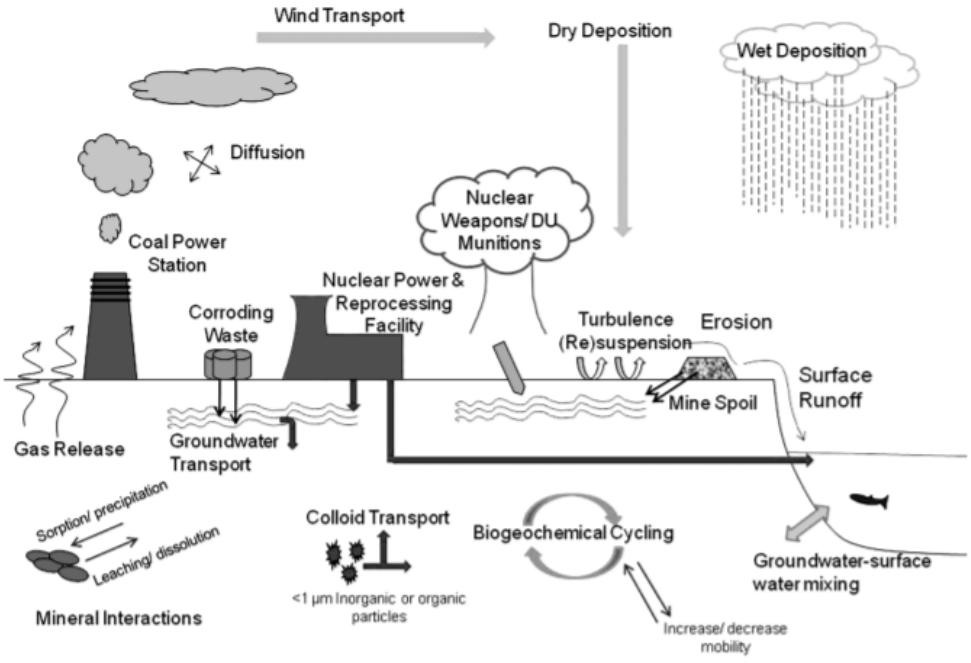

Figure 1.2. Summary of the main sources of radionuclides, the environmental pathways and the key processes controlling radionuclide migration by Renshaw *et al*.[17]

Legacy sites such as Hanford in the USA are now paying the price for the part it played, over 70 years ago, in the production of plutonium for the country's nuclear arsenal.[18] Described as '*the most*

toxic place in America' the site is home to 56 million gallons of chemical and nuclear waste, the clean-up of which will take 50 years to complete through a government contractor that is worth 110 billion US dollars.[19,20] In 2018, Washington state passed a bill into state law recognising the occupational diseases that are a direct consequence of working on the Hanford site and allowing for uncontested compensation to be obtained by those affected.[21]

The fission of uranium and plutonium produces a wide range of different radioisotopes, all of which have unique half-lives, decay energies, and decay pathways. Some waste products, such as Cs-137 and Sr-90, have short half-lives and do not pose as much of a challenge when compared to long lasting radioisotopes, including Cs-135 and Tc-99. Figure 1.3 shows the long legacy that one tonne of nuclear fuel leaves behind and demonstrates the necessity to control nuclear waste carefully to ensure accidental releases are avoided. When releases of radionuclides do occur, there needs to be clear techniques and suitable materials that can minimise spread of these harmful isotopes in the environment.

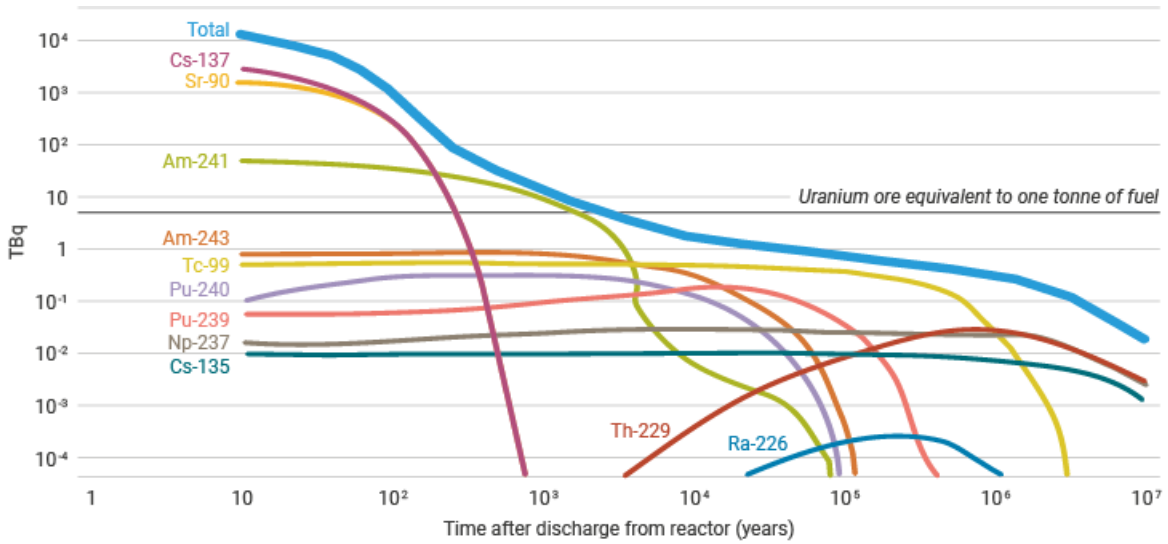

Figure 1.3. Activities of high-level waste from one tonne of nuclear fuel over increasing time. Source: IAEA, 1992, Radioactive waste management.

1.1.1 Iodine-131

Iodine-131 is a key product from the fission of U-235. The highly radioactive isotope has a half-life of just eight days and its volatility results in fast dispersal into the air. Within a few days of the Chernobyl disaster airborne I-131 was detected as far as Sweden, over 1000 km from source. The human thyroid naturally accumulates iodine and thus exposure to I-131 will quickly result in the concentration of the radionuclide. Preventative measures can be taken by administering potassium iodide tablets, containing a non-radioactive isotope, to fill the thyroid and stop the accumulation of I-131 in order for it to be naturally excreted.[22]

1.1.2 Strontium-90

Strontium-90 is a radioactive isotope of strontium that is not naturally occurring. Due to nuclear weapons testing during the 1950s and 60s however, Sr-90 is widely dispersed in our environment. It is also a component of nuclear waste from the energy sector.[23] Strontium *in vivo* behaves much like its alkali metal counterpart calcium, resulting in the incorporation and immobilisation of the radionuclide into bones, teeth, and soft tissue.[24] It has a half-life of 29 years, resulting in long-term exposure to radiation for the contaminated individual. Sr-90 will undergo beta decay into Y-90, which is also a beta emitter and therefore is a long-term problem. Due to its similarity to calcium, milk monitoring is important after large radioactive releases.

1.1.3 Caesium Isotopes

Caesium-137 carries many medical and industrial applications, including the use in radiation therapy devices and Geiger counter calibration.[25] Cs-137 for these purposes is produced from nuclear fission, any Cs-137 present in the environment is therefore as a result of nuclear weapons testing, nuclear accidents such as Chernobyl[26] or discharges from nuclear licenced sites. The radionuclide has a half-life of 30 years and undergoes decay *via* both beta and gamma irradiation. Consequently, the high concentrations of Cs-137 in the Irish Sea as a result of discharges from Sellafield is of high concern. Cs-137 is used as a benchmark to compare other isotopes' half-lives. A half-life shorter than that of Cs-137 is deemed to have a short life, while any half-lives above 30 years are long-lived isotopes.

Caesium-134 is also produced from the nuclear fission of U-235 but has a half-life of only two years. It is therefore of less long-term concern but is very useful as an isotopic signature following nuclear accidents. Cs-134 detection after the Fukushima accident allowed for the monitoring of radionuclide dispersal in the Pacific Ocean.[27]

1.1.4 Technetium-99

Technetium-99 makes up approximately 6.1% of waste from nuclear fuel and is found in the environment due to authorised and accidental releases.[28] The radionuclide has an extremely long half-life of $2x10^5$ years and thus is a major concern in the nuclear sector. It undergoes weak beta-emission (294 keV) to form stable ruthenium-99 (equation 1.2). A technetium neutron transforms into both a proton and electron, resulting in a 1+ increase in its proton number. This decay also releases an neutrino, denoted as ν_e in equation 1.2.

$$^{99}_{43}Tc \rightarrow {}^{99}_{44}Ru + {}^{0}_{-1}e + {}^{0}_{0}\nu_e$$ **Equation 1.2**

Technetium's redox chemistry plays a major role in its environmental mobility. The radionuclide is very susceptible to oxidation and therefore most stable in the form of the TcO_4^- anion, commonly known as pertechnetate (figure 1.4). This tetrahedral anion is known for being a highly soluble (11 mol L^{-1}),[29] nonreactive, and due to its low affinity to mineral surfaces is very mobile.[30,31] This arises due to the negative charge that is often carried by minerals and soil which results in weaker reactivity towards TcO_4^- over other radionuclides such as Cs-137 and Sr-90 which both commonly exist as mono and divalent cations respectively. The radionuclide is regarded as one of the most mobile radioactive species. Leaks of nuclear effluent from Sellafield has resulted in far spread contamination of underlying soil and groundwater. Tc-99 has been found in groundwater outside of the Sellafield perimeter wall in high concentrations (50-60 Bq L^{-1}).[32]

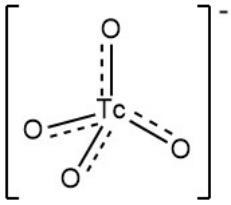

Figure 1.4. Chemical structure of pertechnetate.

When Tc-99 containing effluent is discharged from nuclear licenced sites it can have serious, long-term environmental consequences. Discharges from Sellafield in the UK have been related to a 44-fold increase in technetium found in Irish Sea lobster[33] and the accumulation of the radionuclide in Norwegian seaweed and crab in as little time as four years.[13] These incidents highlight the easy dispersal of pertechnetate by the Gulf Stream to Scandinavian waters, over 1000 km from source (figure 1.5). The highly oxygenated waters of the Irish sea ensures that Tc-99 is present in the form of mobile pertechnetate. Through accumulation of technetium in crab and lobster, the radionuclide is able to enter the human food chain. Technetium is analogous to iodine in that it accumulates in the human thyroid, exposing the body to beta emission over a long period of time.[7] This enhances the risk of the consumer developing cancers.

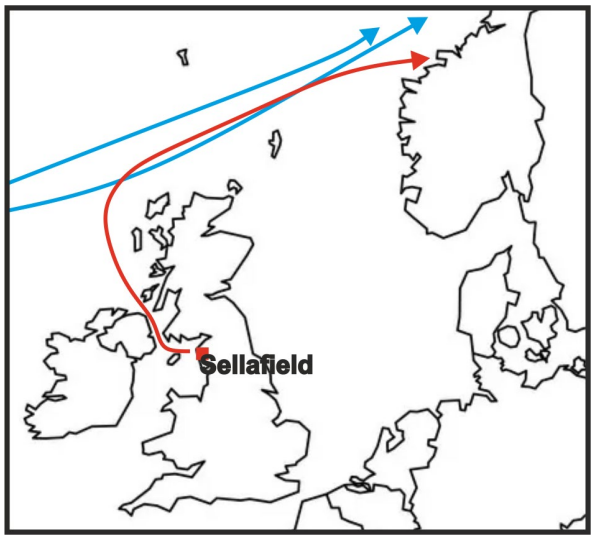

Figure 1.5. Illustrative map of Tc-99 transport (red line) from Sellafield, UK (red square), to Scandinavia *via* the Gulf stream (blue line).

Technetium-99 is not to be confused with technetium-99m, a metastable nuclear isotope used in medicine. Tc-99m has a much shorter half-life of 6 hours and is also a gamma-emitter. The latter property means that the isotope is both less harmful to humans and more penetrating. Consequently, Tc-99m is a very popular radioactive tracer in modern medicine. Tc-99m containing TRODAT-1 has been shown as a promising tracer for the imaging of dopamine transporters in the human brain.[34] Biomolecules, such as the one presented in figure 1.6, have also been labelled with Tc-99m and utilised in tumour imaging.[35]

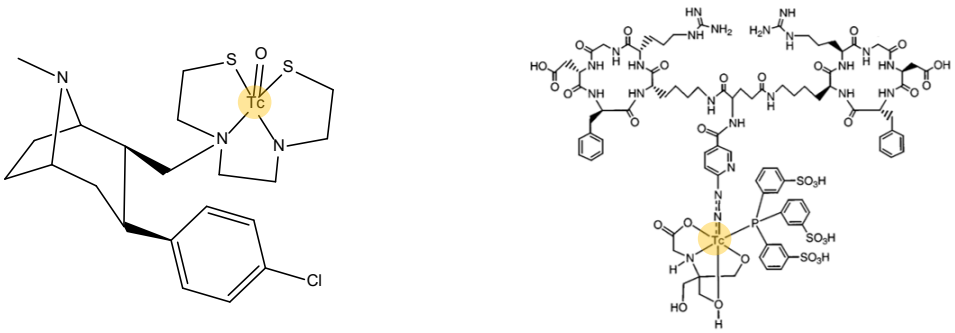

Figure 1.6. Chemical structures of (left) the dopamine transporter imager, TRODAT-1, and (right) Tc-labelled vitronectin receptor antagonist complex.

1.2 An Introduction to Metal-Organic Frameworks

Despite being a relatively young class in materials chemistry, metal-organic frameworks (MOFs) have gained substantial interest in a vast number of fields, including heterogeneous catalysis,[36,37] gas storage[38] and separations.[39] Exploiting the material's porosity has led recent research into more novel directions. This includes the transport and delivery of hydrophobic drugs[40] and the detection of tumours.[41] The mechanical robustness of some MOFs has even envisaged the materials being used in shock absorption.[42]

MOFs are a subclass of coordination networks, which in turn are a subclass of coordination polymers. Figure 1.7 summarises such and contains the IUPAC (International Union of Pure and Applied Chemistry) definitions of each material class.[43] What differentiates MOFs from other coordination polymers is that they contain potential voids, commonly filled with solvent molecules from synthesis, and strictly must be formed from metal nodes and organic linker molecules. These voids are typically filled with solvent molecules from the MOF synthesis. Throughout this thesis we regard all not previously reported materials as a MOF if, as confirmed by single-crystal X-Ray diffraction, they extend in at least two dimensions and display possible porosity. If they do not meet these criteria, we refer to them as coordination polymers. For simplicity, if the material has previously been reported, we categorise it based upon the class it has been assigned in literature.

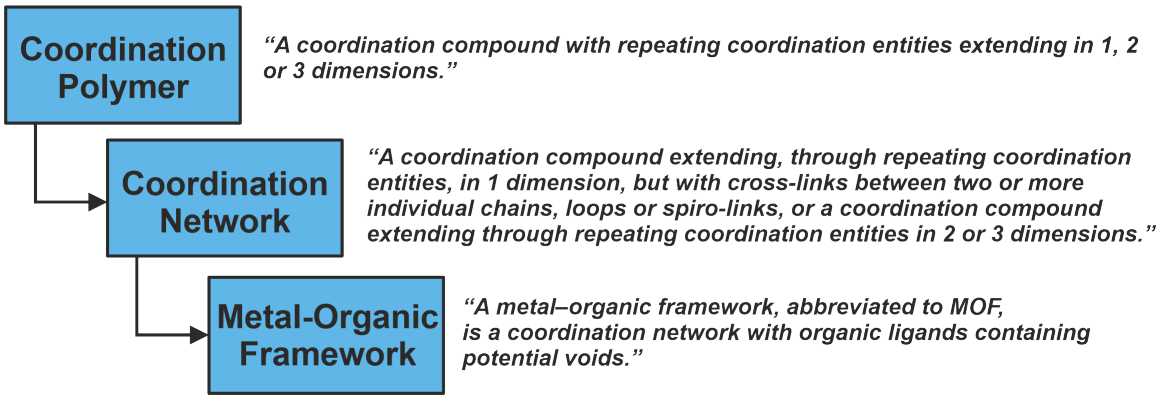

Figure 1.7. Diagram showing the IUPAC definitions of a coordination polymer, coordination network and metal-organic framework,[43] and how they relate to one another.

The term 'metal-organic framework' was first introduced by Yaghi in the late 1990s.[44,45] The combination of different metals with organic linkers can afford materials with varying topologies. Figure 1.8 demonstrates that using metals of different coordination numbers with ligands of varying binding modes results in materials with very differing structures.

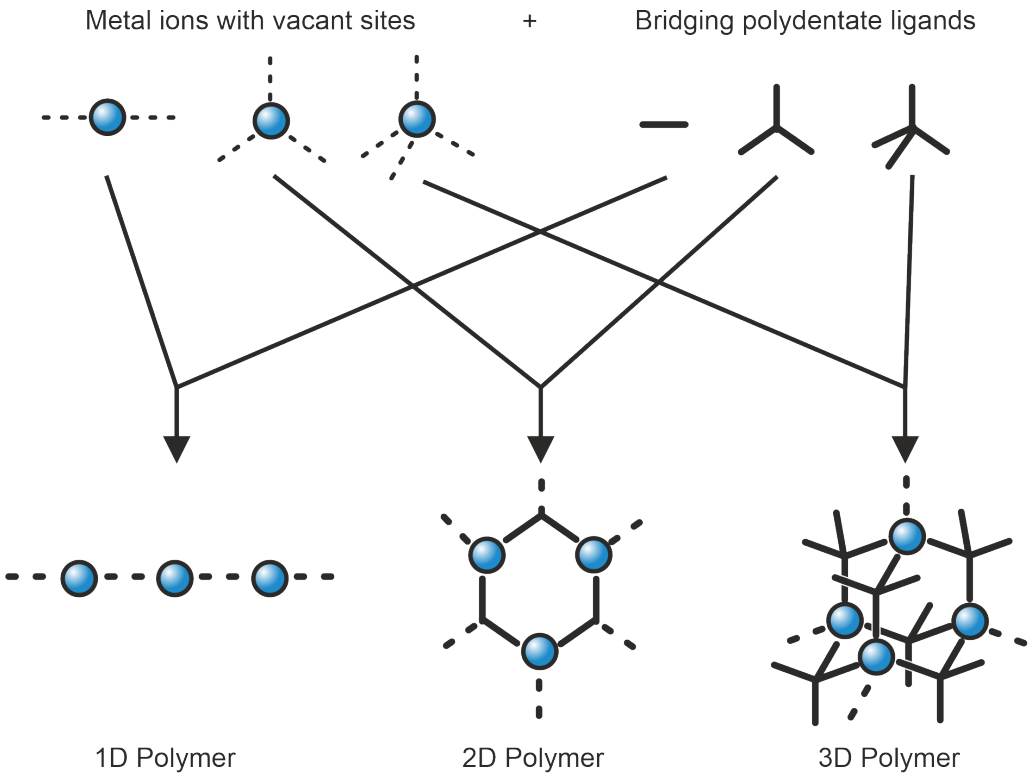

Figure 1.8. Construction of coordination polymers extending in different dimensions from a variety of metal nodes and bridging ligands.

The first efforts into the formation of extended coordination networks were carried out by Robson and Hoskin in 1989.[46] $[Cu(CH_3CN)_4][BF_4]$ and 4,4',4'',4'''-tetracyanotetraphenylmethane (TTPM) were dissolved in nitrobenzene and single crystals of the infinite network, shown in figure 1.9, were formed by slow evaporation of the solvent. The nitrogen atom of the nitrile groups on TTPM coordinate to independent tetrahedral copper metal centres, resulting in an overall diamond topology (**dia**). Charge balancing tetrafluoroborate anions and nitrobenzene solvent molecules are found, but disordered, within the network's large voids. They investigated the material's ability to undergo anion exchange by soaking crystals of the network in a saturated solution of tetrabutylammonium hexafluorophosphate (NBu_4PF_6) and observing the simultaneous migration of PF_6^- into and BF_4^- out of the material *via* Fourier transform infrared spectroscopy (FTIR). With this preliminary work, Robson and Hoskin recognised the potential for this class of materials in the fields of molecular sieves, heterogeneous catalysis, and anion exchangers.

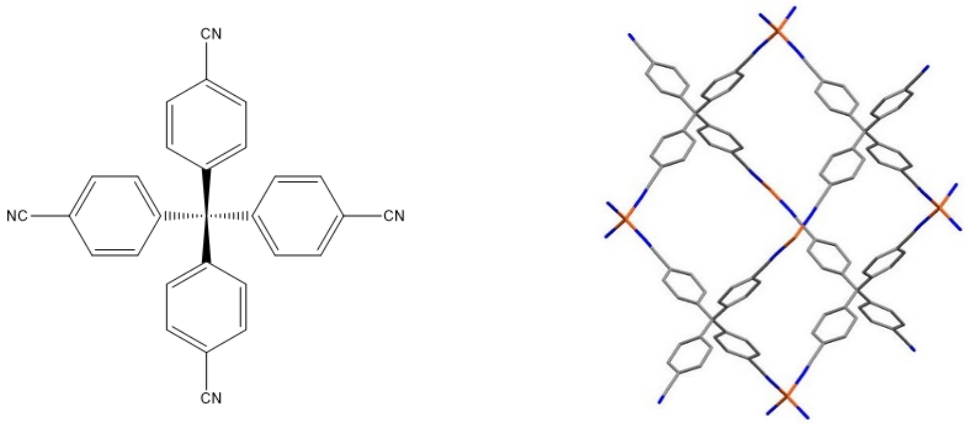

Figure 1.9. (Left) Structure of 4,4',4'',4'''- tetracyanotetraphenylmethane (TTPM). (Right) Crystal structure of Robson and Hoskin's copper-TTPM network. Brown = copper, blue = nitrogen and grey = carbon.

Despite the suggestion by Robson and Hoskin to use coordination networks for heterogeneous catalysis it was not for a further five years that this actually took place. Fujita *et al.* in 1994 designed a cadmium and 4,4'-bipyridine (4,4'-BPY) two-dimensional square networked material ($[Cd(4,4'\text{-}BPY)_2(NO_3)_2]$) (figure 1.10).[47] This material also utilised a nitrogen donor ligand similar to that seen in Robson and Hoskin's structure. The square networked material was able to catalyse the cyanosilylation of aldehydes. The same network was also able to selectively capture ortho dibromobenzene and dichlorobenzene over their meta and para structural isomers suggesting the potential use of these materials in molecular separations.

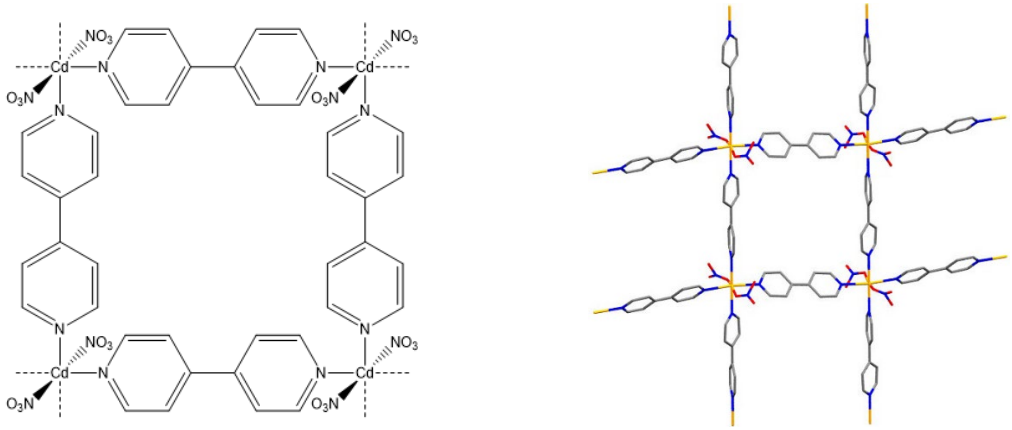

Figure 1.10. (Left) Chemical structure of $[Cd(4,4'\text{-}BPY)_2][NO_3]_2$. (Right) Crystal structure of $[Cd(4,4'\text{-}BPY)_2][NO_3]_2$.[47] Orange = cadmium, blue = nitrogen, red = oxygen and grey = carbon.

1.2.1 Metal-Organic Framework Design

The interchangeable building block nature of MOFs opens up the opportunity for a vast catalogue of different structures. As of 2018, there are estimated to be over 70,000 MOF entries in the Cambridge structural database (CSD).[48] By varying the metal and organic linkers utilised one is able

to manipulate the pore shape and size, aperture dimensions, and the overall topology of a framework.[49] Additionally, the incorporation of different chemical functionalities into frameworks allows for the fine-tuning of host-guest interactions that are integral for many MOF applications.[50] In this section we discuss some of the key MOF building blocks, how predictability of such monomers allows for the design of topologically identical frameworks in an area known as isoreticular chemistry and how MOFs can be altered after their initial synthesis through a process known as post-synthetic modification (PSM).

1.2.1.1 Metal Nodes

The simplest of metal nodes found in MOF structures is a single metal ion. Metal nodes that consist of a lone metal ion are referred to as primary building units (PBU), a term coined from the zeolite field.[51] The most famous group of MOFs that contain PBUs is the zeolitic imidazolate framework (ZIF) family.[52] First developed by Yaghi *et al.* in 2006, this group of materials were inspired by zeolites and as a result share the same topology as many of their aluminosilicate counterparts.[53] Initially 12 different ZIFs, composed of either zinc or cobalt PBUs and imidazole derived organic linkers were synthesised. Imidazole can be deprotonated to form an imidazolate anion that coordinates to the cationic PBUs affording a neutral framework. The topological similarities between ZIFs and zeolites is as a result of the bridging angle of the imidazolate anion equalling close to 145° which is coincident with the Si-O-Si bond angle in many zeolites. This is shown, schematically in figure 1.11.

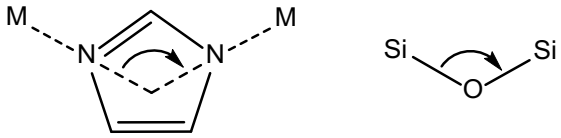

Figure 1.11. Bridging angles of (left) imidazolates to two different metals and (right) its similarity to the Si-O-Si bonds within zeolites.

ZIF-8 ($Zn(2\text{-}MIM)_2$) (2-MIM = 2-methylimidazole), for example, consists of either zinc or cobalt metal ions in a tetrahedral coordination environment. Each metal centre is coordinated to four 2-MIM linker molecules through one of the nitrogen atoms of the organic molecule as seen in figure 1.12. The overall topology of this framework is the **sod** topology, similarly adopted by the sodalite class of zeolites. ZIF-8 was shown to be stable when left in boiling solvents, including 8 M sodium hydroxide solutions, for over 24 hours. In the cases of boiling methanol and water, the framework did not undergo degradation even after seven days demonstrating the robustness of the material. Additionally the biocompatibility of ZIF-8 precursors has led to substantial work into the use of ZIF-8 in biomedical applications.[54–56]

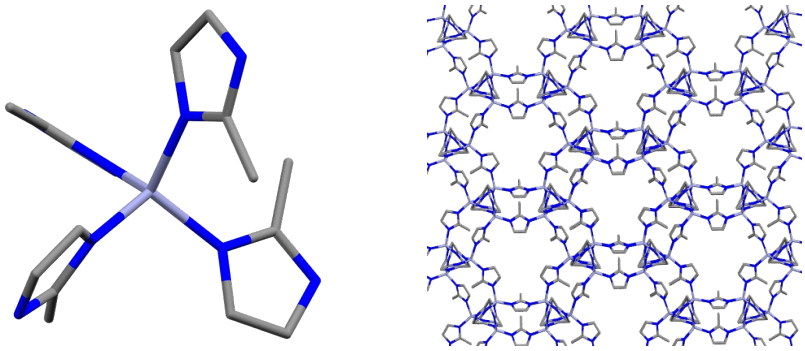

Figure 1.12. (Left) Tetrahedral PBU of ZIF-8. (Right) Crystal structure of ZIF-8.[57]

Additional metal centres can be incorporated into the metal nodes to form clusters. These metal aggregates are supported by bridging interactions from organic linkers and are referred to as secondary building units (SBU). The number of metal ion centres within an SBU vary, but are not limited to, between two and six ions. Linear SBU chains have been reported and hence in these cases the number of metal ions is, in theory, infinite. SBUs are most commonly found within MOFs containing polycarboxylic acid organic linkers. This is consequential of the varying bonding modes available to the carboxylate functionality, presented in figure 1.13, which allows for the coordination of one organic linker to two metal centres within the same SBU.[58] The formation of SBUs allows for a much wider variety of metal node geometries, which in turn affords a vast catalogue of different framework topologies.

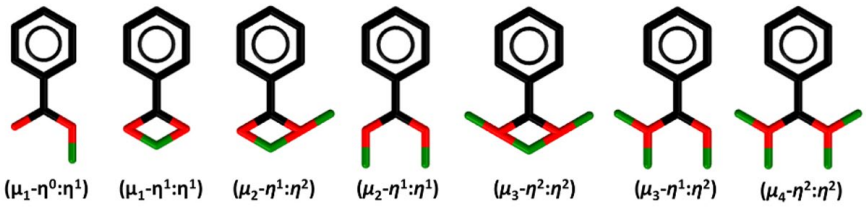

Figure 1.13. The different bonding modes that a carboxylate functionality can undergo to one or more metal centres demonstrating the diversity of connectivity's available with this functional group.[58] **Reproduced with permission from Elsevier.**

The bridging bonding mode of carboxylate functionalities is well demonstrated in the paddlewheel SBU found in the copper-based MOF, HKUST-1 ($[Cu(BTC)_3]$) (HKUST = Hong Kong University of Science and Technology). This SBU consists of two copper (II) centres coordinated to four independent 1,3,5-benzenetricarboxylic acid (H_3BTC) organic linker molecules which are arranged 90° apart, as shown below in figure 1.14. Terminal water molecules cap each copper centre and can be removed by heating the material to yield unsaturated metal sites, useful in catalysis and selective binding. It is also possible to replace the solvent molecules with nitrogen donor ligands, such as 1,4-diazabicyclo[2.2.2]octane (DABCO) or pyridine-based ligands. Additionally, the metal centres can be replaced with a variety of different transition metals. These include zinc,[59] cobalt,[60] and

nickel[61] which all possess a 2+ oxidation state and thus yield a neutral framework. Iron-based paddlewheel materials have also been synthesised, however an imbalance of charge is experienced due to the available 3+ oxidation state of the metal, which therefore requires an additional counter anion within the framework's pores to compensate.[62]

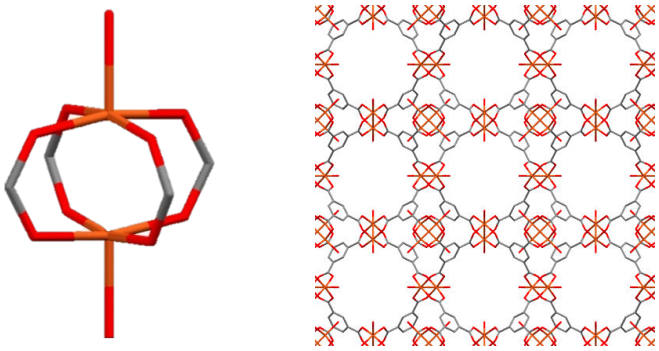

Figure 1.14. (Left) Paddlewheel SBU of HKUST-1. (Right) Crystal structure of HKUST-1.[63]

A well-known octahedral SBU belongs to the IRMOF (**I**so**R**eticular **MOF**) family. This SBU, which is presented in figure 1.15, consists of four tetrahedral zinc metal cations arranged around an oxide anion (μ_4-O^{2-}) that also possesses a tetrahedral geometry.[64] Six organic linkers coordinate to the SBU through their bridging carboxylate functionalities to two of the zinc centres affording the octahedral geometry of the node. When linear organic linkers, such as 1,4-benzenedicarboxylic acid (H_2BDC), are combined with this octahedral SBU the resulting MOF (IRMOF-1) ($[Zn_4O(BDC)_3]$) follows a **pcu** topology, as shown in figure 1.15. The discovery of IRMOF-1 kick started the field of isoreticular chemistry, pioneered by Yaghi and O'Keefe.[44]

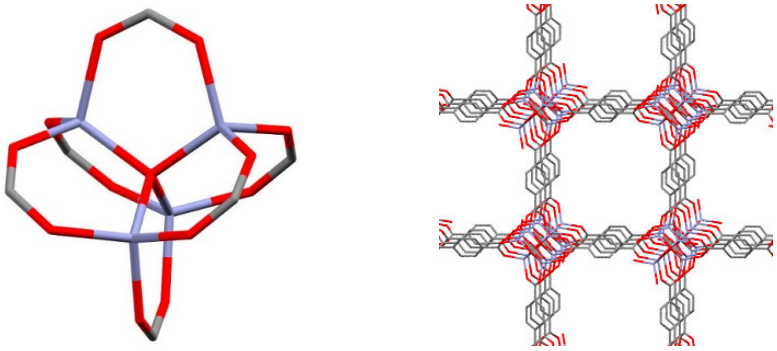

Figure 1.15. (left) Octahedral SBU of IRMOF-1. (Right) Crystal structure of IRMOF-1.[65]

Infinite SBUs consist of carboxylate groups that bridge metal centres in such a fashion that it results in the formation of an infinite chain of metal ions. MIL-53 (Matériaux de l'Institut Lavoisier) is an example of this (figure 1.16). Octahedral metal centres (typically Fe, Al or Cr) are coordinated to six oxygen atoms, four from independent carboxylate groups of BDC and two from bridging μ_2-OH hydroxyl groups.[66] The resulting framework contains diamond shaped channels that respond to external stimuli by either opening to increase the channel volume or closing to cause the reverse.

This ability to adjust to changes in gas composition as well as pressure is referred to as breathing and is of large interest to many.[67]

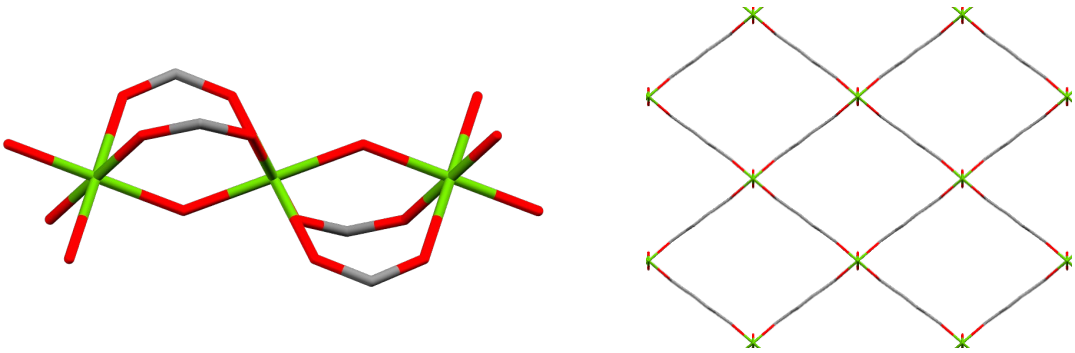

Figure 1.16. (Left) Infinite SBU of MIL-53(Cr). (Right) Crystal structure of MIL-53(Cr).[68]

1.2.1.2 Organic Linkers

Nitrogen donor ligands are popular organic linkers in MOF synthesis. They are typically neutral molecules, thus counter ions are required to balance the positive charge of the metal nodes. Anions present as a by-product from the synthesis of the MOF can be found within the materials voids. These anions can often be exchanged by washing the MOF in a solution of the desired anion. Some commonly used nitrogen donor linkers are shown in figure 1.17.

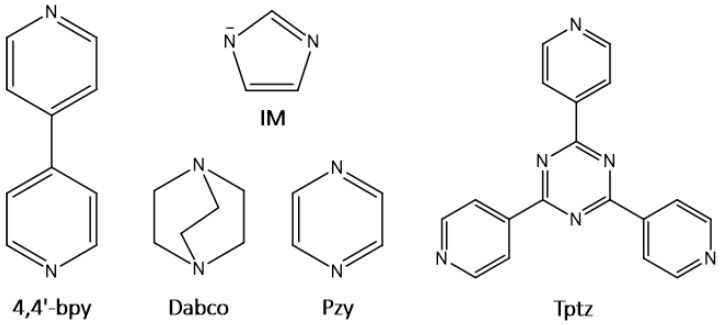

Figure 1.17. Commonly used nitrogen donor linkers in MOF synthesis.

4,4'-bipyridine (4,4'-BPY) is a well-used nitrogen donor linker because of its linear and rigid structure and results in cationic frameworks. Oliver *et al.* reported the linear coordination polymer $[Cu(4,4'\text{-}BPY)][O_3SCH_2CH_2SO_3]$ which consists of Cu (I) cations coordinated to two 4,4'-BPY linkers.[69] π-π stacking between layers of the material add in stabilisation. The loosely bound alkanedisulphonate anions can be easily exchanged for alternative anions.

Polycarboxylates are also very commonly used organic linkers in the synthesis of MOFs for several reasons. Utilising anionic linker molecules, such as polycarboxylates, allows for the formation of neutral frameworks upon combination with the cationic metal nodes. Consequently, counter ions within the pores are not required to balance charge.

Many carboxylate-based frameworks are thermally stable, thus allowing for solvent contained within the material's pores to be removed without deformation of the overall structure. While the metal-carboxylate bonds are relatively strong, aiding in framework thermal stability and robustness, their formation is still reversible. This aids in the formation of crystalline materials.

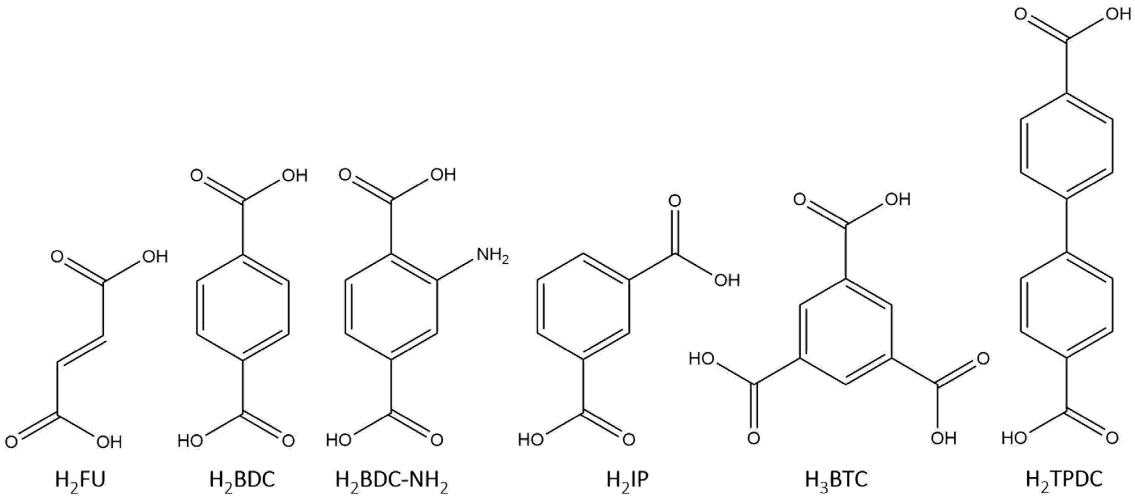

Figure 1.18. Commonly used polycarboxylate linkers in MOF synthesis.

1.2.1.3 Isoreticular Chemistry

In the early 2000s Yaghi and O'Keefe developed isoreticular chemistry. They combined zinc and dicarboxylic acid linkers with known geometries resulting in the formation of the IRMOF series($[Zn_4O(L)_3]$) (L = linker).[70] The IRMOF series all have the same net topology (**pcu**) but differ in pore size and functional group tags.[44,45] By changing the length of the dicarboxylate organic linker, the pore volume and aperture size can also be controlled. This is evident in figure 1.19 which shows the pore sizes of IRMOFs-1, -2, -10 and -14. IRMOF-1 is constructed of the H_2BDC linker and has a crystal free volume of 79.2%. By changing the organic linker for one that is longer such as biphenyl-1,4'-dicarboxylic acid (H_2BPDC), in IRMOF-10, results in an increase in free volume by 7.8%. The organic linkers can also be swapped for molecules that have additional functional groups attached. IRMOF-2 utilises 2-bromobenzene-1,4-dicarboxylic acid. The introduction of a bromine atom does not alter the frameworks topology and can be useful in changing the material's properties. It does however cause a small decrease in free volume, when compared to IRMOF-1, by 0.8%.

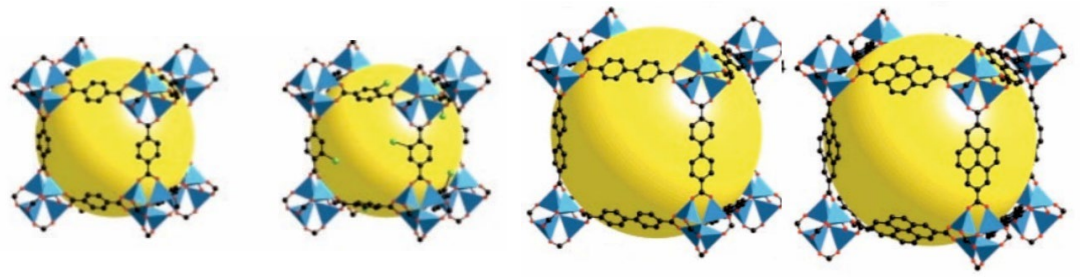

Figure 1.19. Crystal structures of IRMOF-1, IRMOF-2, IRMOF-10 and IRMOF-14. The yellow spheres represent the largest van der Waal spheres that can fit within the cavities of these materials.

Isoreticular chemistry can also be applied to other frameworks, including the UiO series ($[Zr_6O_4(OH)_4L_6]$) (L = linker). The UiO-66 series consists of cuboctahedral SBUs linked by the dicarboxylic acid H_2BDC. As seen for the IRMOF series this organic linker can be replaced by polycarboxylates of different lengths and linkers bearing various chemical functionalities whilst maintaining its **fcu** topology. UiO-67 has the same topology as that of UiO-66, however the organic linker has been interchanged with H_2BPDC. This increases both pore and aperture sizes. Functionalisation of the H_2BDC linker is also well explored. UiO-66-NH_2 is a very commonly used MOF which is formed from the functionalised organic linker, aminobenzene-1,4-dicarboxylic acid (H_2BDC-NH_2).

1.2.1.4 Interpenetration

Interpenetration is a phenomenon seen in some MOFs as a result of the large void spaces generated within some structures. To avoid void spaces, an independent network may form within these spaces. The networks extend continuously through one another and, despite not being chemically bonded together, cannot be separated without the breaking of covalent bonds. Frameworks undergo interpenetration to varying degrees. The two-fold interpenetrated framework $[Zn_4(OH)_2(cpip)_2(4,4'\text{-bipy})]$ (cpip = 5-(4-carboxyphenoxy)isophthalic acid) was discovered by Wang *et al.* Figure 1.20 shows the entangled structures of the two networks. Higher levels of interpenetration have also been found by Sun *et al.*[71] They found a six-fold interpenetrated structure with a **dia** topology, $[Zn(iib)_2]_4{\cdot}H_2O$ (iib = 1-(imidazole-1-yl)-4-(imidazole-4-yl)benzene), which is also shown in Figure 1.20.

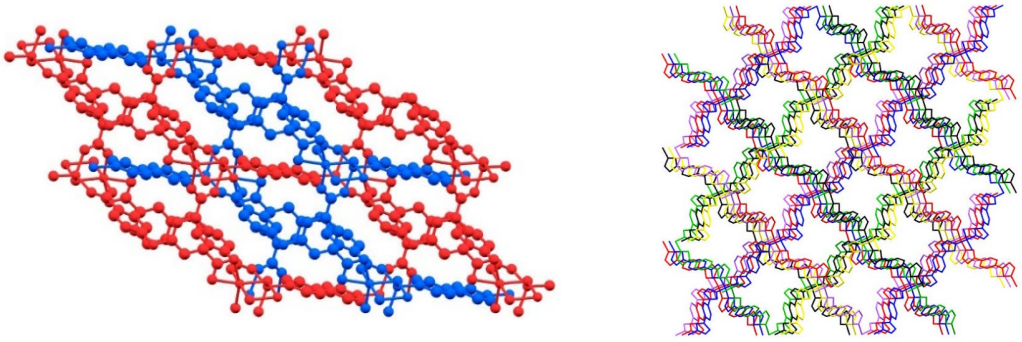

Figure 1.20. (Left) The two-fold interpenetrated structure of $[Zn_4(OH)_2(cpip)_2(4,4'\text{-bipy})]$. (Right) The six-fold interpenetrated structure of $[Zn(iib)_2]_4H_2O$. Colours have been applied to show the different networks.

Interpenetration is also visible in some frameworks of the IRMOF family. IRMOF-9 ($Zn_4O(BDPC)_3$) (H_2BDPC = biphenyl-4,4'-dicarboxylic acid) has been shown to have a doubly interpenetrated structure, consequential of the longer organic linker.[70] Yaghi *et al.* were able to prevent interpenetration in larger pore IRMOFs by considerable dilution of reaction mixtures. For many MOFs, including UiO-66 and HKUST-1, the pores are too small and the nodes are too highly connected to allow for the occupation of an additional network, and therefore do not undergo interpenetration. Non-interpenetrated networks have a much higher free volume and hence lower density. Consequently, it is non-interpenetrated materials that are more suited for gas adsorption and small molecule storage.[72]

1.2.1.5 Post-Synthetic Modification

Simple functionalities, such as amines and halogens, can be included in a MOF structure with the use of pre-functionalised organic linkers. This has been extensively seen for the framework UiO-66-NH_2 that makes use of the dicarboxylic linker $H_2BDC\text{-}NH_2$.[73] Due to the conditions required for MOF synthesis being often harsh and non-innocent, the use of decorated linkers however is not always a viable option in incorporating complex moieties into a framework.[74] In addition, some functional groups can interact with metal centres and thus affect the formation of the framework through SBU coordination. The integration of additional moieties through chemical functionalisation is often essential in the fine-tuning of MOF properties and as a result, a strategy to overcome this limitation has been developed.[75]

Post-synthetic modification (PSM) is the process of altering a MOFs structure after its synthesis to change the chemical properties, pore size and sensing capabilities of the parent framework.[76] These reactions can take many different forms but are generally categorised into four main groups (figure

1.21); (**1**) covalent PSM, (**2**) post-synthetic ligand exchange (PSLE), (**3**) dative PSM and (**4**) post-synthetic transmetalation (PST).[77]

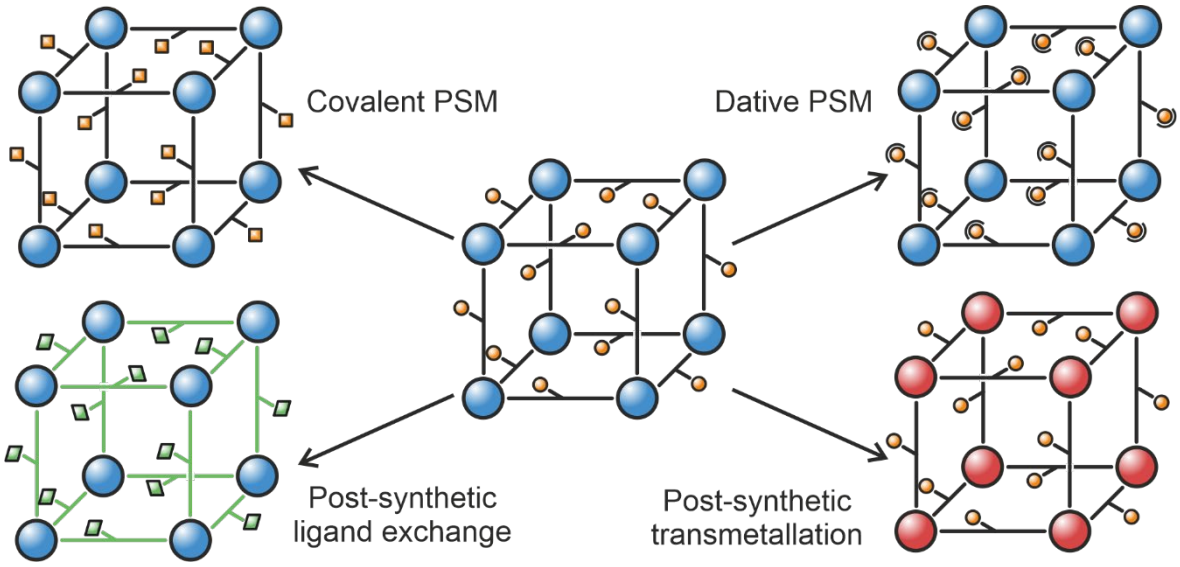

Figure 1.21. Different strategies available for post-synthetic modifications of MOFs.

Covalent PSM is the most common form of PSM reaction. This involves the reaction of a small molecule with a 'tag' functional group on the organic linker of the parent framework. This generates a new moiety that dangles into the pores of the MOF. For this type of reaction to be successful the reacting molecule must be small enough to diffuse through the framework's apertures to reach the inner pores and, in most cases, the reaction should be able to proceed without the use of a catalyst to minimise pore blockage and separation issues.[78] Characterisation of this type of PSM typically involves liquid ^{1}H NMR spectroscopy: the framework is digested with either acid or base into deuterated solvent and the organic linkers of the framework are dissolved into this solution. The integrals of the parent and daughter linkers in the spectrum can be compared to obtain a ratio which elucidates the reaction conversion.[79] Care must be taken however to ensure that framework degradation does not cause a further chemical reaction with the organic linker or the derived conversion will not be representative of the daughter material. FTIR has also been employed to quantitatively measure covalent PSM conversions without the need for material degradation.[80]

Halls *et al.* tested the functionalisation of various amine-based MOFs with ferrocenecarboxylic anhydride to form a ferrocenyl amide group (scheme 1.1).[81] The reaction was highly dependent on the pore size of the MOF due to the size of the reagent and therefore a wide range of conversions, from 100% to as low as 5%, was achieved. The daughter frameworks were redox active due to the presence of the iron centre.

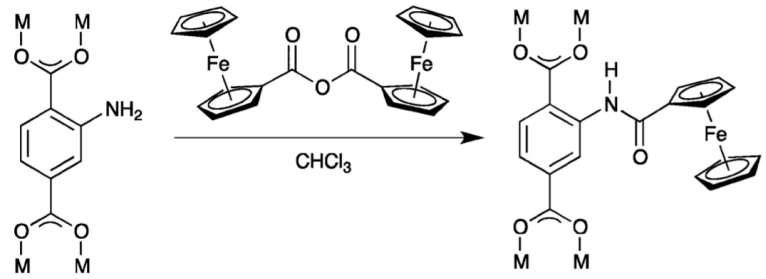

Scheme 1.1. Post-synthetic modification of the amine group with ferrocenecarboxylic anhydride to give a ferrocenyl amide functionalised MOF by Halls *et al*.[81] Reproduced with permission from The Royal Society of Chemistry.

Marshall *et al.* utilised covalent PSM reactions to induce mechanical changes to zirconium-based frameworks through the change in hybridisation of linking alkyl chains.[82,83] $[Zr_6O_4(OH)_4(EDB)_6]$ (EDB = 4,4'-ethynylenedibenzoate) and $[Zr_6O_4(OH)_4(SDC)_6]$ (SDC = 4,4'-stilbene-dicarboxylate) were treated with bromine in chloroform resulting in bromination of the alkyne or alkene functionality respectively (scheme 1.2). The change in hybridisation of the carbon atoms caused single-crystal to single-crystal (SCSC) contraction and in the case of the alkyne-based MOF resulted in a 4% reduction in unit cell volume. They additionally carried out preliminary studies into the alkyne materials ability to permanently trap I_2 vapours through the same mechanism. They reported 41% I_2 removal and thus the potential for use in nuclear waste remediation applications. PSMs are typically used to improve a material's properties for intended applications, but the authors here have sophisticatedly shown that a PSM reaction can itself be used as the desired application.

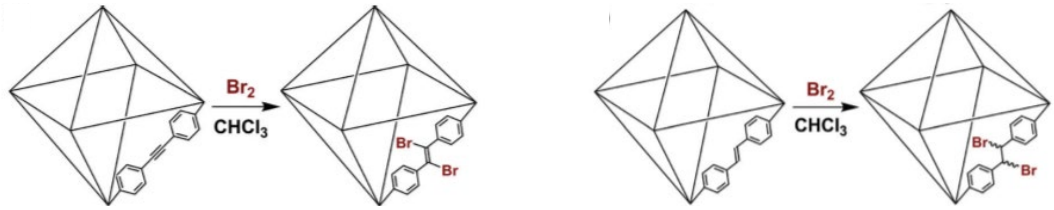

Scheme 1.2. Bromination of (left) $[Zr_6O_4(OH)_4(EDB)_6]$ and (right) $[Zr_6O_4(OH)_4(SDC)_6]$ *via* covalent PSM reactions to yield a change in hybridisation of the carbon atoms within the organic linkers by Marshall *et al*.[82,83] Reproduced under CC-BY license.

Aguilera-Sigalat *et al.* have demonstrated the use of photo-hydroxylation to graft -OH functional groups to the aromatic rings of UiO-66.[78] Various techniques for this PSM were probed and yielded conversions up to 77%. The use of TiO_2 alone resulted in moderate conversion however, the separation of the catalyst and MOF proved problematic. This was overcome through the use of γ-Fe_2O_3@SiO_2@TiO_2 nanoparticles which allowed for easy separation from MOF crystals with a magnet post-reaction, and also obtained the highest photocatalytic activity.

The aldehyde bearing framework ZIF-90 has been well explored for PSM reactions (scheme 1.3). The aldehyde group has undergone an imine condensation, reduction to an alcohol with $NaBH_4$ and conversion to a fluorescent dicyanovinyl group.[84,85] The latter PSM reaction can be further reacted with cyanide which results in the fluorescent quenching of the MOF, proposing its use for the detection of the highly toxic anion.

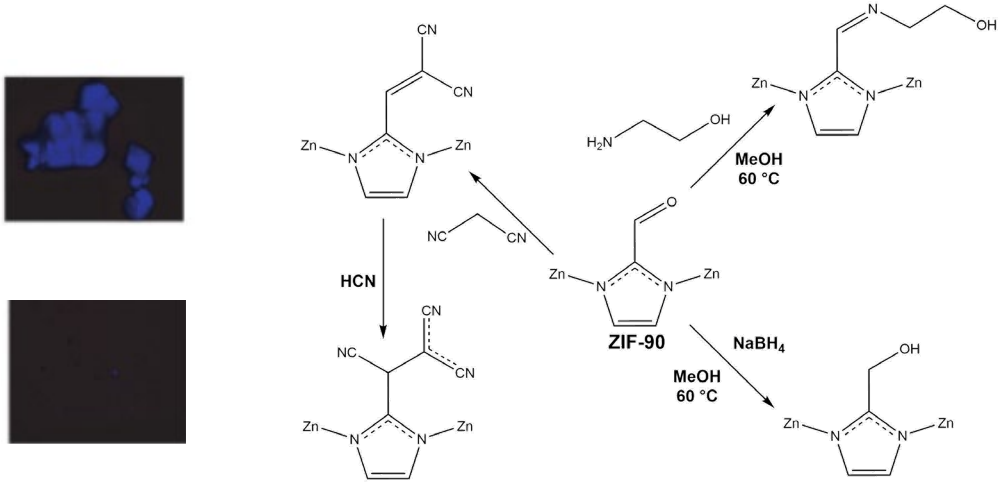

Scheme 1.3. Covalent PSM reactions of ZIF-90 with ethanolamine, $NaBH_4$ and malononitrile. (Left) Fluorescent quenching of ZIF-90 PSM product by reaction with CN^-.[85] Reproduced with permission from Wiley.

Purposefully reacting large and bulky substituents with framework crystals results in the covalent grafting of the reagent to the MOF surface, with no PSM reactions occurring within the material's pores. This methodology has allowed for DNA strands to be attached to MOF crystals, improving the stability of the bio-polymer and improving cellular uptake.[86] Rare-earth MOF nanoparticles have been stabilised by coating the crystals in poly(vinylpyrrolidone) (PVP) and then further coated with silica.[87] The MOF can be decomposed, and removed to produce hollow silica nanoshells.

Post-synthetic ligand exchange (PSLE) involves the replacement of an incorporated organic linker with a different linking molecule. The parent framework is added to a solution of the desired linker and the exchange of the organic linkers is allowed to take place. This method commonly leads to mixed-linker MOFs as the reaction conversion is rarely 100%. It can also be very difficult to control where within the crystal the linker exchange takes place resulting in uneven distribution of organic groups and the potential for core-shell architectures.[88] Fluch *et al.* have shown that in UiO-66 the BDC linker can be uniformly exchanged with BDC-I (BDC-I = 2-iodobenzenedicarboxylate) because the migration of the latter linker through the MOF crystals is much faster than the exchange process.[89] They used synchrotron-based Rutherford backscattering spectroscopy to study this, elucidating the little understood linker exchange mechanism. An appreciation for PSLE mechanisms is essential in understanding the daughter product. Preservation of framework topology can often

only be obtained if the PSLE follows an interconversion process, i.e. the parent linkers are physically replaced by the introduced linker, whilst the overall framework is maintained. If the process involves dissolution of the parent framework, followed by recrystallisation of the desired MOF (dissolution-recrystallisation) then the opportunity for potentially undesired topologies and structures arises. A good example of this is the ZIF family, which despite their high stabilities and physical properties can undergo facile interconversions through a dissolution-recrystallisation mechanism when dispersed in different linker solutions, some of which undergo topology transformations (scheme 1.4).[90]

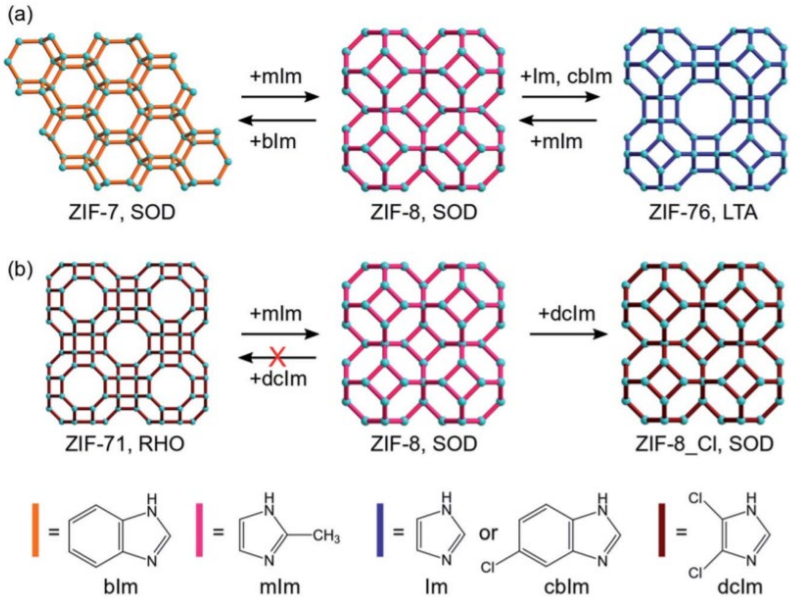

Scheme 1.4. Schematic illustration of a) reversible and b) irreversible PSLE reactions of ZIFs.[90] Reproduced with permission from The Royal Society of Chemistry.

Post-synthetic transmetalation (PST) is the process of replacing metal ions located in the metal nodes of a framework with a different metal and is often referred to as a form of metathesis.[91] PST allows access to mixed-metal frameworks which could be difficult to obtain from direct synthesis[92] and core-shell heterostructures whereby MOF crystals undergo PST to only the external crystal surfaces, as demonstrated by Song *et al.* in 2012.[93] Kim *et al.* showed the first complete and reversible PST reaction which involved the replacement of Cd^{2+} with Pb^{2+} from a Cd-MOF.[94] The reaction did not cause any loss to crystallinity or change to framework topology. It took two weeks for complete conversion to occur but only two hours to reach a conversion of 98%. The obtained Pb-MOF could then be converted back to the Cd-MOF over three weeks with a 50% conversion reached over 24 hours.

There are few reported MOFs constructed of titanium based SBUs despite its group four counterparts, zirconium and hafnium, being well used in various MOF families. Titanium is much lighter and highly oxyphilic and thus its incorporation into a MOF would reduce density and

introduce unique photochemical properties. Kim *et al.* have demonstrated the formation of mixed Zr/Ti and Zr/Hf UiO-66 systems through PST and showed that the reaction did not impede porosity, reduce crystallinity or the daughter materials stability (scheme 1.5).[95]

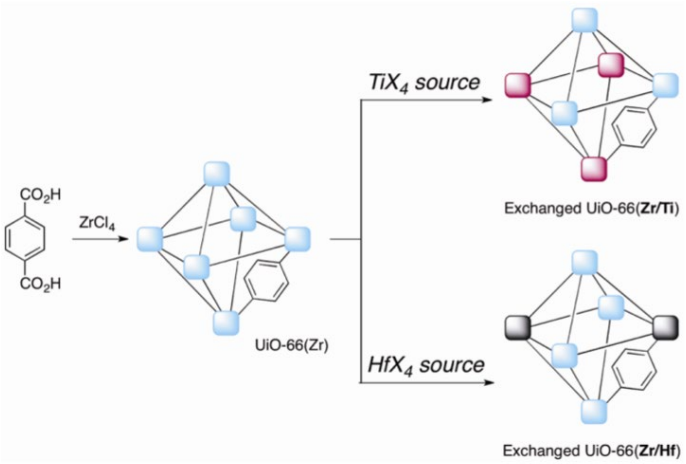

Scheme 1.5. PST of UiO-66 (Zr) to form Zr/Ti and Zr/Hf mixed MOFs.[95] Reproduced with permission from ACS.

Zhao *et al*. in 2015 performed a dative PSM reaction on UiO-66-$(CO_2H)_2$, an isoreticular MOF of UiO-66 which utilises the organic linker 1,2,4,5-benzenetetracarboxylic acid (H_4BTEC) rather than H_2BDC.[96] The MOF was treated with group (I) hydroxides to deprotonate the free carboxylic acid functionalities and counterbalance the now negatively charged framework with the alkali metal cations. It was found that UiO-66-$(CO_2Na)_2$ could capture CO_2 from simulant flue gas with 99.6% selectivity over N_2. HKUST-1 ([Cu_3-BTC_2]) has also been modified with dative PSM and exploited for CO_2 adsorption.[97] The axial positions of the copper paddlewheels of the MOF can undergo exchange with aliphatic amines, such as ethylenediamine and picolylamine, under reflux. Jiang *et al.* demonstrated that (Cr) MIL-101-NH_2 can undergo diazotisation to form a diazonium functionality, counter balanced by either chloride or tetrafluoroborate anions.[98] This dative PSM can be used as a stepping stone to the formation of an azo-dye through addition of phenol, or the diazonium can be converted to a halogen tag by reaction with the appropriate potassium halogen salt (scheme 1.6).

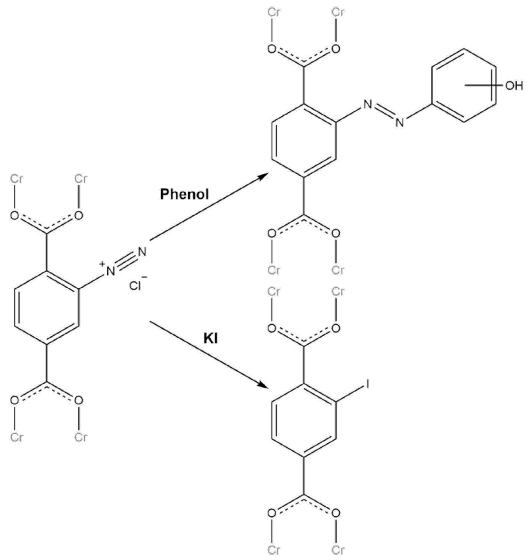

Scheme 1.6. Reaction scheme of diazonium chloride framework and phenol or potassium iodide to respectively generate a phenol azo-dye or iodide functionalised framework.[98]

1.2.2 Synthetic Methods of Metal-Organic Frameworks

Many methods for the growth of MOFs have been developed since the early 2000s. Below we discuss some of the most commonly used methods along with their advantages and limitations.

1.2.2.1 Room Temperature Synthesis

Room temperature techniques are regarded as the most energy efficient route to MOF formation because they do not require an external energy input *via* heating, and in some cases do not need to undergo stirring. A drawback however is the very slow formation of crystals, which in some cases can take days or weeks to form.

As described earlier, the synthesis of Robson and Hoskin's [Cu(TTPM)][BF_4] framework was conducted at room temperature.[46] This allowed for the slow evaporation of nitrobenzene solvent to gradually increase the concentration of the framework precursors towards their threshold solubility. This results in the slow formation of large crystals of the desired material. Altering the solvent affects both the solubility of the reactants and the speed of evaporation, due to differing boiling points. In some cases, a mixture of solvents is required to achieve the right balance for optimal crystallisation. Figure 1.22 schematically shows the various room temperature techniques available for highly crystalline MOF synthesis.

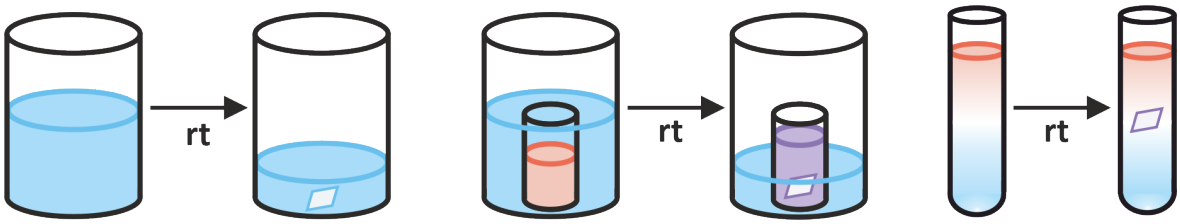

Figure 1.22. Schematic diagram of MOF formation at room temperature. (Left to right) solvent evaporation to increase reagent concentrations, vapour diffusion to reduce the solubility of reagents within a system, and reagent layering which results in a gradual increase in reagent concentrations.

Vapour diffusion is the most commonly used crystallisation technique in protein crystallography[99] but is now regularly adopted by material chemists for MOF synthesis. Stoddart *et al.* reported the growth of γ-cyclodextrin (γ-CD) based MOFs *via* vapour diffusion.[100] γ-CD and potassium hydroxide were dissolved in water and methanol vapours were allowed to diffuse into the aqueous solution over the course of a week. This was achieved by placing the aqueous solution in an open vial and then placing this vial into a larger container that contains the volatile methanol. The larger container is then sealed to contain the methanol vapours. This resulted in the growth of colourless cubic crystals of $[(C_{48}H_{80}O_{40})(KOH)_2]$ (CD-MOF-1). Another example of vapour diffusion in MOF synthesis was reported by Li *et al.* to form $Zn(INA)_2(H_2O)_2(NH_3)_2$ (INA = isonicotinic acid). The MOF precursors were dissolved in water, followed by the diffusion of ammonia into the solution which caused the pH to increase. This increase in pH deprotonates the INA linker gradually, resulting in slow crystallisation.

Reagent layering is a different room temperature technique that requires the dissolution of the metal precursor and organic linker into different solutions. In many cases the solvent choices for the two solutions are different but this is not always necessary. The denser solution is added to an empty test tube and, in some cases, a layer of the same solvent is carefully added above this solution to form a concentration gradient. The second solution is then carefully layered on top of the solution creating an interface. Crystal growth takes place at this interface over a period of days.

1.2.2.2 Conventional Synthesis: Heat

The most conventional synthesis method for MOFs is the dissolution of the reagents in solvent followed by heating for long periods of time, often over 24 hours. This is a less energy efficient method because of the long period of heating at high temperatures however it often yields large crystals. Heating of reagent solutions is regularly carried out using a steel autoclave with a Teflon liner (figure 1.23) that is heated within in an oven. When sealed, the reactions can be heated beyond the boiling point of the solvent without evaporation occurring under autogenous

pressure.[53,101] This is referred to as a solvothermal synthesis, or a hydrothermal synthesis when carried out specifically in water. The term solvothermal is often used, incorrectly, for all reactions carried out in a steel autoclave regardless of whether the temperature is above or below the boiling point of the solvent.

Figure 1.23. Steel autoclave reactor and Teflon liner that fits within the autoclave.

The most common solvents employed are polar aprotic such as N,N'-dimethylformamide (DMF). DMF is capable of dissolving a wide range of metal salts and organic acid linkers. It has a high boiling point of 153 °C and is relatively unreactive making it an ideal solvent for reactions being carried out at high temperature. DMF undergoes hydrolysis into dimethylammonium cations in the presence of water, and its degradation is accelerated with an increase in temperature. The formation of these cations within the MOF synthesis can influence the resulting framework, and in some cases the presence of dimethylammonium cations have been crystallographically isolated as counter cations in anionic systems.[102,103]

1.2.2.3 Metal-Organic Framework Synthesis with Microwave Irradiation

Microwave-assisted synthesis of MOFs utilises microwave radiation to heat the reaction mixture.[104] The advantages to this over conventional heating is that this method is much more energy efficient.[105] Energy is generated directly into the reaction bulk, rather than gradual conduction through external surfaces (such as a steel autoclave). Almost instantaneous heating is achieved with microwave radiation and the high energy of microwaves drastically reduces the reaction time required. Fast reaction times do however make the formation of large single crystals of MOFs more difficult, hence microwave techniques are usually reserved for the synthesis of microcrystalline materials. Chae *et al.* reported in 2006 the first microwave synthesis of $Zn_4(O)(BDC)_3$ (MOF-5/IRMOF-1).[106] The MOF-5 crystals were between 2-4 μm in size and only required heating to 95 ˚C for nine minutes. Microwave synthesis has also been incorporated into continuous flow apparatus for the growth of MOFs such as HKUST-1.[107]

1.2.2.4 Mechanochemistry

Energy can be delivered to a chemical system through physical motion in a process known as mechanochemical synthesis. The simplest form of mechanochemistry is the grinding of reagents together with a pestle and mortar.[108] The friction generated between the materials creates energy that drives the chemical reaction. Ball milling is a popular method which requires a nylon vessel and stainless steel or zirconium oxide balls (figure 1.24). The reagents are added to the vessel along with a few balls and is shaken at high frequency.[109] The collisions between the balls and reagents generate heat that, once again, drives the reaction. Mechanochemistry is receiving more attention in the MOF field due to its short reaction times, the ability for the reaction to be conducted at room temperature and because these reactions require little or no solvent.[110] A drawback however is that this method will not yield single-crystal quality crystals and thus cannot be used in the discovery of new phases easily.

Figure 1.24. Teflon ball milling vessel and zirconia balls that are used in ball milling.

1.2.3 Metal-Organic Framework Applications

The physical properties of MOFs allow for a wide range of applications to be assessed and indeed MOF literature reflects this. In this section we focus on five of the most researched applications within the MOF field and reflect upon the properties of this material class that make them ideal candidates in such areas.

1.2.3.1 Gas Adsorption and Separations

The purification and storage of gases, separation of gaseous isomers and the removal of toxic gases from systems is of huge importance. Porous solids such as MOFs have been employed as potential materials in this area for several years and it can be argued as the top area of focus in the community.[111]

CO_2 can be selectively separated from flue gas by various MOFs, an essential step in the purification of gas by-products from industrial processes.[112] Activation of CPO-27(Mg) ($Mg_2(DHTP)(H_2O)_2 \cdot 8H_2O$) (DHTP = 2,5-dihydroxyterephthalic acid) yields a channelled material (11-12 Å width) with a high concentration of open metal sites that are able to coordinate and hence adsorb CO_2, a typical greenhouse gas, in very impressive quantities (figure 1.25).[113] Cobalt and nickel analogues of CPO-27 have been shown as good materials for hydrogen gas storage.[114] Adsorbents for such gases are important for the development of hydrogen powered vehicles, as current systems require high pressures and low temperatures to be viable.[115] The high surface areas of MOFs allow for lower pressures to be accessed for the same quantity of H_2, although the very low temperatures required is still a parameter of concern.

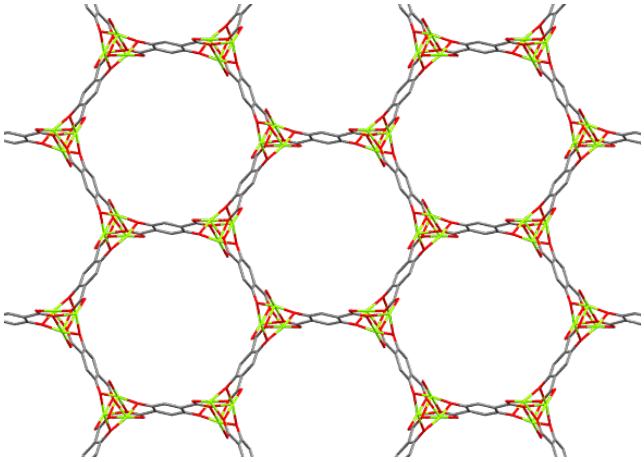

Figure 1.25. Honeycomb structure of CPO-27(Mg).[116]

HKUST-1 has been exploited in the separation of isomeric gas mixtures. Alaerts *et al.* demonstrated that the activated MOF has higher affinity to cis-olefins over their trans- counterparts.[117] They deduced that sterics of the adsorbate played a key role in this selectivity as the cis isomer allowed for close interaction between the alkene and the open metal sites of HKUST-1. This was caused by π-complexation between the metal site and cis-alkene, which could not be obtained for the trans isomer.

1.2.3.2 Sensing

MOFs have been thoroughly researched for their ability to sense minute quantities of a wide range of small molecules, including gases and volatile organic compounds (VOCs).[118] This application is possible due to physical properties such as luminescence, magnetism, electrical conductivity and chromism that many MOFs have, as well as their porosity that allows for the interaction between the analyte and the solid host. In addition, guest molecules that display beneficial properties can be encapsulated within a MOF to allow for sensing. Cadman *et al.* encapsulated viologen species within zinc-based frameworks.[119] The guest molecule could switch between a monocation-radical

species to the dication form upon exposure to air and the reverse reaction could be obtained through either heating or UV irradiation. Accompanying the reaction is a change in colour, from blue to orange, and vice versa, suggesting a switchable sensing material (scheme 1.7).

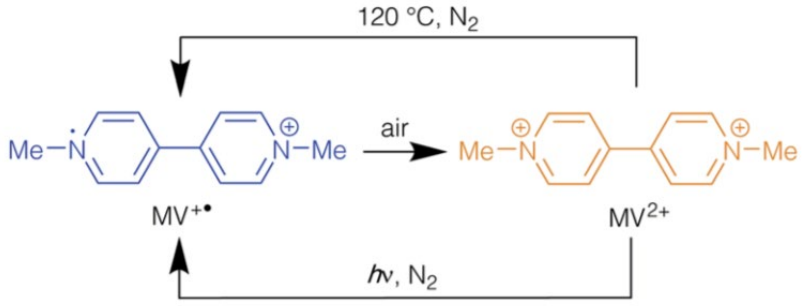

Scheme 1.7. Transformations of methyl viologen under heating or UV irradiation and inert gas.[119] **Reproduced under CC BY-NC license.**

Assen *et al.* have synthesised chemical capacitive rare-earth MOF thin film sensors that display high sensitivity to ammonia, a gaseous environmental pollutant. [120] The material could sense down to 1 ppb at room temperature, even in the presence of humidity, CO_2 and other gases. Glutathione, a key biological regulator, can be sensed by a zirconium-based MOF due to the 4,4'-stilbenedicarboxylic acid linker.[121] Upon adsorption, interaction between the alkene of the linker and the biomolecule resulted in fluorescent enhancement in less than two minutes. Chlorinated hydrocarbons are essential solvents in many procedures but carry many health and environmental issues. Researchers have exploited the luminescent[122] and chromism[123] properties of MOFs to develop sensors for such problematic molecules.

1.2.3.3 Biomedical Applications

The use of MOFs in biomedical applications has been well explored. Although it would be fair to say that the necessary toxicity data of MOFs *in-vivo* is limited.[124] MOFs have been investigated for cargo delivery,[125] biomedical sensing,[126] bioimaging,[127] biocatalysis[128] and antibacterial materials.[129]

Recently UiO-66 was loaded with the anti-cancer drug dichloroacetate and conjugated with triphenylphosphonium (TTP).[130] TTP carries a positive charge and is found to accumulate in the mitochondria of cells. The drug-loaded MOF also accumulated in the mitochondria due to the TTP, releasing the dichloroacetate contents at the key site. They found that this method had the same therapeutic effect as administering dichloroacetate normally, but required only 1% of the drug to do so. Lian *et al.* have encapsulated sensitive enzymes within MOFs to extend their lifetime in oxidative environments.[128] They found that the enzymes could maintain their activities for upwards of a week, far longer than the free enzyme. This was even found to be the case when the MOF

composite was localised in lysosomes, regarded as one of the most degradative environments in living cells.

Silver's antibacterial properties were exploited by Berchel *et al.* against six different bacterial strains by forming a silver-based MOF with the organic linker 3-phosphonobenzoic acid.[129] The material sustainably released Ag^+ into solution which then held antibacterial benefits. They believe that the MOF had intermediate stability which allow for its slow decomposition.

1.2.3.4 Molecular Adsorptions

The porous nature of MOFs allows for the testing and optimisation of the adsorption of a wide range of adsorbates. Often the goal of such is to remove toxic and harmful small molecules such as dyes,[131] ammonia[132] and heavy metals[133] from local environments.[134]

The textile industry is notorious for the release of dyes into waterways, resulting in the decrease of water quality and harming of the aquatic environment.[135] Yang *et al.* have investigated the efficiency of cerium-doped UiO-66 to adsorb various organic dyes such as methyl orange, Congo red and methylene blue (figure 1.26).[136] The doped MOF had far better remediations than pristine UiO-66 due to reduced electrostatic repulsion, an increase in adsorption sites and the cerium promoting π- π interactions between the adsorbate and adsorbent. Tong *et al.* showed in 2013 the importance in careful selection of metal node for MOFs intended for dye separations and adsorptions.[137] MIL-100(Fe) is able to rapidly capture methylene blue and methyl orange simultaneously while MIIL-100(Cr) can selectively separate the two dyes, remediating methylene blue from a 50-50 mixture.

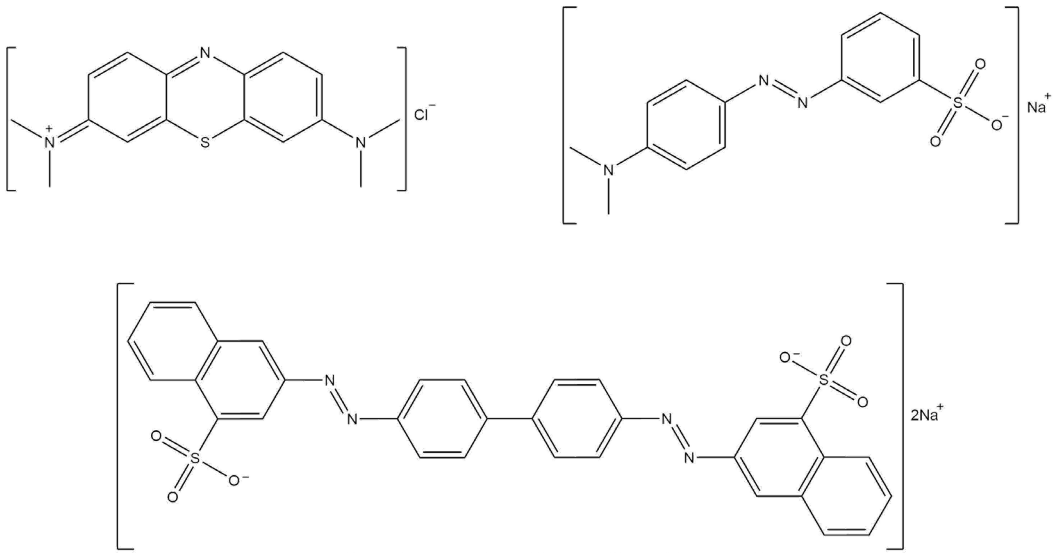

Figure 1.26. (Clockwise from top left) chemical structures of methylene blue, methyl orange and Congo red.

Heavy metals are highly toxic contaminants and are easily released from industrial processes. Detoxification of these species can be difficult and thus good adsorbents are very much necessary. Arsenic,[138] lead,[139] chromium,[140] and mercury[141] to name a few require careful handling and disposal. MOFs have displayed much potential in handling the disposal of such species. Researchers have exploited the high affinity Hg^{+} ions display towards sulphur groups by designing MOFs with sulphurous moieties attached to the framework linkers. Mon *et al.* did so with a bimetallic bioMOF which displayed an impressive mercury (I) adsorption capacity of 900 mg g^{-1}.[141]

1.2.3.5 Heterogeneous Catalysis

Catalysis has proven to be a continuously indispensable area of chemistry.[142] The ability to open up reaction pathways that alone are simply not possible has allowed countless new molecules to be formed. In addition, catalysts allow far better control over enantiomer forming chemical reactions allowing chemists to choose the molecule with the correct properties and benefits. Homogeneous catalysis carries many benefits and has often been the chosen method in organic chemistry.[143] Heterogeneous catalysis can also hold many benefits including easier separation post-reaction, improved recyclability, better size selectivity as well as the ability to mimic enzymes more closely through incorporated metal centres.[144] MOFs have been envisaged as superior heterogeneous catalysts and much work has been done into small molecule transformations.[145,146]

Chiral salen (Mn)(III) complexes have long been used in enantioselective epoxidation reactions of alkenes. Cho *et al.* have successfully incorporated a Mn-salen into a mixed linker zinc-based MOF through the functionalised organic linker (R,R)-(-)-1,2-cyclohexanediamino-N,N'-bis(3-*tert*-butyl-5-(4-pyridyl)salicylidene)MnCl (figure 1.27).[147] The two-fold interpenetrated framework could catalyse the epoxidation of various alkenes with improved recyclability, easier separation, and far better substrate size selectivity.

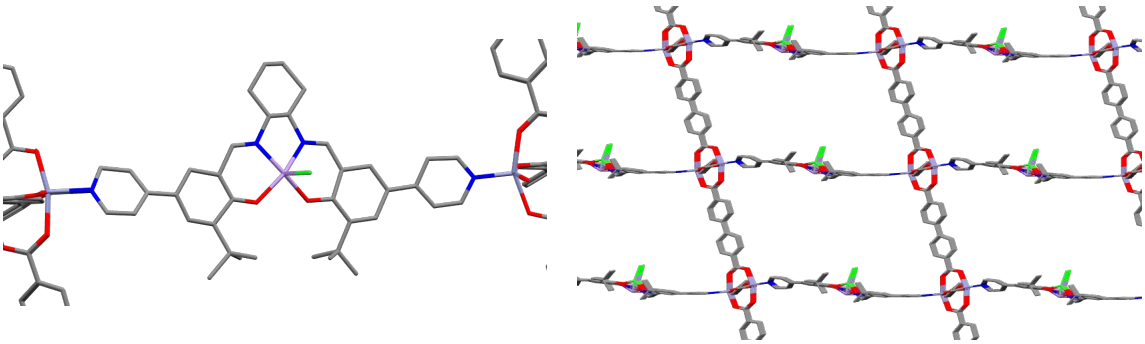

Figure 1.27. Crystal structure of single framework of $Zn_2(BPDC)_2$(Mn-salen).

1.3 Existing Materials for Pertechnetate Remediation

Preventing the release of long living radionuclides such as technetium is essential in not only protecting the local environments surrounding nuclear reprocessing sites but also in minimising the environmental impacts of nuclear disasters. Much work has gone into the development of systems that can adsorb pertechnetate from solution. However, the majority of these lack the necessary selectivity and stability required for effective removal in real world conditions.[148] In some circumstances the systems involve the dissolution of an anion receptor which, while efficient at isolating TcO_4^-, requires additional work up to remove the receptor from solution along with the target anion.[149,150] Therefore, there is much focus, and preference, on the development of water stable, novel porous materials that can adsorb and selectively remove pertechnetate from both aqueous radioactive waste before it reaches the local environment and from contaminated groundwater.[148] The solid material is easier to recover from solution by filtration or magnetic separation, which are much cheaper and easier processes than solvent extraction that also generates additional waste.

Examination of a framework's ability to uptake pertechnetate in conditions that replicate those of the desired application is extremely important. While useful for initial screening of materials for their uptake capacities testing in deionised water alone can give distorted results. This is because the effects of naturally occurring competing anions are not taken into consideration. Therefore, it is very common for MOFs to be tested in solutions that simulate the salt concentrations and pH of the groundwater at nuclear fuel reprocessing sites. While the use of sample water from these locations would yield more realistic results, simulant solutions provide a cheap, and consistent, alternative that can be easily prepared in the laboratory. Each site has a different distribution of anions present in varying concentrations. Table A.1 (A = appendix) shows the composition of two of the most commonly used groundwater simulants, Sellafield in the UK and Hanford in the USA. The sulphate anion is known for being the most disruptive anion in TcO_4^- remediation because of its large charge density and divalent charge. Sellafield groundwater has a concentration of sulphate two magnitudes greater than that of Hanford and therefore a materials selectivity towards pertechnetate over sulphate is much more essential when testing in a Sellafield simulant. Great care must be taken when comparing materials as the conditions used in testing may not be the same and can cause distortion of results.

Rather than handling radionuclides, many research groups opt for safer, non-radioactive and more convenient surrogate molecules when testing materials in laboratory environments. A typical surrogate element to technetium is its group VII partner, rhenium. Its oxo-anion, ReO_4^-, respectively, shares very similar reactivities and physical properties to pertechnetate (TcO_4^-).[12]

Manganese, in the form of permanganate (MnO_4^-), is sometimes also used. The high redox activity of MnO_4^- must however be taken into consideration and thus perrhenate is often preferred.

Both synthetic and natural materials have been explored for TcO_4^- removal all with varying results. Lignin-based anion exchange resins have been shown to be superior perrhenate adsorbents compared to styrene and divinylbenzene-based resins but are pH dependent.[151] These materials work best in highly acidic conditions (pH 1.5-3.5). Naturally occurring materials such as clays,[152] activated carbons,[153] elemental iron filings,[154] and stibnite[155] have all been tested as potential natural adsorbents. Nevertheless, they are found to have low selectivity and limited capacities. Wu *et al*. recently reported nanoparticle@biochar composites that display impressive selectivity for perrhenate over competing ions, but still lack the adsorption capacities that are observed by synthetic materials (figure 1.28).[156] Organic-based polymers have been explored by various groups for pertechnetate remediation. Urea-functionalised mesoporous polymeric nanoparticles and imidazolium-based organic polymers investigated by Zhang *et. al.*[157] and Han *et al.*[158] respectively have been investigated for their ability to remediate TcO_4^-. While the urea-based materials showed good stability under β irradiation and the latter work demonstrated extremely fast uptake kinetics, both groups of materials have issues in regards to anion selectivity. Li *et al.* developed a polymeric cationic network from 1,1,2,2-tetrakis(4-(imidazolyl-4-yl)phenyl)ethene (TIPE) and 1,4-bis(bromomethyl)benzene (BBB).[159] The material has bromide counter-anions that are exchanged with chloride prior to perrhenate remediation. They found the material had excellent capacities, fast exchange kinetics and high stability in acidic, hydrolytic and ionising conditions.

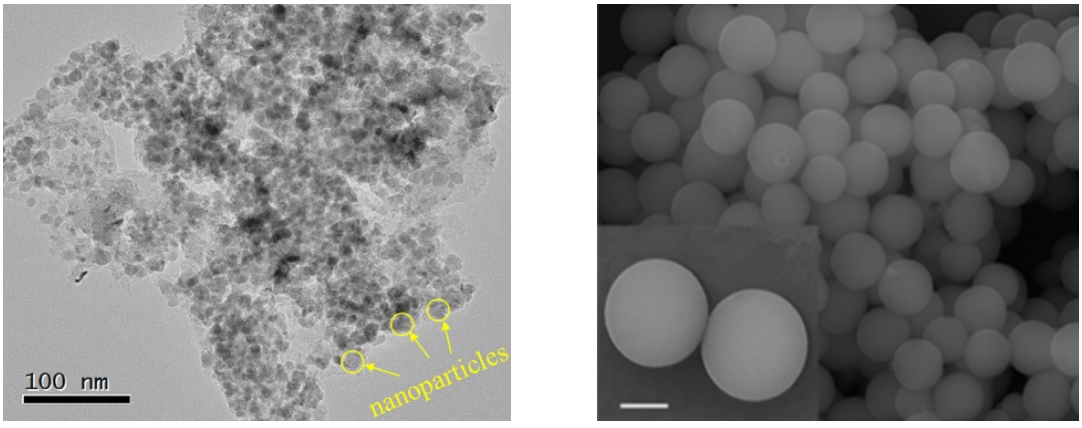

Figure 1.28. (Left) TEM image of nanoparticle@biochar by Wu *et al.*[156] Reproduced with permission from Elsevier. (Right) SEM imaging of 2 µm spherical particles of polymeric cationic network by Li *et. al.*[159] Reproduced under Creative Commons Attribution 4.0 International License.

MOFs have been well explored for the remediation of TcO_4^-/ReO_4^-. The exchangeable components, and wide range of organic linkers available has led to a wide range of bespoke materials that display high capacity, good selectivity, and the potential for recycling. Table 1.1 contains the adsorption

capacities and partition coefficients of 15 different materials all which except three (NDTB-1, $Y_2(OH)_5Cl$ and Mg-Al-LDH) are MOFs. From this table we can identify two, clear patterns; **1**) silver and nickel-based systems have very high performance in perrhenate remediation and **2**) complex, nitrogen-based organic linkers offer hydrophobic pockets that are superior for perrhenate anions adsorption.

Table 1.1. Modified table from Du *et al.*[160] of ReO_4^- adsorption efficiency by various anion-exchange materials. Materials have been ordered based upon their partition coefficients. */¨ Denotes materials that comprise of the same building blocks but differ by parent anion. Reproduced with permission from Royal Society of Chemistry 2019.

	Material	Metal	Organic Linker	Adsorption Capacity ($mg\ g^{-1}$)	K_d ($mL\ g^{-1}$)	Ref
1	SBN*	Ag	4,4'- BIPY	786	8.3×10^5	161
2	TJNU-216	Ag	TIB	417	8.2×10^5	160
3	SCU-101¨	Ni	TIPM	217	7.5×10^5	162
4	SCU-CPN-1	-	tipe & bbb	999	6.2×10^5	159
5	SCU-102¨	Ni	TIPM	291	5.6×10^5	163
6	SLUG-21*	Ag	4,4'- BIPY	602	3.8×10^5	164
7	SCU-100	Ag	TIPM	541	3.3×10^5	165
8	MIL-101-F		$BDC\text{-}CH_2N^+(CH_2)_3Cl^-$	237	2.1×10^5	166
9	PAF-1-F	-	TBM & 2,2'-BIPY	420	2.55×10^4	166
10	MIL-101(Cr)	Cr	H_2BDC	215	8.9×10^3	166
11	SCU-7	U	HTTTPC	0.4	3×10^3	167
12	$UiO\text{-}66\text{-}NH_3^+$	Zr	$H_2BDC\text{-}NH_3^+$	159	837	168
13	NDTB-1	Th	Boron-based	19	652	165
14	Mg-Al-LDH	Mg & Al	-	10	262	165
15	$Y_2(OH)_5Cl$	Y	-	12	112	165
16	SCU-6	U	HTTTPC	0.06	54	167

Farha *et al*. have demonstrated that their material NU-1000 can remediate perrhenate and pertechnetate.[169] SCXRD confirmed the binding of perrhenate to Zr^{4+} centres in the framework's metal nodes, replacing labile OH^- and OH_2 groups (figure 1.29).

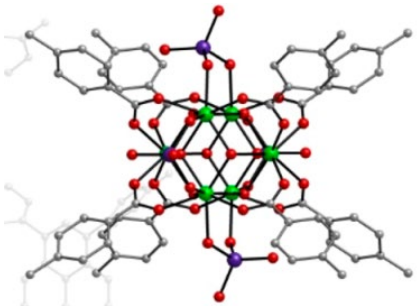

Figure 1.29. Perrhenate coordination to the Zr nodes of NU-1000.[169] Rhenium = purple, green = zirconium, red = oxygen, and grey = carbon. Copyright 2018 American Chemical Society.

Silver coordination polymers and MOFs have been demonstrated as excellent adsorbents for perrhenate. Oliver *et al.* have shown that the simple [Ag(4,4'-bipy)][NO_3] coordination polymer could undergo fast exchange of the nitrate counter anions with perrhenate, achieving an adsorption capacity of 786 mg g^{-1} within 90 minutes and a partition coefficient of 8.3 x 10^5 mL g^{-1}.[161] The material undergoes a phase transformation upon anion exchange, displayed in figure 1.30. Perrhenate does not leach from SBN upon soaking in nitrate solution thus showing both the material's superior immobilisation of ReO_4^-, but lack recyclability. DFT calculations confirmed that the perrhenate-containing system had a lower energy than the nitrate by 35.61 kcal mol^{-1} and the latter material was three orders of magnitude more soluble than the former. Similar work by the same authors has confirmed that the choice of counter anion present in a material's structure plays an important role in its anion exchange capabilities. SLUG-21 is also a [Ag(4,4'-bipy)] coordination polymer but contains 1,2-ethanedisulfonate anions.[164] The adsorption capacity of SLUG-21 is 576 and 602 mg g^{-1} over 24 and 48 hours respectively. These values are lower than that of the nitrate-containing coordination polymer.

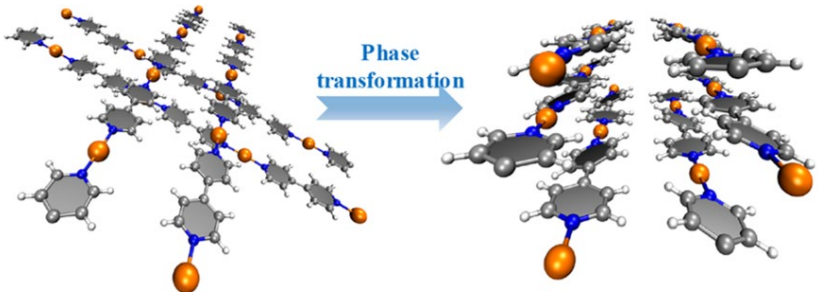

Figure 1.30. Phase transformation observed upon exchange of the nitrate counter-anions with perrhenate in SBN.[161] Copyright 2017 American Chemical Society.

TJNU-216 (TJNU = Tianjin Normal University) is a silver-based cationic MOF containing the neutral organic linker 1,2,4,5-tetra(1H-imidazol-1-yl)benzene (TIB).[160] Triflate ($CF_3SO_3^-$) counter anions, that are crystallographically ordered within the pores of the MOF, can undergo anion exchange with perrhenate. This causes single-crystal to single-crystal (SCSC) transformations resulting in a more

open framework containing perrhenate anions that are stabilised with hydrogen bonding from the phenyl and imidazolyl groups of the organic linker (figure 1.31). They reported that the hydrophobic nature of the MOF allowed for high perrhenate selectivity even in the presence of excesses of sulphate and nitrate.

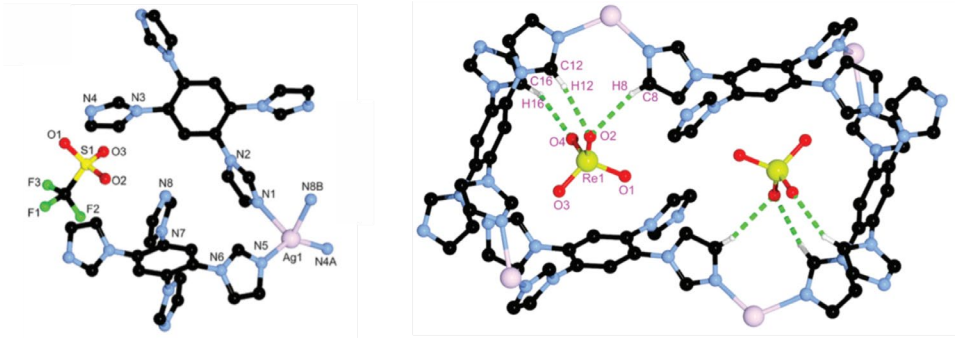

Figure 1.31. (Left) Crystal structure of TJNU-216 with ordered triflate counter-anions. (Right) Crystal structure of TJNU-216(Re) showing the location of ordered perrhenate anions and their hydrogen-bonding interactions within the hydrophobic pockets of the material.[160] Reproduced with permission from Royal Society of Chemistry 2019.

Researchers at Soochow University (SCU) have developed several MOFs for selective TcO_4^-/ReO_4^- remediation. Three of these materials (SCU-100,[165] SCU-101[162] and SCU-102)[163] utilise the tetradentate molecule tetrakis[4-(1-imidazolyl)phenyl]methane (TIPM) (figure 1.32) as its organic linker and contain nitrate counter-balancing anions. SCU-100 ($[Ag_2(TIPM)][NO_3]_2 \cdot 1.5\ H_2O$) differs however as it contains silver centres while the two other frameworks consist of nickel nodes. SCU-101 ($[Ni_2(TIPM)_2(C_2O_4)][NO_3]_2 \cdot 2\ H_2O$) contains oxalate anions that are integral to the framework structure. The authors have then removed the oxalate anion source to generate the final MOF, SCU-102 ($[Ni_2(TIPM)_3][NO_3]_4$).

SCU-100 has a complex, eight-fold interpenetrated structure with small channels (6.9 Å) down the c axis that contain disordered nitrate anions (figure 1.32). This high degree of interpenetration is because of large diamond-shaped channels (≈ 48 Å) of the individual frameworks which must be stabilised. Upon adsorption of ReO_4^-, the MOF undergoes SCSC transformations resulting in a four-fold interpenetrated structure containing ordered perrhenate anions that coordinate directly to the Ag centres and are surrounded by beneficial hydrogen bond donor groups. SCU-100 showed high affinity to ReO_4^- even in the presence of excess competing anions such as nitrate, chloride and sulphate. The MOF had high stability in a full range of pH values and after subjection to 200 kGy of both β and γ radiation.

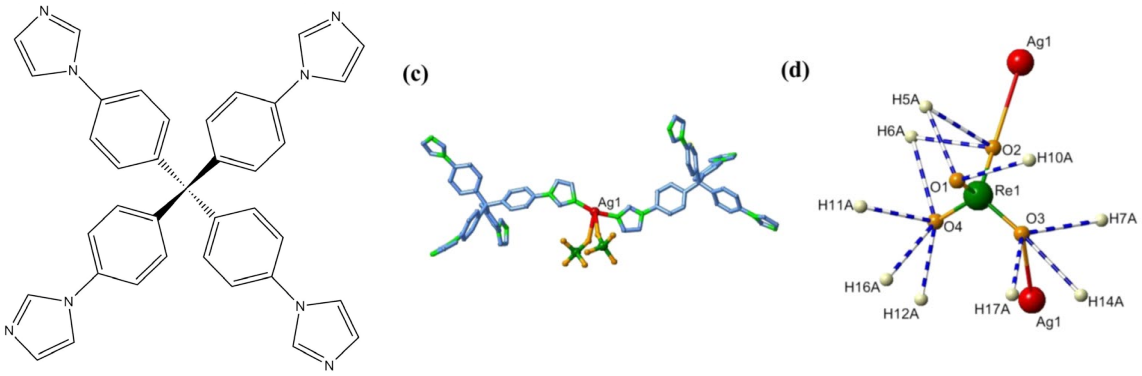

Figure 1.32. (Left) structure of TIPM. (Right) (c) Perrhenate binding to Ag centres and (d) hydrogen bond rich environment within SCU-100.[165] Copyright 2017 American Chemical Society.

Despite SCU-100 being highly efficient in perrhenate remediation, the SCSC transformations due to oxo-anion uptake have serious consequences for material recyclability. To remedy this issue the authors synthesised SCU-101. This framework is much more rigid than SCU-100 and does not undergo any form of transformation upon TcO_4^- adsorption (figure 1.33). The framework does however have a reduced positive charge density due to the incorporated oxalate anions that are introduced by the addition of oxalic acid to the reaction mixture as well as the supposed degradation of TIPM. The authors claim this step improves crystal yield but has greater consequences as it reduces the ability for SCU-101 to effectively remediate TcO_4^-. The exchange capacity for SCU-101 is far lower than SCU-100 (217 mg g^{-1} versus 541 mg g^{-1}) and we attribute this reduced charge density to be a cause. In addition to this the authors claim that TcO_4^- only occupies one of the three available channels in SCU-101 and that the nitrate anions within the other two channels are not exchangeable. This will greatly reduce the material ability to undergo effective anion exchange as a large proportion of the parent anions are unable to be removed.

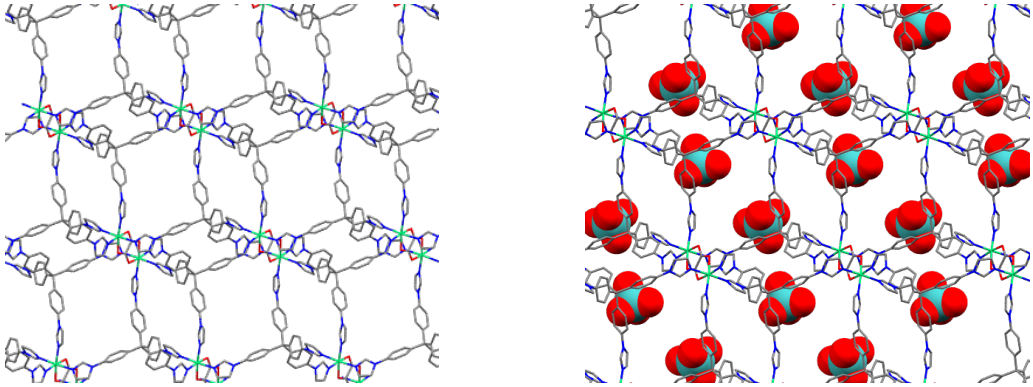

Figure 1.33. Crystal structures of SCU-101 without (left) and with (right) TcO_4^- anions. TcO_4^- are represented with space filling atoms.

SCU-100 and SCU-101 highlight how a materials pros and cons must be weighed up and critically assessed. A high exchange capacity is beneficial for materials that cannot be adequately recycled. While lower capacity MOFs, such as SCU-101, may not be able to remediate to such a high degree,

its ability to be recycled several times due to its rigid structure makes it just as attractive. This is because it may be able to remediate more of the target anion over its longer lifetime. TIPM is also an expensive linker to synthesise, regarding both cost and time, therefore its use in single-use, sacrificial remediation materials are not desired.

The last TIPM-based framework that the researchers at SCU investigated was the nickel-based SCU-102, which lacked the oxalate anions found in SCU-101. SCU-102 synthesis occurred at 100 °C rather than 120 °C and only water and DMF were used as solvents. The milder temperature stopped the degradation of TIPM and thus no oxalate formation can occur. SCU-102 has a higher adsorption capacity than SCU-101 but lower partition coefficient. What is most impressive about SCU-102 is its superior selectivity towards TcO_4^- and ReO_4^-. Density functional theory (DFT) calculations regarding the hydrophobic pockets found within SCU-102 showed binding energies for the TcO_4^- (-107.4 kJ mol^{-1}) was almost double that for sulphate and nitrate (-58.2 kJ mol^{-1} and -64.9 kJ mol^{-1} respectively). It was proposed that the high Gibbs energies of hydration of sulphate (-1090 $kJmol^{-1}$) and nitrate (-306 kJ mol^{-1}) mean that the pockets can accommodate the more hydrophobic pertechnetate (-251 kJ mol^{-1}) anion much more easily.

TIPM was again used to form a nickel-based, cationic MOF ($Ni(TIPM)_2(SO_4)$) with hydrophobic channels by Dutta *et al* (figure 1.34).[170] The MOF was tested for both its perrhenate and chromate remediating capabilities under various competing anions. The authors have taken the interesting step of using sulphate as the parent counter-anion within the material by using $NiSO_4$ as the precursor salt. The highly competing anion would normally be avoided due to its increased charge density and high natural abundance. DFT calculations found that the binding energies of SO_4^{2-}, CrO_4^{2-} and ReO_4^- were -162, -205 and -301 kJ mol^{-1} respectively. They suggested that the hydrophobic channel, due to the TIPM linker, provided an ideal binding site for the perrhenate anion. The sulphate and chromate anions were found to bind very close to the nickel centres as a result of their charge density.

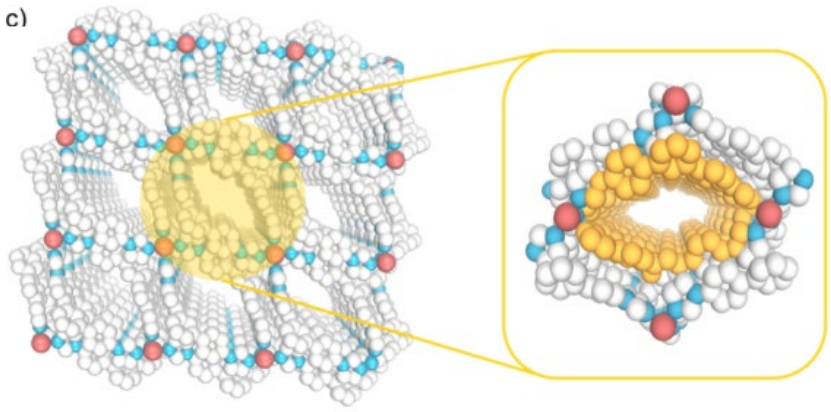

Figure 1.34. Hydrophobic channels within the structure of $Ni(TIPM)_2(SO_4)$.[170] Copyright 2020 American Chemical Society.

Wang *et al.*, from Soochow University have also taken an unusual step of synthesising two MOFs for both ReO_4^- and $H_2PO_4^-$ remediation from uranium salts.[167] SCU-6 ($[(UO_2)_2(TTTPC)(OH)O(COOH)]\cdot$ 1.5 DMF$\cdot$ 7 H_2O) and SCU-7 ($[(UO_2)(HTTTPC)(OH)]Br\cdot$ 1.5 DMF$\cdot$ 4 H_2O) (TTTPC = 1,1′,1″-(2,4,6-trimethylbenzene-1,3,5-triyl)-trimethylenetris(4-carboxypyridinium)) have layered MOF structures and display unique SBU shapes, owing to the interesting coordination chemistry available from the actinide metal cations (figure 1.35). The SBU of SCU-6 consists of six, seven coordinate uranium ions arranged around two (μ_3-O^{2-}) oxygen centres with two bridging (μ_2-OH^-) hydroxide groups. The SBUs are flat in shape and in addition to the oxygen centres coordinate to six TTTPC linkers and two formate groups. The SBU of SCU-7 also coordinates to six TTTPC linkers but, in contrast consists of only two uranium centres and two (μ_2-OH^-) hydroxide groups. By limiting hydrolysis during framework synthesis cationic SCU-7 could be obtained over the neutral SCU-6. Exchange kinetic experiments revealed that 150 mg of SCU-7 could rapidly remediate around 75% of perrhenate from a 1 ppm solution, whereas SCU-6 only remediated 14% under identical conditions.

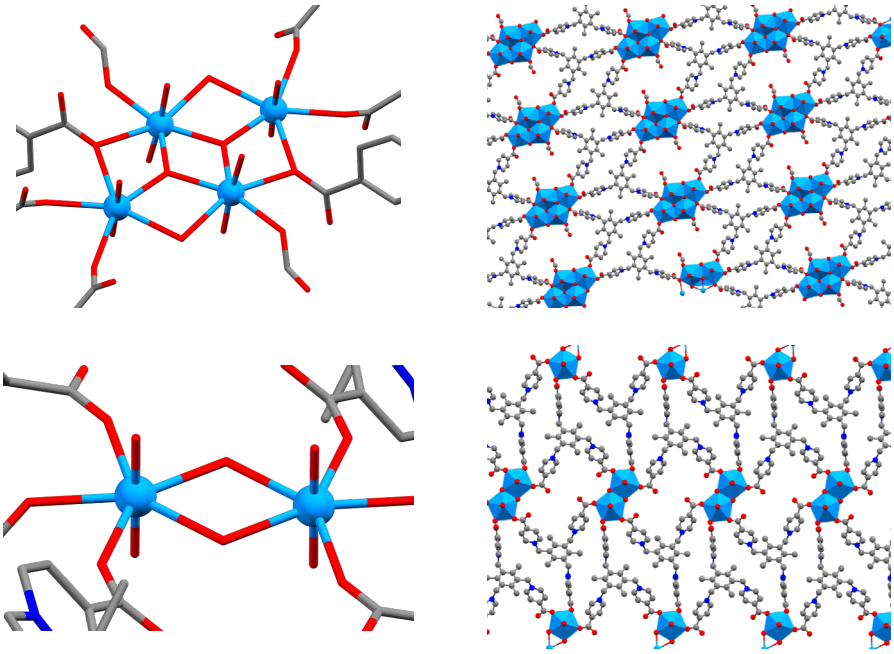

Figure 1.35. (Top row) (left) SBU of SCU-6 and (right) crystal structure of one layer of SCU-6. (Bottom row) (left) SBU of SCU-7 and (right) crystal structure of one layer of SCU-7.

It is very questionable to use a framework that is built upon radioactive metal nodes for radionuclide-based applications and given that the uptake kinetics of SCU-7 are far lower than most other reported MOF materials for ReO_4^-, it is highly unlikely this material would have any potential real-life applications. The difficulty to synthesise, adequately characterise, and handle such frameworks, should however never be understated.

1.4 Metal-Organic Framework Composites

For practical utilisation, MOFs will often require processing into application-specific configurations.[171] This can be achieved by combining MOFs into a hybrid material with a substrate that retains the physical and chemical properties of the porous material while also benefiting from the substrate material. These benefits include encapsulation and immobilisation of the MOF, for improved recyclability,[172] precise orientation of MOF crystals within thin films[173] and the coating of surfaces.[174]

MOF@aerogel composites (MOFACs) have been widely researched as hierarchal multimodal porous materials.[175] These are easily processed materials that can be formed into various shapes including fibres and beads. Many MOF composites have been formed using direct methods which requires synthesis of the bulk MOF separately followed by its addition to a scaffold synthesis. HKUST-1 has been successfully incorporated into a silica aerogel.[176] The MOF was added to the aerogel precursors, which, following gelation and supercritical drying, yielded the MOFAC. A schematic diagram is shown in figure 1.36. Additionally an aluminium-based MOF has been loaded

with ethylene and encapsulated within alginate.[177] Ethylene release from the composite could be enhanced *via* the addition of sodium citrate which slowly degrades the alginate. While degradation is beneficial for this application, the chemical stability of biopolymers, such as alginate, needs to be thoroughly explored to ensure that it remains stable under the conditions and lifetime of the intended application.

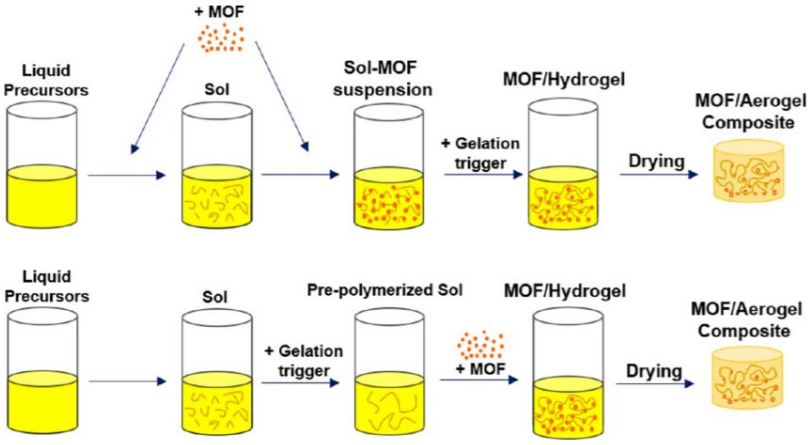

Figure 1.36. MOFAC preparation by MOF incorporation into gel matrices using the direct mixing method.[175] Copyright 2018 American Chemical Society.

In-situ synthesis, occasionally referred to as 'ship-in-a-bottle' synthesis, of MOFs inside gels has also been reported. The MOF is formed within the pores of the gel by the addition of the MOF precursors after formation of the support, as depicted in figure 1.37. Purification is important for *in-situ* methods due to the presence of unreacted precursors and the possible formation of the MOF outside of the composite within the reaction solution. Binding of the MOF to the scaffold is very beneficial to avoid removing the material during the washing process and can be achieved through MOF-scaffold interactions with the functional groups present on the composite. It is even possible to use the metal sites of the scaffold as nucleation sites for MOF growth, physically attaching the MOF to the scaffold.

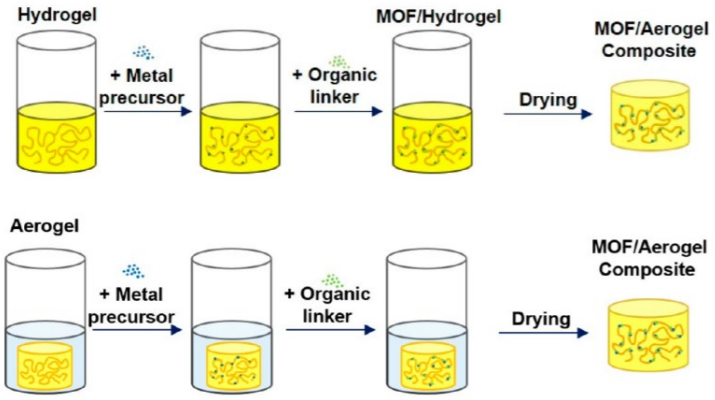

Figure 1.37. Typical preparation of MOFACs in-situ on hydrogels and aerogels.[175] Copyright 2018 American Chemical Society.

A ZIF-8@cellulose MOFAC was formed by dissolving the metal precursor into a cellulose solution prior to crosslinking and freeze drying.[178] This obtains a Zn^{2+}/cellulose aerogel that when added to a solution of the linker (2-methylimidazole) forms ZIF-8 within the aerogel. HKUST-1 has been formed in hollow fibres of chitin by exploiting the high affinity of the support to copper (II) ions (figure 1.38).[179] The chitin was submerged in a copper nitrate solution followed by the addition of H_3BTC. This resulted in the nucleation of MOF particles within the chitin, forming a hierarchical material with a MOF loading of 55% and surface areas of up to 800 m^2g^{-1}.

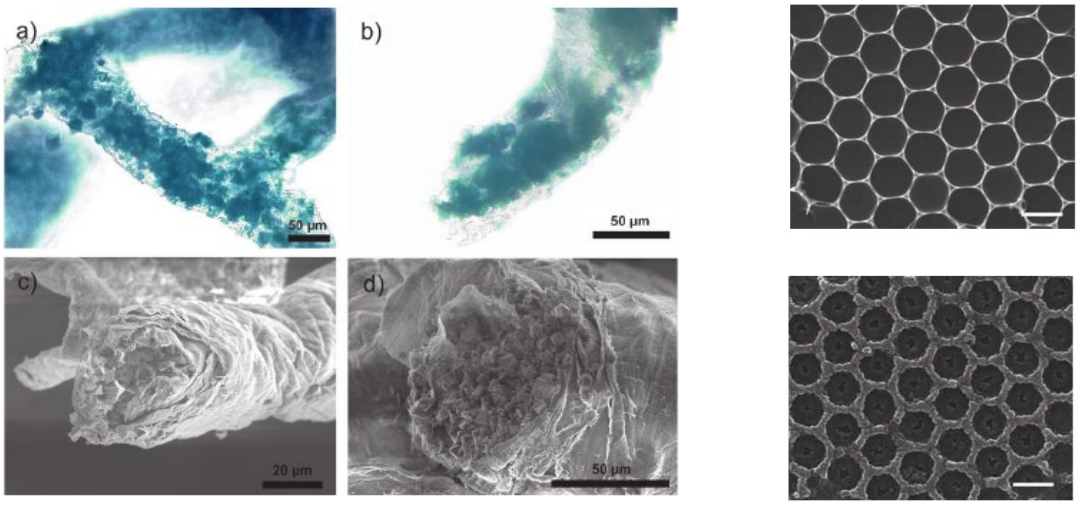

Figure 1.38. (Left) (A-B) stacked microscopic images and (C-D) scanning microscope (SEM) images of HKUST-1@chitin fibers.[179] Reproduced with permission from John Wiley and Sons. (Right) (top) SEM images of the alumina hexagonal pattern and (bottom) SEM image of the aluminium MOF composite.[180] Reproduced with permission from Springer Nature.

Kitagawa *et al.* have designed mesoscopic architectures through the use of a shaped sacrificial metal oxide template.[180] An aluminium oxide template, shown in figure 1.38, was formed by coating a monolayer of small polystyrene beads (1 µm) in a solution of aluminium tri-sec-butoxide, ethanol and nitric acid. The resulting material was calcined to removal all organics and then the three-dimensional alumina template was propagated by repeating the process. Conversion of the oxide to an aluminium MOF was achieved by submerging the material in an aqueous solution of either H_3BTC or H_2BDC followed by microwave treatment. This affords the MOF composite in figure 1.37.

The incorporation of magnetic nanoparticles into MOF composites offers an alternative strategy to the recovery and recycling of materials such as catalysts.[181] Bradshaw *et al.* recently reported the inclusion of Fe_3O_4 nanoparticles into macroporous polyacrylamide (MPam) which when introduced into the synthesis of various MOFs resulted in MOF@MPam composites that could be recovered from solution simply with a magnet.[182] The use of magnetic nanoparticles as templates to seed the growth of MOFs have also been explored. Li *et al.* have grown MOF-5 crystals onto the surface of

SiO_2@Fe_3O_4 nanoparticles resulting in spherical core-shell magnetic composites for catalysis of Friedel-Crafts alkylation reactions.[183] SiO_2@Fe_3O_4 nanoparticles were also similarly used as a scaffold for the growth of HKUST-1. A sacrificial layer of $Cu(OH)_2$ was formed over the nanoparticles before being submerged in a solution of the H_3BTC linker, resulting in MOF growth.[184] Remediation of heavy metals, such as Pb(II),[139] Cr(VI),[185] U(VI) and Th(IV)[186] have also been demonstrated with various MOF@Fe_3O_4 composites and more recently with UiO-66-NH_2@polymer beads by Queen *et al.* where the polymer utilised was a modified polyethersulfone.[187]

Figure 1.39. Chromate removal by a Cu MOF@Fe_3O_4 composite and the easy separation of the material from solution with a magnet.[185] Copyright 2018 American Chemical Society.

1.5 Experimental Methods

1.5.1 Powder X-Ray Diffraction

Powder X-ray diffraction (PXRD) is an essential characterisation tool for crystalline materials. The technique is easy to carry to, non-destructive, and the results of which are quick to qualitatively assess. The output of this method is a measure of intensity of diffracted X-rays from the material in question while varying the incident angle (θ). By changing θ, Bragg's Law is satisfied at specific angles, which results in an intensity peak. To satisfy Bragg's Law, diffraction must result in constructive interference of parallel X-rays. This occurs when the extra distance travelled by an X-ray is an integral number of wavelengths (figure 1.40). As θ is changed, constructive interference occurs with different miller planes (hkl) and therefore a ground sample is necessary to ensure that crystallites are in every orientation for each miller plane to be characterised. The resulting peaks are plotted against 2θ and form a powder pattern. This powder pattern is a fingerprint of the assessed crystalline material and can be compared with other patterns to deduce the synthesised material's crystallinity and phase purity. The comparison can take place with either a simulated powder pattern that has been computationally derived from a material's crystal structure or, with a pattern that has also been obtained experimentally. Peak shape can be used to calculate the crystallite size of the sample

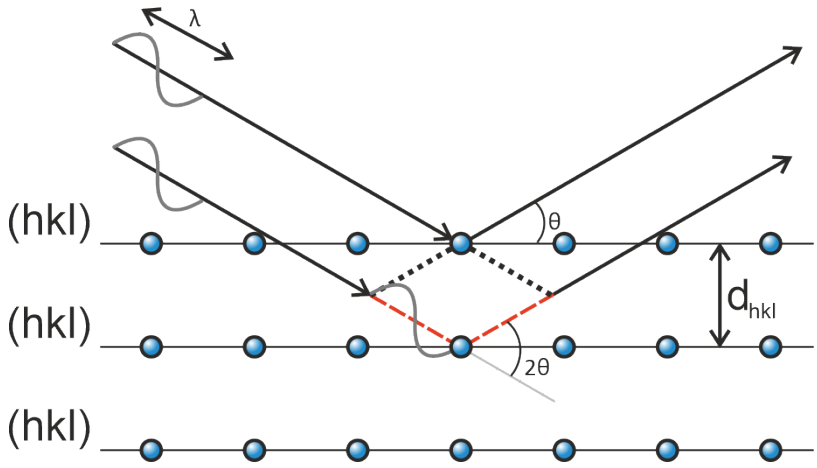

Figure 1.40. Derivation of Bragg's Law.

$$n\lambda = 2dsin\theta$$

n = integer

λ = wavelength

d = hkl spacing

θ = angle of incidence

Equation 1.3. Braggs Law equation.

All PXRD patterns in this thesis were collected on a Bruker D2 Phaser diffractometer with a Cu tube (λ = 1.5406 Å) using a 6 mm incident slit. Samples were loaded onto a silicon mirrored sample holder prior to analysis. Unless otherwise stated all PXRD data was collected between 5 and 60° using a step of 0.02°.

1.5.2 Single-Crystal X-Ray Diffraction

Single-crystal X-Ray diffraction (SCXRD) is a crystallographic method for determining the atomic structures of molecules and materials through non-destructive probing of an individual crystal of a material with X-rays. Bond lengths and angles can be accurately deduced from the structure as well as the possibility for other intermolecular bonding within the structure.

During a SCXRD experiment, a crystal is mounted on a pip in inert oil and mounted on a goniometer. X-rays hit the crystal at various angles and, when Bragg's Law is satisfied, are diffracted, and detected with a detector. This results in a diffraction pattern of spots with varying positions and intensity. Each pattern (or frame) is collated, and data reduction of the set takes place. This involves solving the phase problem to find a unique set of phases that when combined with the structure factors can produce an electron density map. This electron density map provides relative positions of atoms within the crystal structure. These positions are assigned atom types by comparing the electron density of each position. A high electron density typically represents heavy atoms, such as metals, while lighter atoms such as carbon and nitrogen will have a lower electron density. The crystal data is then refined, and steps are taken to improve the fit of the experimental data to that calculated data by the resulting structure. SCXRD is not able to accurately assign hydrogen atoms due to the lack of electron density on the atom type. Hydrogen atoms are therefore assigned based upon the hybridisation and geometry of each atom to produce a sensible crystal structure.

Further characterisation of a material is essential to confirm that the resulting structure from SCXRD is representative of the bulk material because this technique is only concerned with the structure of the individual crystal.

SCXRD data in this thesis was collected on a Rigaku AFC12 4-circle goniometer equipped with an enhanced sensitivity (HG) Saturn724+ detector mounted at the window of an FR-E+ SuperBright molybdenum (Mo K1/Kα2 = 0.71073Å) rotating anode generator with HF Varimax optics (100 µm focus) operating at 2.475kW (45kV, 55mA). On some occasions data reduction was carried out using CrysAlisPro. All crystal structures were solved and refined using Olex2-1.3. All crystal structure images were collected using Mercury. Topological analysis was conducted using ToposPro.

1.5.3 Proton Nuclear Magnetic Resonance Spectroscopy

Nuclear magnetic resonance spectroscopy (NMR) is the probing of intrinsic spin properties of atomic nuclei within molecules with the use of a strong magnetic field. An nuclei's environment within a molecule i.e., the atoms it is directly bonded to, affects the magnetic field that it experiences, and thus different nuclei environments can be distinguished due to their inequivalence to other nuclei. ^{1}H NMR explores the different proton environments within a molecule and provides a relative distribution of those proton environments. This allows for the number of different proton environments, and the number of protons in those environments, to be deduced.

Within this thesis we probe the organic linker molecules from our frameworks' with ^{1}H NMR. This allows us to confirm the transformation of organic linkers in our post-synthetic modification reactions and to quantitively confirm the yield of these reactions. ^{1}H NMR analysis was carried out on a Bruker AVIIIHD400 FT-NMR Spectrometer at 298 K. All spectra were processed using Top Spin 4.0.7, reported in ppm, and are referenced to the chosen deuterated solvent which is stated in each spectrum's caption.

1.5.4 Thermogravimetric Analysis

Thermogravimetric analysis (TGA) is the characterisation of a material's thermal stability and composition through continuous weighing of a sample while it undergoes heating. The resulting data from a TGA experiment is mass loss (%) versus temperature (°C). TGA can confirm the loss of solvent molecules from MOF pores or SBUs, the temperature at which a material undergoes detrimental thermal degradation, and through calculations can allow for a comparison of a material's composition to its theoretical values.

TGAs within this thesis were completed on a Netzsch TG 209 F1 Libra. Samples were loaded into an Al_2O_3 crucible and heated from 30 to 900 °C at a rate of 10 °C/min. The experiment was conducted under an air atmosphere with a gas flow rate of 20 ml/min. The material was dried prior to characterisation to ensure all solvent had been removed from the surface of the material.

1.5.5 Fourier Transform Infrared Spectroscopy

Fourier transform infrared (FTIR) spectroscopy is the measurement of electromagnetic radiation, in the infrared region, absorbed by a material. FTIR spectroscopy elucidates the functional groups present within a material due to their characteristic absorbances at specific wavenumbers (cm^{-1}). Infrared (IR) radiation is passed through a sample resulting in specific wavelengths of this radiation being absorbed. A detector measures the IR radiation that is not absorbed by the sample.

Absorbance of IR radiation occurs when the radiation matches the specific vibrational frequency of a bond and results in a change in dipole moment.

FTIR spectra within this thesis were obtained on a Thermo Scientific Nicolet iS5 Spectrometer and measurements were taken between 500 and 4000 cm^{-1}.

1.5.6 Scanning Electron Microscopy

Scanning electron microscopy (SEM) is an imaging technique that uses an electron beam to visual samples on the micrometre scale. A high voltage electron beam is focused on a conductive sample which interacts with the surface electrons of the sample. This produces secondary electrons that are detected and produces an image of the sample. This technique is integral in confirming crystal morphology and size of samples.

Within this thesis, SEM imaging were collected on various instruments due to instrument availability. In most cases a voltage of 15 kV was applied. Samples were coated with 5 nm of gold, through sputter coating, prior to imaging to improve sample conductivity and reduce charge build up within samples.

1.5.7 Inductively Coupled-Plasma Mass Spectrometry

Inductively coupled-plasma mass spectrometry (ICP-MS) is an elemental analysis technique that can detect elemental ions in minute quantities. The technique uses a plasma to convert an aerosol sample into ions which can then be detected with a mass spectrometer. ICP-MS can quantify almost every element and can detect as low as parts per trillion.

ICP-MS results within this thesis was conducted on an Agilent Technologies 8800 triple Quadrupole instrument with integrated autosampler.

1.5.8 Gas Adsorption

A gas adsorption experiment simply measures the quantity of said gas adsorbed onto a material as the relative pressure is increased. From this we obtain a relative pressure (p/p^o) vs quantity adsorbed (cm^3/g) isotherm. In order to calculate the BET surface area we must take the quantity of N_2 adsorbed at various relative pressures, within the linear BET range of 0.05 – 0.35 and plot the BET equation (Equation 1.4).

Equation 1.4. The *BET Equation.*

$$\frac{1}{Q(^{P_o}/_{P}-1)} = \frac{C-1}{Q_m C}\left(\frac{P}{P_O}\right) + \frac{1}{Q_m C}$$

Q = adsorbed gas quantity; Q_m = monolayer volume; P_O = saturation pressure of adsorbate; P = equilibrium pressure of adsorbate; C = BET constant; CSA = cross-sectional area.

A graphical example of a BET plot is presented in Figure 1.41. From this plot, the surface area of the sample can be calculated using Equation 1.6 and Equation 1.7.

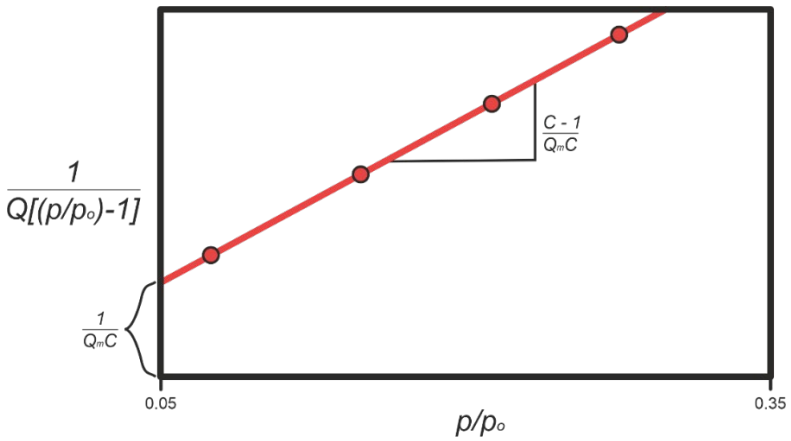

Figure 1.41. BET plot example.

Equation 1.5. Calculating monolayer coverage.

$$Q_m = \frac{1}{slope + intercept}$$

Equation 1.6. Calculating the BET constant.

$$C = \frac{1}{(Q_m \times intercept)}$$

Equation 1.7. Calculating the surface area (m^2).

$$SA = \frac{(CSA \times Q_m \times 6.02 \times 10^{23})}{22414}$$

1.6 Project Aims

Within this project we are concerned with the development of polymeric materials, and their composites, for the remediation of a pertechnetate surrogate (perrhenate) from solution. The literature that we have presented in section 1.3 shows that a wide range of different MOFs have been trialled with this application in mind. There is a clear focus in the community on developing novel materials with superior selectivity's and ultra-high capacities towards pertechnetate.

While the pursuit of these 'record-breaking' properties carries its own merits, this project aims to take a different approach *via* three different strategies. Our interests predominantly lie in using, and modifying, water stable MOFs that are well known from literature. Therefore, our first approach will be to employ post-synthetic modifications to UiO-66-NH_2 and assess the effect that the functionalisation of this MOF has on its ability to remediate perrhenate from solution. Our second strategy will be to process UiO-66-NH_2 into application-specific configurations to assess the effect that immobilisation to a scaffold has on perrhenate removal from solution. Our work into UiO-66-NH_2 and its composites will be reported in Chapter Two.

Our third strategy will use a crystal engineering approach to design new silver and zinc-based coordination polymers and MOFs. The use of selective crystallisation as a remediation mechanism is not well reported on. We will therefore pursue the selective crystallisation of perrhenate, as a counter anion, within silver-based cationic coordination polymers. This will require deducing a system that only crystallises upon the presence of perrhenate and will be carried out through a crystal engineering study. The formation of silver coordination polymers that are counterbalanced by competing anions, such as sulphate or nitrate, would suggest that that particular metal ion and organic linker combination is not selective towards the perrhenate anion, and thus not a suitable system for its selective crystallisation. This novel strategy to isolate perrhenate will be investigated in Chapter Three.

An overarching theme that we have tried to carry through our work is sustainable, and responsible syntheses. Wherever possible, we employ room temperature methods and benign solvents to form our materials. The focus on sustainable, and scalable, MOF syntheses has drastically grown over the last few years as commercialisation of this class of materials becomes a realisation. We therefore pursue the formation of a variety of calcium-based MOFs from sustainable precursors, using low energy and solvent-minimised techniques and report our related findings in Chapter Four.

1.7 References

1 A. Petrov, History of Nuclear Energy - World Nuclear Association, http://www.world-nuclear.org/information-library/current-and-future-generation/outline-history-of-nuclear-energy.aspx, (accessed 21 August 2022).

2 The UK's nuclear history - GOV.UK, https://www.gov.uk/guidance/the-uks-nuclear-history, (accessed 21 August 2022).

3 Energy UK, Electricity generation | Energy UK, https://www.energy-uk.org.uk/our-work/generation/electricity-generation.html, (accessed 21 August 2022).

4 A. Abdelouas, *Elements*, 2006, **2**, 335–341.

5 C. A. Sharrad, L. M. Harwood and F. R. Livens, in *Nuclear Power and the Environment*, 2011, pp. 40–56.

6 G. Choppin, J.-O. Liljenzin, J. Rydberg and C. Ekberg, *Radiochemistry and Nuclear Chemistry*, Academic Press, Fourth Edi., 2013.

7 P. Wilson, in *The Nuclear Fuel Cycle*, Oxford University Press, 1996, p. 207.

8 N. A. Chapman, I. G. McKinley and M. D. Hill, *The geological disposal of nuclear waste*, John Wiley and Sons, United Kingdom, 1987.

9 EDF, Sizewell B starts review to extend operation by 20 years | EDF, https://www.edfenergy.com/media-centre/news-releases/sizewell-b-starts-review-extend-operation-20-years, (accessed 21 August 2022).

10 A. H. Orabi, *J. Radiat. Res. Appl. Sci.*, 2013, **6**, 1.

11 Understanding activities that produce radioactive wastes in the UK Spent fuel reprocessing Overview, https://ukinventory.nda.gov.uk/wp-content/uploads/2014/01/Fact-sheet-spent-fuel-reprocessing.pdf, (accessed 21 August 2022).

12 D. Kim and A. A. Kruger, *J. Non. Cryst. Solids*, 2018, **481**, 41.

13 J. E. Brown, A. K. Kolstad, A. L. Brungot, B. Lind, A. L. Rudjord, P. Strand and L. FØyn, *Mar. Pollut. Bull.*, 1999, **38**, 560.

14 GOV.UK, Nuclear Provision: the cost of cleaning up Britain's historic nuclear sites, https://www.gov.uk/government/publications/nuclear-provision-explaining-the-cost-of-cleaning-up-britains-nuclear-legacy/nuclear-provision-explaining-the-cost-of-cleaning-up-britains-nuclear-legacy#latest-estimate, (accessed 21 August 2022).

15 V. Kortov and Y. Ustyantsev, in *Radiation Measurements*, 2013, vol. 55, p. 12.

16 Fukushima Daiichi Accident, http://www.world-nuclear.org/information-library/safety-and-security/safety-of-plants/fukushima-accident.aspx, (accessed 21 August 2022).

17 J. C. Renshaw, S. Handley-Sidhu and D. R. Brookshaw, in *Issues in Environmental Science & Technology, 32. Nuclear Power & the Environment*, 2011, pp. 152–176.

18 R. Farrow and R. Mchugh, Welcome to 'the Most Toxic Place in America', https://www.nbcnews.com/news/us-news/welcome-most-toxic-place-america-n689141, (accessed 5 January 2021).

19 K. Chapman, *Superheavy*, Bloomsbury Sigma, London, 2019.

20 U. S. Department of Energy, About Hanford Cleanup - Hanford Site, https://www.hanford.gov/page.cfm/AboutHanfordCleanup, (accessed 21 August 2022).

21 B. Dreyer, *Substitute House Bill 1723*, Washington State Legislature, 2018.

22 Potassium Iodide (KI) and Radiation Emergencies: Fact Sheet, https://www.health.ny.gov/environmental/radiological/potassium_iodide/fact_sheet.htm, (accessed 11 November 2021).

23 EPA, Radionuclide Basics: Strontium-90, https://www.epa.gov/radiation/radionuclide-basics-strontium-90,

(accessed 22 November 2021).

24 Radioisotope Brief: Strontium-90, https://www.cdc.gov/nceh/radiation/emergencies/isotopes/strontium.htm, (accessed 22 November 2021).

25 U.S. Department of Health & Human Services, CDC Radiation Emergencies | Radioisotope Brief: Cesium-137 (Cs-137), https://www.cdc.gov/nceh/radiation/emergencies/isotopes/cesium.htm, (accessed 8 December 2021).

26 L. A. Ilyin, M. I. Balonov, L. A. Buldakov, V. N. Bur'Yak, K. I. Gordeev, S. I. Dement'Ev, I. G. Zhakov, G. A. Zubovsky, A. I. Kondrusev, Y. O. Konstantinov, I. I. Linge, I. A. Likhtarev, A. M. Lyaginskaya, V. A. Matyuhin, O. A. Pavlovsky, A. I. Potapov, A. E. Prysyazhnyuk, P. V Ramsaev, A. E. Romanenko, M. N. Savkin, N. T. Starkova, N. D. Tron'Ko and A. F. Tsyb, *J. Radiol. Prot.*, 1990, **10**, 174.

27 K. Buesseler, M. Aoyama and M. Fukasawa, *Environ. Sci. Technol.*, 2011, **45**, 9931–9935.

28 P. Lindahl, C. Ellmark, T. Gäfvert, S. Mattsson, P. Roos, E. Holm and B. Erlandsson, *J. Environ. Radioact.*, 2003, **67**, 145.

29 G. E. Boyd, *J. Solution Chem.*, 1978, **7**, 229.

30 E. A. Bondietti and C. W. Francis, *Science (80-.).*, 1979, **203**, 1337.

31 I. T. Burke, C. Boothman, J. R. Lloyd, R. J. G. Mortimer, F. R. Livens and K. Morris, *Environ. Sci. Technol.*, 2005, **39**, 4109.

32 Sellafield, *Groundwater monitoring report: Sellafield annual data review 2013.*, 2014.

33 J. H. P. Watson and D. C. Ellwood, *Nucl. Eng. Des.*, 2003, **226**, 375.

34 P. C. Meltzer, B. K. Madras, H. F. Kung, H. J. Kim, M. P. Kung, S. K. Meegalla, K. Plossl and H. K. Lee, *Eur. J. Nucl. Med.*, 1996, **23**, 1527.

35 S. Liu, D. S. Edwards, M. C. Ziegler, A. R. Harris, S. J. Hemingway and J. A. Barrett, *Bioconjug. Chem.*, 2001, **12**, 624.

36 L. Oar-Arteta, T. Wezendonk, X. Sun, F. Kapteijn and J. Gascon, *Mater. Chem. Front.*, 2017, **1**, 1709.

37 Y. B. Huang, J. Liang, X. S. Wang and R. Cao, *Chem. Soc. Rev.*, 2017, **46**, 126.

38 Z. Chen, K. Adil, Ł. J. Weseliński, Y. Belmabkhout and M. Eddaoudi, *J. Mater. Chem. A*, 2015, **3**, 6276.

39 H. Li, K. Wang, Y. Sun, C. T. Lollar, J. Li and H. C. Zhou, *Mater. Today*, 2018, **21**, 108.

40 D. P. Ferris, C. L. Stern, J. F. Stoddart, M. S. Nassar, Y. Y. Botros, J. M. Holcroft, K. J. Hartlieb and I. Kandela, *Mol. Pharm.*, 2017, **14**, 1831.

41 X. Gao, R. Cui, G. Ji and Z. Liu, *Nanoscale*, 2018, **10**, 6205.

42 Z. Su, Y. R. Miao, G. Zhang, J. T. Miller and K. S. Suslick, *Chem. Sci.*, 2017, **8**, 8004.

43 S. R. Batten, N. R. Champness, X. M. Chen, J. Garcia-Martinez, S. Kitagawa, L. Öhrström, M. O'Keeffe, M. P. Suh and J. Reedijk, *Pure Appl. Chem.*, 2013, **85**, 1715.

44 H. Li, M. Eddaoudi, M. O'Keefe and O. M. Yaghi, *Nature*, 1999, **402**, 276.

45 O. M. Yaghi and H. Li, *J. Am. Chem. Soc.*, 1995, **117**, 10401.

46 B. F. Hoskin and R. Robson, *J. Am. Chem. Soc.*, 1989, **111**, 5962.

47 M. Fujita, S. Washizu, K. Ogura and Y. J. Kwon, *J. Am. Chem. Soc.*, 1994, **116**, 1151.

48 P. Z. Moghadam, A. Li, S. B. Wiggin, A. Tao, A. G. P. Maloney, P. A. Wood, S. C. Ward and D. Fairen-Jimenez, *Chem. Mater.*, 2017, **29**, 2618.

49 H. Furukawa, K. E. Cordova, M. O'Keeffe and O. M. Yaghi, *Science (80-.).*, 2013, **341**, 974.

50 A. E. Baumann, D. A. Burns, B. Liu and V. S. Thoi, *Commun. Chem.*, 2019, **2**, 86.

51 Y. M. Sani, W. M. A. W. Daud and A. R. Abdul Aziz, *Appl. Catal. A Gen.*, 2014, **470**, 140.

52 R. Banerjee, A. Phan, B. Wang, C. Knobler, H. Furukawa, M. O'Keeffe and O. M. Yaghi, *Science (80-.).*, 2008, **319**, 939.

53 K. S. Park, Z. Ni, A. P. Côté, J. Y. Choi, R. Huang, F. J. Uribe-Romo, H. K. Chae, M. O'Keeffe and O. M. Yaghi, *Proc. Natl. Acad. Sci. U. S. A.*, 2006, **103**, 10186.

54 L. Su, Q. Wu, L. Tan, Z. Huang, C. Fu, X. Ren, N. Xia, Z. Chen, X. Ma, X. Lan, Q. Zhang and X. Meng, *ACS Appl. Mater. Interfaces*, 2019, **11**, 10520.

55 Q. Wu, M. Niu, X. Chen, L. Tan, C. Fu, X. Ren, J. Ren, L. Li, K. Xu, H. Zhong and X. Meng, *Biomaterials*, 2018, **162**, 132.

56 C. Doonan, R. Riccò, K. Liang, D. Bradshaw and P. Falcaro, *Acc. Chem. Res.*, 2017, **50**, 1423.

57 W. Morris, C. J. Stevens, R. E. Taylor, C. Dybowski, O. M. Yaghi and M. A. Garcia-Garibay, *J. Phys. Chem. C*, 2012, **116**, 13307.

58 D. Yang, Y. Chen, Z. Su, X. Zhang, W. Zhang and K. Srinivas, *Coord. Chem. Rev.*, 2021, **428**, 213619.

59 J. I. Feldblyum, M. Liu, D. W. Gidley and A. J. Matzger, *J. Am. Chem. Soc.*, 2011, **133**, 18257.

60 Z. Zhang, L. Zhang, L. Wojtas, M. Eddaoudi and M. J. Zaworotko, *J. Am. Chem. Soc.*, 2012, **134**, 928.

61 P. Maniam and N. Stock, *Inorg. Chem.*, 2011, **50**, 5085.

62 S. A. Sotnik, S. V Kolotilov, M. A. Kiskin, Z. V Dobrokhotova, K. S. Gavrilenko, V. M. Novotortsev, I. L. Eremenko, V. K. Imshennik, Y. V Maksimov and V. V Pavlishchuk, *Russ. Chem. Bull.*, 2014, **63**, 862.

63 A. A. Yakovenko, J. H. Reibenspies, N. Bhuvanesh and H.-C. Zhou, *J. Appl. Crystallogr.*, 2013, **46**, 346.

64 N. L. Rosi, J. Eckert, M. Eddaoudi, D. T. Vodak, J. Kim, M. O'Keeffe and O. M. Yaghi, *Science (80-.).*, 2003, **300**, 1127.

65 N. Lock, Y. Wu, M. Christensen, L. J. Cameron, V. K. Peterson, A. J. Bridgeman, C. J. Kepert and B. B. Iversen, *J. Phys. Chem. C*, 2010, **114**, 16181.

66 E. Alvarez, N. Guillou, C. Martineau, B. Bueken, B. Vandevoorde, C. Leguillouzer, P. Fabry, F. Nouar, F. Taulelle, D. Devos, J. S. Chang, K. H. Cho, N. Ramsahye, T. Devic, M. Daturi, G. Maurin and C. Serre, *Angew. Chemie - Int. Ed.*, 2015, **54**, 3664.

67 L. Bolinois, T. Kundu, X. Wang, Y. Wang, Z. Hu, K. Koh and D. Zhao, *Chem. Commun.*, 2017, **53**, 8118.

68 F. M. Mulder, B. Assfour, J. Huot, T. J. Dingemans, M. Wagemaker and A. J. Ramirez-Cuesta, *J. Phys. Chem. C*, 2010, **114**, 10648.

69 H. Fei, D. L. Rogow and S. R. J. Oliver, *J. Am. Chem. Soc.*, 2010, **132**, 7202.

70 M. Eddaoudi, J. Kim, N. Rosi, D. Vodak, J. Wachter, M. O'Keeffe and O. M. Yaghi, *Science (80-.).*, 2002, **295**, 469.

71 J. Xu, Z. S. Bai, M. S. Chen, Z. Su, S. S. Chen and W. Y. Sun, *CrystEngComm*, 2009, **11**, 2728.

72 Y. Yan, M. Juríček, F.-X. Coudert, N. A. Vermeulen, S. Grunder, A. Dailly, W. Lewis, A. J. Blake, J. F. Stoddart and M. Schröder, *J. Am. Chem. Soc.*, 2016, **138**, 3371.

73 H. R. Abid, J. Shang, H. M. Ang and S. Wang, *Int. J. Smart Nano Mater.*, 2013, **4**, 72.

74 A. D. Burrows, in *Metal Organic Frameworks as Heterogeneous Catalysts*, The Royal Society of Chemistry, 2013, p. 31.

75 M. Kalaj and S. M. Cohen, *ACS Cent. Sci.*, 2020, **6**, 1046.

76 J. G. Nguyen and S. M. Cohen, *J. Am. Chem. Soc.*, 2010, **132**, 4560.

77 Z. Yin, S. Wan, J. Yang, M. Kurmoo and M. H. Zeng, *Coord. Chem. Rev.*, 2019, 378, 500.

78 J. Aguilera-Sigalat, A. Fox-Charles and D. Bradshaw, *Chem. Commun.*, 2014, **50**, 15453.

79 H. A. Hamzah, T. S. Crickmore, D. Rixson and A. D. Burrows, *Dalt. Trans.*, 2018, **47**, 14491.

80 C. Volkringer and S. M. Cohen, *Angew. Chemie Int. Ed.*, 2010, **49**, 4644.

81 J. E. Halls, A. Hernán-Gómez, A. D. Burrows and F. Marken, *Dalt. Trans.*, 2012, **41**, 1475.

82 R. J. Marshall, S. L. Griffin, C. Wilson and R. S. Forgan, *J. Am. Chem. Soc.*, 2015, **137**, 9527.

83 R. J. Marshall, T. Richards, C. L. Hobday, C. F. Murphie, C. Wilson, S. A. Moggach, T. D. Bennett and R. S. Forgan, *Dalt. Trans.*, 2016, **45**, 4132.

84 W. Morris, C. J. Doonan, H. Furukawa, R. Banerjee and O. M. Yaghi, *J. Am. Chem. Soc.*, 2008, **130**, 12626.

85 A. Karmakar, N. Kumar, P. Samanta, A. V. Desai and S. K. Ghosh, *Chem. - A Eur. J.*, 2016, **22**, 864.

86 W. Morris, W. E. Briley, E. Auyeung, M. D. Cabezas and C. A. Mirkin, *J. Am. Chem. Soc.*, 2014, **136**, 7261.

87 W. J. Rieter, K. M. L. Taylor and W. Lin, *J. Am. Chem. Soc.*, 2007, **129**, 9852.

88 K. C. Jayachandrababu, D. S. Sholl and S. Nair, *J. Am. Chem. Soc.*, 2017, **139**, 5906.

89 U. Fluch, V. Paneta, D. Primetzhofer and S. Ott, *Chem. Commun.*, 2017, **53**, 6516.

90 M. Tu, S. Wannapaiboon and R. A. Fischer, *J. Mater. Chem. A*, 2020, **8**, 13710.

91 T.-F. Liu, L. Zou, D. Feng, Y.-P. Chen, S. Fordham, X. Wang, Y. Liu and H.-C. Zhou, *J. Am. Chem. Soc.*, 2014, **136**, 7813.

92 S. Abednatanzi, P. Gohari Derakhshandeh, H. Depauw, F.-X. Coudert, H. Vrielinck, P. Van Der Voort and K. Leus, *Chem. Soc. Rev.*, 2019, **48**, 2535.

93 X. Song, T. K. Kim, H. Kim, D. Kim, S. Jeong, H. R. Moon and M. S. Lah, *Chem. Mater.*, 2012, **24**, 3065.

94 S. Das, H. Kim and O. Kim, *J. Am. Chem. Soc.*, 2009, **131**, 3814.

95 M. Kim, J. F. Cahill, H. Fei, K. A. Prather and S. M. Cohen, *J. Am. Chem. Soc.*, 2012, **134**, 18082.

96 Z. Hu, M. Khurana, Y. H. Seah, M. Zhang, Z. Guo and D. Zhao, *Chem. Eng. Sci.*, 2015, **124**, 61.

97 C. Montoro, E. García, S. Calero, M. A. Pérez-Fernández, A. L. López, E. Barea and J. A. R. Navarro, *J. Mater. Chem.*, 2012, **22**, 10155.

98 D. Jiang, L. L. Keenan, A. D. Burrows and K. J. Edler, *Chem. Commun.*, 2012, **48**, 12053.

99 M. A. Dessau and Y. Modis, *J. Vis. Exp.*, 2010, **47**, 2285.

100 R. A. Smaldone, R. S. Forgan, H. Furukawa, J. J. Gassensmith, A. M. Z. Slawin, O. M. Yaghi and J. F. Stoddart, *Angew. Chemie - Int. Ed.*, 2010, **49**, 8630.

101 J. H. Cavka, S. Jakobsen, U. Olsbye, N. Guillou, C. Lamberti, S. Bordiga and K. P. Lillerud, *J. Am. Chem. Soc.*, 2008, **130**, 13850.

102 A. D. Burrows, K. Cassar, R. M. W. Friend, M. F. Mahon, S. P. Rigby and J. E. Warren, *CrystEngComm*, 2005, **7**, 548.

103 S. M. Hawxwell and L. Brammer, *CrystEngComm*, 2006, **8**, 473.

104 I. Thomas-Hillman, A. Laybourn, C. Dodds and S. W. Kingman, *J. Mater. Chem. A*, 2018, **6**, 11564.

105 J. Klinowski, F. A. Almeida Paz, P. Silva and J. Rocha, *Dalt. Trans.*, 2011, **40**, 321.

106 J. Y. Choi, J. Kim, S. H. Jhung, H.-K. Kim, H.-S. Chang and H. K. Chae, *Bull. Korean Chem. Soc*, 2006, **27**, 1523.

107 A. Laybourn, A. M. López-Fernández, I. Thomas-Hillman, J. Katrib, W. Lewis, C. Dodds, A. P. Harvey and S. W. Kingman, *Chem. Eng. J.*, 2019, **356**, 170.

108 C. E. Willans, S. French, K. M. Anderson, L. J. Barbour, J. A. Gertenbach, G. O. Lloyd, R. J. Dyer, P. C. Junk and J. W. Steed, *Dalt. Trans.*, 2011, **40**, 573.

109 T. Stolar, A. Prašnikar, V. Martinez, B. Karadeniz, A. Bjelić, G. Mali, T. Friščić, B. Likozar and K. Užarević, *ACS Appl. Mater. Interfaces*, 2021, **13**, 3070.

110 D. Chen, J. Zhao, P. Zhang and S. Dai, *Polyhedron*, 2019, **162**, 59.

111 C. Jiang, X. Wang, Y. Ouyang, K. Lu, W. Jiang, H. Xu, X. Wei, Z. Wang, F. Dai and D. Sun, *Nanoscale Adv.*, 2022, **4**, 2077.

112 Z. Zhang, Y. Zhao, Q. Gong, Z. Lib and J. Li, *Chem. Commun.*, 2013, **49**, 653.

113 P. D. C. Dietzel, V. Besikiotis and R. Blom, *J. Mater. Chem.*, 2009, **19**, 7362.

114 M. T. Kapelewski, T. Runčevski, J. D. Tarver, H. Z. H. Jiang, K. E. Hurst, P. A. Parilla, A. Ayala, T. Gennett, S. A. Fitzgerald, C. M. Brown and J. R. Long, *Chem. Mater.*, 2018, **30**, 8179.

115 R. M. Giappa, E. Tylianakis, M. Di Gennaro, K. Gkagkas and G. E. Froudakis, *Int. J. Hydrogen Energy*, 2021, **46**, 27612.

116 B. Pato-Doldán, M. H. Rosnes and P. D. C. Dietzel, *ChemSusChem*, 2017, **10**, 1710.

117 L. Alaerts, M. Maes, M. A. van der Veen, P. A. Jacobs and D. E. De Vos, *Phys. Chem. Chem. Phys.*, 2009, **11**, 2903.

118 H. Y. Li, S. N. Zhao, S. Q. Zang and J. Li, *Chem. Soc. Rev.*, 2020, **49**, 6364.

119 L. K. Cadman, M. F. Mahon and A. D. Burrows, *Faraday Discuss.*, 2021, **225**, 414.

120 A. H. Assen, O. Yassine, O. Shekhah, M. Eddaoudi and K. N. Salama, *ACS Sensors*, 2017, **2**, 1294.

121 J. Zhu, T. Xia, Y. Cui, Y. Yang and G. Qian, *J. Solid State Chem.*, 2019, **270**, 317.

122 F. Y. Yi, S. C. Wang, M. Gu, J. Q. Zheng and L. Han, *J. Mater. Chem. C*, 2018, **6**, 2010.

123 Z. Hu, C. A. Tao, H. Liu, X. Zou, H. Zhu and J. Wang, *J. Mater. Chem. A*, 2014, **2**, 14222.

124 Y. Sun, L. Zheng, Y. Yang, X. Qian, T. Fu, X. Li, Z. Yang, H. Yan, C. Cui and W. Tan, *Nano-Micro Lett.*, 2020, **12**, 103.

125 P. Horcajada, C. Serre, M. Vallet-Regí, M. Sebban, F. Taulelle and G. Férey, *Angew. Chemie - Int. Ed.*, 2006, **45**, 5974.

126 Y. Hu, H. Cheng, X. Zhao, J. Wu, F. Muhammad, S. Lin, J. He, L. Zhou, C. Zhang, Y. Deng, P. Wang, Z. Zhou, S. Nie and H. Wei, *ACS Nano*, 2017, **11**, 5558.

127 J. Deng, K. Wang, M. Wang, P. Yu and L. Mao, *J. Am. Chem. Soc.*, 2017, **139**, 5877.

128 X. Lian, A. Erazo-Oliveras, J.-P. Pellois and H.-C. Zhou, *Nat. Commun.*, 2017, **8**, 2075.

129 M. Berchel, T. Le Gall, C. Denis, S. Le Hir, F. Quentel, C. Elléouet, T. Montier, J. M. Rueff, J. Y. Salaün, J. P. Haelters, G. B. Hix, P. Lehn and P. A. Jaffrès, *New J. Chem.*, 2011, **35**, 1000.

130 S. Haddad, I. Abánades Lázaro, M. Fantham, A. Mishra, J. Silvestre-Albero, J. W. M. Osterrieth, G. S. Kaminski Schierle, C. F. Kaminski, R. S. Forgan and D. Fairen-Jimenez, *J. Am. Chem. Soc.*, 2020, **142**, 6661.

131 V. K.-M. Au, *Front. Chem.*, 2020, **8**, 708.

132 K. Vikrant, V. Kumar, K. H. Kim and D. Kukkar, *J. Mater. Chem. A*, 2017, **5**, 22877.

133 Y. Chen, X. Bai and Z. Ye, *Nanomaterials*, 2020, **10**, 1481.

134 T. Kundu, L. Gilmanova, W. F. Yong and S. Kaskel, *Cell Reports Phys. Sci.*, 2021, **2**, 100348.

135 B. Lellis, C. Z. Fávaro-Polonio, J. A. Pamphile and J. C. Polonio, *Biotechnol. Res. Innov.*, 2019, **3**, 275.

136 J. M. Yang, R. J. Ying, C. X. Han, Q. T. Hu, H. M. Xu, J. H. Li, Q. Wang and W. Zhang, *Dalt. Trans.*, 2018, **47**, 3913.

137 M. Tong, D. Liu, Q. Yang, S. Devautour-Vinot, G. Maurin and C. Zhong, *J. Mater. Chem. A*, 2013, **1**, 8534.

138 Z. Q. Li, J. C. Yang, K. W. Sui and N. Yin, *Mater. Lett.*, 2015, **160**, 412.

139 M. A. Karimi, H. Masrouri, H. Karami, S. Andishgar, M. A. Mirbagheri and T. Pourshamsi, *J. Chinese Chem. Soc.*, 2019, **66**, 1327.

140 L. L. Li, X. Q. Feng, R. P. Han, S. Q. Zang and G. Yang, *J. Hazard. Mater.*, 2017, **321**, 622.

141 M. Mon, F. Lloret, J. Ferrando-Soria, C. Martí-Gastaldo, D. Armentano and E. Pardo, *Angew. Chemie - Int. Ed.*, 2016, **55**, 11167.

142 F. Schmidt, ed. M. Baerns, Springer Berlin Heidelberg, Berlin, Heidelberg, 2004, pp. 3–16.

143 R. Karan, R. Bhatia and R. K. Rawal, in *Green Sustainable Process for Chemical and Environmental Engineering and Science: Solid State Synthetic Methods*, Elsevier, 2021, pp. 159–188.

144 J. Guo, Y. Qin, Y. Zhu, X. Zhang, C. Long, M. Zhao and Z. Tang, *Chem. Soc. Rev.*, 2021, **50**, 5366.

145 W. G. Cui, G. Y. Zhang, T. L. Hu and X. H. Bu, *Coord. Chem. Rev.*, 2019, **387**, 79.

146 P. García-García, M. Müller and A. Corma, *Chem. Sci.*, 2014, **5**, 2979.

147 S. H. Cho, B. Ma, S. B. T. Nguyen, J. T. Hupp and T. E. Albrecht-Schmitt, *Chem. Commun.*, 2006, **24**, 2563.

148 J. Li, X. Wang, G. Zhao, C. Chen, Z. Chai, A. Alsaedi, T. Hayat and X. Wang, *Chem. Soc. Rev.*, 2018, **47**, 2322.

149 K. T. Holman, M. M. Halihan, J. W. Steed, S. S. Jurisson and J. L. Atwood, *J. Am. Chem. Soc.*, 1995, **117**, 7848.

150 D. C. Stepinski, G. F. Vandegrift, I. A. Shkrob, J. F. Wishart, K. Kerr, M. L. Dietz, D. T. D. Qadah and S. L. Garvey, *Ind. Eng. Chem. Res.*, 2010, **49**, 5863.

151 N. N. Chopabaeva, E. E. Ergozhin, A. T. Tasmagambet and A. I. Nikitina, *Solid Fuel Chem.*, 2009, **43**, 99.

152 A. Milutinović-Nikolić, D. Maksin, N. Jović-Jovičić, M. Mirković, D. Stanković, Z. Mojović and P. Banković, *Appl. Clay Sci.*, 2014, **95**, 294.

153 E. Holm, T. Gäfvert, P. Lindahl and P. Roos, in *Applied Radiation and Isotopes*, 2000, vol. 53, p. 153.

154 L. Liang, B. Gu and X. Yin, *Sep. Technol.*, 1996, **6**, 111.

155 M. Simonoff, B. Thomas, M. H. Vesvres, S. Poulain, G. Deves, C. Sergeant and V. Peretroukhine, *Radiochim. Acta*, 2006, **94**, 665.

156 H. Hu, L. Sun, Y. Gao, T. Wang, Y. Huang, C. Lv, Y. F. Zhang, Q. Huang, X. Chen and H. Wu, *J. Hazard. Mater.*, 2020, **387**, 121670.

157 J. Shen, W. Chai, K. Wang and F. Zhang, *ACS Appl. Mater. Interfaces*, 2017, **9**, 22440.

158 Z. W. Liu and B. H. Han, *Environ. Sci. Technol.*, 2020, **54**, 59.

159 J. Li, X. Dai, L. Zhu, C. Xu, D. Zhang, M. A. Silver, P. Li, L. Chen, Y. Li, D. Zuo, H. Zhang, C. Xiao, J. Chen, J. Diwu, O. K. Farha, T. E. Albrecht-Schmitt, Z. Chai and S. Wang, *Nat. Commun.*, 2018, **9**, 3007.

160 C. P. Li, J. Y. Ai, H. Zhou, Q. Chen, Y. Yang, H. He and M. Du, *Chem. Commun.*, 2019, **55**, 1841.

161 L. Zhu, C. Xiao, X. Dai, J. Li, D. Gui, D. Sheng, L. Chen, R. Zhou, Z. Chai, T. E. Albrecht-Schmitt and S. Wang, *Environ. Sci. Technol. Lett.*, 2017, **4**, 316.

162 L. Zhu, D. Sheng, C. Xu, X. Dai, M. A. Silver, J. Li, P. Li, Y. Wang, Y. Wang, L. Chen, C. Xiao, J. Chen, R. Zhou, C. Zhang, O. K. Farha, Z. Chai, T. E. Albrecht-Schmitt and S. Wang, *J. Am. Chem. Soc.*, 2017, **139**, 14873.

163 D. Sheng, L. Zhu, X. Dai, C. Xu, P. Li, C. I. Pearce, C. Xiao, J. Chen, R. Zhou, T. Duan, O. K. Farha, Z. Chai and S. Wang, *Angew. Chemie Int. Ed.*, 2019, **58**, 4968.

164 H. Fei, M. R. Bresler and S. R. J. Oliver, *J. Am. Chem. Soc.*, 2011, **133**, 11110.

165 D. Sheng, L. Zhu, C. Xu, C. Xiao, Y. Wang, Y. Wang, L. Chen, J. Diwu, J. Chen, Z. Chai, T. E. Albrecht-Schmitt and S. Wang, *Environ. Sci. Technol.*, 2017, **51**, 3471.

166 D. Banerjee, S. K. Elsaidi, B. Aguila, B. Li, D. Kim, M. J. Schweiger, A. A. Kruger, C. J. Doonan, S. Ma and P. K. Thallapally, *Chem. - A Eur. J.*, 2016, **22**, 17581.

167 Z. Bai, Y. Wang, Y. Li, W. Liu, L. Chen, D. Sheng, J. Diwu, Z. Chai, T. E. Albrecht-Schmitt and S. Wang, *Inorg. Chem.*, 2016, **55**, 6358.

168 D. Banerjee, W. Xu, Z. Nie, L. E. V Johnson, C. Coghlan, M. L. Sushko, D. Kim, M. J. Schweiger, A. A. Kruger, C. J. Doonan and P. K. Thallapally, *Inorg. Chem.*, 2016, **55**, 8241.

169 R. J. Drout, K. Otake, A. J. Howarth, T. Islamoglu, L. Zhu, C. Xiao, S. Wang and O. K. Farha, *Chem. Mater.*, 2018, **30**, 1277.

170 S. Dutta, P. Samanta, B. Joarder, S. Let, D. Mahato, R. Babarao and S. K. Ghosh, *ACS Appl. Mater. Interfaces*, 2020, **12**, 41810.

171 D. Bradshaw, A. Garai and J. Huo, *Chem. Soc. Rev.*, 2012, **41**, 2344.

172 Y. Zhang, V. Degirmenci, C. Li and E. J. M. Hensen, *ChemSusChem*, 2011, **4**, 59.

173 K. Ikigaki, K. Okada, Y. Tokudome, T. Toyao, P. Falcaro, C. J. Doonan and M. Takahashi, *Angew. Chemie*, 2019, **131**, 6960.

174 J. Meng, X. Liu, C. Niu, Q. Pang, J. Li, F. Liu, Z. Liu and L. Mai, *Chem. Soc. Rev.*, 2020, **49**, 3142.

175 Z. Inonu, S. Keskin and C. Erkey, *ACS Appl. Nano Mater.*, 2018, **1**, 5959.

176 Z. Ulker, I. Erucar, S. Keskin and C. Erkey, *Microporous Mesoporous Mater.*, 2013, **170**, 352.

177 Y. Guan, Z. Teng, L. Mei, J. Zhang, Q. Wang and Y. Luo, *J. Colloid Interface Sci.*, 2019, **533**, 207.

178 S. Bo, W. Ren, C. Lei, Y. Xie, Y. Cai, S. Wang, J. Gao, Q. Ni and J. Yao, *J. Solid State Chem.*, 2018, **262**, 135.

179 D. Wisser, F. M. Wisser, S. Raschke, N. Klein, M. Leistner, J. Grothe, E. Brunner and S. Kaskel, *Angew. Chemie - Int. Ed.*, 2015, **54**, 12588.

180 J. Reboul, S. Furukawa, N. Horike, M. Tsotsalas, K. Hirai, H. Uehara, M. Kondo, N. Louvain, O. Sakata and S. Kitagawa, *Nat. Mater.*, 2012, **11**, 717.

181 G. Zhao, N. Qin, A. Pan, X. Wu, C. Peng, F. Ke, M. Iqbal, K. Ramachandraiah and J. Zhu, *J. Nanomater.*, 2019, **2019**, 1454358.

182 L. Chen, X. Ding, J. Huo, S. El Hankari and D. Bradshaw, *J. Mater. Sci.*, 2019, **54**, 370.

183 Q. Li, S. Jiang, S. Ji, D. Shi and H. Li, *J. Porous Mater.*, 2015, **22**, 1205.

184 L. Huang, M. He, B. Chen and B. Hu, *J. Mater. Chem. A*, 2015, **3**, 11587.

185 H. Li, Q. Li, X. He, N. Zhang, Z. Xu, Y. Wang and Y. Wang, *Cryst. Growth Des.*, 2018, **18**, 6248.

186 A. A. Alqadami, M. Naushad, Z. A. Alothman and A. A. Ghfar, *ACS Appl. Mater. Interfaces*, 2017, **9**, 36026.

187 B. Valizadeh, T. N. Nguyen, S. Kampouri, D. T. Sun, M. D. Mensi, K. Stylianou, B. Smit and W. L. Queen, *J. Mater. Chem. A*, 2020, **8**, 9629.

Chapter 2 UiO-66-NH_2: Post-Synthetic Modifications & Green Approaches to its Composites

2.1 Introduction

The development of isoreticular chemistry in the early 2000s resulted in a boom of research activity in the MOF area and along with this the creation of new MOF structures at an ever-growing pace.[1] It was however rare to find MOFs among these new materials with appreciable stability. Ultimately, this comes down to the chosen metal and the resulting ligand-metal bonds that form between the metal nodes and organic linkers.[2,3] Transition metals such as copper and zinc are very popular as they typically yield highly crystalline products. This level of crystallinity is reached due to the lability of the metal-oxygen bonds in these MOFs which allows for reversible bond formation, slow growth of crystals, but ultimately the overall instability of the material. Lillerud *et al.* first reported in 2008 a MOF series with previously unseen levels of stability.[4] The UiO (Universitetet i Oslo) series utilised group four elements, that are renowned for their strong metal-oxygen bonds, with linear polycarboxylate organic linkers. Prior to this, only ZIFs or aluminium-based MIL-53 held a reputation for high stability.[5,6]

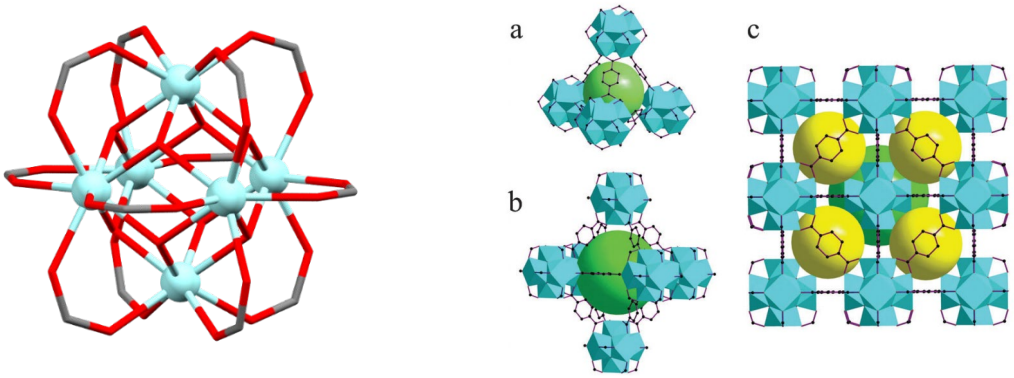

Figure 2.1 . (Left) SBU of UiO-66. (Right) The tetrahedral and octahedral pores and overall crystal structure of UiO-66.[7] Reproduced with permission from The Royal Society of Chemistry.

The SBU of the UiO series consists of six zirconium/hafnium (IV) ions arranged in an octahedral geometry (figure 2.1). Each metal centre displays square antiprismatic geometries, coordinating to four oxygen atoms from independent organic linkers as well as four face capping μ_3-O/μ_3-OH groups. This affords a metal node that displays 12-fold connectivity and thus defines a cuboctahedral geometry. The UiO series typically follows an **fcu** topology and therefore contains octahedral pores capped by smaller tetrahedral pores. UiO-66 ($[Zr_6O_4(OH)_4(BDC)_6]$) is the simplest MOF from the series consisting of terephthalic acid linkers. Functionalised UiO-66 MOFs that

contain moieties such as amines, halogens or hydroxyl groups are easily obtained with the appropriate linker. Longer linkers can be incorporated to form MOFs with larger apertures and surface areas without loss of material stability (table 2.1). TG-MS (thermogravimetric-mass spectrometry) analysis on UiO-66 recorded the generation of benzene upon decomposition. This establishes that the weakest bond in this MOF is not in fact the zirconium-oxygen bond but the C-C bond within the organic linker itself.

Table 2.1. Physical information for MOFs from the UiO series. Structures and data obtained from Lillerud *et al.*[4] Copyright 2008 American Chemical Society.

	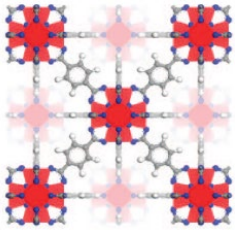	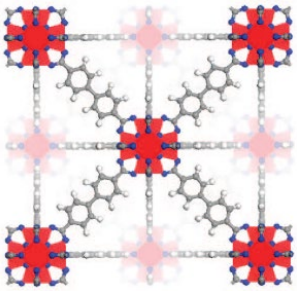	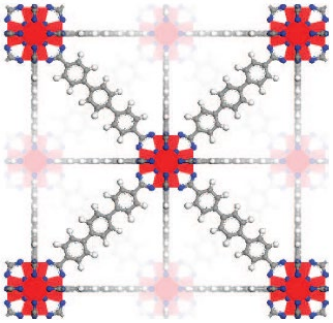
MOF	UiO-66	UiO-67	UiO-68
Linker	1,4-Benzenedicarboxylic acid	4,4'-biphenyl-dicarboxylic acid	terphenyl dicarboxylic acid
Surface area (m^2/g)	1187	3000	4170
Aperture size (Å)	6	8	10

UiO-66-NH_2 is an amine tagged MOF which utilises aminoterephthalic acid ($H_2BDC-NH_2$) as the organic linker. It is a very commonly used MOF and has found many applications including, selective CO_2 capture,[8] removal of dyes[9] and toxic molecule remediation.[10,11] It has also been investigated for perrhenate remediation by Thallapally *et al.* whereby the authors protonated UiO-66-NH_2 with 2M HCl to form the cationic framework $[UiO-66-NH_3][Cl]_6$.[12] Energy dispersive X-Ray spectroscopy (EDX) was used to measure the increase in chloride content expected following protonation due to the presence of Cl^- counter anions present in the material. The MOF has a modest perrhenate uptake capacity of 159 mg g^{-1} however it carries the benefits of superior thermal stability and chemical stability in water. Synchrotron-based XRD experiments were conducted on both the MOF and perrhenate-loaded MOF samples to allow for the oxo-anion location within the MOF pores to be confirmed (figure 2.2).

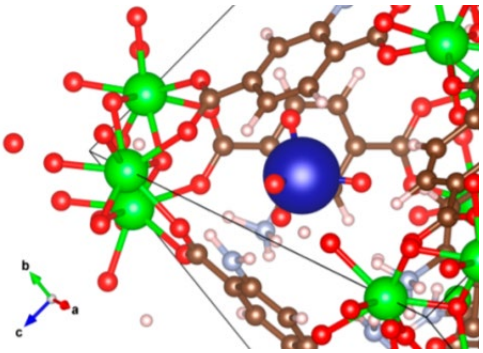

Figure 2.2. Perrhenate location within [UiO-66-NH_3][ReO_4] derived from a combination of synchrotron PXRD and molecular simulations.[12] Blue = rhenium, red = oxygen, green = zirconium, gold = carbon, grey = nitrogen and pink = hydrogen. Copyright 2016 American Chemical Society.

2.1.1 UiO-66-NH_2 Post-Synthetic Modifications

UiO-66-NH_2 is a common parent framework in covalent PSM reactions. The high abundance of amine tags is ideal for a wide range of chemical reactions to graft different moieties onto the material. It has an aperture size large enough to allow for the passage of a fully methylated benzene and thus small organics are easily able to diffuse into the pores of the MOF.[4] In addition, the UiO series can be engineered to contain defects[13,14] which would, in theory, allow for the reaction of larger molecules with the amine tags of the MOF.[15,16] Burrows *et al.* have demonstrated that the amine functionality on the BDC-NH_2 linker could be reacted with the β-carbon of electron deficient alkenes *via* aza-Michael addition reactions, to generate new frameworks (Scheme 2.1).[17,18] ^{1}H NMR proved that the reactions had, in the case of acrylic acid and acrylonitrile, achieved 100% conversion. Typically, this reaction requires a Lewis acid catalyst such as SmI_2, which if used in a PSM reaction has the potential to cause pore blockage. This reaction however could proceed without the addition of a catalyst, most likely due to advantageous hydrogen bonding within the pores and the immobilisation of the -NH_2 moiety. The nitrile functionalised daughter MOF could be further reacted with sodium azide in the presence of zinc chloride to form a tetrazole-bearing MOF.

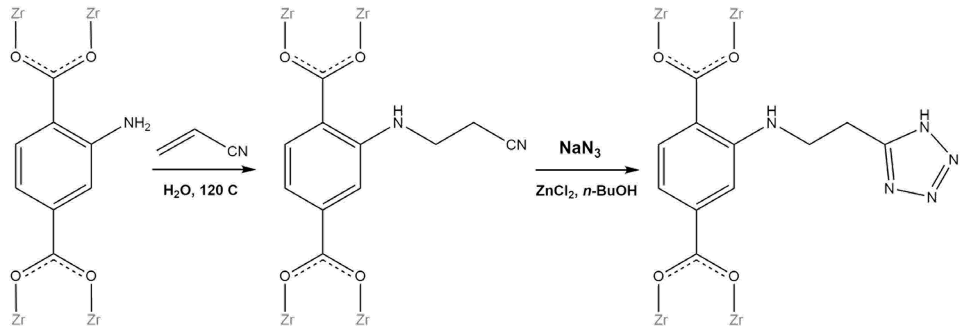

Scheme 2.1. Reaction of acrylonitrile and UiO-66-NH_2 followed by the generation of a tetrazole by reaction with sodium azide.[17]

Additional PSM reactions with UiO-66-NH_2, include the generation of various amide functionalities through the reaction of the -NH_2 group with different anhydrides,[19,20] the anchoring of diphenylphosphinyls moieties with diphenylphosphinic chloride,[21] and the generation of Pd binding sites by reacting 2-pyridinecarboxaldehyde with the amine tag followed by the addition of a palladium complex.[21,22] It is noted that reaction conversions widely vary depending on the reagent used; for example, acetic anhydride yields a conversion of 73% while maleic anhydride is much lower at 33%. The BET surface areas of daughter MOFs are expectedly much lower than the parent framework, given the often-bulky pendants occupying the pore space; diphenylphosphinyl-containing MOFs for example have surface areas over 50% lower than UiO-66-NH_2.

2.1.1.1 Urea functionalisation of MOFs through Post-Synthetic Modifications

The primary route to urea functionalisation of MOFs is to start with a parent framework that bares an amine group. This amine is reacted with an isocyanate to generate the urea moiety with no side products. Dugan *et al.* first explored this route with IRMOF-3 ([$Zn_4O(BDC\text{-}NH_2)_3$]) (IRMOF = Isoreticular metal-organic framework) and several different isocyanate reagents (figure 2.3). The MOF and isocyanate were simply combined in chloroform for three days at room temperature. Reaction conversions differed from quantitative yields to no reaction at all. Interestingly, the use of tetramethylsilyl isocyanate yielded a primary urea, suggesting hydrolysis of the product from residual water. Bulky isocyanates, unsurprisingly, yielded very poor conversions due to sterically hinderance within the MOF pores.

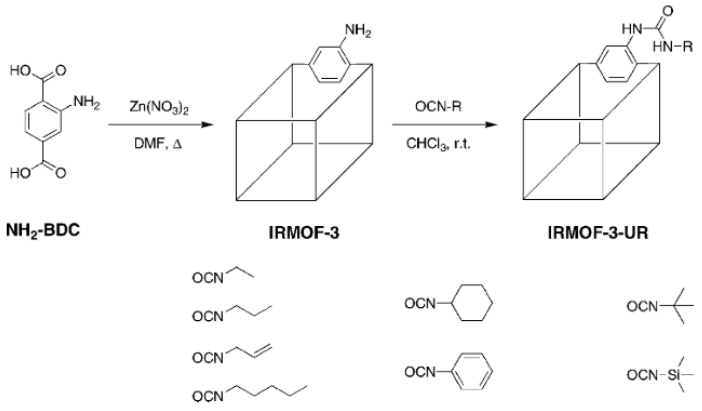

Figure 2.3. Generation of urea groups on IRMOF-3, with various isocyanate molecules.[23] Reproduced with permission from The Royal Society of Chemistry.

Dong *et al.* functionalised (Cr) MIL-101-NH_2 ([$Cr_3(O)OH(BDC)_3(H_2O)_2$]) (MIL = Matériaux de l'Institut Lavoisier) with various urea groups achieving near quantitative conversions.[24] The amine tags were reacted with excess amounts of phenyl, butyl, and 3,5-bis(trifluoromethyl)phenyl isocyanates in independent reactions to form their respective daughter MOFs. These functionalised MOFs were then explored for catalysis of Friedel-Craft reactions. The aluminium form of MIL-101-NH_2 was also

demonstrated as a good parent MOF for the formation of phenyl urea moieties by Wittmann *et al.*[25] which improved the water stability of the material.

Volkringer and Cohen took an alternative approach to obtaining urea-functionalised MOFs by modifying amine groups on (Al) MIL-53-NH_2 ([AlO(BDC-NH_2)]) with diphosgene to form isocyanate groups which ultimately were reacted with various amines.[26]

From our knowledge, there are only three reports of urea functionalities being incorporated within UiO-66-NH_2. It is however important to note that these reports are not conventional covalent PSM reactions within the framework pores but occur exclusively on the surfaces of the MOF crystals. Yao *et al.* first formed UiO-66-NH_2 membranes by reacting the -NH_2 groups on the nanoparticle surfaces with a polyurethane oligomer (figure 2.4).[27] These membranes were used for dye capture and separations. Separately, Akbarian *et al.* reacted the amine groups between UiO-66-NH_2 nanoparticles with 1,4-phenylene diisocyanate to polymerise the MOF crystals to one another through urea linkages.[28] Finally, Fotovat *et al.* formed a UiO-66-NH_2@POP (porous organic polymer) hybrid material whereby the urea groups of the POP underwent hydrogen bonding with the surface amines of the MOF for application in uranium remediation.[29]

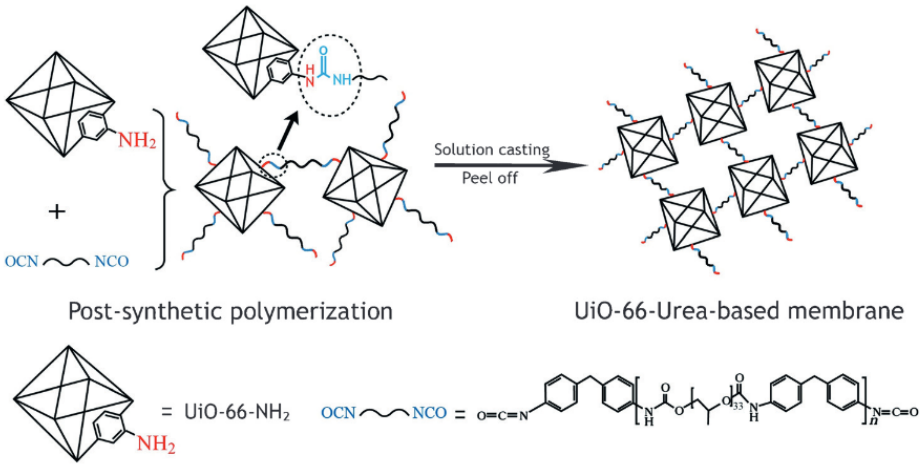

Figure 2.4. Schematic illustration of the fabrication of UiO-66-Urea-based membranes.[27] © 2016 WILEY-VCH Verlag GmbH & Co. KGaA, Weinheim.

2.1.2 MOF@Biopolymer Composites

The combination of MOFs with biopolymers to form composites is a popular area of MOF research. The scaffold material is often a cheap resource due to their high abundance in nature, and they are usually chemically resistant, particularly to water. They are also a green resource and present no harm to organisms or the environment. When considering materials for use in the clean-up of local environments, a biopolymer is a very good starting point as the potential of releasing harmful

synthetic polymers such a poly(styrene terephthalate) and poly(styrene) into the environment is avoided from the design concept stage.

2.1.2.1 MOF@Alginate Composites

Alginic acid is incredibly abundant and as such is one of the most widely used biopolymers in the pharmaceutical and food industries[30]. The biopolymer is extracted from brown algae and well known for its non-toxicity, biocompatibility and low costs.[31,32] Alginic acid is composed of two sugar-based monomer units, D-mannuronic acid and L-glucuronic acid (figure 2.5), affording a linear, non-branched, polysaccharide. Carboxylic acid groups on the monomer units can undergo deprotonation to form an anionic polymer, referred to as alginate. Typically, alginic acid is purchased in its powdered sodium salt form, sodium alginate, where the Na(I) cations counterbalance the charge of the deprotonated biopolymer. Sodium alginate is readily dissolved in water to form alginate solutions. When these solutions are submerged into solutions that contain gel-inducing agents, alginate will undergo ionotropic gelation to form a stable hydrogel. Gel-inducing agents are typically multivalent cationic salts, such as calcium (II) chloride, that cross link with the carboxylate functionalities on the glucuronate monomers of alginate in a so-called 'egg-box' configuration to cause coagulation (Figure 2.5).[33–35]

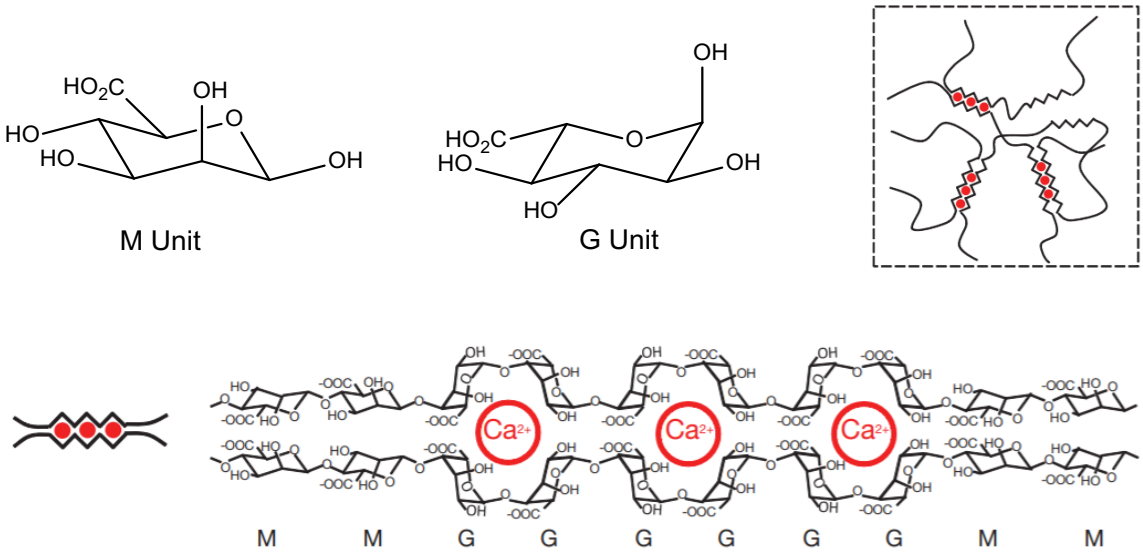

Figure 2.5. (Top left) Chemical structures of mannuronic acid (M unit) and guluronic acid (G unit) and (right) schematic of the ionotropic gelation within alginate gels. (Bottom) The location of cross-linking calcium (II) ions within calcium alginate.[34] Reproduced with permission from Springer Nature 2012.

The formation of MOF@alginate composites can be achieved *via* two synthetic routes. The most common method is to form the MOF separately and then disperse it into a sodium alginate solution. Upon ionotropic gelation, the MOF crystals are immobilised within the alginate scaffold affording

the composite. Lee *et al.* completed an extensive study into the formation of UiO-66@alg beads *via* this direct method.[36] UiO-66 crystals were dispersed into a sodium alginate solution and dripped from a syringe into a solution of calcium chloride. Gelation of the individual droplets resulted in the formation of UiO-66@alg beads. The UiO-66@alg beads were then heated in an oven to remove all water, affording an aerogel (figure 2.6). They investigated altering variables such as alginate and cation concentration and cation type to measure their effects on porosity and compressibility. Daradmare *et al*. also formed ZIF-8@alg composites through this same method[37]; ZIF-8 crystals were dispersed in a solution of sodium alginate and dripped into a barium acetate solution to form ZIF-8@alginate beads.

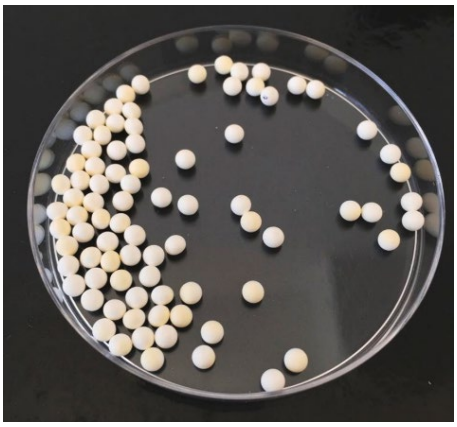

Figure 2.6. (Left) UiO-66@alg beads after heat treatment.[36] Reproduced with permission from Elsevier.

Alternatively, an *in-situ* method can be used, whereby the MOF crystals are grown within an existing alginate hydrogel. Zhu *et al.* successfully formed HKUST-1 and MIL-100(Fe) within copper(II) alginate and iron(III) alginates respectively, by submerging the hydrogels into solutions of trimesic acid and heating to 85 °C for between 18 and 24 hours.[38] They shaped their hydrogels into continuous ribbons, by injecting sodium alginate into the salt baths with a syringe (figure 2.7). This work was furthered by Li *et al.* in 2020 when they were able to afford MOF@alg composites of the trimesic acid-based MOFs Zn-BTC and Cr-BTC through similar methods.[39] In both referenced works, the metal ions that are used for gelation of the biopolymer are also utilised in MOF formation.

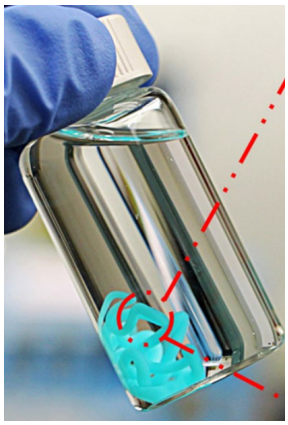

Figure 2.7. HKUST-1@alg ribbons synthesised *via* an *in-situ* method.[38] Copyright 2016 American Chemical Society.

MOF@alginate composites have been used in a variety of different applications. Recently, Li *et al.* showed that encapsulating gallate-based MOFs and MIL-53 in calcium alginate aerogel beads formed useful materials for the separation of ethane/ethylene mixtures.[40] The water compatibility of MOF@alginates have been exploited in various aqueous applications such as chromium remediation,[37] desalination,[41] and the photo catalysed degradation of malachite green dye.[42]

From our literature search we have not been able to identify any prior studies into UiO-66-NH_2@alg composites.

2.1.2.2 MOF@Cellulose Composites

Cellulose is the most abundant naturally occurring polymer on Earth, found in the cell walls of every plant.[43] The polymer consists of β-glucose monomers that are linked through 1,4-glycosidic bonds (figure 2.8). A very wide variety of applications for cellulose have been found including textiles, paper making and biofuels.[44,45]

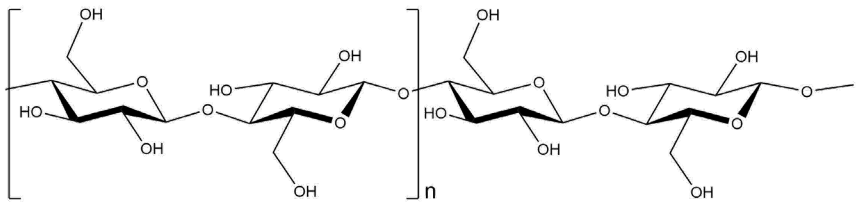

Figure 2.8. Chemical structure of cellulose.

The biopolymer is cheap to purchase due to its abundance, is easily processible, and can be easily recycled. These properties have made cellulose a popular scaffold material in many composites including cellulose@metal nanoparticle composites,[46,47] cellulose@zinc oxide papers for arsenic remediation[48] and cellulose@montmorillonite electrospun composites for Cr^{6+} removal.[49]

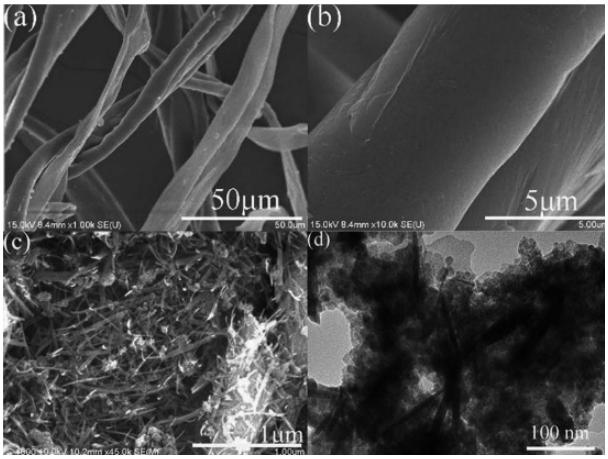

Figure 2.9. SEM images of the cotton (a and b) and the cellulose@Fe_2O_3 composites (c). TEM image of the cellulose@Fe_2O_3 composites (d).[48] Copyright 2017 American Chemical Society.

Cellulose has also been incorporated into a variety of MOF composites.[50] Laurila *et al.* have deposited HKUST-1 on electrospun nanofibres of cellulose.[51] Deposition took place *via* a layer-by-layer synthesis whereby the composite was submerged in alternating metal ion and linker solutions. The same MOF was deposited on cotton fabric by Neufeld *et al.* and used as a catalyst for the release of nitric oxide.[52] Remediation of pollutants from aqueous solutions are a key application for MOF@cellulose composites due to the compatibility of the scaffold and water. ZIF-8@cellulose foams have been used for Cr^{6+} removal[53] while MIL-100(Fe)@cellulose papers were used to remediate paracetamol from waste water.[54]

UiO-66-NH_2@cellulose filter papers were first developed by Hashem *et al.* through the addition of functionalised filter papers to a traditional UiO-66-NH_2 synthesis in DMF for the capture of methyl orange and chromium anions (figure 2.10).[55] They confirmed that the formation of UiO-66-NH_2 on non-functionalised cellulose yields almost no MOF formation. This step is therefore essential in the formation of these composites. In the majority of cases, including the work by Hashem *et al.*, this involved carboxymethylation of the hydroxyl groups on cellulose proceed *via* a base catalysed reaction with chloroacetic acid.[51,52,55] We have seen one report by Mirkovic *et al.* in which MOF-5 was grafted onto cellulose fibres by pre-treating the scaffold with dopamine dissolved in Tris buffer solution (figure 2.10).[56] Mercerisation with highly caustic solutions has also been shown as a promising step to pre-treat cotton for the formation of UiO-66-NH_2@cotton composites. This process is said to reduce the density of microfibrils by breaking down the hydrogen bond interactions between cellulose chains[57], increasing the level of hydroxyl groups on the cellulose surface that are free for MOF grafting.

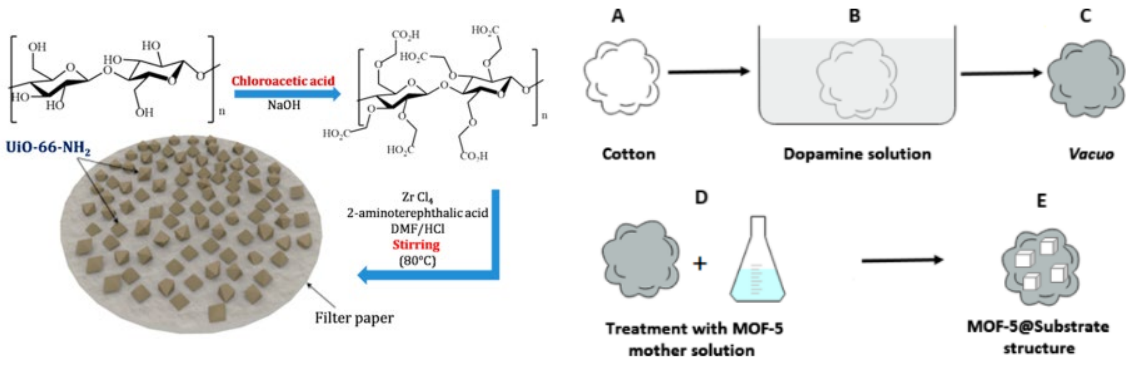

Figure 2.10. (Left) Schematic of UiO-66-NH_2@FFP formation by Hashem *et al.* (Right) Schematic of MOF-5@cotton formation by Mirkovic *et al.*[55,56] Copyright 2019 American Chemical Society.

It was found that for the formation of UiO-66-NH_2@cellulose aerogels, by Lei *et al.*,[58] no chemical modification prior to composite formation was required, despite the filter papers and aerogels consisting of the same biopolymer, which we attributed to the difference in the porous nature of the cellulose aerogels. SEM microscopy of the aerogels shows pores of varying size in the micrometre region. This would allow for absorption and entrapment of MOF precursors, and ultimately, the formation of the MOF within the scaffold. A cellulose filter paper is not enhanced by these pores and needs to be regarded as more of a surface. Thus, chemical modification to the cellulose filter paper is essential to graft UiO-66-NH_2 directly onto the cellulose fibres.

2.2 Chapter Outlook

Within this chapter we establish a PSM reaction to covalently graft an ethyl urea functionality to UiO-66-NH_2. This follows the rationale that the incorporation of a bidentate hydrogen bond donor group may improve the adsorption and retainment of oxo-anions such as perrhenate by providing a binding site for the adsorbate. The PSM product undergoes a further dative PSM to protonate the urea and remaining amine groups to afford an anion-exchange material for perrhenate remediation.

UiO-66-NH_2 is then immobilised into two different bio-composites: UiO-66-NH_2@alg beads and UiO-66-NH_2@functionalised cellulose filter papers (FFP) for the remediation of perrhenate. We demonstrate water-based room temperature procedures for growing UiO-66-NH_2 *in-situ* on the latter biopolymer, supporting our long-term sustainable green chemistry goals. We believe that UiO-66-NH_2@FFP has potential applications as decorated filters and in dipstick testing of water samples (figure 2.11). While UiO-66-NH_2@Alg composites have been envisaged as compact columns for the filtration of polluted wastewater.

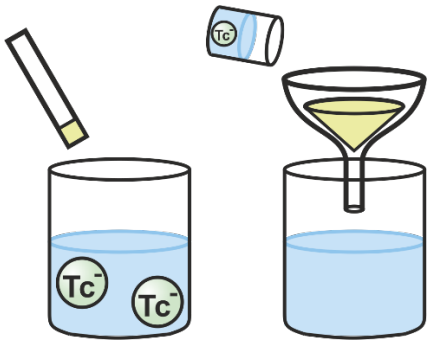

Figure 2.11. Envisaged applications of UiO-66-NH_2@FFP composites.

Our experience of repeating reported syntheses of UiO-66-NH_2@FFP found that these routes yielded high quantities of UiO-66-NH_2 in solution, with little grafting of the MOF to the FFP surface. This is inevitable given that the scaffold is simply being added to a standard MOF synthesis. While the non-deposited MOF can be recovered through centrifugation and has potential uses elsewhere, we believe that approaching the synthesis of UiO-66-NH_2@FFP through a dip coating process may reduce the quantity of unbound MOF produced.

There are many reports in literature of materials for perrhenate remediation, but they often test at anion concentrations that are far higher than the levels of contamination found at nuclear licensed sites. Banerjee *et al.* tested [UiO-66-NH_3][Cl]$_6$ with perrhenate concentrations as high as 150 ppm ($6x10^{-4}$ M) while Li *et al.* investigated TJNU-216 under 76 and 2,500 ppm (0.01 M) solutions.[12,59] While these high levels of the target analyte allow for the calculation of maximum adsorption capacities and can elucidate perrhenate location within materials *via* the correct characterisation technique, they do not offer conditions that are realistic to real situations. It is also worth questioning whether the ideal material requires superior capacities when the contaminant is found in low ppb concentrations. Our aim with this work is to investigate our materials at a perrhenate concentration far closer to what is found in the contaminated environment, providing more realistic observations. We know from existing research that UiO-66-NH_2 does not have the highest uptake capacities, but our key interests here are to observe the effects that; 1) immobilisation on scaffolds and 2) PSM reactions have on perrhenate uptake by this MOF.

2.3 Results and Discussion

2.3.1 Post-Synthetic Modification Reactions to Generate Urea Moieties in UiO-66-NH_2

To generate urea moieties within the pores of UiO-66-NH_2 we have followed a similar process to those described by Dong *et al.*[24] and Dugan *et al*.[23] by reacting the amine functional groups of the parent framework with a small isocyanate. In this case we are utilising ethyl isocyanate, with the aim of generating an ethyl urea group (scheme 2.2).

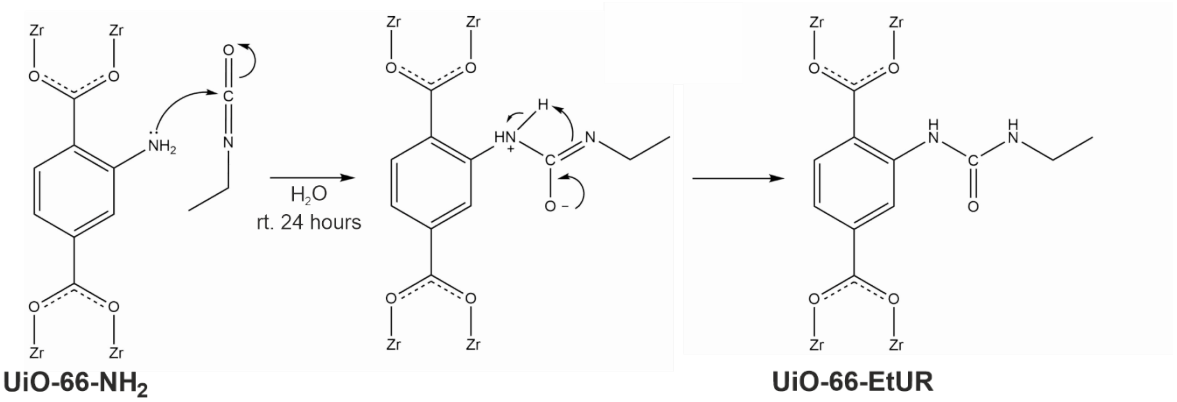

Scheme 2.2. The reaction of ethyl isocyanate with the amine tag of UiO-66-NH_2 to generate an ethyl urea moiety (UiO-66-EtUr).

2.3.1.1 Solvent Effect on Ethyl Isocyanate PSM Reaction

UiO-66-NH_2 was first synthesised following a procedure previously described by Katz *et al.*[60] The synthesised material was washed with ethanol followed by centrifugation thrice and then dried overnight. To find the optimal solvent for this PSM reaction, UiO-66-NH_2 was added to 5 mL of water, ethanol, tetrahydrofuran (THF), N,N'-dimethylformamide (DMF), toluene and acetonitrile independently. Each mixture was charged with excess ethyl isocyanate (10 mole equivalents of -NH_2 groups). The mixtures were sealed and stirred at room temperature for 24 hours before the MOF was isolated through centrifugation. The MOF solid was then washed *via* three methanol/centrifugation cycles, followed by overnight drying at room temperature. Washing with methanol was opted for over ethanol because the ethyl group of the latter alcohol overlap and complicates the ^{1}H nuclear magnetic resonance (NMR) spectra of the reaction product.

To ensure that this reaction does not alter the crystallinity of the framework, all products were subject to PXRD and compared to the parent MOF (figure A.1). We found that in all cases the crystallinity was not affected by either the solvent or ethyl isocyanate. ^{1}H NMR was used to calculate the conversion of the PSM reaction. One can do so by first digesting the MOF into its constituent

parts so that the organics of the framework are in solution and can undergo liquid characterisation. By comparing the integrals of the peaks of the parent linker to that of the PSM linker we can obtain a ratio that ultimately allows us to calculate a reaction conversion. Historically, MOF digestion has proceeded with the use of hydrofluoric acid. To avoid the use of hazardous HF, alternative fluoride-containing compounds have been explored, such as CsF by Hintz *et al*.[61] and, more recently NH_4F by Hamzah *et al*.[17] The latter involves dissolving NH_4F in D_2O, diluting in DMSO-d_6, followed by the addition of the MOF. It is also possible to exploit the low stability of UiO-66-NH_2 in base and employ deuterated hydroxide as the digesting agent. The MOF is digested in a small quantity of sodium deutoxide, diluted in D_2O, and precipitated $Zr(OH)_4$ is removed *via* centrifugation. This is the preferred digestion method in our group because it avoids the use of any hazardous fluoride sources. The initial reaction conversions in different solvents, using NaOD as the digestion agent, are presented in table 2.2. The ^{1}H NMR spectra that these values have been derived from can be found in the appendix (section A.2.2). It is evidently clear from these conversion values that water is the optimal solvent for this PSM reaction, reaching a value of 55%. All other solvents yield minimal conversions between 5 – 10%.

Table 2.2. PSM conversions of UiO-66-NH_2 with ethyl isocyanate in various solvents, derived from ^{1}H NMR. 5 mL of solvent, 30 mg of UiO-66-NH_2 and 10 mole equivalents of ethyl isocyanate were used for each reaction.

Solvent	Digestion Method	Conversion	Product Formula
Water	NH_4F (D_2O/DMSO-d_6)	**71%** (74%)[a]	$Zr_6O_4(OH)_4$(BDC-NH_2)$_{1.6}$(BDC-EtUr)$_{4.4}$
Water	NaOD (D_2O)	**55%**	$Zr_6O_4(OH)_4$(BDC-NH_2)$_{2.7}$(BDC-EtUr)$_{3.3}$
Acetonitrile	NH_4F (D_2O/DMSO-d_6)	**29%**	$Zr_6O_4(OH)_4$(BDC-NH_2)$_{4.3}$(BDC-EtUr)$_{1.7}$
Acetonitrile	NaOD (D_2O)	**10%**	$Zr_6O_4(OH)_4$(BDC-NH_2)$_{5.4}$(BDC-EtUr)$_{0.6}$
Toluene	NaOD (D_2O)	**10%**	$Zr_6O_4(OH)_4$(BDC-NH_2)$_{5.4}$(BDC-EtUr)$_{0.6}$
Ethanol	NaOD (D_2O)	**8%**	$Zr_6O_4(OH)_4$(BDC-NH_2)$_{5.5}$(BDC-EtUr)$_{0.5}$
THF	NaOD (D_2O)	**7%**	$Zr_6O_4(OH)_4$(BDC-NH_2)$_{5.6}$(BDC-EtUr)$_{0.4}$
DMF	NaOD (D_2O)	**6%**	$Zr_6O_4(OH)_4$(BDC-NH_2)$_{5.6}$(BDC-EtUr)$_{0.4}$

[a] On one occasion this reaction achieved a 74% conversion, however a consistent yield of 70% was obtained.

To ensure that we had selected the correct digestion method, the products from the water and acetonitrile experiments were also digested following the ammonium fluoride method described by Hamzah *et al.* and underwent ^{1}H NMR characterisation. We found that the derived reaction conversions for these digestions were higher than when the products were digested with NaOD. The water and acetonitrile conversions had increased to 70% and 29% respectively. On one occasion we yielded a conversion of 74% when carried out in water, however a more consistent yield of 70% was obtained. The use of deutoxide clearly has a negative effect on the ethyl urea group of the product, resulting in degradation back to BDC-NH_2. We opted not to repeat the remaining experiments using NH_4F because of the clear advantage over using water as the solvent

for this reaction. The labelled ^{1}H NMR spectrum of the water product, digested with NH_4F, is shown in figure 2.12.

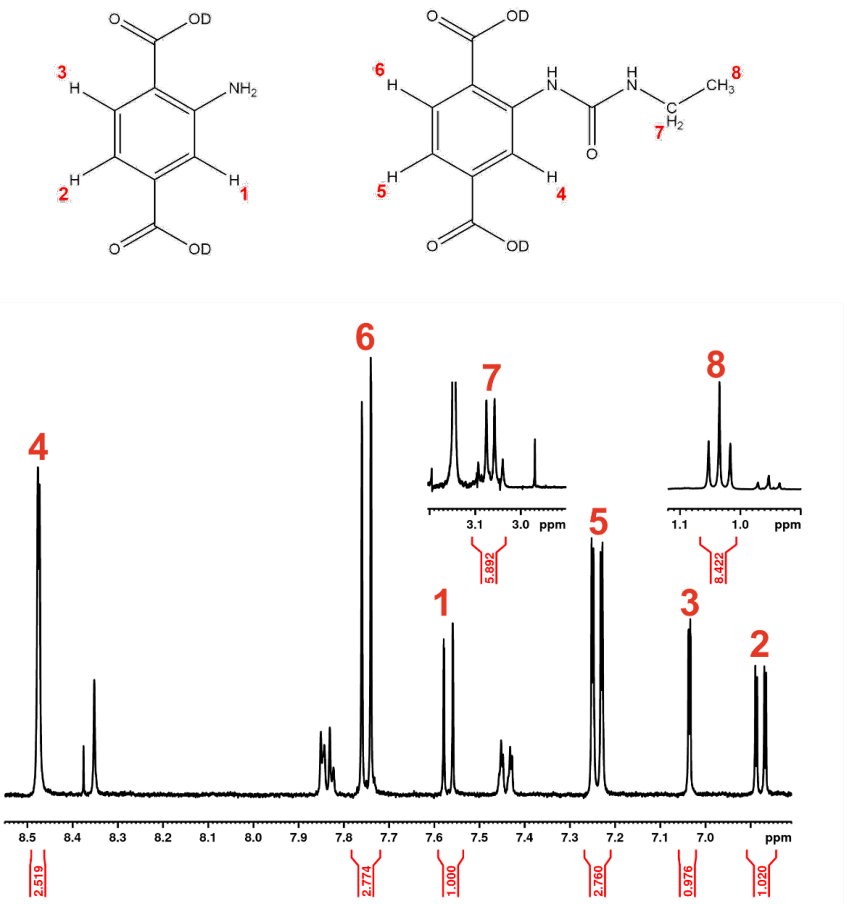

Figure 2.12. (Top) Labelled chemical structures of starting linker (BDC-NH_2) and PSM product linker (BDC-EtUr) that correspond to the spectrum. (Bottom) ^{1}H NMR spectrum of the digested PSM product from the reaction of ethyl isocyanate with UiO-66-NH_2 for one day at room temperature. 10 mole equivalents of ethyl isocyanate compared to -NH_2 groups was used. Reaction was conducted in water. Singlet at 3.16 ppm corresponds to residual methanol from washings. Product was digested in NH_4F (D_2O/DMSO-d_6).

The ^{1}H NMR spectrum of the PSM product from the reaction in water (figure 2.12) shows a mixture of products in the aromatic region. The doublet of doublets and two doublets at 6.88 (**2**), 7.04 (**3**) and 7.57 ppm (**1**) respectively correspond to the aromatic protons of the starting linker, BDC-NH_2. This was confirmed by digesting the parent MOF, UiO-66-NH_2, and the resulting solution undergoing ^{1}H NMR to locate the chemical shifts of BDC-NH_2 (figure A.5). The PSM reaction has resulted in a downfield shift of aromatic peaks for the organic linkers that have undergone reaction with ethyl isocyanate to form BDC-EtUr. The doublet peaks at 7.23 (**5**), 7.75 (**6**) and 8.47 ppm (**4**) correspond to the aromatic peaks of BDC-EtUr. Additionally, we can identify the aliphatic protons of the ethyl chain in this spectrum as the quartet (**7**) and triplet (**8**) at 3.07 and 1.03 ppm respectively. This peak

assignment for BDC-EtUr can be further rationalised by comparing the integrals of the five peaks. We expect to find the aromatic integrals to be similar and for the -CH_2 quartet and -CH_3 triplet to be in a ratio of 2:3:1 (CH_2:CH_3:CH) with the aromatic peaks, which is indeed what we find to be the case. By comparing the integrals of peaks 6 and 2 we have calculated a reaction conversion of 74%.

2.3.1.2 Temperature, Time, and Reagent Stoichiometry Optimisation of Ethyl Isocyanate PSM Reaction

Having found an optimal solvent for this reaction, our next step was to assess whether temperature, time, or reagent stoichiometry can affect the reaction conversion of UiO-66-NH_2 to UiO-66-EtUr.

To assess reaction time, identical experiments were carried out and left for 48 and 96 hours. UiO-66-NH_2 (30 mg) was added to a vial containing 5 mL of deionised water, and the mixtures were gently stirred and charged with ethyl isocyanate. The vials were capped and left for the defined length of time. Following this, the MOF product was isolated, washed, and dried following the procedure described in section 2.3.1.1. Conversions obtained through digestion and ^{1}H NMR spectroscopy are displayed in table 2.3. The 48- and 96-hour reactions have not yielded any better reaction conversions (68% and 70% respectively) than the 24-hour reaction. It appears that the reaction has plateaued at a conversion of around 70%.

Doubling the quantity of ethyl isocyanate added to the reaction, resulting in a 20 times excess of the reagent to -NH_2 moieties of UiO-66-NH_2, resulted in a very minor increase of reaction conversion to 74%. We also halved the quantity of ethyl isocyanate to five equivalents of the reagent and found that the conversion dropped to 55%. We therefore believe that 10 mole equivalents is the optimal quantity of ethyl isocyanate for this reaction. Increasing beyond a ten times excess has little benefit to the conversion of the reaction and thus would be a waste of reagents.

Table 2.3. PSM Conversions of UiO-66-NH_2 with ethyl isocyanate in water, derived from ^{1}H NMR. Digestions were carried out with NH_4F. The sum of organic linker subscripts equal six, correlating to the number of moles of linker in one mole of UiO-66-NH_2. UiO-66-NH_2 = $[Zr_6O_4(OH)_4(BDC\text{-}NH_2)_6]$.

Time (hours)	Temperature (°C)	Mole equiv. of isocyanate	Conversion	Product Formula
24	Room temperature	**10**	**70%** (74%)[a]	$[Zr_6O_4(OH)_4(BDC\text{-}NH_2)_{1.8}(BDC\text{-}EtUr)_{4.2}]$
24	Room temperature	**20**	**74%**	$[Zr_6O_4(OH)_4(BDC\text{-}NH_2)_{1.6}(BDC\text{-}EtUr)_{4.4}]$
24	100	**10**	-[b]	-
48	Room temperature	**10**	**68%**	$[Zr_6O_4(OH)_4(BDC\text{-}NH_2)_{1.9}(BDC\text{-}EtUr)_{4.1}]$
96	Room temperature	**10**	**70%**	$[Zr_6O_4(OH)_4(BDC\text{-}NH_2)_{1.8}(BDC\text{-}EtUr)_{4.2}]$
96	Room temperature	**5**	**55%**	$[Zr_6O_4(OH)_4(BDC\text{-}NH_2)_{2.6}(BDC\text{-}EtUr)_{3.4}]$

PXRD of UiO-66-$(NH_2)_{1.8}(EtUr)_{4.2}$ compared to a simulated pattern of the parent framework (figure 2.13) confirms that the PSM reaction does not alter the framework and that high crystallinity is retained.

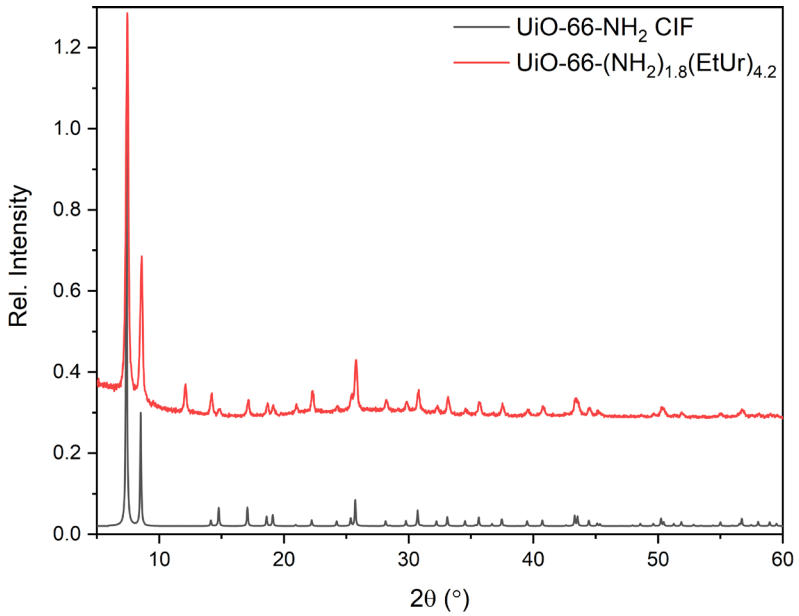

Figure 2.13. PXRD pattern of UiO-66-$(NH_2)_{1.8}(EtUr)_{4.2}$ (70% PSM conversion) compared to simulated UiO-66-NH_2.

Thermogravimetric analysis of the post-synthetically modified framework confirms that its thermal stability has not been altered by the additional urea functionality (figure 2.14). We note that the non-functionalised MOF sample contains a higher solvent content than the post-synthetically modified MOF, this results in a lower-than-expected residual mass for UiO-66-NH_2. We attribute this difference in solvent loading a result of the ethyl urea moieties on UiO-66-$(NH_2)_{1.8}(EtUr)_{4.2}$ which reduces the material's surface area.

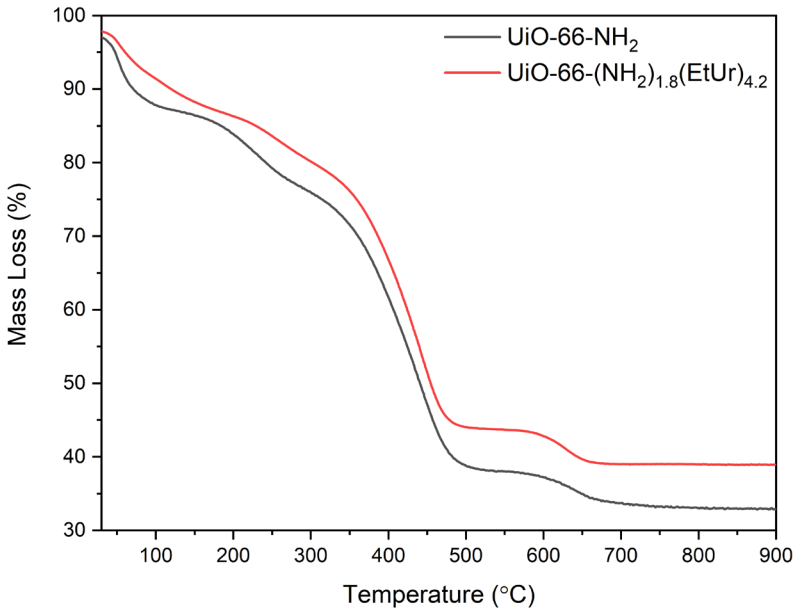

Figure 2.14. TG analysis of UiO-66-$(NH_2)_{1.8}(EtUr)_{4.2}$ and its parent framework. Conducted under an air environment.

FTIR spectroscopy was utilised to confirm the conversion of the amine tags of UiO-66-NH_2 to urea groups (figure 2.15). Peaks at 3475 and 3362 cm^{-1} in the parent framework spectrum are characteristic of the asymmetric and symmetric vibrational bands respectively of the primary amine group respectively.[62] These peaks are clearly masked in the PSM framework by a very broad absorbance centred at 3322 cm^{-1} which corresponds to the N-H stretch of the incorporated urea group.[63] Additionally, we observe a large decrease in the intensity of the 1657 cm^{-1} peak between the parent and PSM frameworks, which corresponds to the N-H bend of the amine. The integrity of the framework is confirmed by the presence of Zr-O, aromatic C-C, C-O symmetric and C-O asymmetric stretches at 767,[64] 1426, 1385 and 1562 cm^{-1} respectively, in the spectra of both frameworks.

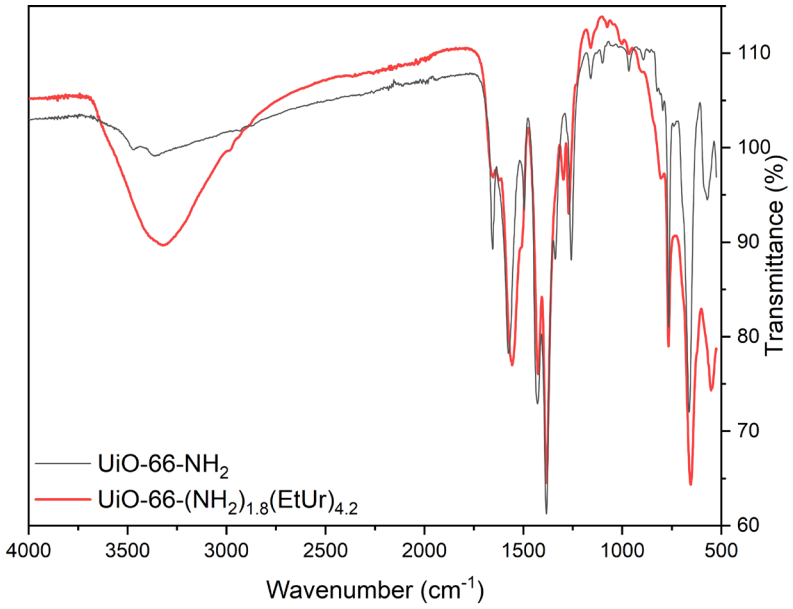

Figure 2.15. FTIR of UiO-66-$(NH_2)_{1.8}(EtUr)_{4.2}$ and its parent framework.

To assess the effect on porosity that the PSM reaction has had on UiO-66-NH_2 the PSM product and parent frameworks were probed with N_2 gas adsorption (figure 2.16). Both materials were degassed under vacuum at 120 °C overnight prior to characterisation.

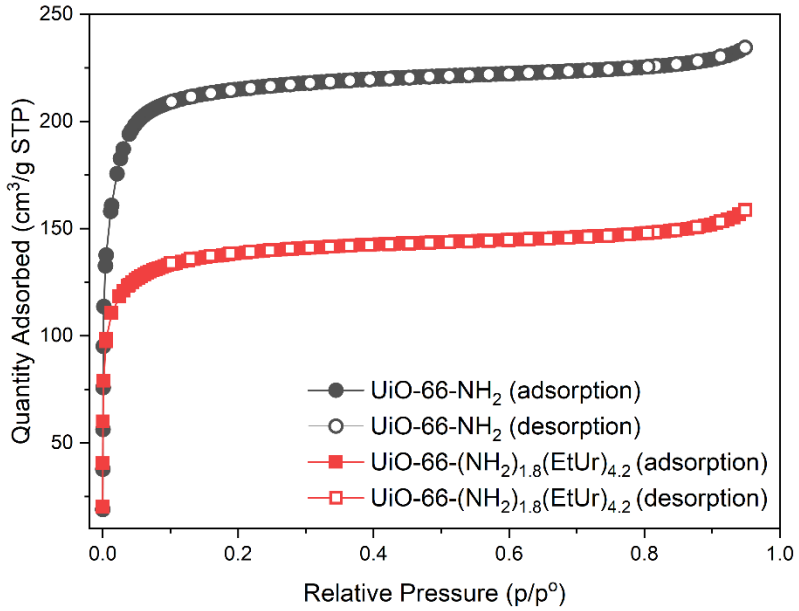

Figure 2.16. N_2 isotherms of UiO-66-$(NH_2)_{1.8}(EtUr)_{4.2}$ and its parent framework.

The resulting N_2 adsorption isotherms demonstrates that both materials display porosity. We would expect a decrease in the surface area due to the incorporated ethyl urea moiety and this indeed is the case. This is proven by the lower quantity of N_2 adsorbed at monolayer coverage. BET surface areas can be derived from these isotherms and are found to be 831 ± 8.4 and 529 ± 5.4 $m^2\ g^{-1}$ for UiO-66-NH_2 and UiO-66-$(NH_2)_{1.8}(EtUr)_{4.2}$ respectively (see section A.2.3).

Due to the microporous natural of UiO-66-NH_2 and its topologically identical frameworks careful application of BET must be applied. We find that deviation of BET theory occurs at the higher end of the BET range for these materials, a typical characteristic of microporous materials, thus one must only regard these BET values as *apparent* surface areas.[65] The lower BET surface area for the PSM product when compared to the parent framework confirms that the reaction of ethyl isocyanate with the framework is occurring within the framework pores, and not just on the surface of the MOF crystals.

SEM imaging of the parent and daughter frameworks confirm that crystal morphology and size are not affected by the PSM reaction (figure 2.17).

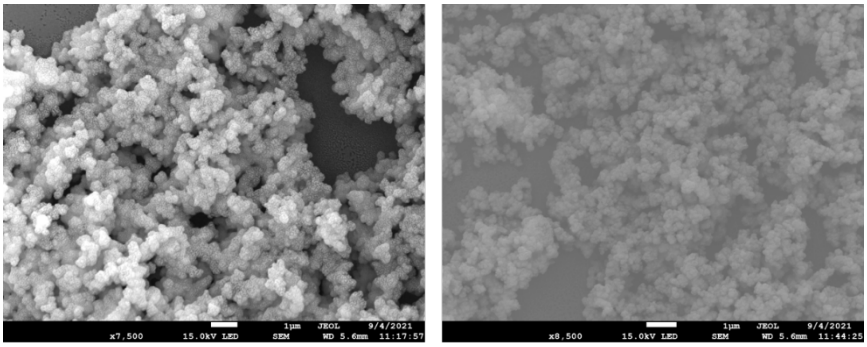

Figure 2.17. SEM images of (left) UiO-66-NH_2 and (right) UiO-66-$(NH_2)_{1.8}(EtUr)_{4.2}$. Scale bars = 1 µm.

2.3.1.3 Acidification of UiO-66-$(NH_2)_{1.8}(EtUr)_{4.2}$

Evidence from Banerjee *et al.* shows that protonation of the amine groups of UiO-66-NH_2 with HCl to yield a cationic framework ($[UiO\text{-}66\text{-}NH_3][Cl]_6$)[i] with counterbalancing chloride anions within the pores has far greater perrhenate remediation capabilities than the neutral parent framework.[12] The post-synthetically modified UiO-66-$(NH_2)_{1.8}(EtUr)_{4.2}$ therefore underwent an additional PSM reaction to protonate the urea and amine groups that dangle within the framework pores. To do so, the MOF was soaked in 2M HCl for 2 hours. Acidification of the urea group occurs at the carbonyl oxygen (scheme 2.3).

[i] Here we restate that one mole of UiO-66-NH_2 ($[ZrO_4(OH)_4(BDC\text{-}NH_2)_6]$) contains six moles of -NH_2 groups, therefore the correct number of moles of chloride to counterbalance UiO-66-$(NH_3)^{6+}$ is six. For all protonated PSM products, we have assumed that both the -NH_2 and ethyl-urea groups have been protonated, which again requires six moles of chloride per mole of MOF.

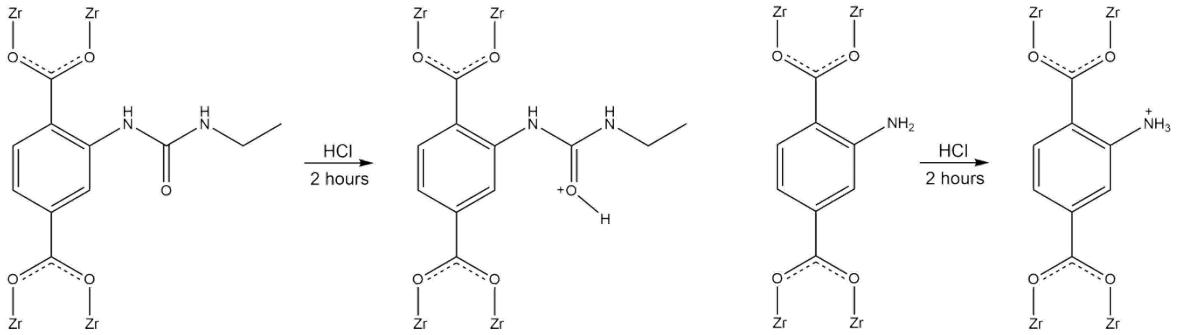

Scheme 2.3. The acidification of (left) UiO-66-(ErUr) to [UiO-66-(ErUr-H)][Cl]$_6$ and (right) UiO-66-NH$_2$ to [UiO-66-NH$_3$][Cl]$_6$ with HCl.

FTIR spectroscopy (figure 2.18) of the acidified product shows a broader and more intense absorbance of the N-H stretch centred at 3322 cm^{-1}. This has arisen from the protonation of the carbonyl oxygen of the urea group. O-H stretches typically absorb within the same range as the N-H stretch and thus results in a higher absorbance.

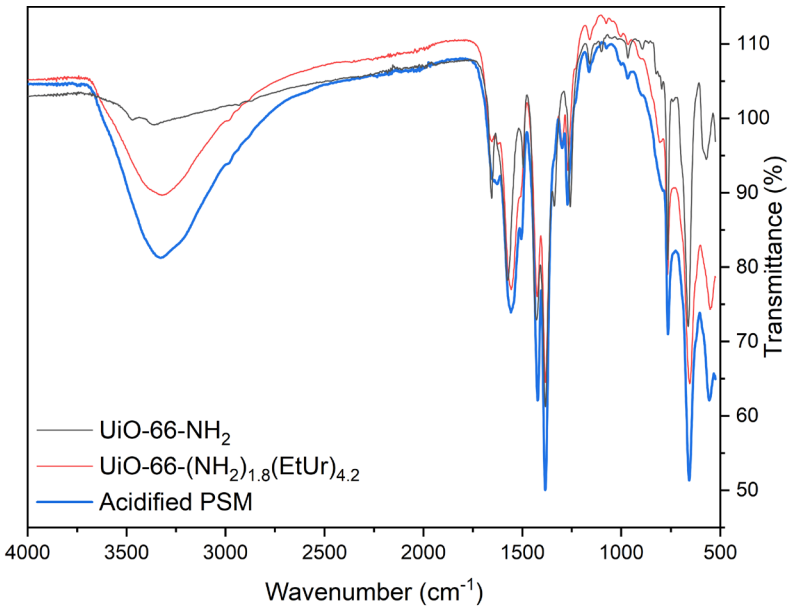

Figure 2.18. FTIR spectra of parent framework and UiO-66-(NH$_2$)$_{1.8}$(EtUr)$_{4.2}$ before and after its acidification.

Once again, PXRD can be employed to ensure crystallinity of the MOF has not been affected by the PSM reaction. Figure 2.19 confirms that acidification of UiO-66-(NH$_2$)$_{1.8}$(EtUr)$_{4.2}$ has not affected its crystallinity.

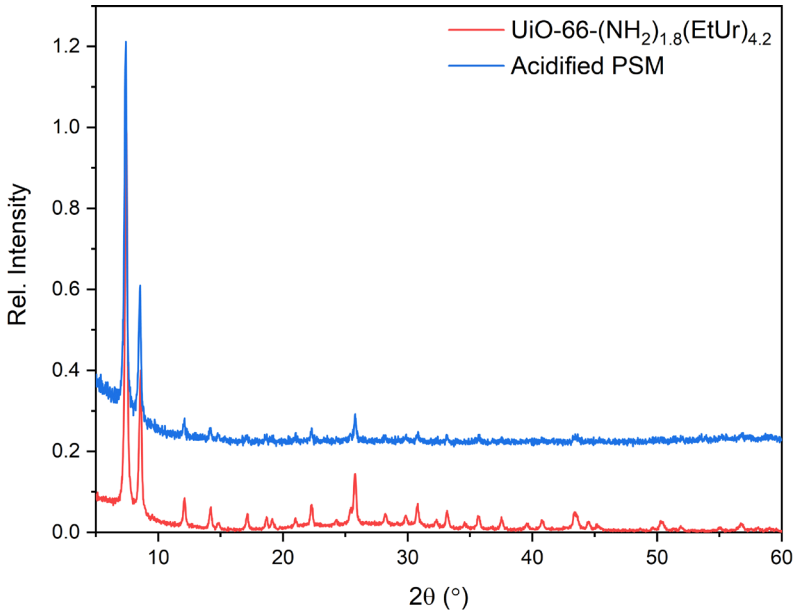

Figure 2.19. PXRD comparison of UiO-66-$(NH_2)_{1.8}(EtUr)_{4.2}$ before and after acidification.

Acidification of UiO-66-$(NH_2)_{1.8}(EtUr)_{4.2}$ has resulted in degradation of the ethyl urea group to some degree. ^{1}H NMR spectroscopy (figure 2.20) shows a reduction in the integral ratio of BDC:BDC-EtUr. Comparison of the integrals of the peaks at 7.57 and 7.75 ppm, which correspond to BDC-NH_2 and BDC-EtUr respectively, reveal a conversion of 53%. This is a decrease of 21%. The formula of the acidified MOF is therefore [UiO-66-$(NH_3)_{2.8}$(EtUr-H)$_{3.2}$][Cl]$_6$.

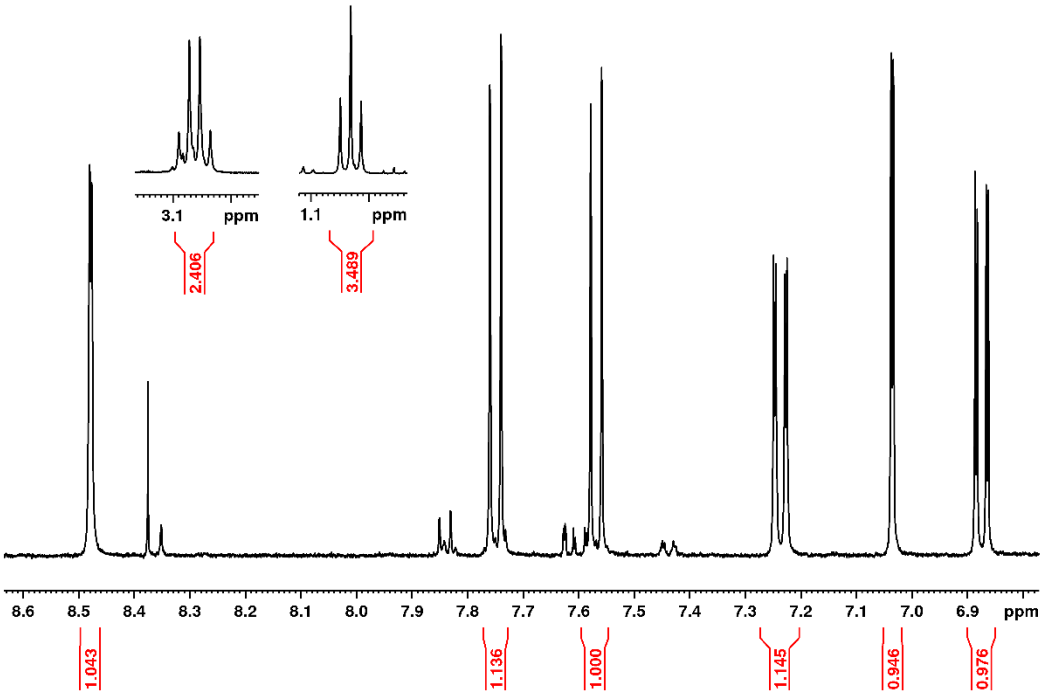

Figure 2.20. ^{1}H NMR spectrum of digested [UiO-66-$(NH_3)_{2.8}$(EtUr-H)$_{3.2}$][Cl]$_6$.

SEM imaging shows that crystal morphology and size is not altered by the acidification PSM reaction (figure 2.21).

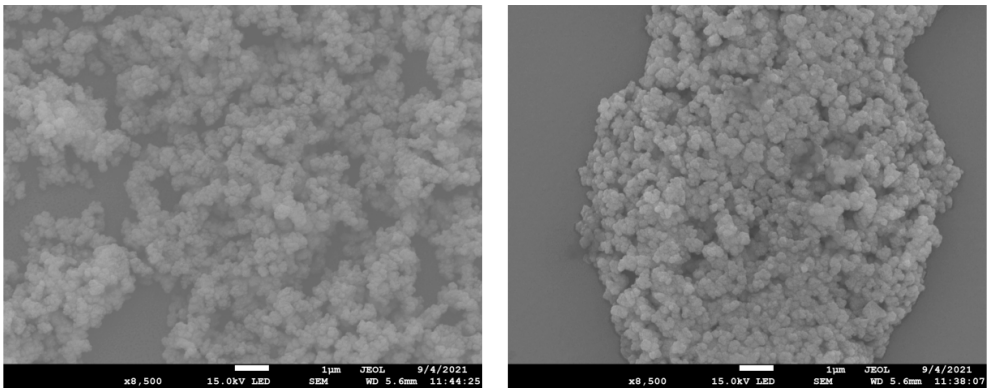

Figure 2.21. SEM images of (left) UiO-66-$(NH_2)_{1.8}(EtUr)_{4.2}$ (reproduced from figure 2.17) and (right) [UiO-66-$(NH_3)_{2.8}(EtUr\text{-}H)_{3.2}$][Cl]$_6$. Scale bars = 1 µm.

2.3.1.4 Perrhenate Remediation of Post-Synthetically Modified UiO-66-NH_2

The remediation of perrhenate from aqueous solutions by UiO-66-NH_2, UiO-66-$(NH_2)_{2.1}(EtUr)_{3.9}$ and their protonated daughter MOFs was assessed. Approximately 50 mg of MOF was suspended in 9.95 mL of ultrapure deionised water and gently stirred. To this suspension, 0.05 mL of a 1000 ppm stock solution of sodium perrhenate was added, creating a 5 ppm perrhenate solution. The suspension was then left for a desired length of time before being filtered with a 25 µm syringe filter. The experiments were left for time periods varying from one minute to 24 hours (1440 min). The filtrate was then diluted 500-fold prior to ICP-MS analysis to determine the perrhenate concentration. Figure 2.22 shows the level of perrhenate removed over 24 hours by UiO-66-NH_2 (**NH_2**), [UiO-66-NH_3][Cl]$_6$ (**NH_3^+**) , UiO-66-$(NH_2)_{2.1}(EtUr)_{3.9}$ (**PSM**) and [UiO-66-$(NH_3)_{2.8}(EtUr\text{-}H)_{3.2}$][Cl]$_6$ (**PSM$^+$**). For all materials we observe very fast uptake kinetics of perrhenate to varying levels of remediation.

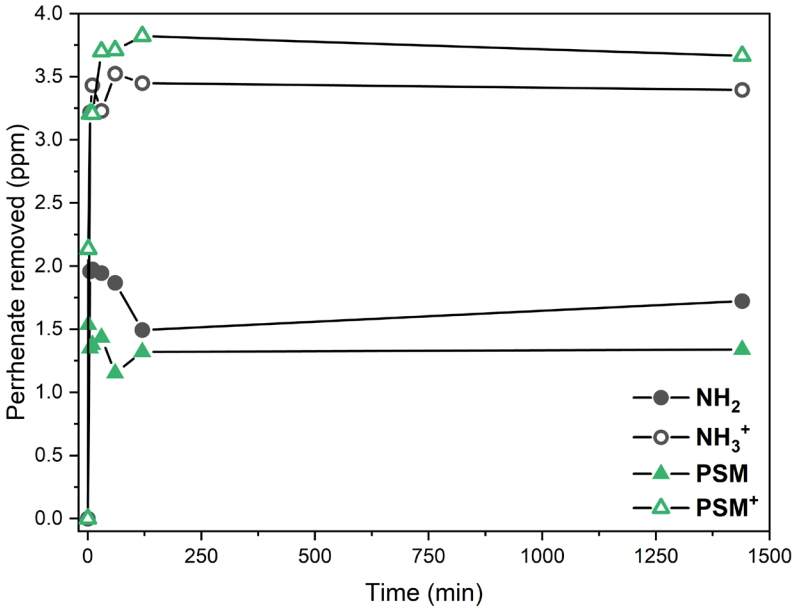

Figure 2.22. Perrhenate uptake by UiO-66-NH_2 (NH_2), UiO-66-$(NH_2)_{2.1}(EtUr)_{3.9}$ (PSM), and their protonated daughter frameworks (NH_3^+ and PSM^+ respectively), over 24 hours. Uptake experiments were carried out in aqueous sodium perrhenate solutions with a starting concentration of 5 ppm.

The non-protonated frameworks have poorer remediation of perrhenate from solution than their protonated daughter MOFs. After 24 hours 1.72 and 1.34 ppm of perrhenate have been removed by **NH_2** and **PSM** respectively. This minor reduction in uptake is likely to be because of the reduction in pore volume from the PSM reaction. The perrhenate uptake of these neutral frameworks is ultimately caused by the natural diffusion of perrhenate from an area of high concentration (solution) to an area of relatively low concentration (adsorbent) and therefore a reduction in porosity of the adsorbent will also cause a reduction in anion capacity. The protonation of these materials to form cationic, anion exchange materials causes a substantial increase in perrhenate removal from solution achieving 3.40 and 3.67 ppm of perrhenate removed by **NH_3^+** and **PSM^+** respectively.

The mass of perrhenate removed by each MOF at the measured time intervals was calculated from the perrhenate concentrations in figure 2.22. To account for the different MOF masses present in each uptake experiment the perrhenate masses were normalised based upon the associated MOF mass.

Figure 2.23 shows the removal of perrhenate by the MOF adsorbents over a period of 24 hours, measured in mg/g. We now observe a clear difference in the protonated framework's abilities to remediate perrhenate.

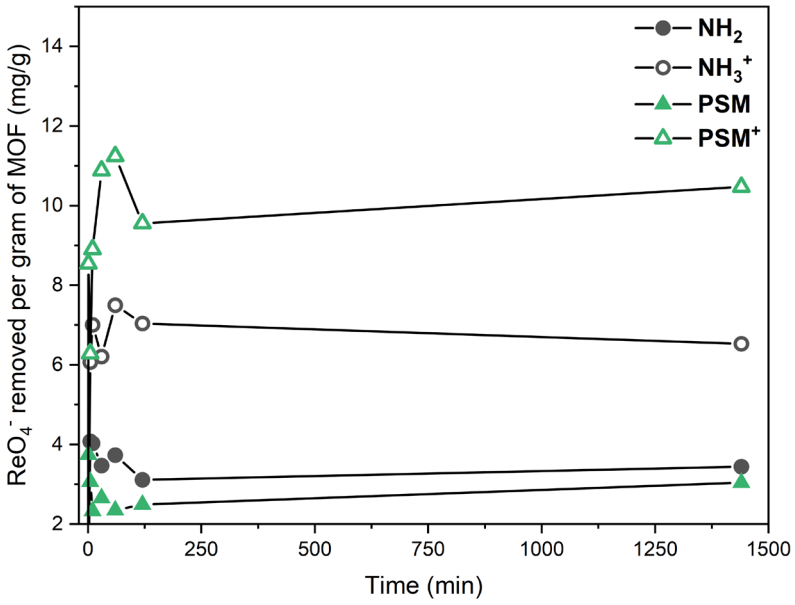

Figure 2.23 Uptake of ReO_4^- from solution over time by UiO-66-NH_2 (NH_2), UiO-66-$(NH_2)_{2.1}(EtUr)_{3.9}$ (PSM), and their protonated daughter frameworks (NH_3^+ and PSM^+ respectively), over 24 hours. Uptake experiments were carried out in aqueous sodium perrhenate solutions with a starting concentration of 5 ppm.

Perrhenate remediation by both protonated materials peaks at 60 minutes, whereby 7.5 and 11.2 mg/g of the anion has been removed by **NH_3^+** and **PSM^+** respectively (figure 2.24) from 5 ppm solutions. In comparison to their parent frameworks these uptakes are 2.0 and 4.7 times greater respectively, demonstrating the importance of the further PSM reaction with HCl to improve perrhenate uptake. The urea-containing cationic framework remediates 1.5 times more perrhenate from a 5 ppm solution than pristine **NH_3^+** after 60 minutes. We observe apparent leaching of perrhenate from the protonated MOFs, back into solution after 60 minutes. In the case of **NH_3^+** this is a slow release of perrhenate that continues up to 1400 minutes and quantifies as 0.97 mg of the anion leaching per gram of MOF. For **PSM^+**, leaching of 1.69 mg of perrhenate per gram of MOF occurs between 60 and 120 minutes however, there appears to be some degree of recovery of this released anion (0.92 mg/g) between 120 and 1440 minutes. We believe this recovery is down to the system finding equilibrium for the distribution of perrhenate.

From these observations we propose that the uptake of perrhenate by **PSM^+** predominately occurs *via* an anion-exchange mechanism, much like what has been reported for **NH_3^+**. We believe that perrhenate anions exchange with the chloride anions that occupy the pores of the MOF. These chloride anions counterbalance the protonated urea and amine tags of the **PSM^+** framework. To account for the higher uptake observed for **PSM^+** over **NH_3^+** we believe that the urea-modification creates a hydrogen-bond rich environment within the pores of the framework which promotes inclusion of oxo-anions such as perrhenate, over point charge anions like chloride. This hydrogen

bond environment is further strengthened by the protonation of the carboxyl oxygen of the urea groups which withdraws electron density from the N-H groups of the urea and thus making the hydrogen bonding protons more Δ positive with a higher affinity to perrhenate. The lower uptake for the non-protonated urea-based MOF over the non-protonated parent MOF (**NH_2**) can be accounted for by the reduced pore volume, due to the grafted urea groups, and therefore reduced ability in adsorbing perrhenate *via* diffusion. Protonation of these MOFs is therefore essential in reaching any appreciable uptake levels.

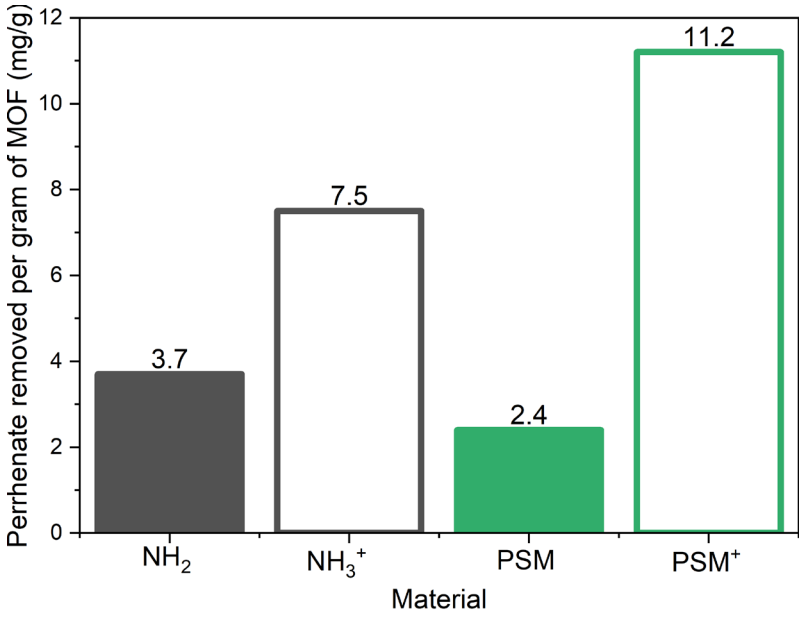

Figure 2.24. Removal of perrhenate after 60 minutes by UiO-66-NH_2 (NH_2), UiO-66-$(NH_2)_{2.1}(EtUr)_{3.9}$ (PSM), and their protonated daughter frameworks (NH_3^+ and PSM^+).

Partition coefficients (K_d) are very useful to compare the uptake capabilities of different materials that have been tested under differing conditions. K_d values that exceed $1x10^5$ mL g^{-1} are generally regarded as reflecting materials with excellent remediation properties.[66] Calculated K_d values for the four MOFs we have tested are shown in figure 2.25. The non-protonated MOFs both have partition coefficients of ≈1000 mL g^{-1} across all samples, confirming these materials have relatively poor perrhenate remediation. The K_d of **NH_3^+** at 60 minutes was 5087 ± 508 mL g^{-1}. This value is far higher than what has previously been reported in literature (837 mL g^{-1})[59] although previous work within our group has afforded K_d values for this MOF as high as 3263 ± 194 mL g^{-1}. After 60 minutes **PSM^+** achieved a partition coefficient of 8724 ± 873 mL g^{-1} which is significantly higher than the literature reported and our experimentally derived K_d values for **NH_3^+**.

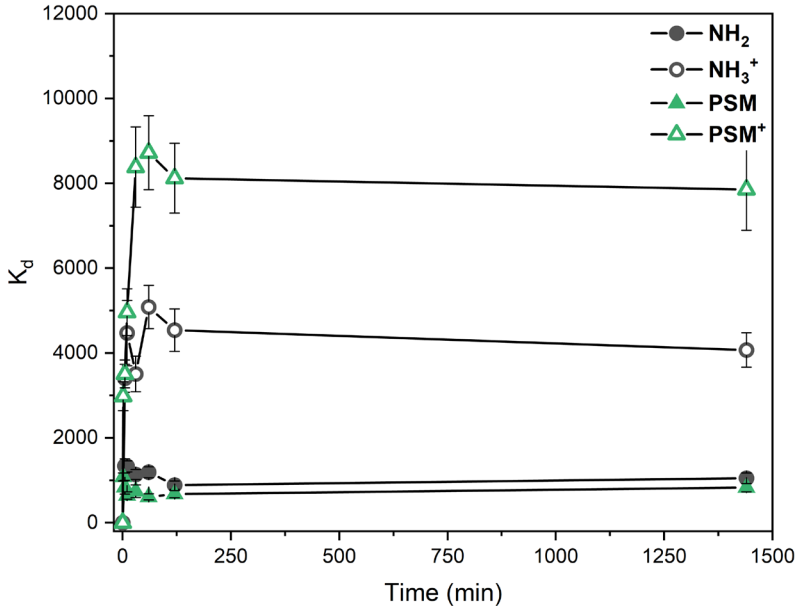

Figure 2.25. Partition coefficient values for UiO-66-NH_2 (NH_2), UiO-66-$(NH_2)_{2.1}(EtUr)_{3.9}$ (PSM), and their protonated daughter frameworks (NH_3^+ and PSM^+ respectively), over 24 hours. Uptake experiments were carried out in aqueous sodium perrhenate solutions with a starting concentration of 5 ppm. Combined method uncertainty given as standard error ($2\sigma K_d$).

2.3.2 UiO-66-NH_2@Functionalised Filter Paper Composites via Dip Coating

Deposition of UiO-66-NH_2 onto cellulose scaffolds first requires functionalisation of the cellulose to provide anchoring sites for the MOF crystals to nucleate from. The most sensible approach to chemical modification is to follow the well reported carboxymethylation route using chloroacetic acid. It does however need to be appreciated that chloroacetic acid is far from environmentally friendly. Alternative safer routes may exist, however the translation and optimisation of these to cellulose filter papers would be far beyond the scope of our work and therefore we have chosen to follow this tried and tested method. Mercerisation was initially attempted however shrinkage of the material is unavoidable if it cannot be suitably restrained during treatment. Mercerisation involves suspending the scaffold material in a highly caustic solution, which disrupts the hydrogen bonding between cellulose fibres as a result of the deprotonation of hydroxyl groups on the polymer chains. This provides additional nucleation sites for MOF crystallisation but also results in size reduction of the scaffold material. We found that 3 cm diameter circular cellulose filter papers would shrink by 37% during mercerisation in 16M NaOH(aq) (figure A.16). The filter paper size was chosen to specifically fit a filtration rig we had designed and thus this shrinkage was not acceptable.

Cellulose filter papers (FP) were therefore functionalised by immersing them into a 1M chloroacetic acid 15 wt% NaOH aqueous solution (scheme 2.4). The papers were left undisturbed for three days at room temperature. The functionalised filter papers (FFP) were removed and washed with

copious amounts of deionised water and dried overnight. This procedure was first described by Laurila *et al*.[51]

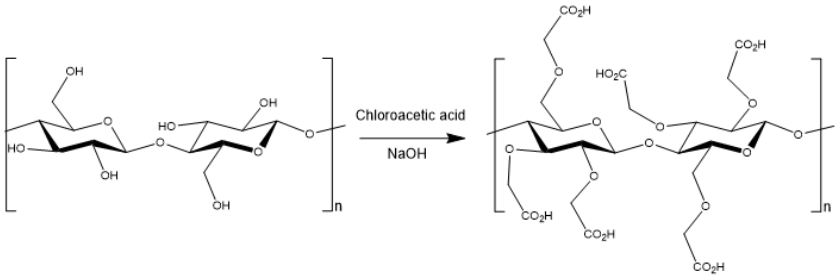

Scheme 2.4. Reaction of cellulose with chloroacetic acid to yield carboxylic acid functionalities along the biopolymer chains.

The successful carboxymethylation of the hydroxyl groups of cellulose was confirmed by FTIR spectroscopy, shown in figure 2.26. The additional absorbance at 1590 cm^{-1} corresponds to the C=O stretch of the carboxylic acid group. Retention of the cellulose structure is confirmed through the near identical spectra of FP and FFP. SEM imaging (figure 2.26) confirms that the fibres are not physically altered by functionalisation.

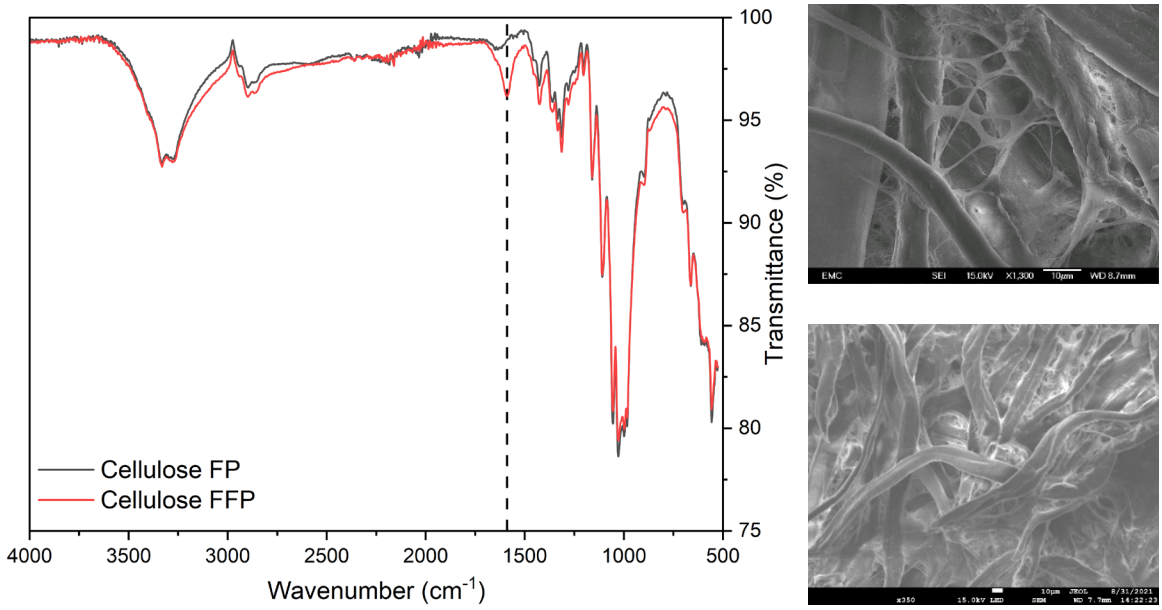

Figure 2.26. (Left) FTIR spectra of non-functionalised filter paper (FP) and functionalised filter paper (FFP). Absorbance at 1590 cm^{-1} is marked by the dashed line. (Right) SEM images of cellulose filter papers before (top) and after (bottom) functionalisation. Scale bars = 10 µm.

UiO-66-NH_2 was grown on FFP *via* a dip coating procedure whereby the scaffold material was alternately immersed in metal and linker solutions. This is shown schematically in scheme 2.5. The FFP was first immersed in a $ZrOCl_2 \cdot 8H_2O$ water/acetic acid (50:50) solution and left for one minute. The FFP was then removed and dabbed dry on a paper towel for 10 seconds to remove excess solution. It was then immersed in an aqueous BDC-NH_2/NaOH solution for one minute, followed by

dabbing dry once again and returning to the metal solution. This completes one MOF deposition cycle.

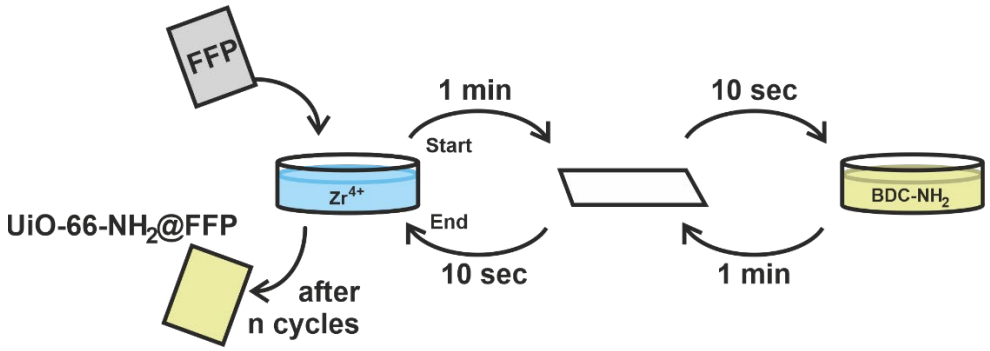

Scheme 2.5. Dip coating process to synthesise UiO-66-NH_2@FFP. FFP is immersed in alternating Zirconium and BDC-NH_2 solutions to yield the composite.

We initially investigated this process by cycling FFP pieces that were roughly 2 x 1 cm in size, ten times in freshly prepared solutions. The composites were washed with copious amounts of ethanol before drying overnight. The ethanol wash allowed for the removal of a thick layer of UiO-66-NH_2 and unreacted BDC-NH_2 that was not adhered to the FFP. We confirmed the crystalline composition of this layer through PXRD (figure A.2). PXRD of a washed and dried composite is presented in figure 2.27.

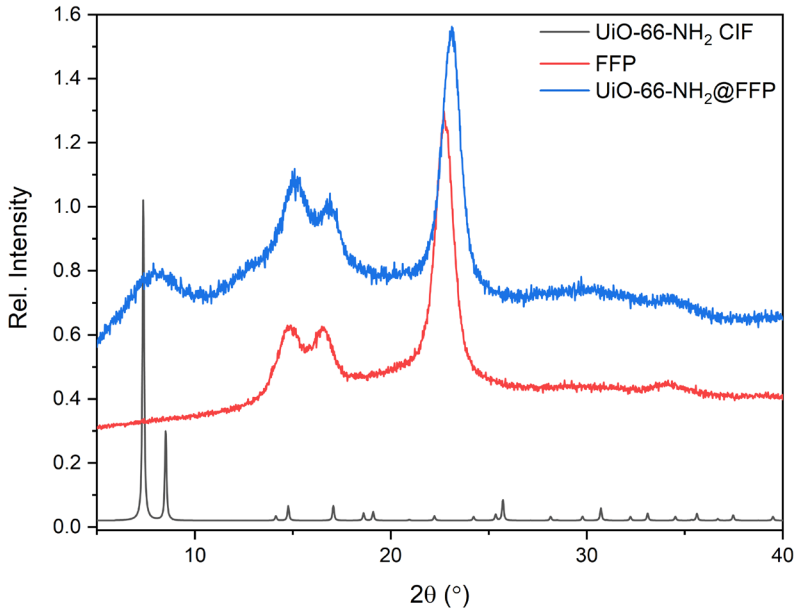

Figure 2.27. PXRD comparison of UiO-66-NH_2@FFP to FFP and UiO-66-NH_2. This composite was prepared by 10 dip coat cycles in freshly prepared solutions.

It is evident from figure 2.27 that very little MOF growth has occurred on the FFP surface due to the very broad and amorphous peak between 7-9°. A key step in the green synthesis of bulk UiO-66-NH_2 by Pakamorė *et al.* is to pre-treat the modulator-containing zirconium solution.[67] They did so by heating the solution to 50 °C for two hours in order to allow for the formation of

$[Zr_6O_4(OH)_4(CH_3CO_2)_{12}]$ clusters prior to linker addition. They found that skipping this step results in an amorphous solid. Therefore, we incorporated a slightly modified pre-treatment step into our dip coating process by simply leaving the metal solution at room temperature for five days under static conditions. The dip coating reaction was then repeated for 5, 10, 15 and 20 cycles on FFP. We can conclude from PXRD (figure 2.28) that UiO-66-NH_2 growth on the surface of FFP has been very successful by the introduction of diffraction peaks to the composite pattern at 7.4, 8.5 and 25.6 ° from as little as five cycles. These peaks account for the 111, 200 and 442 reflections of UiO-66-NH_2 respectively. The crystallinity of the MOF also appears to be high in all cases.

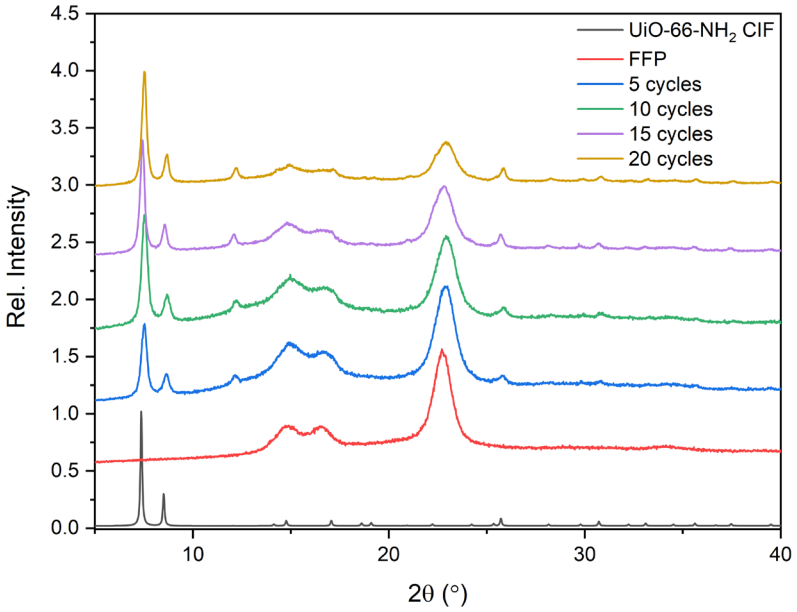

Figure 2.28. PXRD comparison of UiO-66-NH_2@FFP to FFP and UiO-66-NH_2. Composites were prepared by dip coating in 5, 10,15 and 20 cycles. A five-day aged $ZrOCl_2$ solution and fresh BDC-NH_2 solution were used.

A portion of each sample underwent TG analysis. The samples were heated to 900 °C under an air atmosphere (figure 2.29). The mass loss profiles of the composites follow the profile of pristine FFP. Degradation of the cellulose scaffold and the organic component of the MOF starts at around 250 °C. The residual mass of the composites consists of metal oxide, which in this case is ZrO_2. This was confirmed *via* PXRD characterisation (figure A.3).

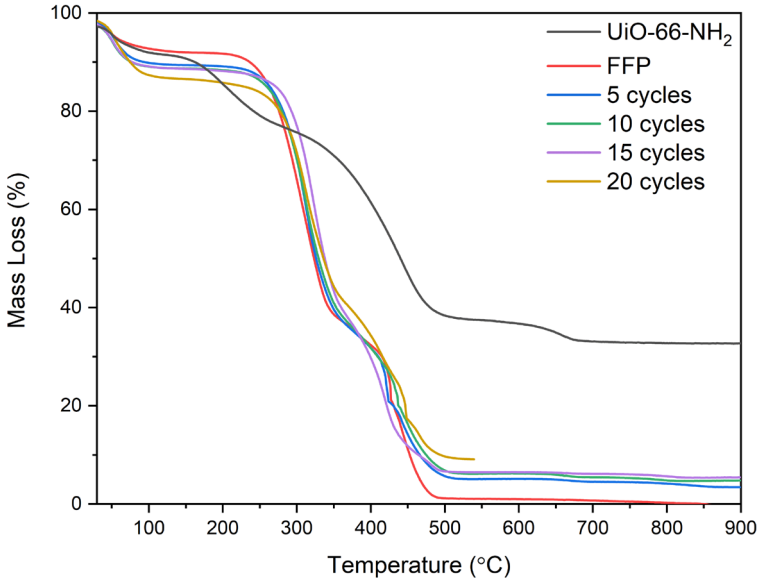

Figure 2.29. TG analysis of UiO-66-NH_2@FFP composites, compared to FFP and UiO-66-NH_2. Conducted under an air atmosphere. Instrumental error occurred during data collection of the 20 cycle and thus the full mass loss profile is not available.

The mass of ZrO_2 from the decomposition of the samples can be measured and used to derive their respective MOF loadings. Figure 2.30 demonstrates how the quantity of UiO-66-NH_2 grafted to the FFP increases with the number of dip coat cycles. After five cycles the loading had reached 9.4wt%, which is the equivalent to a coverage of 1.0 mg/cm^2. We find that the coverage increases almost linearly, at between 4-5 mg/cm^2 every five cycles. After 20 dip coat cycles the coverage is 2.3 mg/cm^2 with a loading of 12.9wt%.

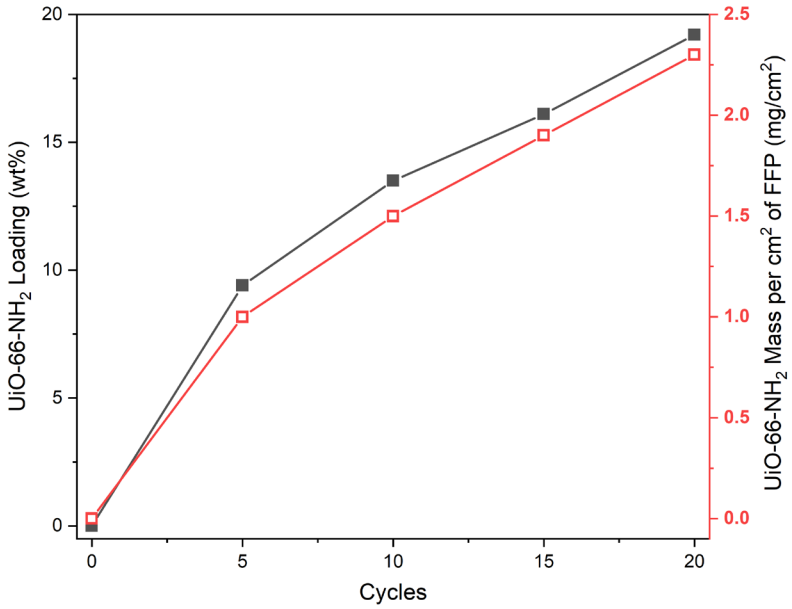

Figure 2.30. MOF loading of UiO-66-NH_2@FFP (black filled squares). MOF mass per cm^2 of composite (red squares).

The MOF loading of UiO-66-NH_2@FFP after 20 cycles appears to be quite a modest level of grafting. However, upon comparison of our results to those found in the literature, 12.9wt% is very impressive when considering our experimental conditions. Hashem *et al.* achieved a MOF loading of 5.8wt% using a DMF/HCl solvent mixture and heating for 180 minutes at 80 °C, while Kim *et al.* reached as high as 51wt%.[55,57] The latter method however involves repeating a 24-hour synthesis five times and thus requires an excessive quantity of solvent and reagents. A comparison of these reported procedures to our methods are provided in table 2.4.

Table 2.4. Comparison of procedures to synthesis UiO-66-NH_2@FFP.

Reagent quantities (mmol)	**Solvents**	**Solvent volume (mL)**	**Reaction time**	**Temperature (°C)**	**MOF loading (wt%)**	**Ref.**
$ZrOCl_2 \cdot 8H_2O$ = 90 $H_2BDC\text{-}NH_2$ = 130	DMF	2125	5 days	80	51	[57]
$ZrOCl_2 \cdot 8H_2O$ = 7 $H_2BDC\text{-}NH_2$ = 4	H_2O / Acetic acid	60	30 min	Room temperature	12.9	**Our work**
$ZrCl_4$ = 0.54 $H_2BDC\text{-}NH_2$ = 0.75	DMF / HCl	10	180 min	80	5.8	[55]

SEM imaging of the UiO-66-NH_2@FFP composites shows the increase in quantity of deposited MOF over the increasing number of dip coat samples (figure 2.31). We find that the MOF crystal morphology is irregular in size and shape. It is evidential, particularly from the cycle 10 and 20 SEM images, that we do not observe MOF growth on cellulose fibres that are not tightly bound to the FFP bulk. We postulate that these fibres are physically agitated by the dip coating process and thus any MOF crystals deposited on such fibres are not adhered strongly enough to remain bound during the repeated dip coating and washing steps.

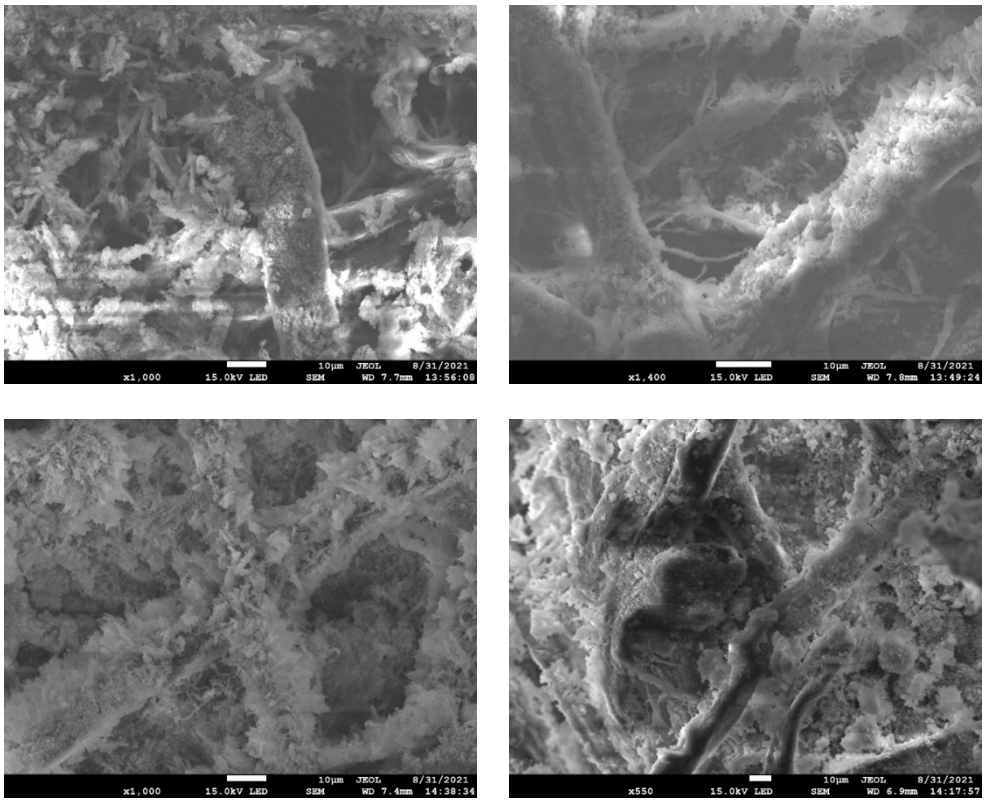

Figure 2.31. SEM images of UiO-66-NH_2@FFP after (top row, left to right) 5 cycles; 10 cycles; (bottom row, left to right) 15 cycles; 20 cycles. Scale bars = 10 µm.

Having successfully deposited UiO-66-NH_2 onto the surface of a FFP scaffold we next acidified the MOF with 2 M HCl to yield [UiO-66-NH_3][Cl]$_6$@FFP. The MOF composite was submerged in the acid for two hours, with no agitation. Following this the composite was washed thoroughly with deionised water to remove excess acid. PXRD characterisation confirms that [UiO-66-NH_3][Cl] is retained on the FFP surface (figure 2.32). An increase in intensity of the broad FFP peaks in the acidified composites suggests that the PSM results in a reduction in MOF loading of the composite. This was confirmed through TGA which revealed a MOF loading of 7.4wt% (figure A.14). The acidification of UiO-66-NH_2@FFP causes a reduction in MOF loading by 3wt%. We note that acidification of bulk UiO-66-NH_2 results in a decrease in MOF yield, due to minor degradation. We therefore assume that the same is occurring during the acidification of the MOF composite.

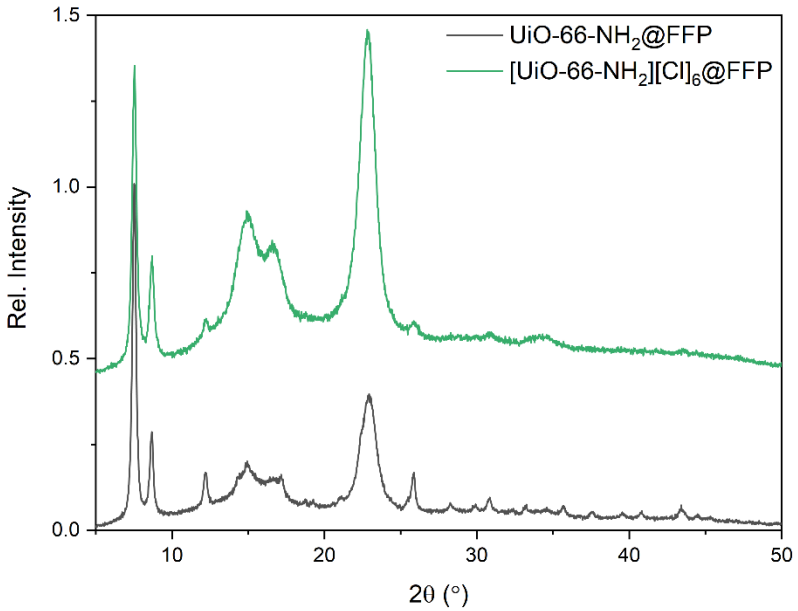

Figure 2.32. PXRD pattern comparison of (bottom to top) UiO-66-NH_2@FFP after 20 cycles before and after acidification.

FTIR spectroscopy of the neutral and acidified composites, alongside the FFP and UiO-66-NH_2 bulk are presented in figure 2.33. The spectra of the composites show a clear overlap of the two parent components. The acidified composite shows smaller intensities for the MOF absorbances than the neutral composite, particularly at absorbances found between 1250 and 1500 cm^{-1}, further corroborating a reduction in MOF loading as a result of the acid treatment to protonate the MOF.

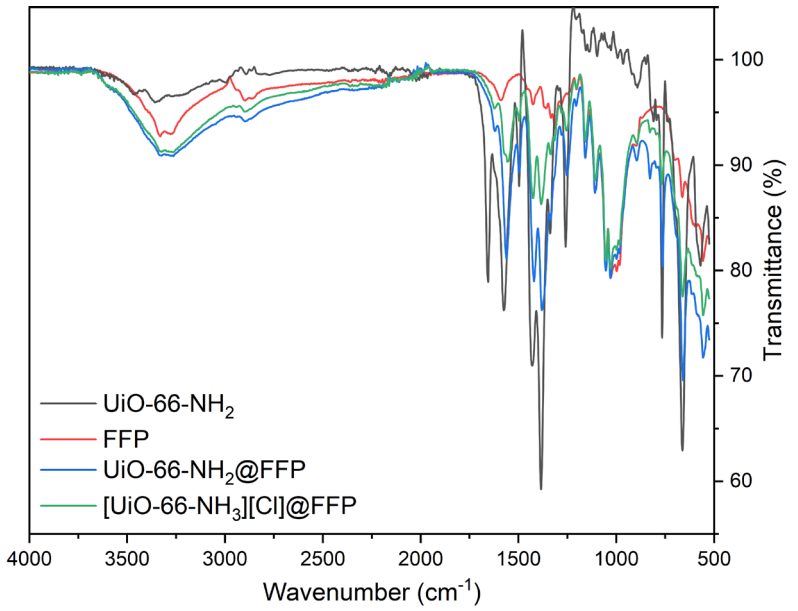

Figure 2.33. FTIR spectra of FFP, UiO-66-NH_2, and its FFP composites.

2.3.2.1 Perrhenate Remediation of UiO-66-NH_2@FFP Composites

To test the filtration capabilities of the synthesised composites a separation rig modified from a 50 mL centrifuge tube was designed. Two holes were created in the tube, one for the connection of an inert gas supply and the other as a sample inlet. A hole in the tube lid, roughly 2 cm in diameter was also created to allow for the removal of the filtrate. The composite material was loaded into the lid before being sealed onto the tube. Circular FP/FFP measuring 3 cm in diameter were used as these fit well into the lid and did not allow filtrate leakage around the edge, ensuring that all the filtrate travels through the supported composite.

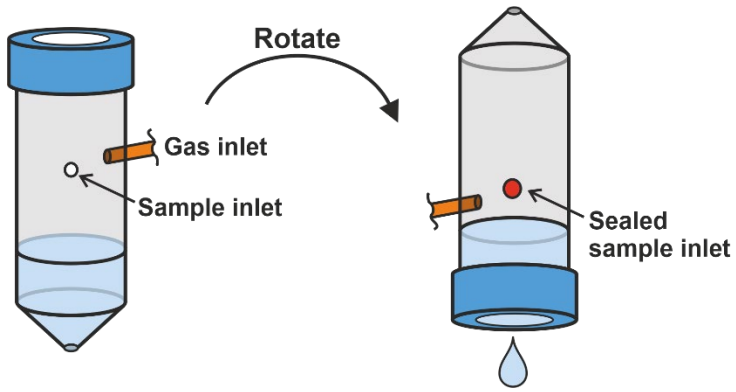

Figure 2.34. Diagram of a filtration rig, to test our UiO-66-NH_2@FFP composites, modified from a centrifuge tube.

To operate the rig, a preweighed [UiO-66-NH_3][Cl]$_6$@FFP composite disk was loaded into the lid and secured onto the tube. A 5 ppm perrhenate solution was loaded into the tube with a syringe through the sample inlet, which was then sealed. Inert gas supplied *via* a Schlenk line was very gently flowed through the rig. The rig was then inverted, and the sample filtered slowly through the composite where it was collected in a vial. It was estimated that it took one minute for the solution to entirely pass through the filter, followed by a 30 second wait time to allow any remaining droplets to fall into the collection vial. The solution was then reloaded into the rig and the process repeated. A 0.01 mL aliquot was taken from the solution after every two cycles for a total of ten cycles to measure the concentration of perrhenate. Figure 2.35 shows the removal of perrhenate from the solution over the 10 cycles.

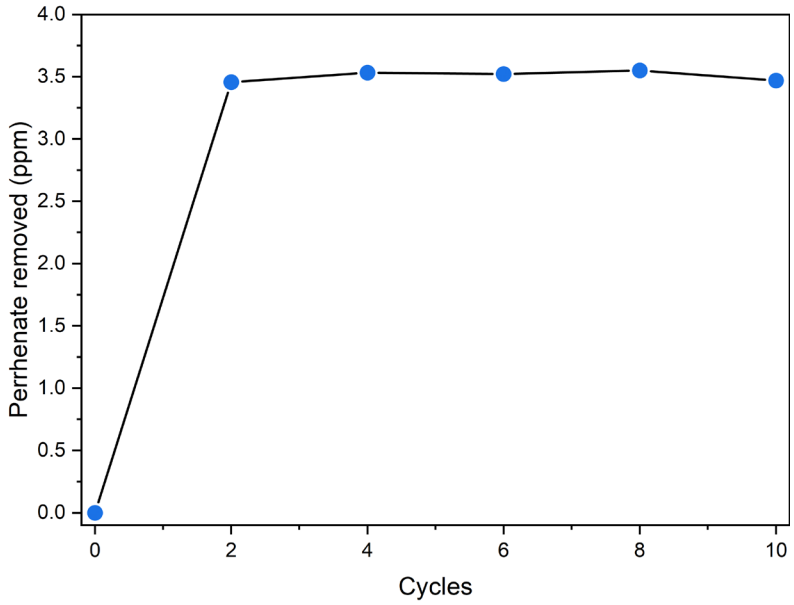

Figure 2.35. Perrhenate uptake by [UiO-66-NH_3][Cl]$_6$@FFP over 10 filtration cycles. Starting perrhenate concentration was 5 ppm.

We again observe very fast uptake kinetics of perrhenate by the [UiO-66-NH_3][Cl]$_6$ deposited on the FFP fibres. After two cycles, and thus a maximum contact time of three minutes with the composite, the perrhenate concentration of the solution has decreased by 3.46 ppm (69%) and plateaus after this point, meaning no further perrhenate uptake is observed. It is also evident that no leaching of perrhenate from the composite during subsequent cycles takes place. This remediation translates to 6.4 mg/g of perrhenate removed per gram of MOF (figure 2.36). In comparison, free [UiO-66-NH_2][Cl]$_6$ achieved 7.5 mg/g of perrhenate remediation, but it took 60 minutes to do so. After five minutes, the free MOF had reached a remediation of 6.1 mg g^{-1}. The composite therefore reaches a comparable level of remediation under a much shorter time scale.

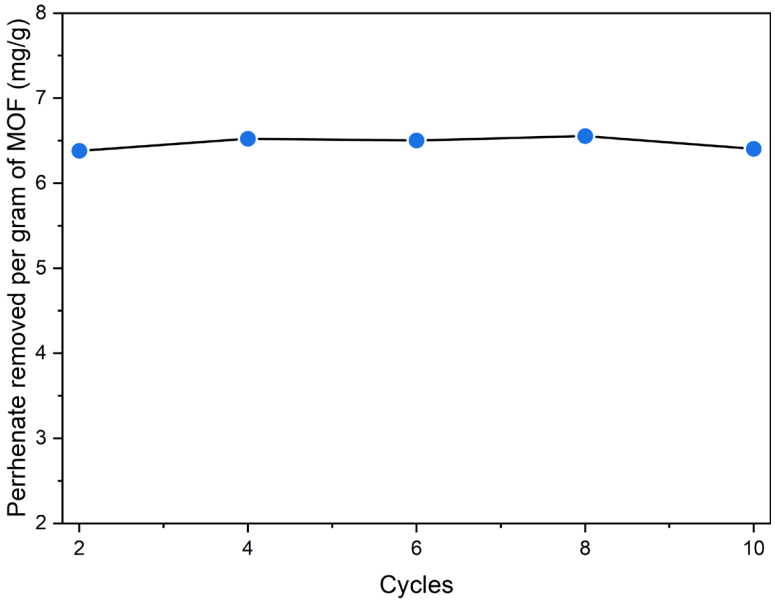

Figure 2.36. Quantity of perrhenate removed by [UiO-66-NH_3][Cl]@FFP over 10 filtration cycles of the same solution.

Maximum partition coefficients for [UiO-66-NH_3][Cl]@FFP were calculated to be 4524 ± 331 mL g^{-1} and 335 ± 25 mL g^{-1} when considering the MOF mass and material mass respectively (figure A.15), In comparison to pristine [UiO-66-NH_3][Cl]$_6$, which achieved a K_d of 5087 ± 508 mL g^{-1} after 60 minutes (section 2.3.1.4), the composite has performed equally well when considering method uncertainty. It is particularly impressive when we consider that the composite has achieved this partition coefficient in a much smaller time scale than the free MOF.

2.3.3 UiO-66-NH_2@Alginate Composites

2.3.3.1 Direct Synthesis of UiO-66-NH_2@Alg Composite Beads

UiO-66-NH_2@Alg composite beads were synthesised *via* a direct method. This procedure involves synthesising bulk UiO-66-NH_2 from a reported synthesis described by Katz *et al*.[60] The MOF was then suspended in an aqueous solution of sodium alginate (5 wt%) through vigorous stirring. The mixture was transferred to a syringe tube that was fixed above an aqueous calcium chloride salt bath (3 mol dm^{-3}) undergoing gentle stirring. The syringe was held at a height to ensure that the outlet was 5 cm above the surface of the salt bath. No external pressure was applied to the syringe barrel, instead the MOF@Alg solution was allowed to drip under gravity into the salt bath. Ionotropic gelation of the droplet surface occurred immediately, resulting in encapsulation of the MOF@alginate solution as a spherical bead. The salt bath was stirred for ten minutes after the last droplet had dropped into the bath to ensure that bead aggregates did not form. After ten minutes the solution was left, unagitated overnight to allow for complete gelation of the UiO-66-NH_2@Alg

beads. The beads were then thoroughly washed with deionised water and stored under water (figure 2.37).

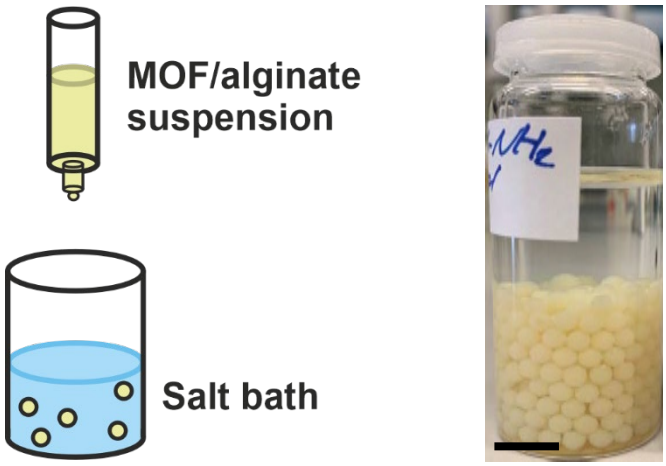

Figure 2.37. (Left) direct synthesis of UiO-66-NH_2@alginate composite beads by dropping a solution of sodium alginate with dispersed UiO-66-NH_2 crystals into a $CaCl_2$ salt bath. (Right) UiO-66-NH_2@alg beads after 24 hours of gelation. Scale bar = 1 cm.

A portion of the UiO-66-NH_2@Alg beads were dried on a paper towel and then underwent freeze drying overnight for appropriate characterisation. PXRD confirms the retention of UiO-66-NH_2 within the biopolymer beads after gelation as well as its stability within the alginate solution (figure 2.38). The alginate scaffold displays no crystalline characteristics.

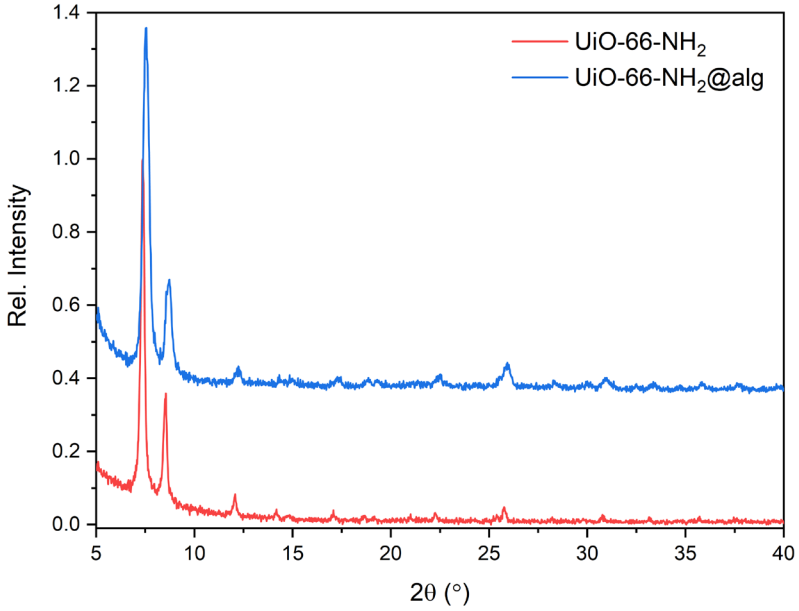

Figure 2.38. PXRD pattern comparison of UiO-66-NH_2@Alg to the parent MOF.

From previous reports, as well as our work in section 2.3.1, we know that acidification of UiO-66-NH_2 to yield [UiO-66-NH_3][Cl]$_6$ is essential in remediating any meaningful quantities of

perrhenate. It is therefore imperative that the alginate retains its structure under acidic conditions so that the encapsulated MOF can be undergo this dative PSM reaction prior to application. Alginate composites are reported to physically respond to change in pH by swelling or contracting in basic or acidic mediums respectively.[68] This arises due to the deprotonation of the carboxylic acid functionalities in high pH conditions which cause repulsion of alginate chains, or the protonation of said groups at low pH which allow for stabilising hydrogen bonding interactions between chains. We observe the same findings when our UiO-66-NH_2@Alg composite beads are left in aqueous solutions of varying pH for 24 hours (table 2.5).

Table 2.5. UiO-66-NH_2 alginate composite beads in various pHs. HCl/NaOH were used to control pH of aqueous solutions.

pH	2.37	5.24	7.24	9.62	12.18
Size	1.5 mm	2.0 mm	2.0 mm	3.5 mm	4.0 mm
				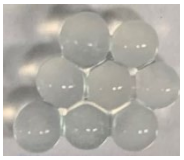	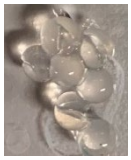

Submersion of the beads in a solution of pH 2.37 causes the bead diameters to contract by 0.5 mm, whereas swelling of the beads to 4 mm in diameter results in their rupturing at pH 12.18. PXRD characterisation of freeze-dried samples of these beads confirm that low pH does not result in substantial degradation of the UiO-66-NH_2 component (figure A.4), however this was found to not be the case for basic conditions. At pH 9.62, the bead diameter has increased by 175% based upon their size in neutral conditions. While the beads have not ruptured at this pH, UiO-66-NH_2 has undergone detrimental degradation and is not present in the PXRD pattern. Therefore, the pH stability of UiO-66-NH_2@Alg is dependent on the MOF stability rather than that of the biopolymer in this case.

Our investigations found that while pristine UiO-66-NH_2 is mostly stable under acidic conditions it can undergo some degradation. We therefore hypothesised that the composite acidified with 2 M HCl would have a lower MOF loading than the neutral parent composite beads. TG analysis was employed to calculate the MOF loadings for both composites. A portion of each composite was freeze-dried and subject to TGA (figure 2.39). Both composites show a higher residual mass than that of the calcium alginate sample. This confirms that the MOF has been retained in both composites as it confirms the presence of additional metal oxide that remains present in the residual mass. We also observe a smaller residual mass for the acidified product than the neutral composite which also suggests MOF degradation by the acidification reaction. A comparison of the

residual masses of the composites and the calcium alginate samples can elucidate the MOF loading within the composite. TGA reveals MOF loadings of 49wt% and 36wt% for UiO-66-NH_2@alg and $[UiO\text{-}66\text{-}NH_3][Cl]_6$@alg respectively when the targeted loading was 50wt%. These values demonstrate the ability to accurately control the MOF loading of alginate composites *via* the direct synthesis method but also confirms MOF degradation as a result of acidification of UiO-66-NH_2 to $[UiO\text{-}66\text{-}NH_3][Cl]_6$.

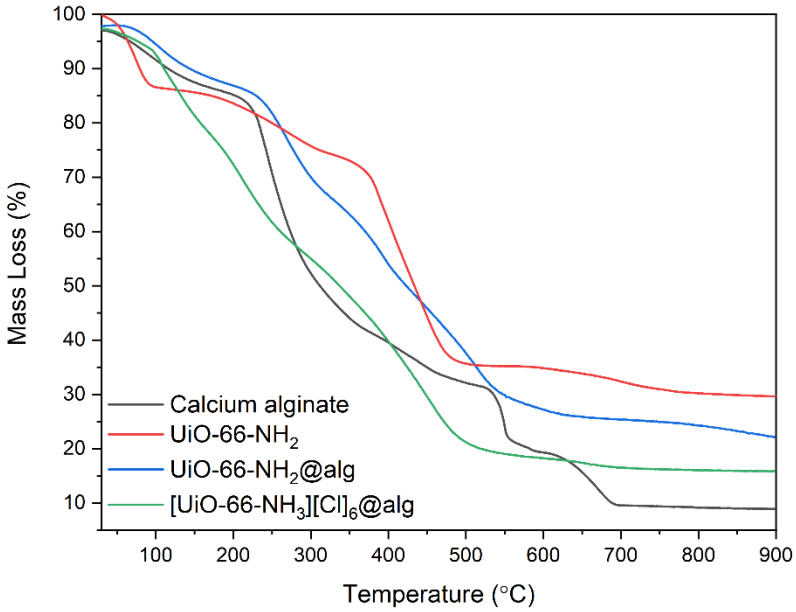

Figure 2.39. TG analysis of UiO-66-NH_2@Alg and $[UiO\text{-}66\text{-}NH_3][Cl]_6$ compared to their parent components, UiO-66-NH_2 and calcium alginate.

FTIR was employed to attempt to assess the acidification of UiO-66-NH_2 within the alginate composites (figure 2.40).

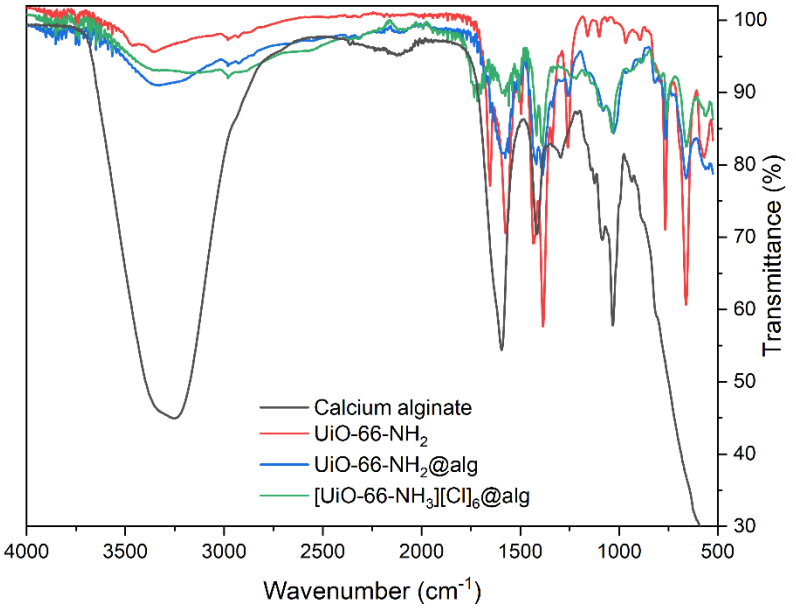

Figure 2.40. FTIR of UiO-66-NH_2@alg and $[UiO\text{-}66\text{-}NH_3][Cl]_6$ and their parent materials.

The abundance of carboxylic acid groups on the polymer chains of calcium alginate results in a very strong, and broad, absorbance centred at 3280 cm^{-1} (O-H stretch) in the calcium alginate spectrum. In addition, there are also absorbances present at 1410 and 1597 cm^{-1} corresponding to the O-H bend and C=O stretch of the carboxylic acid group. Both composite spectra show a combination of absorbances that align with both the calcium alginate and the UiO-66-NH_2 absorbances, the latter of which we previously assigned in section 2.3.1. The acidified composite spectrum shows a much broader absorbance at higher wavenumber which we attribute to the protonation of the amine groups on UiO-66-NH_2. We also observe a weak absorption in the spectrum of [UiO-66-NH_3][Cl]$_6$@alg, centred at 2548 cm^{-1}, which is also found in the spectrum of [UiO-66-NH_3][Cl]$_6$ (figure 2.18). We believe this is evidence of successful protonation of the MOF.

SEM imaging of the freeze dried UiO-66-NH_2@Alg composite shows that UiO-66-NH_2 is well distributed through the interior and on the surface of the composite beads (figure 2.41). SEM imaging of [UiO-66-NH_3][Cl]$_6$ was not carried out due to time constraints.

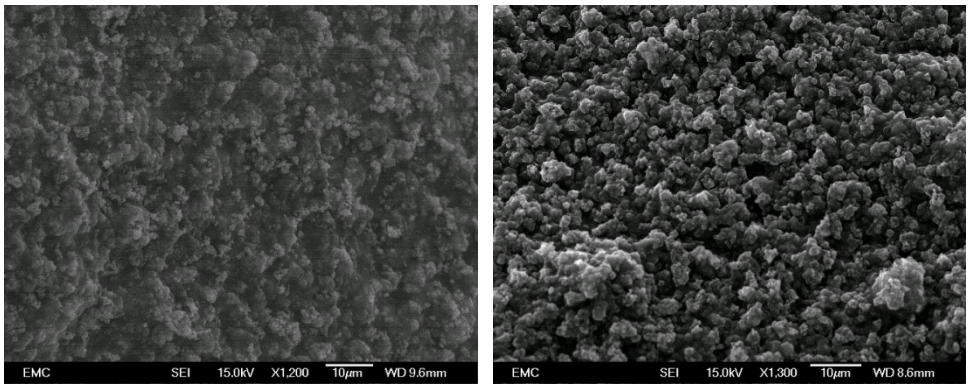

Figure 2.41. SEM imaging of (left) interior and (right) exterior of UiO-66-NH_2@Alg composite beads synthesised *via* direct methods. MOF loading is confirmed at 50wt%. Scale bars = 10 µm.

We also qualitatively assessed the ability of UiO-66-NH_2@Alg to adsorb methylene blue dye from aqueous solution to confirm that the beads are permeable to small molecules. Table 2.6 demonstrates how the dye travels through the bead over different lengths of time and confirms the composite's permeability to small molecules. After five minutes, clear adsorption of the dye has occurred at the surface of the bead. After 120 minutes the dye has fully permeated the composite.

Table 2.6. UiO-66-NH_2 alginate composite beads in methylene blue solution for varying periods of time. (Top) Cross sections of beads and (bottom) exterior of beads. Scale bar = 10 mm.

1 min	5 min	30 min	120 min
	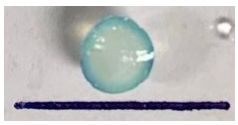		
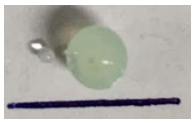	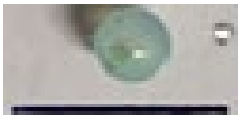	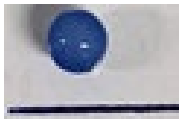	

2.3.3.2 Perrhenate Remediation of UiO-66-NH_2@Alg Composites

Assessment of UiO-66-NH_2@alg and [UiO-66-NH_3][Cl]@alg composites for perrhenate remediation was carried out using aqueous 5 ppm solutions of perrhenate. MOF loadings of 50wt% and 36wt% were used for the neutral and protonated composites respectively. Figure 2.42 shows how the concentration of perrhenate changes over 24 hours (1440 min) when hydrated (@hyd) and freeze-dried (@FD) samples of both UiO-66-NH_2@alg and [UiO-66-NH_3][$Cl]_6$@alg composite beads were added to 5 ppm perrhenate solutions.

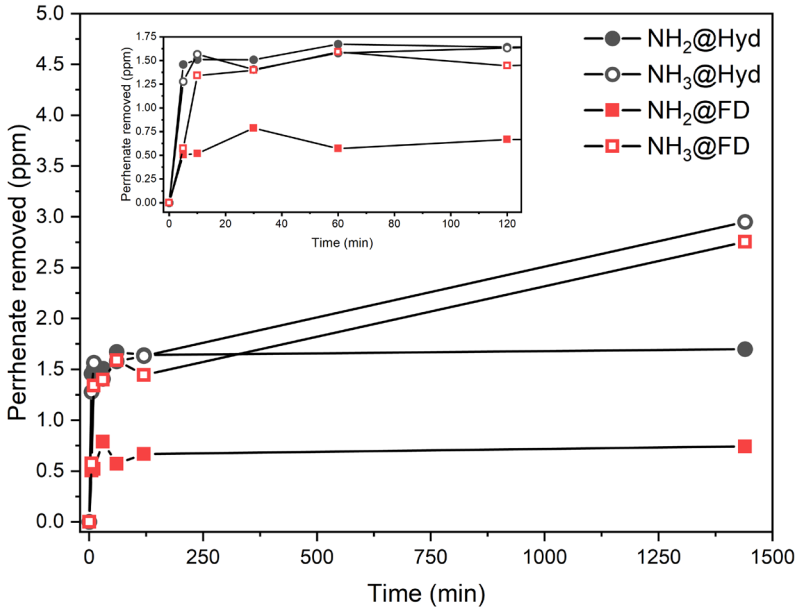

Figure 2.42. Perrhenate uptake from solution by UiO-66-NH_2@alginate composites that have been protonated and/or freeze dried. Hyd = hydrated composite and FD = freeze dried composite.

We quantified the mass of perrhenate removed at each time interval by the four different composites. These perrhenate masses were then normalised based upon the mass of MOF present in each composite sample. Calculating the MOF present in the freeze-dried samples was very simple because the composite was weighed prior to the uptake experiment, and we had calculated the proportion of MOF present in the neutral and acidified composites from our TGA experiments in

figure 2.39. Doing the same for the hydrated samples was not as straight forward because each bead contained an unknown quantity of water. We derived the MOF quantities for the hydrated composites by weighing 50 freeze-dried beads of the neutral and acidified composites to obtain an average bead mass for both. The quantity of MOF in one bead was then calculated based upon the TGA derived MOF loadings and these average bead masses. The MOF mass in the hydrated composite experiments was then calculated based upon the number of beads present. Figure 2.43 shows the quantity of perrhenate removed per gram of MOF from the 5 ppm aqueous solutions by the four composites.

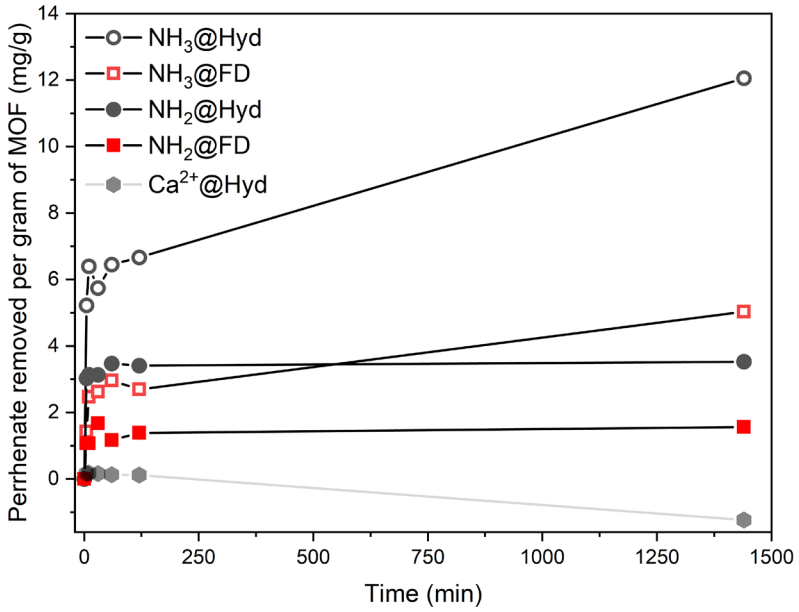

Figure 2.43. Perrhenate removal per gram of MOF in [UiO-66-NH_3][Cl]@alginate composites. Hyd = hydrated composites; FD = freeze dried composite; NH_2 = neutral composite; NH_3 = protonated composite.

Comparing the composites' abilities to remediate perrhenate based upon the quantity of MOF present within the materials shows a more distinguishable difference in performance. The [UiO-66-NH_3][Cl]$_6$@hyd composite beads remediated the highest quantity of perrhenate over 24 hours, reaching 12.06 mg/g. In addition, this composite remediates a similar quantity of perrhenate as the pristine MOF ([UiO-66-NH_3][Cl]$_6$) (section 2.3.1.4) after two hours (6.67 mg/g versus 7.04 mg/g respectively). The [UiO-66-NH_3][Cl]$_6$@hyd composite however continues to remediate perrhenate after two hours, reaching 12.06 mg/g after 24 hours. On the other hand, [UiO-66-NH_3][Cl]$_6$ starts to release the anion back into solution after two hours and obtains a remediation of 6.53 mg/g after 24 hours. While the two materials behave similarly under short timescales, when left over a longer period the composite performs far better, remediating 1.6 times more perrhenate over 24 hours.

Due to time constraints, we were not able to assess the perrhenate uptake of calcium alginate that had been submerged in 2 M HCl. Doing so would allow us to assess the acid-treated scaffolds ability to remediate perrhenate, and thus quantify any additional performance that is induced by the further incorporation of [UiO-66-NH_3][Cl]. Without this control experiment it is difficult to confirm why the [UiO-66-NH_3][Cl]$_6$@hyd composite performs better over 24 hours than [UiO-66-NH_3][Cl]$_6$.

We postulate that the protonation of the carboxylate groups on the alginate polymer by HCl, causes a possible imbalance of charge within the calcium alginate scaffold. This imbalance is corrected by the migration of chloride anions into the composite to counterbalance the Ca^{2+} charge. There is therefore a replacement of immobile carboxylic acid groups with mobile chloride which creates an anion exchange scaffold. Upon exposure to ReO_4^-, the chloride anions within the scaffold undergo exchange with the perrhenate, following their respective concentration gradients (figure 2.44). Once the perrhenate has migrated into the alginate scaffold it can then further transfer into the pores of the MOF, exchanging with the chloride within the framework. This simultaneously decreases the perrhenate concentration and restores the chloride concentration within the alginate scaffold, and thus promotes further perrhenate uptake from solution into the alginate. This mechanism would account for the fast initial uptake by the composite within two hours, followed by the slower yet continued uptake up to 24 hours.

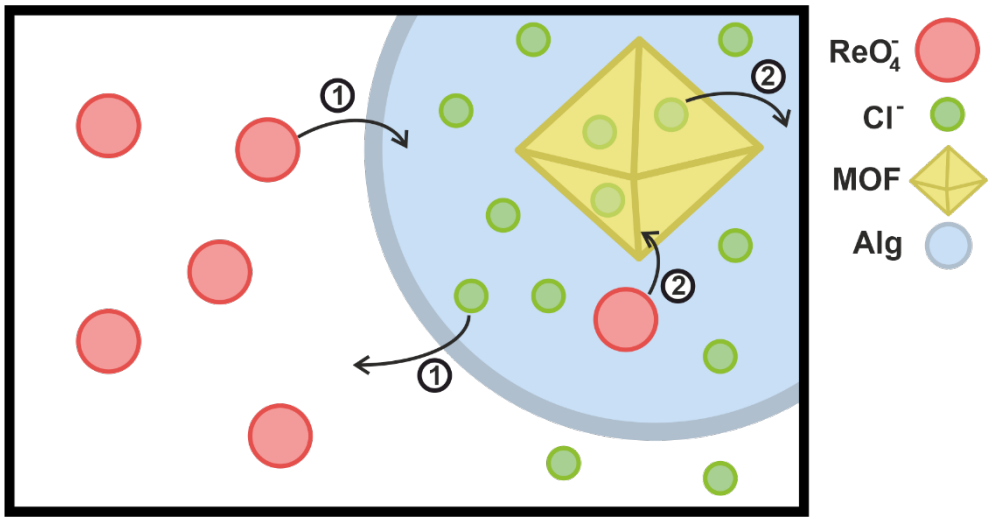

Figure 2.44. Schematic of proposed mechanism of perrhenate uptake by [UiO-66-NH_3][Cl]$_6$@hyd.

We observe no remediation of perrhenate by pristine calcium alginate. We attribute this to the biopolymer carrying a negative charge because of the carboxylate groups present on the polymer chains. These COO^- groups are immobilised and thus there is no opportunity for anion exchange to occur, meaning no perrhenate migration into the calcium alginate beads takes place. Any remediation by UiO-66-NH_2@hyd is therefore caused by the MOF component and not the biopolymer scaffold. Indeed the neutral composite (UiO-66-NH_2@hyd) does display some perrhenate uptake, reaching 3.41 mg/g and plateauing after 120 minutes. We believe this uptake

arises from perrhenate migrating from an area of high concentration (solution) to an area of low concentration (MOF crystals on composite surface). When compared to the results of UiO-66-NH_2 (section 2.3.1.4) we find that encapsulation of the MOF within the alginate scaffold does not have a negative effect on perrhenate remediation. Pristine UiO-66-NH_2 remediated 3.11 mg/g of perrhenate in the same time period.

Freeze drying the composites has a detrimental effect on perrhenate remediation by the neutral and protonated composites. When the neutral composite undergoes freeze drying the perrhenate uptake after 24 hours falls from 3.53 to 1.56 mg/g. A similar pattern is observed for the protonated composites. Freeze drying the protonated composites causes the perrhenate uptake to fall from 12.06 to 5.03 mg/g after 24 hours.

K_d values were calculated for both protonated composites, based upon their material and MOF masses (figure 2.45). Due to their high-water content, the hydrated samples have much lower partition coefficients when considering their greater material mass. When the MOF mass is considered, the hydrated composite outperforms the freeze-dried material greatly. At 1440 min [UiO-66-NH_3][Cl]$_6$@hyd and [UiO-66-NH_3][Cl]$_6$@FD achieved K_d values of 5887 ± 529 and 2242 ± 807 mL/g respectively.

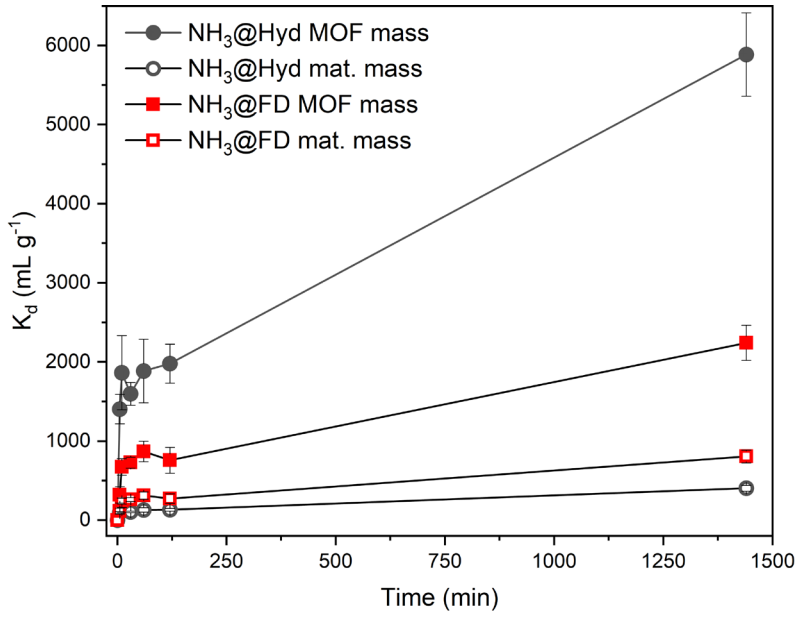

Figure 2.45. Partition coefficients for [UiO-66-NH_3][Cl]$_6$@Alg over 24 hours based on both MOF and composite masses. NH_3@Hyd = hydrated composites and NH_3@FD = freeze dried composite.

2.4 Conclusion and Further Work

In this body of work we have taken the well-known MOF UiO-66-NH_2, and performed a new PSM reaction on the amine groups to generate an ethyl urea moiety. The reaction requires simple and benign conditions, achieving an upper conversion of 74% in deionised water at room temperature and within 24 hours. This conversion was confirmed quantitatively *via* ^{1}H NMR spectroscopy. Further proof of the PSM reaction was obtained through gas adsorption experiments and FTIR spectroscopy, and TGA confirmed material stability and composition. Acidifying the PSM product with HCl yielded a cationic framework with chloride counter anions found within the pores. Anion exchange experiments with 5 ppm aqueous perrhenate solutions found that [UiO-66-$(NH_3)_{2.8}(EtUr)_{3.2}$][Cl]$_6$ could remediate 1.5 times more of the target anion than the parent framework [UiO-66-NH_3][Cl]$_6$, achieving a partition coefficient of 8724 mL g^{-1} after 60 minutes (table 2.7). This K_d value for [UiO-66-$(NH_3)_{2.8}(EtUr)_{3.2}$][Cl]$_6$ is over 3000 mL g^{-1} more than that achieved by [UiO-66-NH_3][Cl]$_6$.

Table 2.7. Maximum perrhenate adsorption values for each material tested, from our experimental conditions, and their associated K_d values. For materials that undergo a plateau of perrhenate uptake we have taken the first point of that plateau and not necessarily the highest perrhenate mass remediated.

Material	Time of highest uptake (min)	Maximum Perrhenate adsorption per gram of MOF (mg g^{-1})	Maximum Partition coefficient, K_d (mL g^{-1})
[UiO-66-$(NH_3)_{2.8}(EtUr)_{3.2}$][Cl]$_6$ (**PSM$^+$**)	60	11.25	8724
[UiO-66-NH_3][Cl]$_6$@Hyd	1440	12.06	5887
[UiO-66-NH_3][Cl]$_6$ (**NH_3^+**)	60	7.50	5087
[UiO-66-NH_3][Cl]$_6$@FFP	2 cycles	6.38	4137
[UiO-66-NH_3][Cl]$_6$@FD	1440	5.03	2242
UiO-66-NH_2 (**NH_2**)	60	3.74	1193
UiO-66-$(NH_2)_{2.1}$(BDC-Ur)$_{3.9}$ (**PSM**)	1	3.75	1082
UiO-66-NH_2@Hyd	1440	3.53	1069
UiO-66-NH_2@FD	30	1.68	398

This confirms our hypothesis that the incorporation of a urea moiety within this framework can improve the capture of oxo-anions such as perrhenate. The introduction of the hydrogen bond donor group provides a binding site for perrhenate to undergo a reinforcing bridging hydrogen bond interaction.

We do however recognise that these results only concern perrhenate removal from aqueous solutions and not that resembling the composition of contaminated groundwater. Additional

experiments are therefore essential in assessing the material's ability to recover perrhenate, and ultimately pertechnetate, in the presence of competing anions such as sulphate. An assessment on the maximum adsorption capacity of [UiO-66-$(NH_3)_{2.8}$($EtUr)_{3.2}$][Cl]$_6$ would also prove beneficial. Literature reports the adsorption capacity of [UiO-66-NH_3][Cl]$_6$ as 159 mg/g of perrhenate.[12] We believe that while our materials have improved remediation it likely has a lower overall adsorption capacity than [UiO-66-NH_3][Cl]$_6$ due to the reduction in porosity from the ethyl urea groups.

UiO-66-NH_2 has been deposited on functionalised filter papers *via* a room temperature and aqueous method for the first time. We avoid producing high quantities of non-deposited UiO-66-NH_2 as a by-product, as seen in literature reports, by taking a dip coating approach. TGA shows that the deposition of the MOF on FFP increases linearly as the number of dip coat cycles increase reaching 12.9wt% after 20 cycles, and that our technique produces composites with MOF loadings that compete well with literature reports. Once again, we perform a dative PSM reaction with HCl on the deposited UiO-66-NH_2 to yield [UiO-66-NH_3][Cl]$_6$@FFP. The acidification of the composite resulted in a decrease in MOF loading to 7.4wt%. The cationic composite was tested for perrhenate remediation and found to remove 71% of the anion from a 5 ppm solution after only two filtration cycles. The material achieved a K_d value of 4137 ± 369 mL/g which is comparable to that of the pristine protonated MOF.

Our work here has shown that deposited UiO-66-NH_2 onto FFP can be achieved quickly at room temperature and without the use of harsh solvents. It also demonstrates that deposition onto the scaffold does not have a detrimental effect on the MOFs ability to remediate perrhenate. We again recognise that this composite also requires more thorough testing, particularly with groundwater simulant solutions, to fully assess the material's ability as an anion exchange medium.

Finally, we have synthesised UiO-66-NH_2@alg composite beads through a direct, ionotropic gelation method. Here we synthesised the MOF separately, before encapsulating it within the hydrogel bead. The synthesis of MOF@alg composites is not a new area of MOF research, however based upon our literature search, it is the first occasion that UiO-66-NH_2 has been used. Full characterisation of the composite was carried out, followed by acidification with HCl to protonate the framework for perrhenate remediation. We find that acidification reduces the MOF loading of the composite, from 50 to 36wt%. Perrhenate uptake experiments for these composites proved very interesting and suggest that the PSM reaction to acidify the MOF also influences the alginate scaffold. Over 24 hours, [UiO-66-NH_3][Cl]$_6$@Hyd remediates 1.6 times more perrhenate per gram of MOF than [UiO-66-NH_3][Cl]$_6$. While uptake values up to 120 minutes of both materials are similar to one another. This suggests that the perrhenate uptake mechanism for [UiO-66-NH_3][Cl]$_6$@Hyd is not as simple as direct diffusion of the anion from solution into the framework pores. Further

experimentation of acidified calcium alginate is therefore necessary to assess the effect of the PSM on the scaffold material and provide additional proof of our hypothesis.

The effect of freeze-drying the MOF composites showed that the formation of an aerogel did not enhance the material's ability to remediate perrhenate. While [UiO-66-NH_3][Cl]$_6$@FD performed better than UiO-66-NH_2@FD at remediating perrhenate, the change from a hydrogel to an aerogel was very detrimental to the composite's performance.

The aim of our composite work was to assess the effect immobilisation of [UiO-66-NH_3][Cl]$_6$ onto biopolymer scaffolds has on the MOF's ability to remediate perrhenate from solution as a non-radioactive surrogate for pertechnetate. Our findings conclude that there is no detrimental effect by forming the composite and there may be a synergistic effect on perrhenate remediation by alginate when UiO-66-NH_2@hyd is acidified.

2.5 Experimental

2.5.1 MOF Digestion for ^{1}H NMR Analysis

Two methods were used for MOF digestion in this chapter.

a. 0.1 mL of NaOD was added to 0.9 mL of D_2O followed by approximately 20 mg of the MOF. The mixture was shaken until all visible MOF had dissolved. To remove precipitated $Zr(OH)_4$ the mixture was centrifuged at 12,000 rpm for three minutes. The supernatant was removed and underwent NMR characterisation.
b. NH_4F (0.014 g, 0.38 mmol) was dissolved in 0.1 mL of D_2O followed by dilution with 0.9 mL DMSO-d_6. This resulted in the precipitation of NH_4F which was ignored. Approximately 20 mg of MOF was added to the mixture and shaken until the MOF and most of the NH_4F had dissolved. To remove any remaining NH_4F the mixture was centrifuged at 12,000 rpm for three minutes. The supernatant was removed and underwent NMR characterisation. This method was developed by Hamza *et al.*[17]

2.5.2 Synthesis of $[ZrO_4(OH)_4(BDC\text{-}NH_2)_6]$ (UiO-66-NH_2)

A procedure described by Katz *et al.* was used to synthesise UiO-66-NH_2.[60] $ZrCl_4$ (0.75 g, 3 mmol) was dissolved in a mixture of 15 mL DMF and 6 mL HCl. Separately, BDC-NH_2 (0.78 g, 4 mmol) was dissolved in 50 mL DMF. The solutions were combined, separated into scintillation vials, sealed, and heated to 80 °C overnight. The resulting yellow powder was washed with ethanol/centrifugation cycles thrice and dried at 70 °C overnight.

2.5.3 PSM of UiO-66-NH_2 with Ethyl Isocyanate

UiO-66-NH_2 (30 mg, 0.017 mmol), prepared by the method described in section 2.5.2, was added to 5 mL of the required solvent along with ethyl isocyanate (0.08 mL, 1.2 mmol) in a vial. The vial was sealed and stirred at room temperature for the desired length of time. The mixture was then centrifuged to collect and washed with methanol/centrifugation cycles thrice and dried at room temperature overnight. Yield = 0.0267 g (75% based on UiO-66-NH_2).

2.5.4 Acidification of UiO-66-NH_2 and its PSM Products

UiO-66-NH_2 or UiO-66-$(NH_2)_{1.8}(EtUr)_{4.2}$ were suspended in 2M HCl for two hours. No stirring of the mixtures was undertaken. Following this, the solids were isolated by centrifugation. The solids were

then washed with deionised water and dried at room temperature. Yield of UiO-66-NH_2 = (%). Yield of UiO-66-$(NH_2)_{1.8}(EtUr)_{4.2}$ = (%).

2.5.5 Perrhenate Remediation of UiO-66-NH_2 and its PSM Products

Approximately 50 mg of the MOF was added to a pre-weighed vial. 9.95 mL of ultra-pure HPLC grade deionised water was added. The mixture was gently stirred and to it 0.05 mL of a 1000 ppm sodium perrhenate stock solution was added. The vial was capped and left for the desired time. After this time, the solution was filtered with a 10 µm syringe filter to remove the MOF. The solution was then diluted to 500-fold and [ReO_4^-] determined through ICP-MS.

2.5.6 Synthesis of UiO-66-NH_2@FFP *via* dip-coating

Cellulose filter papers were first functionalised following a method described by Hashem *et al*.[55] $ZrOCl_2 \cdot 8H_2O$ (2.56 g, 7 mmol) was dissolved in 40 mL of a 50:50 deionised water/acetic acid solution. The solution was left undisturbed for five days. 20 mL of the solution was transferred to a petri dish (solution A). NaOH (0.32 g, 8 mmol) was dissolved in 20 mL of deionised water. Following this, H_2BDC-NH_2 (0.70 g, 4 mmol) was dissolved in this solution before it was transferred to a petri dish (solution B). FFP was submerged in A for one minute. The FFP was then removed with tweezers and the excess solution removed from the FFP with a paper towel. The FFP was then added to B and submerged for one minute. The FFP was then removed with tweezers and the excess solution removed from the FFP with a paper towel. This completes one cycle.

2.5.7 Perrhenate Filtration by [UiO-66-NH_3][Cl]@FFP Composites

A preweighed and dry [UiO-66-NH_3][Cl]@FFP composite was loaded into the lid of the filtration rig that was secured in a clamp stand. 10 mL of a 5 ppm perrhenate aqueous solution was added to the rig through the solution port with a syringe. The solution port was sealed, and the rig inverted 180 degrees. Gas was very gently flowed through the rig *via* the gas port resulting in the continuous flow of solution through the composite. The solution was collected with a funnel into a clean vial. Once the solution had completely transferred through the composite the rig was left for 30 seconds before the gas supply was shut off and the rig returned to its upright position. This completes one cycle. 0.01 mL aliquots were taken after every two cycles for ICP-MS analysis to calculate [ReO_4].

2.5.8 Direct Synthesis of UiO-66-NH_2@Alg Beads

A procedure described by Katz *et al.* was first used to synthesise UiO-66-NH_2.[60] Following this, sodium alginate (0.51 g, mmol) was dissolved in 10 mL deionised water. Once fully dissolved,

UiO-66-NH_2 (0.50 g, mmol) was dispersed in the alginate mixture with vigorous stirring for 10 minutes. The MOF@alginate solution was then transferred to a syringe barrel and dropped into a calcium chloride (3M) salt bath, forming UiO-66-NH_2@alg beads. The salt bath was stirred to stop bead aggregation. Ten minutes after the solution had completely transferred to the salt bath the stirring was halted and the beads left overnight to allow for complete gelation. The beads were then thoroughly washed by repeated soaking in fresh deionised water and stored under water.

2.5.9 Perrhenate Remediation of UiO-66-NH_2@Alg Beads

The composite was weighed into a vial along with 9.95 mL of ultra-pure HPLC grade deionised water. ***For hydrated composites it is important to remove excess water on the bead surfaces by rolling on clean filter paper prior to weighing. It is also necessary to carry out the drying and weighing quickly so that the beads do not dry out.*** The solution was gently stirred with a stirrer bar to ensure that the beads were agitated. To this solution 0.05 mL of a 1000 ppm sodium perrhenate stock solution was added. The vial was capped and left for the desired time. After this time, the solution was filtered with a 10 µm syringe filter to remove the MOF. The solution was then diluted to 500-fold and [ReO_4^-] determined through ICP-MS.

2.6 References

1 S. M. Moosavi, A. Nandy, K. M. Jablonka, D. Ongari, J. P. Janet, P. G. Boyd, Y. Lee, B. Smit and H. J. Kulik, *Nat. Commun.*, 2020, **11**, 4068.

2 M. Ding, X. Cai and H. L. Jiang, *Chem. Sci.*, 2019, **10**, 10209.

3 N. C. Burtch, H. Jasuja and K. S. Walton, *Chem. Rev.*, 2014, **114**, 10575.

4 J. H. Cavka, S. Jakobsen, U. Olsbye, N. Guillou, C. Lamberti, S. Bordiga and K. P. Lillerud, *J. Am. Chem. Soc.*, 2008, **130**, 13850.

5 K. S. Park, Z. Ni, A. P. Côté, J. Y. Choi, R. Huang, F. J. Uribe-Romo, H. K. Chae, M. O'Keeffe and O. M. Yaghi, *Proc. Natl. Acad. Sci. U. S. A.*, 2006, **103**, 10186.

6 T. Loiseau, C. Serre, C. Huguenard, G. Fink, F. Taulelle, M. Henry, T. Bataille and G. Férey, *Chem. - A Eur. J.*, 2004, **10**, 1373.

7 Y. Bai, Y. Dou, L. H. Xie, W. Rutledge, J. R. Li and H. C. Zhou, *Chem. Soc. Rev.*, 2016, **45**, 2327.

8 A. Huang, L. Wan and J. Caro, *Mater. Res. Bull.*, 2018, **98**, 308.

9 Q. Chen, Q. He, M. Lv, Y. Xu, H. Yang, X. Liu and F. Wei, *Appl. Surf. Sci.*, 2015, **327**, 77.

10 G. W. Peterson, J. B. Decoste, F. Fatollahi-Fard and D. K. Britt, *Ind. Eng. Chem. Res.*, 2014, **53**, 701.

11 G. W. Peterson, M. R. Destefano, S. J. Garibay, A. Ploskonka, M. McEntee, M. Hall, C. J. Karwacki, J. T. Hupp and O. K. Farha, *Chem. - A Eur. J.*, 2017, **23**, 15913.

12 D. Banerjee, W. Xu, Z. Nie, L. E. V Johnson, C. Coghlan, M. L. Sushko, D. Kim, M. J. Schweiger, A. A. Kruger, C. J. Doonan and P. K. Thallapally, *Inorg. Chem.*, 2016, **55**, 8241.

13 G. C. Shearer, S. Chavan, S. Bordiga, S. Svelle, U. Olsbye and K. P. Lillerud, *Chem. Mater.*, 2016, **28**, 3749.

14 M. Taddei, *Coord. Chem. Rev.*, 2017, **343**, 1.

15 S. Øien, D. Wragg, H. Reinsch, S. Svelle, S. Bordiga, C. Lamberti and K. P. Lillerud, *Cryst. Growth Des.*, 2014, **14**, 5370.

16 C. A. Trickett, K. J. Gagnon, S. Lee, F. Gándara, H. Bürgi and O. M. Yaghi, *Angew. Chemie Int. Ed.*, 2015, **54**, 11162.

17 H. A. Hamzah, T. S. Crickmore, D. Rixson and A. D. Burrows, *Dalt. Trans.*, 2018, **47**, 14491.

18 H. A. Hamzah, W. J. Gee, P. R. Raithby, S. J. Teat, M. F. Mahon and A. D. Burrows, *Chem. – A Eur. J.*, 2018, **24**, 11094.

19 S. J. Garibay and S. M. Cohen, *Chem. Commun.*, 2010, **46**, 7700.

20 C. Tudisco, G. Zolubas, B. Seoane, H. R. Zafarani, M. Kazemzad, J. Gascon, P.-L. Hagedoorn and L. Rassaei, *RSC Adv.*, 2016, **6**, 108051.

21 S. Tripathi, B. Sreenivasulu, A. Suresh, C. V. S. B. Rao and N. Sivaraman, *RSC Adv.*, 2020, **10**, 14650.

22 C. J. Doonan, W. Morris, H. Furukawa and O. M. Yaghi, *J. Am. Chem. Soc.*, 2009, **131**, 9492.

23 E. Dugan, Z. Wang, M. Okamura, A. Medina and S. M. Cohen, *Chem. Commun.*, 2008, **29**, 3366.

24 X.-W. Dong, T. Liu, Y.-Z. Hu, X.-Y. Liu and C.-M. Che, *Chem. Commun.*, 2013, **49**, 7681.

25 T. Wittmann, R. Siegel, N. Reimer, W. Milius, N. Stock and J. Senker, *Chem. Eur. J*, 2015, **21**, 314.

26 C. Volkringer and S. M. Cohen, *Angew. Chemie Int. Ed.*, 2010, **49**, 4644.

27 B. J. Yao, W. L. Jiang, Y. Dong, Z. X. Liu and Y. Bin Dong, *Chem. - A Eur. J.*, 2016, **22**, 10565.

28 M. Akbarian, E. Sanchooli, A. R. Oveisi and S. Daliran, *J. Mol. Liq.*, 2021, **325**, 115228.

29 H. Fotovat, M. Khajeh, A. R. Oveisi, M. Ghaffari-Moghaddam and S. Daliran, *Microchim. Acta*, 2018, **185**, 469.

30 R. G. Puscaselu, A. Lobiuc, M. Dimian and M. Covasa, *Polymers (Basel).*, 2020, **12**, 2417.

31 H. H. Tønnesen and J. Karlsen, *Drug Dev. Ind. Pharm.*, 2002, **28**, 621.

32 M. S. Shoichet, *Macromolecules*, 2010, **43**, 581.

33 C. H. Yang, M. X. Wang, H. Haider, J. H. Yang, J. Y. Sun, Y. M. Chen, J. Zhou and Z. Suo, *ACS Appl. Mater. Interfaces*, 2013, **5**, 10418.

34 J.-Y. Sun, X. Zhao, W. R. K. Illeperuma, O. Chaudhuri, K. H. Oh, D. J. Mooney, J. J. Vlassak and Z. Suo, *Nature*, 2012, **489**, 133.

35 J. Y. Leong, W. H. Lam, K. W. Ho, W. P. Voo, M. F. X. Lee, H. P. Lim, S. L. Lim, B. T. Tey, D. Poncelet and E. S. Chan, *Particuology*, 2016, **24**, 44.

36 D. W. Lee, T. Didriksen, U. Olsbye, R. Blom and C. A. Grande, *Sep. Purif. Technol.*, 2020, **235**, 116182.

37 S. Daradmare, M. Xia, V. N. Le, J. Kim and B. J. Park, *Chemosphere*, 2021, **270**, 129487.

38 H. Zhu, Q. Zhang and S. Zhu, *ACS Appl. Mater. Interfaces*, 2016, **8**, 17395.

39 M. Li, W. Huang, B. Tang, Q. Fang, X. Ling and A. Lv, *Ind. Eng. Chem. Res.*, 2020, **59**, 18835.

40 J. Li, X. Wang, P. Liu, X. Liu, L. Li and J. Li, *Chinese J. Chem. Eng.*, 2022, **42**, 17.

41 S. J. Lee, T. Hann and S. H. Park, *ACS Appl. Mater. Interfaces*, 2020, **12**, 16319.

42 Y. Li, Z. Wang, X. Wang, B. Yan, Y. Peng and R. Ran, *Carbohydr. Polym.*, 2021, **269**, 118269.

43 K. H. Gardner and J. Blackwell, *Biopolymers*, 1974, **13**, 1975.

44 S. Boufi, I. González, M. Delgado-Aguilar, Q. Tarrès, M. À. Pèlach and P. Mutjé, *Carbohydr. Polym.*, 2016, **154**, 151.

45 M. Mascal and E. B. Nikitin, *Angew. Chemie - Int. Ed.*, 2008, **47**, 7924.

46 R. J. B. Pinto, M. C., C. Pascoal and T. Trindade, in *Nanocomposites - New Trends and Developments*, 2012, p. 24.

47 X. Yu, S. Tong, M. Ge, J. Zuo, C. Cao and W. Song, *J. Mater. Chem. A*, 2013, **1**, 959.

48 S. W. Zhao, M. Zheng, X. H. Zou, Y. Guo and Q. J. Pan, *ACS Sustain. Chem. Eng.*, 2017, **5**, 6585.

49 J. Cai, M. Lei, Q. Zhang, J. R. He, T. Chen, S. Liu, S. H. Fu, T. T. Li, G. Liu and P. Fei, *Compos. Part A Appl. Sci. Manuf.*, 2017, **92**, 10.

50 H. N. Abdelhamid and A. P. Mathew, *Coord. Chem. Rev.*, 2022, **451**, 214263.

51 E. Laurila, J. Thunberg, S. P. Argent, N. R. Champness, S. Zacharias, G. Westman and L. Öhrström, *Adv. Eng. Mater.*, 2015, **17**, 1282.

52 M. J. Neufeld, J. L. Harding and M. M. Reynolds, *ACS Appl. Mater. Interfaces*, 2015, **7**, 26742.

53 S. Ma, M. Zhang, J. Nie, J. Tan, S. Song and Y. Luo, *Carbohydr. Polym.*, 2019, **208**, 328.

54 Ş. Yılmaz, A. Zengin and T. Şahan, *Environ. Technol. Innov.*, 2021, **24**, 101799.

55 T. Hashem, A. H. Ibrahim, C. Wöll and M. H. Alkordi, *ACS Appl. Nano Mater.*, 2019, **2**, 5804.

56 I. Mirkovic, L. Lei, D. Ljubic and S. Zhu, *ACS Omega*, 2019, **4**, 169.

57 M. K. Kim, S. H. Kim, M. Park, S. G. Ryu and H. Jung, *RSC Adv.*, 2018, **8**, 41633.

58 C. Lei, J. Gao, W. Ren, Y. Xie, S. Y. H. Abdalkarim, S. Wang, Q. Ni and J. Yao, *Carbohydr. Polym.*, 2019, **205**, 35.

59 C. P. Li, J. Y. Ai, H. Zhou, Q. Chen, Y. Yang, H. He and M. Du, *Chem. Commun.*, 2019, **55**, 1841.

60 M. J. Katz, Z. J. Brown, Y. J. Colón, P. W. Siu, K. A. Scheidt, R. Q. Snurr, J. T. Hupp and O. K. Farha, *Chem. Commun.*, 2013, **49**, 9449.

61 H. Hintz and S. Wuttke, *Chem. Mater.*, 2014, **26**, 6722.

62 X. Zhang, Y. Zhang, T. Wang, Z. Fan and G. Zhang, *RSC Adv.*, 2019, **9**, 24802.

63 R. B. Penland, S. Mizushima, C. Curran and J. V Quagliano, *J. Am. Chem. Soc.*, 1957, **79**, 1575.

64 C. Li, Y. Zhang, M. Yong, W. Liu and J. Wang, *RSC Adv.*, 2019, **9**, 10702.

65 M. Thommes, K. Kaneko, A. V Neimark, J. P. Olivier, F. Rodriguez-Reinoso, J. Rouquerol and K. S. W. Sing, *Pure Appl. Chem.*, 2015, **87**, 1051.

66 B. Li, Q. Sun, Y. Zhang, C. W. Abney, B. Aguila, W. Lin and S. Ma, *ACS Appl. Mater. Interfaces*, 2017, **9**, 12511.

67 I. Pakamorė, J. Rousseau, C. Rousseau, E. Monflier and P. Á. Szilágyi, *Green Chem*, 2018, **20**, 5292.

68 G. Liu, H. Zhou, H. Wu, R. Chen and S. Guo, *J. Biomater. Sci. Polym. Ed.*, 2016, **27**, 1808.

Chapter 3 Crystal-Engineering of Urea-based Coordination Polymers, Metal-Organic Frameworks and Layered Metal-Organic Frameworks

3.1 Introduction

The ability to predict how molecules will interact in the solid state through intermolecular interactions is of significant importance in many different research fields. This is most visible in pharmaceuticals, where appreciating the interactions in co-crystals gives us a better understanding into pharmacological activities of drugs,[1–3] semiconductor production for improved electronics[4] and heterogeneous catalysis in petrochemical industries.[5] This interplay between chemistry and crystallography has grown and developed over 50 years into what we now refer to as crystal engineering.

"The understanding of intermolecular interactions in the context of crystal packing and the utilisation of such understanding in the design of new solids with desired physical and chemical properties".[6]

The formation of a crystalline solid arises from the long-range order of constituent molecules of the said material.* The driving force for this crystal packing is the formation of intermolecular interactions including, hydrogen bonds,[7] halogen bonds,[8] and π-π interactions.[9] An understanding of these interactions combined with structure solution, most commonly through single crystal X-ray diffraction (SCXRD), allows one to rationalise the physical properties of a material and furthermore makes the prediction of future crystal designs possible.

It is highly recognised that predicting the crystal packing of materials is no mean feat. Simply analysing a molecule's different functional groups is not sufficient. For example, 4-aminophenol and 3-aminophenyl only differ by substituent positions on the phenyl ring, but this completely changes the observed interactions in the crystal packing (figure 3.1).[10,11] The N-H···π interactions are able to sufficiently override the expected N-H···O hydrogen bonds present in 3-aminophenyl,

* It is important to recognise that while the term 'crystal' classically refers to an extended periodic array it now also encompasses materials with varying degrees of order.[57] Amorphous solids are receiving ever growing attention in the fields of catalysis[58] and optics,[59] where elucidation of local structure is beneficial. Despite this, all the work that we have carried out in this chapter concerns crystals of long-term order that, where appropriate, can be characterised through SCXRD.

resulting in a very different packing to the para structural isomer. This however, is a relatively simple example when compared to the phenomena of polymorphism in which the same chemical compound can exhibit several, and in some cases hundreds, of different crystal packings.[12]

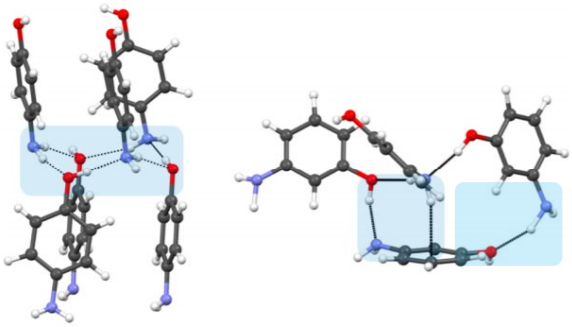

Figure 3.1. Crystal packing in aminophenyls. (Left) N-H···O and O-H···N hydrogen bonds in 4-aminophenyl. (Right) N-H···O, O-H···N and N-H···π hydrogen bonds in 3-aminophenyl.[6] Copyright 2013 American Chemical Society.

Crystal engineering to some extent is applied to the design and synthesis of MOFs whenever we combine metal nodes and organic linkers with defined geometries together. We are able to make good predictions of the structure's shape, topology, and overall charge. A great example of this is the IRMOF series, previously discussed in chapter one. The combination of linear organic linkers and metal centres that readily form octahedral nodes can be predicted, and ultimately do, form a cubic structure that follows the **pcu** topology.[13] The same cannot be said however when we start to investigate mixed-linker systems or when flexible organic linkers are utilised as these characteristics complicate the resulting structures. This is evident in some of our own work that is presented within this chapter. We also have to consider solvent molecules, as occasionally it is possible for DMF or water molecules to coordinate to SBUs and therefore affect the topology of the material. This is evident in materials such as HKUST-1 which has capping water molecules on the axial positions of the metal paddlewheel.[14] Guest molecules need to also be considered, often the incorporation of different ions will result in changes to the overall structure of a charged framework. Recent work by Ghosh *et al.* showed the effect of different anions on a cadmium-based MOF which utilised the neutral organic linker tris(4-(1H-imidazol-1-yl)phenyl)amine.[15] They found that MOF topologies greatly differed when the counter anion was changed from non-coordinating perchlorate to highly coordinating sulphates and acetates. These materials were then probed for their ability to undergo anion exchange in the presence of MnO_4^- and ReO_4^- to simulate pertechnetate remediation.

The influence of incorporated anions into cationic framework structures is well explored. The Hofmeister series, presented in figure 3.2, is an order of anions based upon their ability to influence the physical behaviour of macromolecules, in particular proteins.[16] It is fairly common for MOFs to

follow the Hofmeister series for anion selectivity, although the series is only referred to as a guide as anti-Hofmeister[17] and non-Hofmeister selectivities are also known. The series is split into two categories, either side of the chloride anion. Kosmotropes are defined as 'water structure makers' due to the high degree of hydration they undergo. They are known for stabilising and salting out proteins. Chaotropes however, are defined as 'water structure breakers' and do the reverse processes to that of kosmotropes.

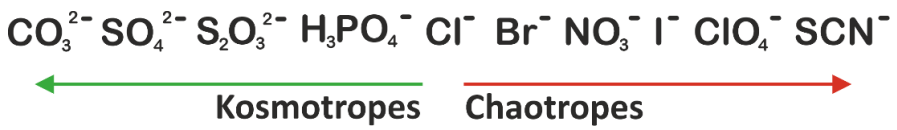

Figure 3.2. Anion order of the Hofmeister series.

Custelcean and Moyer published a well-recognised review article in 2007 discussing anion separation with MOFs in which they discuss the importance of the Hofmeister series and strategies to tailor materials to either follow the series or adopt non/anti-Hofmeister selectivities.[18] Highly solvated anions such as sulphates are typically more difficult to crystallise within MOFs due to their high degree of solvation thus the energy compensation of MOF formation must be great enough to account for desolvation. The inclusion of binding groups, primarily hydrogen bond donor moieties, are essential in pushing against the Hofmeister bias.

3.1.1 Urea-Based Metal-Organic Framework Crystal Engineering

A well-recognised building block in crystal engineering is the urea functionality. Its ability to undergo N,N'-disubstitution with ease has resulted in the formation of an extended catalogue of symmetric and asymmetric organic molecules that have been utilised in the design of many crystalline organic solids.[19] N,N'-disubstituted ureas readily self-associate as a result of the hydrogen bond donor and hydrogen bond acceptor components of the urea functionality. This complementarity can result in persistent bifurcated hydrogen bond chains, often referred to as alpha networks or urea ladders, formed between the two N-H protons and the lone pairs of the oxygen atom of an adjacent C=O moiety (see Figure 3.3). These interactions are very robust and thus not limited to just the solid state,[20] but are also present in solution[21] as well as gels and fibers.[22] Etter *et al.* showed in 1988 that electron withdrawing groups positioned on the meta carbons of bis-phenylureas resulted in the breaking of self-associating hydrogen bonds and the formation of N-H···guest molecule interactions.[23] Trifluoromethyl and nitro groups on all three positions of the phenyl rings were trialled but only the meta structural isomers formed cocrystals with acetone, THF and DMSO solvent molecules. It was suggested that in the meta species weakly acidic ortho C-H protons lie close to the carbonyl oxygen of the urea functionality forming a weak C-H···O interaction that reduces the urea's ability to undergo self-association. This theory was further proved by

Custelcean *et al.* in 2006 through computational and experimental investigations into urea-based MOFs.[24]

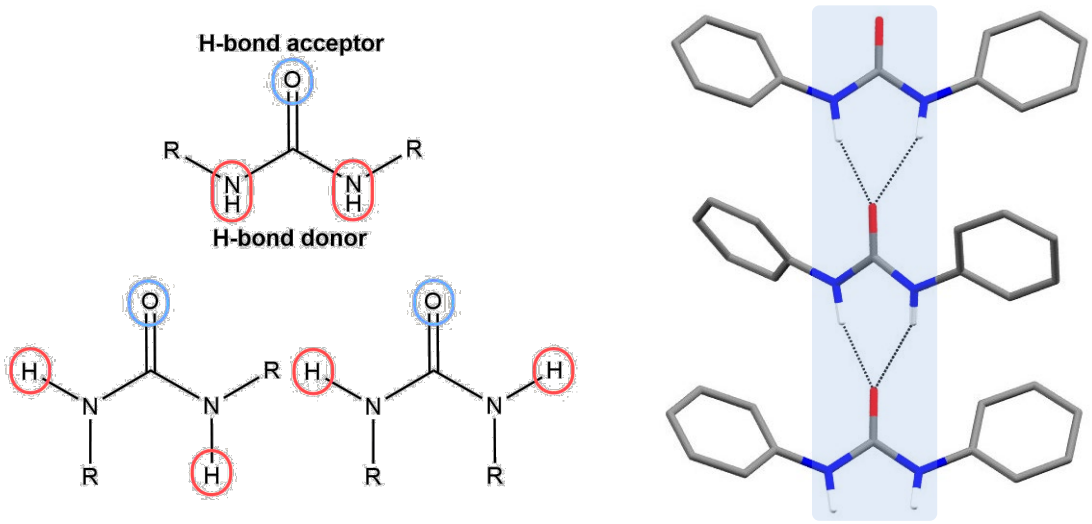

Figure 3.3. (Left) chemical structure of urea and its differing configurations. (Right) alpha networks found within 4,4'-diphenylurea.[20]

N,N'-disubstituted ureas have been extensively used in the formation of various MOFs by including functionalities such as carboxylates, pyridines, and nitriles on each end of the urea to coordinate to different metal centres. Examples of the N,N'-disubstituted urea linkers reported in literature are shown in figure 3.4. Organic linkers 2-, 3-, and 4-MeUR-N (MeUR-N = N,N'-bis(pyridylmethyl)urea) were first used as building blocks in coordination polymers by Lauher *et al.* in 1997.[25] A sub-structure search of the Crystal Structure Database (CSD) of 2-MeUR-N, 3-MeUR-N, and 4-MeUR-N organic linkers revealed 30, 57, and 27 crystal structure results, respectively. Of the 114 structures found only 20 are polymeric materials. The organic linker 4-UR-N (UR-N = 1,3-di(pyridyl)urea) as well as the ortho and meta structural isomers were derived by Parthasarathi *et. al.* from Lauher's molecules in the early 2000s.[26]

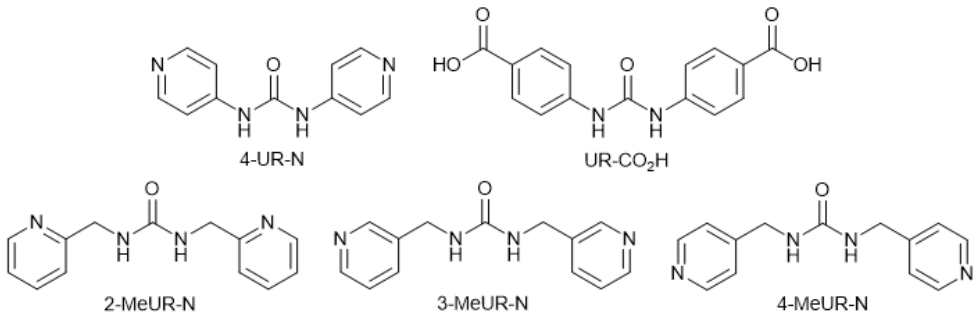

Figure 3.4. Selection of urea-based organic linkers utilised for MOF and coordination polymer synthesis.

It has long been recognised that the hydrogen bonding nature of ureas make them ideal binding sites for anions, such as TcO_4^-, in the solid state. Doing so however necessitates the disruption of the hydrogen bond chains of the ureas that are regularly observed in solids. Competition between self-association, solvent molecules, and the anion is often seen and therefore can lead to inconsistences in anion binding within frameworks. This was demonstrated with work by Plater *et al.* in which the copper-based coordination networks $[Cu(3\text{-MeUR-N})(NO_3)_2]\cdot 2H_2O\cdot 2EtOH$ and $[Cu(4\text{-MeUR-N})(H_2O)(NO_3)]\cdot H_2O\cdot NO_3$ were formed using 3-MeUR-N and 4-MeUR-N respectively.[27] The 3-MeUR-N linker results in the self-association of the urea groups and coordination of both nitrate anions to the copper (II) centre. By using the para structural isomer however, the urea group is free to hydrogen bond to nitrate anions found within the materials voids. Interestingly, in the latter structure there is a preference for the anion to undergo hydrogen-bonding to the urea rather than coordinating to the copper centre as seen for the other nitrate anion. Further reports of structural isomerism of organic linkers affecting the structure of coordination polymers has been reported by Dastidar *et al*.[28] Reacting zinc perchlorate with either 3-MeUR-N or 4-MeUR-N resulted in either a two-dimensional square network or a five-fold interpenetrated diamondoid network respectively. The former material underwent a rare anion-induced temperature-dependent phase transition when cooled to 100 K.

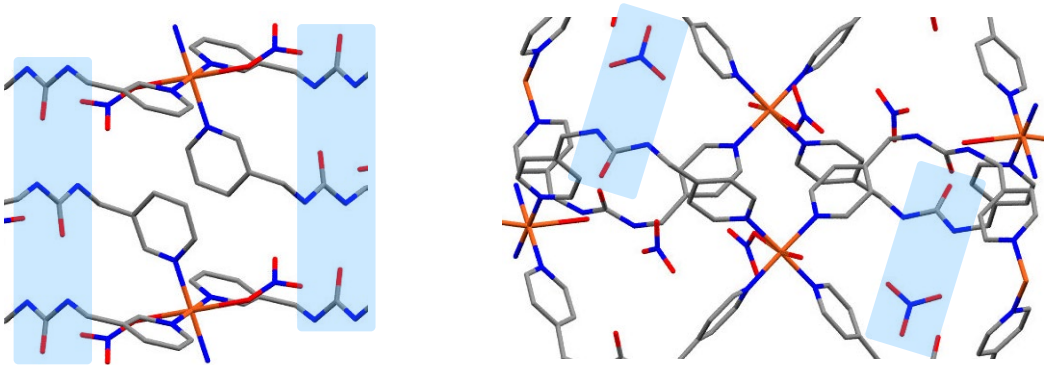

Figure 3.5. (Left) Self-association of ureas in $[Cu(3\text{-MeUR-N})(NO_3)_2]\cdot 2H_2O\cdot 2EtOH$. (Right) Nitrate binding in $[Cu(4\text{-MeUR-N})(H_2O)(NO_3)]\cdot H_2O\cdot NO_3$.[27]

It has long been understood that counter-anion choice plays an integral role in the overall architecture of cationic coordination polymers, with largely the focus of research being on MOFs. N,N'-bis(3-pyridyl)urea (3-UR-N) (the meta structural isomer of 4-UR-N) was utilised in six copper-based MOFs in which various anions including perchlorate, nitrate, sulphate, and hexafluorosilicates were incorporated into the frameworks through different copper salts.[29] Observed structures ranged from typical zig-zag coordination polymers to looped chain topologies as a direct result of altering the counter anion. The thiourea analogue (N,N'-bis(3-pyridylmethyl)thiourea) of 3-MeUR-N was incorporated into a series of materials where the anion choice resulted in either discrete macrocycles, polymeric helicases and looped chains.[30]

The degree of interpenetration of MOFs can, in limited cases, be controlled by simply altering the metal precursor salt which incorporates a different anion into the structure. Cheng *et al.* presented an example of this in 2013 with their mixed metal 4,4'-dicarboxylate-2,2'-dipyridine based frameworks in which coordinating chloride anions formed a 2-fold interpenetrated structure with **pcu** topology however non-coordinating anions resulted in a non-interpenetrated MOF while preserving the same topology.[31]

3.1.2 Selective Crystallisation of Anions

The vast majority of cationic structures for anion remediation make use of an anion exchange mechanism. There have therefore been limited reports into the alternative strategy of anion separation through selectively crystallising the target anion within extended structures such as MOFs during the synthesis of the immobilising material. A clear advantage to this latter method is that it avoids the slow solid-state ion-exchange kinetics that is sometimes observed in traditional anion exchange mechanisms.[32]

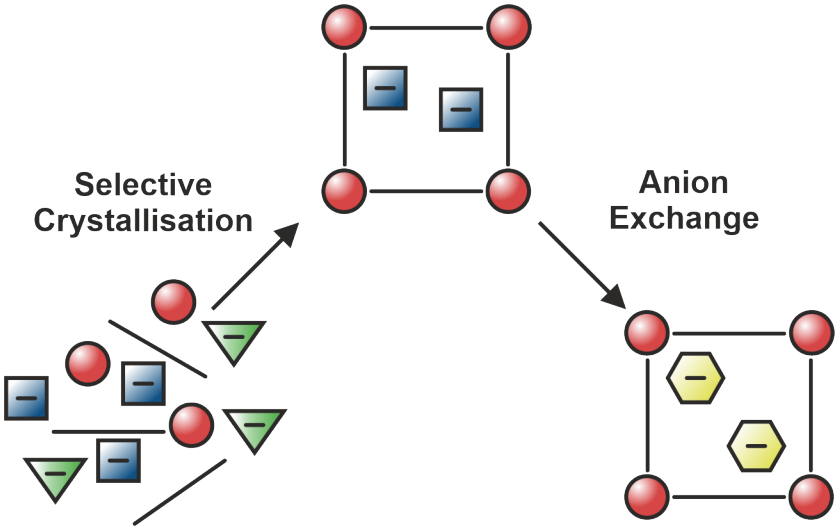

Figure 3.6. Two of the available anion immobilisation techniques available with crystalline materials.

Selective crystallisation of anions in MOFs was first reported by Custelcean *et al.* in 2006 when they demonstrated that one-dimensional zinc coordination polymers containing 3-UR-N organic linkers could exploit the coordinating nature of halide anions resulting in selective crystallisation of chloride and bromide anions while excluding sulphate and perchlorate competing oxo-anions in solution.[17] An ethanolic solution of 3-UR-N was layered over an aqueous solution of $Zn(NO_3)_2{\cdot}4H_2O$ and equimolar quantities of sodium salts of chloride, iodide, bromide, sulphate and perchlorate. This resulted in the crystallisation of material in as little as 30 minutes. Single-crystal studies revealed that all halide containing extended structures were one-dimensional chains. Competition

experiments predominantly formed the $[Zn(3\text{-UR-N})][Cl]_2$ structure (figure 3.7) however, this is a metastable phase. The more thermodynamic phase is in fact $[Zn(3\text{-UR-N})][Br]_2$ and the chloride phase undergoes eventual conversion to the bromide analogue.

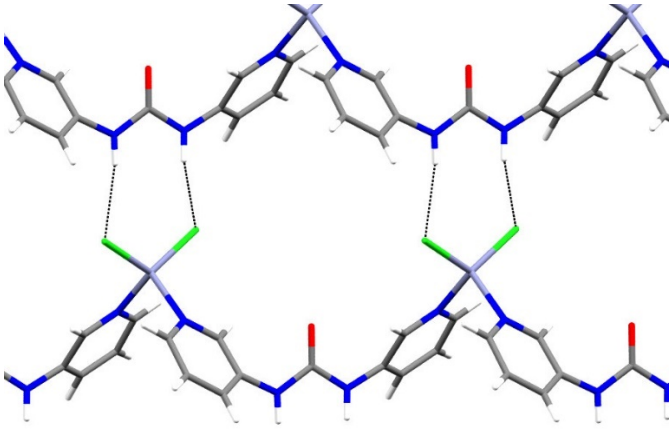

Figure 3.7. Halide coordination to the zinc centres and resulting N-H···Cl hydrogen bonding within $[Zn(3\text{-UR-N})][Cl]_2$.[17]

Work to selectively crystallise sulphate anions out of solution has been carried out with cadmium-based coordination polymers[32] and cages.[33,34] The former coordination polymer work investigated five urea-based organic linkers, including 3- and 4-UR-N as well as asymmetric N,N'-disubstituted ureas. Coordination polymers containing each organic linker were synthesised independently from $CdSO_4$ and their structures solved *via* SCXRD. This revealed the anion interactions with the urea functionalities of the framework. To test the selectivity of each material, solutions of each organic linker were added to cadmium salt solutions that contained sulphate, nitrate, acetate, perchlorate, chloride and bromide counter ions. In all cases except one the resulting precipitates yielded coordination polymers containing a mixture of anions. In the case of the organic linker N-(4-picolyl)-N'-(3-pyridyl)urea (figure 3.8) block crystals were obtained after two weeks. FTIR and PXRD confirmed that only the sulphate anion was present in the material.

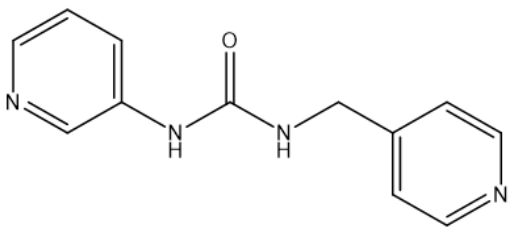

Figure 3.8. Chemical structure of N-(4-picolyl)-N´-(3-pyridyl)urea.

Tzeng *et al.* took a crystal engineering approach to a series of coordination polymers and molecular-looped complexes based off two organic linkers: 1,3-bis-pyridin-4-ylmethyl urea (4-MeUR-N) and N,N'-bis-4-methylpyridyl oxalamide (L2).[35] The majority of the synthesised

materials were dense structures, with one-dimensional (1D) chain/ladder topologies and beneficial hydrogen bond interactions between chains to afford two-dimensional (2D) hydrogen bonded frameworks. Manipulation of the coordination polymers through anion choice was possible in Cd(L2) systems. Coordinating acetate anions would result in a 1D system while non-coordinating nitrate anions allowed for the formation of 2D sheets. This is consequential of the additional metal coordination sites available when non-coordinating anions are chosen. Discrete molecular-loops can be afforded in mixed-organic palladium systems. Two square planar Pd(II) centres form a loop using two L2 ligands with the remaining Pd coordination sites occupied by 2-phenylpyridine (PPy) ligands (figure 3.9). The loop had a boat structure and a hydrogen-bond rich cavity for the occupation of a perchlorate anion.

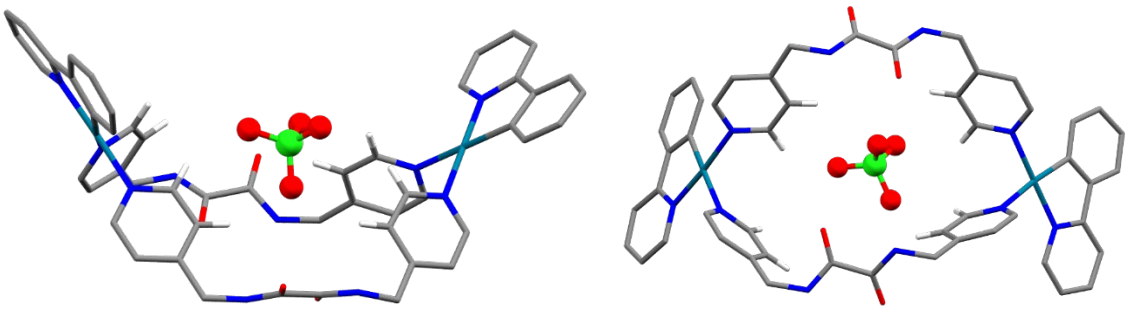

Figure 3.9. The boat structure of $[Pd(PPy)(L2)]_2(ClO_4)_2$ showing the cavity present for perchlorate entrapment.

Banerjee *et al.* have studied the effect solvent plays on the resulting zinc structures of 4-MeUR-N, 3-MeUR-N, and N,N'-bis(3-pyridyl)urea (3-UR-N).[36] The resulting solvatomorphs were found to contain guest solvent molecules when aromatic solvents were used as opposed to guest devoid structures when polar solvents were used. All resulting structures were found to be extremely unstable outside of their mother liquors, suggesting fast desolvation.

3.2 Chapter Outlook

In 1998 Lauher *et al.* explored the combination of coordination polymer and hydrogen bond interactions through their study of reacting silver salts with urea-based organic linkers.[37] They used silver tetrafluoroborate and silver nitrate as metal precursors and the organic linkers 2-, 3-, and 4-MeUR-N (figure 3.4). Crystal structures of the resulting coordination polymers are shown in figure 3.10.

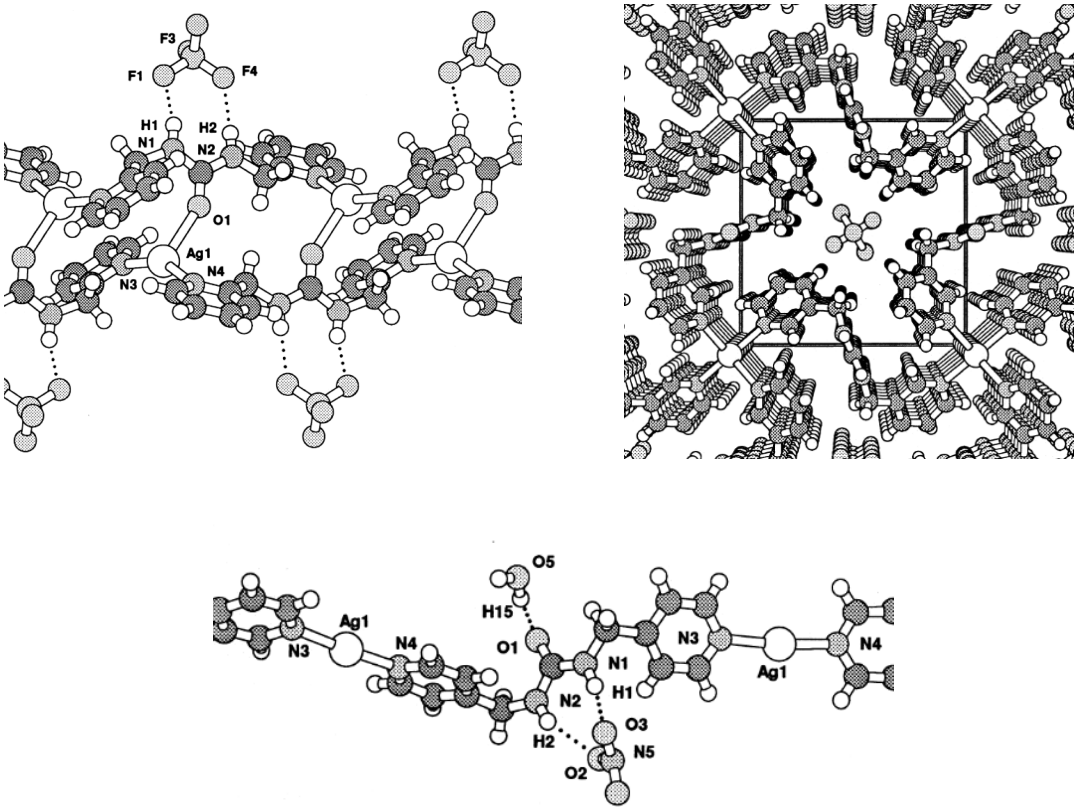

Figure 3.10. (Clockwise from top left) Crystal structures of [Ag(2-MeUR-N)][BF_4], [Ag(3-MeUR-N)][BF_4], and [Ag(4-MeUR-N)][NO_3].[37] Reproduced with permission from Elsevier.

[Ag(2-MeUR-N)][BF_4] formed a ladder structure consisting of linear [Ag(2-MeUR-N)]$^+$ chains and coordination of the silver centres to urea oxygen's of adjacent chains affording a T-shaped silver geometry. The tetrafluoroborate anion hydrogen bonds to available N-H protons of the urea groups in a bridging fashion. Flattened tetrahedral silver centres of [Ag(3-MeUR-N)][BF_4] afford a square sheet coordination polymer with the formation of alpha networks from the association of urea moieties from different sheets. Tetrafluoroborate anions sit in channels at the centre of the square voids and do not undergo hydrogen bonding with the coordination polymer. [Ag(4-MeUR-N)][NO_3] forms a similar one-dimensional chain to that observed with the 2-MeUR-N linker. The nitrate anion hydrogen bonds to the N-H protons of the urea and a water molecule undergoes hydrogen bonding to the carbonyl oxygen.

These coordination polymers are of very strong interest regarding our work for selective pertechnetate remediation. They combine a silver centre that has been proven to be a key component of good TcO_4^- adsorbents[38–41] as well as the urea functionality which we wish to explore crystallographically for its ability to hydrogen bond to perrhenate anions. In this chapter, we take these existing systems and explore their diversity by incorporating various anions into the structures. Through (SCXRD) we will assess how the roles anion and organic linker structural isomerism both play on topology and coordination polymer-anion interactions. The chosen target

counter anions are based off the common composition of Sellafield groundwater which consists of nitrates, sulphates, carbonates, chlorides and perrhenate, as a surrogate for pertechnetate. We have also extended these systems into the incorporation of two common, noncoordinating anions, tetrafluoroborate and hexafluorophosphate. Studying BF_4^- alongside ReO_4^- and SO_4^{2-} will help us rationalise the interactions of tetrahedral anions with the coordination polymer. PF_6^- is a larger anion and readily crystallises in cationic systems, hence it would be interesting to assess the flexibility of the coordination polymer systems with such an anion. An understanding into how anions interact with the coordination polymers as well as what crystal rearrangements are likely to occur as a result of anion exchange is vastly important when assessing suitable materials for pertechnetate remediation.

We hope to be able to identify a suitable system for the selective crystallisation of ReO_4^- from solution as well as viable anion exchange materials for ReO_4^- remediation.

Inspired by the existing studies into urea-based coordination polymers we are interested in assessing the effect of incorporating MeUR-N into mixed-linker, zinc systems. We have chosen MeUR-N because of the soft pyridine nitrogen available for coordination to a metal centre, the introduced flexibility because of the methyl group located between the aromatic ring and urea moiety as well that this would be the first occasion that MeUR-N is used in a mixed-linker system. In addition, the symmetric isomers of MeUR-N are easily accessed through facile, cheap, and high yielding syntheses. We have opted to focus on zinc in this area of the chapter because the metal is cheap to purchase as a hydrated salt and often produces single-crystal quality products. Here we are continuing efforts to focus on sustainable, and where possible, green chemistry.

3.3 Results and Discussion of Crystal Engineering of Silver-Based Coordination Polymers

3.3.1 Synthesis and Characterisation of Urea-Based Organic Linkers

Typical organic linkers such as 2-methylimidazole (2MIM), terephthalic acid (H_2BDC) and trimesic acid (H_3BTC) can be readily bought in bulk, cheaply, from companies such as Sigma Aldrich and Alfa. More novel and less regularly used linkers however must be synthesised in house. The urea-based organic linkers utilised in this chapter have been synthesised through reliable methods reported in the literature, with only minor modifications.

Organic linkers N,N'-bis(2-pyridylmethyl)urea (2-MeUR-N), N,N'-bis(3-pyridylmethyl)urea (3-MeUR-N) and N,N'-bis(4-pyridylmethyl)urea (4-MeUR-N) were synthesised *via* modified

procedures described by Lauher *et al*.[37] Briefly, diphenyl carbonate was combined with the corresponding aminomethyl pyridine (2-,3- or 4-aminomethyl pyridine) in a test tube and heated with stirring, for two hours at 150 °C and under an argon atmosphere. The mixture was then cooled and the product was crystallised upon addition of ethyl acetate.

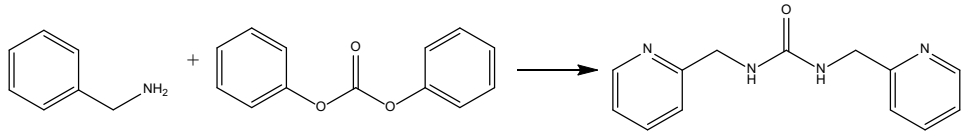

Scheme 3.1. Reaction scheme for the synthesis of N,N'-bis(2-pyridylmethyl)urea (2-MeUR-N).

4,4'-(carbonylbis(azanediyl))dibenzoic acid (UR-CO_2H) was synthesised *via* a modified procedure described by Morsali *et al.*[42] Briefly, ethyl-4-aminobenzoate and 1,1'-carbonyldiimidazole were dissolved in anhydrous THF and heated under reflux and an argon atmosphere for eight hours. The resulting material was washed with HCl and brine before being refluxed in base for five hours. The resulting white precipitate was collected by filtration, washed with ethanol, and dried at 80 °C overnight to give UR-CO_2H in good yield.

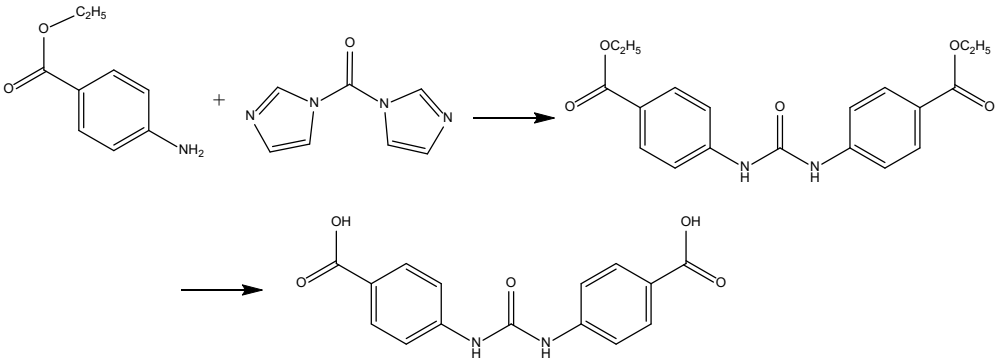

Scheme 3.2. Reaction scheme for the synthesis of 4,4'-(carbonylbis(azanediyl))dibenzoic (UR-CO_2H).

All linker molecules were characterised by ^1H NMR spectroscopy, FTIR and mass spectrometry. The results of which can be found in appendix (sections A.3.1 – A.3.3). No further purification of the compounds was required prior to use in further material synthesis.

3.3.2 Synthesis and Characterisation of Silver N,N'-bis(2-pyridylmethyl)urea Coordination Polymers

Silver N,N'-bis(2-pyridylmethyl)urea tetrafluoroborate (**2-BF_4**), silver N,N'-bis(2-pyridylmethyl)urea hexafluorophosphate (**2-PF_6**) and silver N,N'-bis(2-pyridylmethyl)urea sulphate (**2-SO_4**) were synthesised by dissolving 0.07 mmol of the appropriate sodium or potassium salt (sodium tetrafluoroborate, potassium hexafluorophosphate or disodium sulphate) into 2mL of a 0.03 M

aqueous solution of silver nitrate. This solution was then combined with a 2 mL ethanolic solution of 2-MeUR-N (0.03 M) in a vial. The vial was capped, shaken, and left in the dark for five days at room temperature with no further agitation to allow for crystals to form. To synthesise adequate crystals of silver N,N'-bis(2-pyridylmethyl)urea perrhenate (**2-ReO_4**) an alternative procedure was carried out. Silver perrhenate (0.08 mmol) was dissolved in 2.5 mL of deionised water and added to an empty test tube. 2.5 mL of deionised water was carefully layered on top, followed by an ethanolic layer of 2-MeUR-N (0.04 mmol). The reaction was left undisturbed in the dark for five days. After five days, clear and colourless crystals of all four materials had formed in all four vials.

Attempts to synthesise coordination polymers which contained nitrate or chloride counter anions proved unsuccessful. The latter anion yielded a precipitate of AgCl, confirmed through PXRD (figure A.28), while there was no crystallisation of any material for the nitrate anion.

2-BF_4, 2-PF_6 and 2-ReO_4 structures were solved using SHELXT structure solution program *via* the intrinsic phasing method in Olex2 while 2-SO_4 was solved using SHELXS structure solution program *via* direct methods. Refinements of all structures used SHELXL with least squares minimisation. Anion disorder was present in 2-PF_6 and 2-SO_4 which was modelled using the split SAME feature. Occupancy of the anions was found to be split 72:28 and 85:15 for PF_6^- in 2-PF_6 and SO_4^{2-} in 2-SO_4 respectively. The split occupancy is shown only in the asymmetric units in figure 3.11 and figure 3.16 otherwise the minor occupancy form has been omitted for clarity. Table 3.1 contains the relevant crystal data and structure refinement information for the 2-MeUR-N silver coordination polymers.

Table 3.1. Crystal data and structure refinement for 2-MeUR-N silver coordination polymers.

Identification code	**2-BF_4**	**2-PF_6**	**2-ReO_4**	**2-SO_4**
Empirical formula	$C_{13}H_{14}AgBF_4N_4O$	$C_{13}H_{14}AgF_6N_4OP$	$C_{13}H_{14}AgN_4O_5Re$	$C_{26}H_{41}Ag_2N_8O_{13}S$
Formula weight	436.96	495.12	600.35	921.47
Temperature/K	100	100	100	100
Crystal system	triclinic	triclinic	triclinic	monoclinic
Space group	P-1 (2)	P-1 (2)	P-1 (2)	$P2_1/c$ (14)
a/Å	8.2041(7)	8.4681(2)	8.2970(3)	9.1682(2)
b/Å	9.2257(7)	9.2547(2)	9.2469(4)	21.3151(5)
c/Å	11.2352(5)	11.6607(3)	11.5727(5)	17.8632(4)
α/°	71.612(5)	71.650(2)	73.026(4)	90
β/°	74.467(5)	76.309(2)	75.170(4)	92.182
γ/°	73.405(7)	72.414(2)	73.544(4)	90
Volume/Å^3	758.44(10)	816.66(4)	799.75(6)	3488.33(14)
Z	2	2	2	4
ρ_{calc}g/cm^3	1.913	2.010	2.493	1.755
μ/mm^{-1}	1.382	1.408	8.818	1.256
F(000)	432.0	488.0	564.0	1868.0
Crystal size/mm^3	0.2 × 0.05 × 0.02	0.1 × 0.06 × 0.04	0.3 × 0.02 × 0.01	0.6 × 0.05 × 0.03
Radiation	Mo Kα (λ = 0.71073)	Mo Kα (λ = 0.71073)	Mo Kα (λ = 0.71073)	Mo Kα (λ = 0.71073)
2Θ range for data collection/°	3.896 to 60.39	3.726 to 60.142	3.748 to 62.148	4.446 to 64.336
Reflections collected	8176	11274	18485	37921
Independent reflections	3667 [R_{int} = 0.0115, R_{sigma} = 0.0122]	3978 [R_{int} = 0.0129, R_{sigma} = 0.0109]	4407 [R_{int} = 0.0759, R_{sigma} = 0.0582]	8671 [R_{int} = 0.0741, R_{sigma} = 0.0479]
Final R indexes [I>=2σ (I)]	R_1 = 0.0180, wR_2 = 0.0632	R_1 = 0.0153, wR_2 = 0.0521	R_1 = 0.0425, wR_2 = 0.1085	R_1 = 0.0728, wR_2 = 0.1733
Final R indexes [all data]	R_1 = 0.0196, wR_2 = 0.0713	R_1 = 0.0158, wR_2 = 0.0523	R_1 = 0.0498, wR_2 = 0.1169	R_1 = 0.0939, wR_2 = 0.1881

The asymmetric units of **2-BF_4**, **2-PF_6** and **2-ReO_4** each contain one silver centre, one 2-MeUR-N linker and one full occupancy anion. The silver centre adopts a T-shaped geometry, coordinating to two independent 2-MeUR-N linkers and the carbonyl oxygen of an adjacent 2-MeUR-N urea group. The silver centre environments differ only slightly between the three systems (table 3.2). Ag-N and Ag-O bond lengths fall within the ranges of 2.167 – 2.181 Å and 2.470 – 2.528 Å respectively. Expected bond angles of a T-shaped geometry are two 90° and one 180° angles. The silver centres of these three structures show distorted T-shape geometries with the bond angles of N1-Ag1-N4, N1-Ag1-O1 and N4-Ag1-O1 falling into the ranges 148.69 – 155.12°, 96.02 – 98.24° and 108.00 – 111.65° respectively. The small bond and angle ranges, in combination with the very similar unit cell parameters presented in table 3.1, suggest a coordination polymer that is readily able to adjust accordingly to a change in non-coordinating counter anion.

Table 3.2. Bond angle and lengths around the silver centres of 2-BF_4, 2-PF_6 and 2-ReO_4.

2-BF_4	**2-PF_6**	**2-ReO_4**
Ag1 – N1 = 2.177(16) Å	Ag1 – N1 = 2.181(12) Å	Ag1 – N1 = 2.173(5) Å
Ag1 – N4 = 2.171(16) Å	Ag1 – N4 = 2.167(13) Å	Ag1 – N4 =2.168(5) Å
Ag1 – O1 = 2.502(15) Å	Ag1 – O1 = 2.470(11) Å	Ag1 – O1 =2.528(4) Å
N1 – Ag1 – N4 = 152.11(6)°	N1 – Ag1 – N4 = 148.69(5)°	N1 – Ag1 – N4 = 155.12(17)°
N1 – Ag1 – O1 = 96.43(5)°	N1 – Ag1 – O1 = 98.24(4)°	N1 – Ag1 – O1 = 96.02(16)°
N4 – Ag1 – O1 = 110.24(5)°	N4 – Ag1 – O1 = 111.65(4)°	N4 – Ag1 – O1 = 108.00(16)°

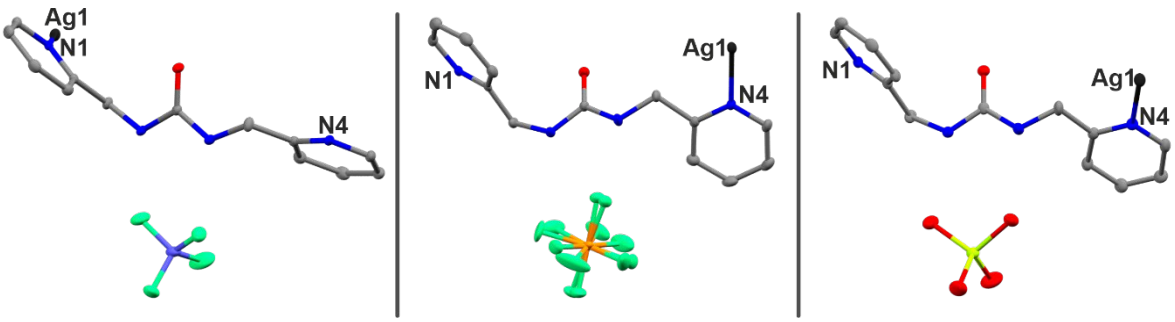

Figure 3.11. (Left to right) Asymmetric units of 2-BF_4, 2-PF_6 and 2-ReO_4. Thermal ellipsoids are set to 40% probability. Hydrogen atoms have been omitted for clarity. Grey = carbon, black = silver, blue = nitrogen, red = oxygen, green = fluorine, purple = boron, orange = phosphorus and lime = rhenium.

All three anions form bridging hydrogen bonds to the two N-H protons in the urea group of 2-MeUR-N, as seen in figure 3.12. Hydrogen bond distances within these systems are presented in table 3.3. The distances vary between 2.024 and 2.330 Å, and both the shortest and longest distances are seen in **2-PF_6**. This low range of distances suggests strong interactions between the

coordination polymer and the counter anions. Along with the dense packing of the coordination polymers, these strong hydrogen bonds elucidate why the anions are well ordered within these systems.

Table 3.3. Hydrogen bond distances between urea N-H protons and anions in [Ag(2-MeUR-N)] coordination polymers.

	2-BF_4	**2-PF_6**	**2-ReO_4**
N-H···X distances (Å) (X = O/F)	2.044	2.024	2.079
	2.115	2.330	2.314

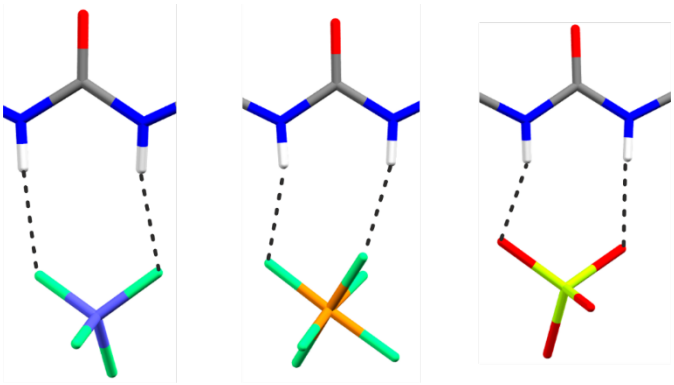

Figure 3.12. Hydrogen bond interactions between urea N-H protons and anions in [Ag(2-MeUR-N)] coordination polymers. (Left to right) 2-BF_4, 2-PF_6 and 2-ReO_4.

Unsurprisingly due to their similar asymmetric units, all three materials have identical crystal packings (figure 3.13). The anions sit in-between the coordination polymer chains undergoing stabilisation through hydrogen bonding to one adjacent chain (figure 3.13), as seen in figure 3.12.

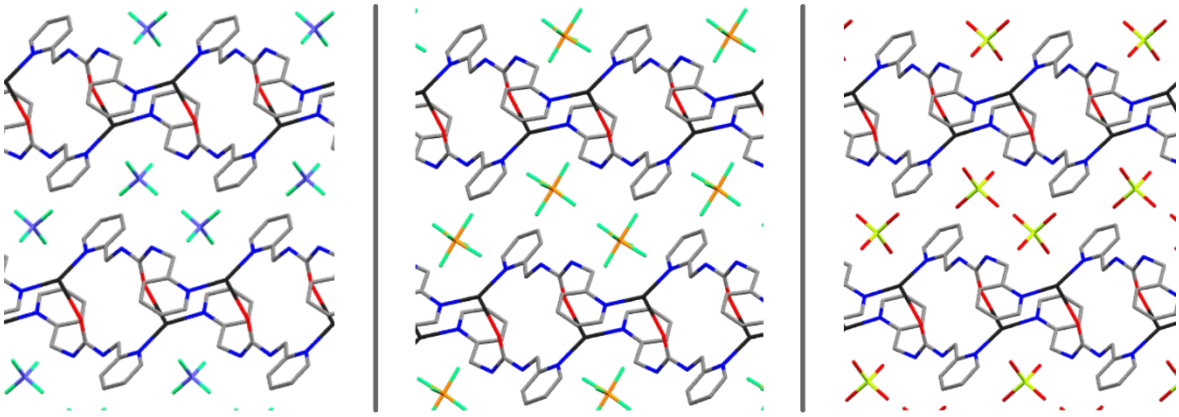

Figure 3.13. Identical crystal packing of 2-BF_4, 2-PF_6 and 2-ReO_4. Hydrogen atoms have been omitted for clarity.

Topological analysis of **2-BF_4**, **2-PF_6** and **2-ReO_4** confirms that all three structures exhibit a uninodal net with the Schläfli symbol $\{4^2.6\}$, signifying a two rung laddered topology (figure 3.14) that arises from the T-shaped geometries of the silver centres and the three coordinate 2-MeUR-N linkers.

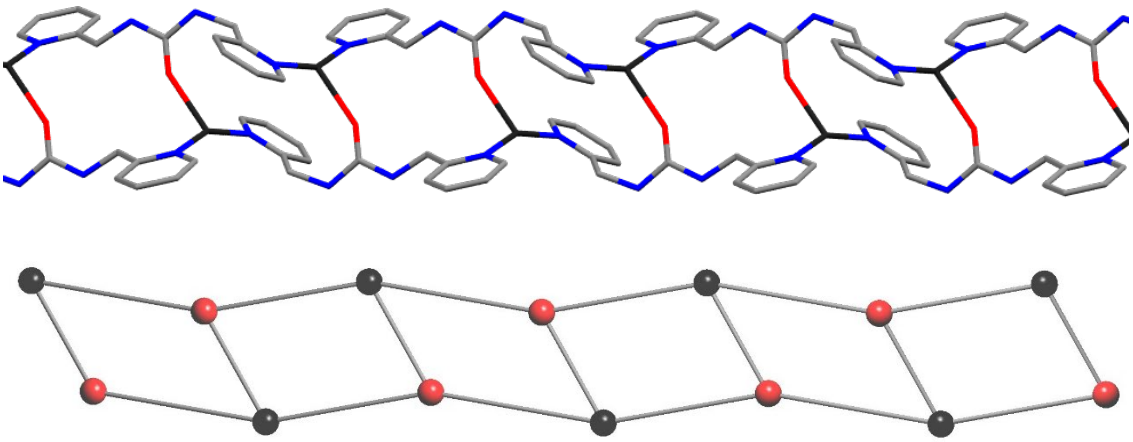

Figure 3.14. (Top) The laddered structure of 2-ReO_4, identical to the coordination polymers 2-BF_4 and 2-PF_6. Hydrogen atoms have been omitted for clarity. (Bottom) The simplified node structure of 2-ReO_4 showing the two-rung laddered topology (red nodes = silver centres and black nodes = 2-MeUR-N).

PXRD comparison between the bulk crystals and the simulated patterns derived from the crystal structure is important to confirm that the structure we have solved is representative of the synthesised sample. Figure 3.15 shows the PXRD pattern comparison between **2-BF_4** and the simulated pattern. There is a good peak overlap between the two patterns suggesting the crystal structure does represent our bulk sample. A variance in peak intensity suggests either preferred orientation is present in the experimental pattern or solvent has had an effect here. PXRD confirmed that the crystal structure of **2-PF_6** is representative of the material formed from $AgPF_6$.

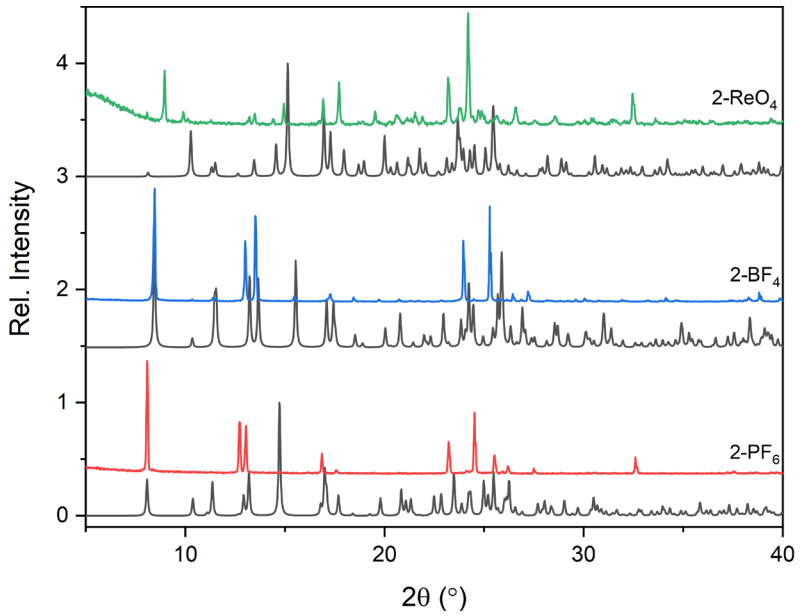

Figure 3.15. Experimentally obtained PXRD patterns of [Ag(2-MeUR-N)] coordination polymers compared to their computationally derived patterns. Black = CIF file, colour = synthesised material.

Altering the counter anion of the [Ag(2-MeUR-N)] coordination polymer to one which has a larger charge density, such as sulphate, has a dramatic effect on the resulting material. Figure 3.16 shows the asymmetric unit of **2-SO$_4$** which comprises of two silver centres, two 2-MeUR-N linkers, one disordered sulphate anion and seven water molecules. Both silver centres adopt a near linear coordinate geometry coordinating to two pyridine nitrogen atoms from independent linkers in the axial positions.

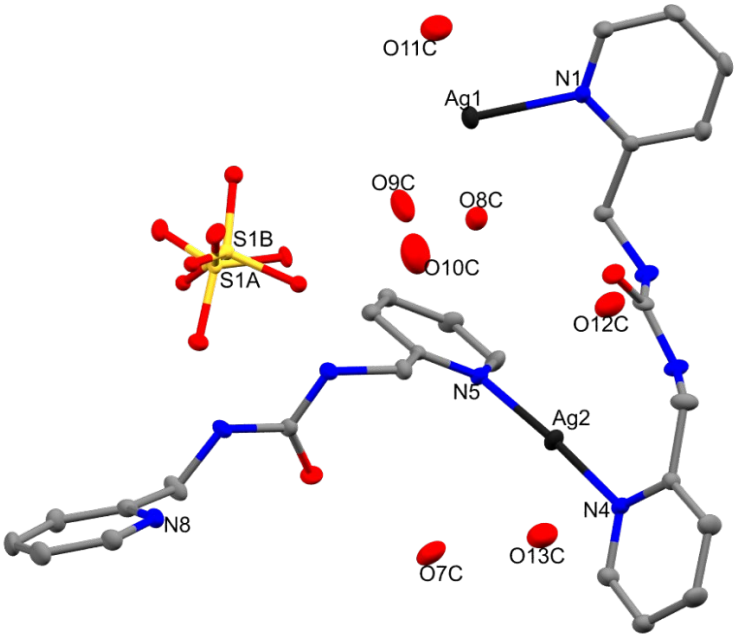

Figure 3.16. Asymmetric unit of 2-SO$_4$ containing the disordered sulphate anion. S1A denotes the major occupancy sulphate anion, and S1B, the minor form. Thermal ellipsoids are set to 40% probability. Hydrogen atoms have been omitted for clarity.

The sulphate anion in **2-SO$_4$** sits within a cavity between two independent silver 3-MeUR-N chains and undergoes a bridging, bidentate hydrogen bond interaction between its oxygen atoms and the N-H hydrogens of the urea groups (figure 3.17). This occurs to both oxygen pairs (O3A-O4A and O5A-O6A) resulting in four hydrogen bond interactions with lengths ranging from 1.998 to 2.162 Å. Each oxygen atom of the sulphate receives an additional hydrogen bond from ordered water molecules (1.854-1.949 Å) thus the total number of stabilising hydrogen bonds is eight.

Table 3.4. Hydrogen bond lengths within 2-SO$_4$.

Water as hydrogen bond donor (O-H···O)		**Urea as hydrogen bond donor (N-H···O)**	
Bond	**Distance (Å)**	**Bond**	**Distance (Å)**
O11C – O3A	1.854	N3 – O5A	1.988
O12C – O6A	1.869	N6 – O4A	2.002
O10C – O5A	1.913	N7 – O3A	2.034
O9C – O4A	1.949	N2 – O6A	2.162

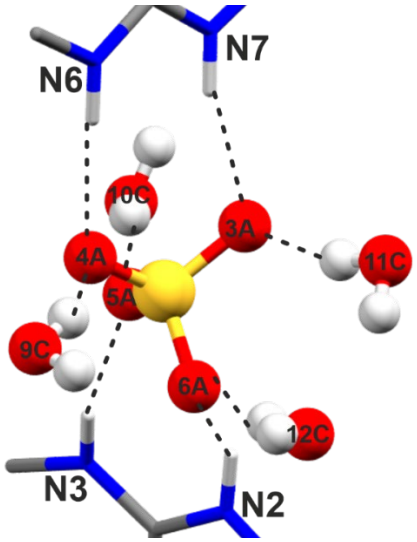

Figure 3.17. Hydrogen bond rich environment of the sulphate anion (S1A) in 2-SO_4. The sulphate anion undergoes hydrogen bonding to four water molecules and two urea moieties from 2-MeUR-N linkers.

The one-dimensional chains of **2-SO_4** (figure 3.18) undergo a concertina packing due to the ortho position of the nitrogen in relation to the methyl urea group on the pyridine rings in 2-MeUR-N, resulting in densely packed chains. Sulphate anions are packed in-between chains within the cavities described above (figure 3.17), undergoing substantial hydrogen bonding with both chains.

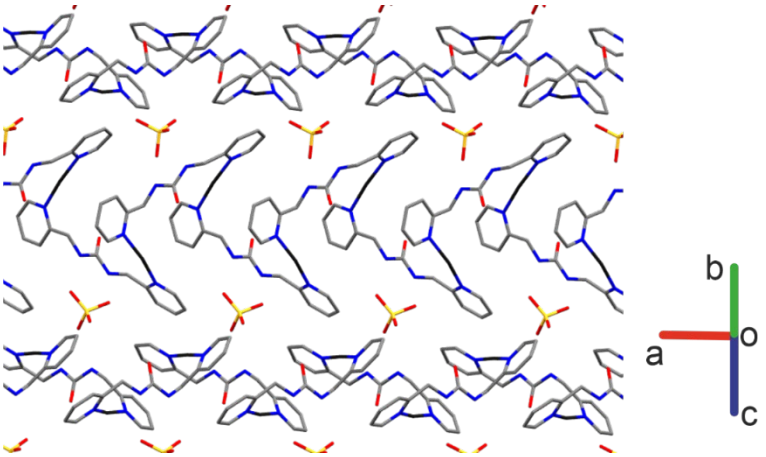

Figure 3.18. One-dimensional chains in 2-SO_4 that extend along the a axis. Hydrogen atoms and water molecules have been omitted for clarity.

3.3.3 Synthesis and Characterisation of Silver N,N'-bis(3-pyridylmethyl)urea Coordination Polymers

Three silver N,N'-bis(3-pyridylmethyl)urea (3-MeUR-N) coordination polymers have been synthesised. One of which, silver N,N'-bis(3-pyridylmethyl)urea tetrafluoroborate (**3-BF_4**), has been previously reported but no CIF file exists of its structure. The synthesis of **3-BF_4** followed the

procedure described by Lauher *et al.* and involved layering an ethanolic layer of 3-MeUR-N on top of an aqueous layer of $AgBF_4$ within a test tube. Needle crystals of **3-BF_4** formed at the layer interface over 24 hours. Silver N,N'-bis(3-pyridylmethyl)urea perrhenate (**3-ReO_4**) was formed by dissolving equimolar quantities of silver nitrate and sodium perrhenate in deionised water, followed by combining with an ethanolic solution of 3-MeUR-N. Crystals of **3-ReO_4** formed at the base of the vial. Finally, Silver N,N'-bis(3-pyridylmethyl)urea sulphate (**3-SO_4**) was synthesised by combining an aqueous solution of silver nitrate and sodium sulphate with an ethanolic solution of 3-MeUR-N. The resulting solution was left for five days undisturbed, resulting in the formation of clear, colourless, needle crystals of **3-SO_4**. Suitable crystals of each system were chosen for SCXRD characterisation. The resulting crystal data and structure refinement details are presented in table 3.5.

Table 3.5. Crystal data and structure refinement for silver 3-MeUR-N coordination polymers.

Identification code	**3-BF_4**	**3-ReO_4**	**3-SO_4**
Empirical formula	$C_{26}H_{28}AgBF_4N_8O_2$	$C_{26}H_{28}AgN_8O_6Re$	$C_{26}H_{32}Ag_2N_8O_{9.6}S$
Formula weight	679.24	842.63	857.91
Temperature/K	100	103	100
Crystal system	tetragonal	tetragonal	triclinic
Space group	P-4 (81)	P-4 (81)	P-1 (2)
a/Å	11.91670(10)	12.1926(3)	6.78370(10)
b/Å	11.91670(10)	12.1926(3)	15.1968(3)
c/Å	4.60100(10)	4.5852(2)	16.7196(3)
α/°	90	90	69.305(2)
β/°	90	90	89.6510(10)
γ/°	90	90	80.927(2)
Volume/Å^3	653.378(18)	681.63(4)	1589.94(5)
Z	1	1	2
ρ_{calc}g/cm^3	1.726	2.053	1.792
Crystal size/mm^3	0.15 × 0.1 × 0.1	0.25 × 0.02 × 0.02	0.19 × 0.13 × 0.05
Radiation	Mo Kα (λ = 0.71073)	Mo Kα (λ = 0.71073)	Mo Kα (λ = 0.71073)
2Θ range for data collection/°	4.834 to 63.95	6.684 to 60.838	5.812 to 59.546
Reflections collected	4951	4723	38308
Independent reflections	1894 [R_{int} = 0.0233, R_{sigma} = 0.0217]	1753 [R_{int} = 0.0300, R_{sigma} = 0.0382]	8405 [R_{int} = 0.0256, R_{sigma} = 0.0205]
Final R indexes [I>=2σ (I)]	R_1 = 0.0149, wR_2 = 0.0381	R_1 = 0.0230, wR_2 = 0.0419	R_1 = 0.0402, wR_2 = 0.0960
Final R indexes [all data]	R_1 = 0.0158, wR_2 = 0.0381	R_1 = 0.0233, wR_2 = 0.0421	R_1 = 0.0431, wR_2 = 0.0980

Both **3-BF_4** and **3-ReO_4** crystallise in the space group P-4 which contains inversion tetrad and two-fold rotation symmetry operations. Ag1 and the central atom of the tetrahedral anion sit on independent inversion tetrad symmetry operation positions and thus the asymmetric units contain only 0.25 of the metal centres and their respective anions. Half of the 3-MeUR-N linker is present in both asymmetric units. The carbonyl bond of the urea group in both structures sit on two-fold rotation axes which generate the full organic linker.

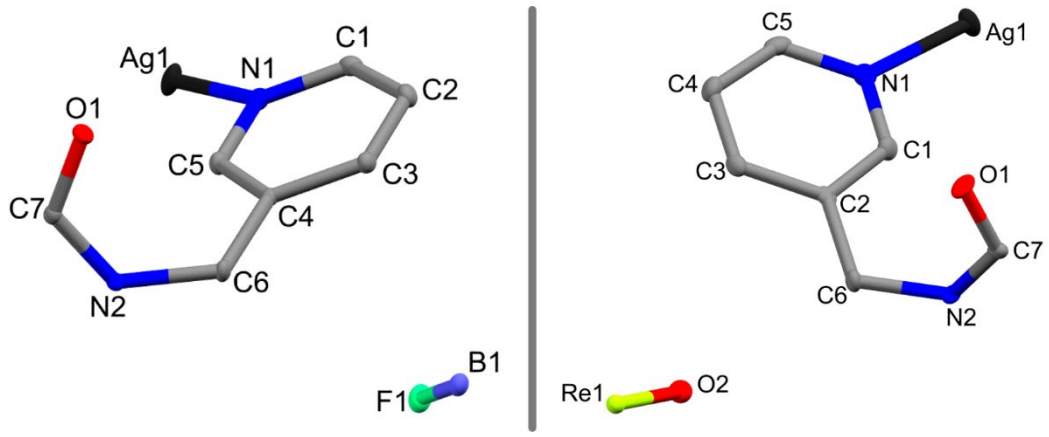

Figure 3.19. Asymmetric units of (left) 3-BF_4 and (right) 3-ReO_4. Thermal ellipsoids are set to 40% probability. Hydrogen atoms have been omitted for clarity. Grey = carbon, black = silver, red = oxygen, blue = nitrogen, green = fluorine, purple = boron and lime = rhenium.

The silver centres in both structures adopt a flattened tetrahedral geometry through the coordination of the pyridine nitrogen (N1) from four independent 3-MeUR-N linkers (figure 3.20). The distortion from an ideal tetrahedral geometry result in two different bond angles around the metal. The angle between two opposite pyridine nitrogens in **3-ReO_4** and **3-BF_4** are 135.86(17)° and 135.20(7)° while two adjacent nitrogens have bond angles of 98.12(6)° and 98.35(2)° respectively. The silver to nitrogen bond lengths (Ag1-N1) are 2.367(4) and 2.3712(14) Å for **3-ReO_4** and **3-BF_4** respectively.

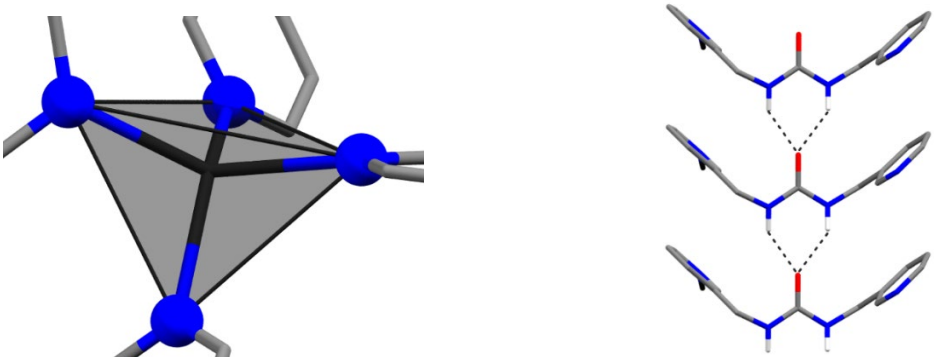

Figure 3.20. (Left) Coordination environment of silver centre in 3-ReO_4 confirming its flattened tetrahedral geometry. (Right) Urea ladder formation between parallel sheets in 3-ReO_4.

The coordination of both pyridine nitrogen atoms in 3-MeUR-N results in a two-dimensional coordination polymer sheet for both materials (figure 3.21). **3-BF_4** and **3-ReO_4** structures can be simplified to the **sql** net topology which follows the $\{4^4.6^2\}$ Schläfli symbol. Figure 3.21 shows the small channels present in the structures which are occupied by well-ordered counter anions in both structures as well as the AA layering of the individual sheets. The Ag···Ag distance between two parallel sheets in **3-ReO_4** and **3-BF_4** are 4.585 and 4.601 Å respectively, signifying very densely packed structures. The AA layering is stabilised through the formation of alpha networks between

the urea groups of 3-MeUR-N linkers in parallel layers (figure 3.20). The hydrogen bond lengths (N-H···O) are 2.106 and 2.098 Å for **3-ReO$_4$** and **3-BF$_4$** respectively.

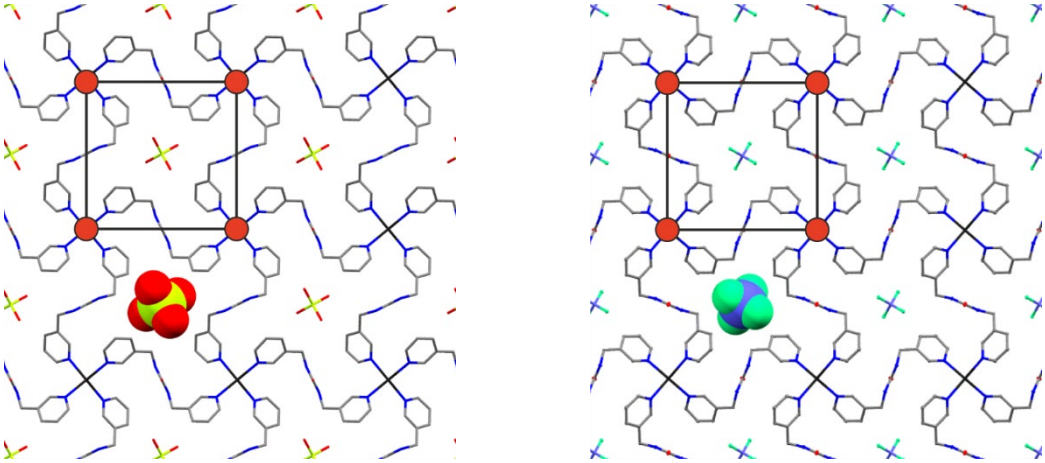

Figure 3.21. Crystal packing of (left) 3-ReO$_4$ and (right) 3-BF$_4$ viewed down the c axis showing the anion packing within the sql sheets. Hydrogen atoms have been omitted for clarity.

PXRD characterisation of synthesised **3-ReO$_4$** and **3-BF$_4$** confirms that the solved crystal structures are representative of the bulk samples (figure 3.22) because both simulated patterns align very well to the experimental patterns. An increasing shift in peak position at higher angle is observed in both samples which suggests the crystal structures have undergone a degree of strain.

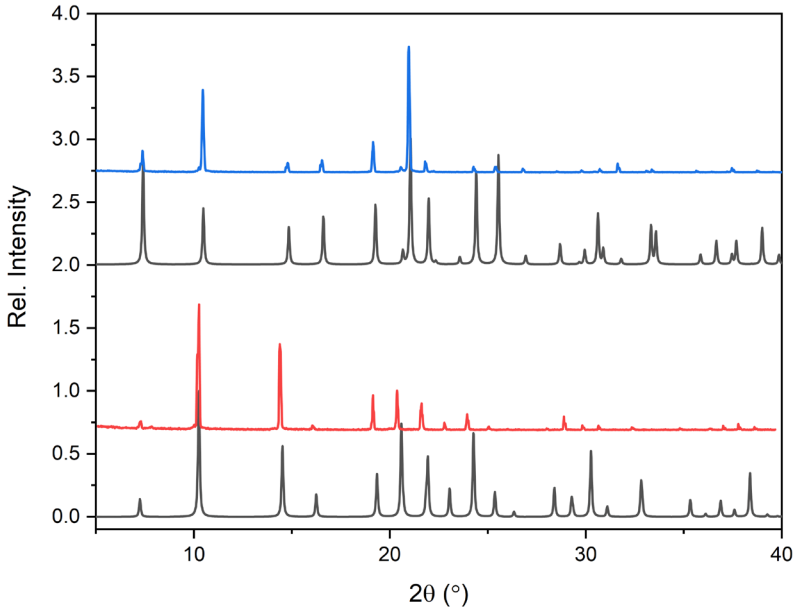

Figure 3.22. Experimentally obtained PXRD patterns of [Ag(3-MeUR-N)] coordination polymers compared to their computationally derived patterns. Black = CIF files; red = 3-ReO$_4$; and blue = 3-BF$_4$.

Altering the tetrahedral counter anion to a more coordinating anion with a larger charge density, such as sulphate, has a drastic effect on the resulting coordination polymer. The asymmetric unit of **3-SO$_4$** is shown in figure 3.23 and comprises of two full occupancy silver centres, two full

occupancy 3-MeUR-N linker molecules and one full occupancy sulphate anion. Additionally, two full occupancy water molecules (O7A and O8A), one partially occupied water molecule (O10A at 59% occupancy) and a split water molecule that occupies sites, O9A and O9B in an 85:15 ratio, can be located within the asymmetric unit. Both silver centres exhibit a distorted T-shape geometry, coordinating to an oxygen atom from the sulphate anion and two pyridine nitrogen atoms from independent 3-MeUR-N linkers (figure 3.23).

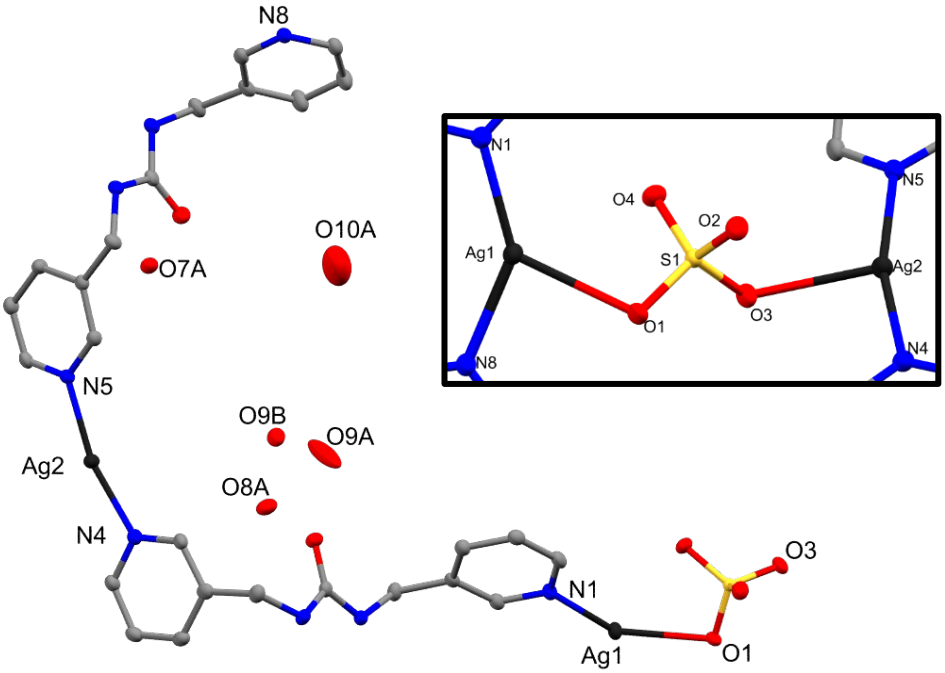

Figure 3.23. Asymmetric unit of 3-SO_4. Thermal ellipsoids are set to 40% probability. (Inset) coordination environment of the T-shaped silver centres. Hydrogen atoms have been omitted for clarity. Grey = carbon, black = silver, red = oxygen, blue = nitrogen and yellow = sulphur.

3-SO_4 demonstrates the highly coordinating character of sulphate anions. As opposed to the anions within **2-SO_4** which are non-coordinated to the silver centres and display higher disorder, we find that the sulphate anions in **3-SO_4** are integral to the coordination polymer structure by bridging two silver centres through two of its oxygen atoms. While coordination to the metal centres does require desolvation of the sulphate to some degree there is still a high level of stabilising hydrogen bonds from both ordered water molecules and the N-H moieties of the urea functionalities (figure 3.24). One water molecule (O7A) bridges two sulphate molecules (O2 and O4) through hydrogen bond interactions to form a sulphate-water chain. The hydrogen bond lengths (table 3.6) within these chains are below 2 Å and thus are strong interactions. In addition, O7A hydrogen bonds to the N-H moiety (N7) of a urea group in the organic linker. We also observe a water molecule (O8A) which bridges the carbonyl oxygen (O5) of a urea group and a sulphate oxygen (O3) while also hydrogen bonding to a different N-H (N3) group. This explains why O7A and O8A are well ordered and why their thermal ellipsoids are more isotropic, and less diffuse than O10A, O9A and O9B. The

sulphate anion receives additional stabilisation from the coordination polymer through hydrogen bonds (N2···O1 and N6···O2) from the urea functionalities of 3-MeUR-N.

Table 3.6. Hydrogen bond lengths within 3-SO_4.

Water as hydrogen bond donor (O-H···O)		Urea as hydrogen bond donor (N-H···O)	
Bond	**Distance (Å)**	**Bond**	**Distance (Å)**
O7A – O4	1.941	N2 – O1	2.176
O7A – O2	1.981	N6 – O2	2.081
O8A – O3	1.945	N3 – O8A	2.029
O8A – O5	1.971	N7 – O7A	2.210

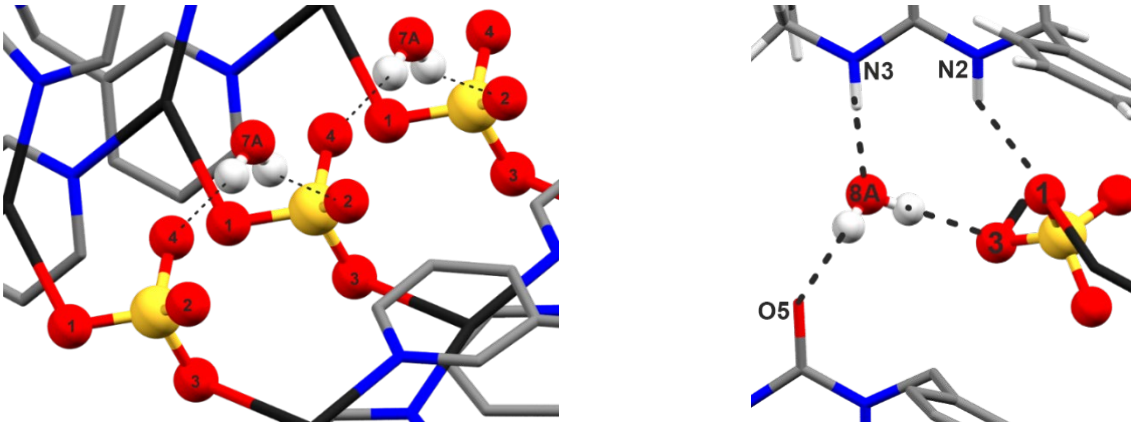

Figure 3.24. (Left) Bridging water molecules through hydrogen bonding to sulphate anions. (Right) Water molecule acting as a hydrogen bond donor and acceptor in 4-SO_4.

The bridging sulphate anions result in the connection of independent coordination polymer chains which have adopted a zig-zag conformation, affording hexagonal shaped windows. Topological analysis of **3-SO_4** yields a uninodal net with the Schläfli symbol $\{6^3\}$ thus the coordination polymer follows the **hcb** topology. Figure 3.25 contains the honeycomb **hcb** nets viewed down the a axis. The red and green nets clearly demonstrate the ABAB layering that occurs in **3-SO_4**.

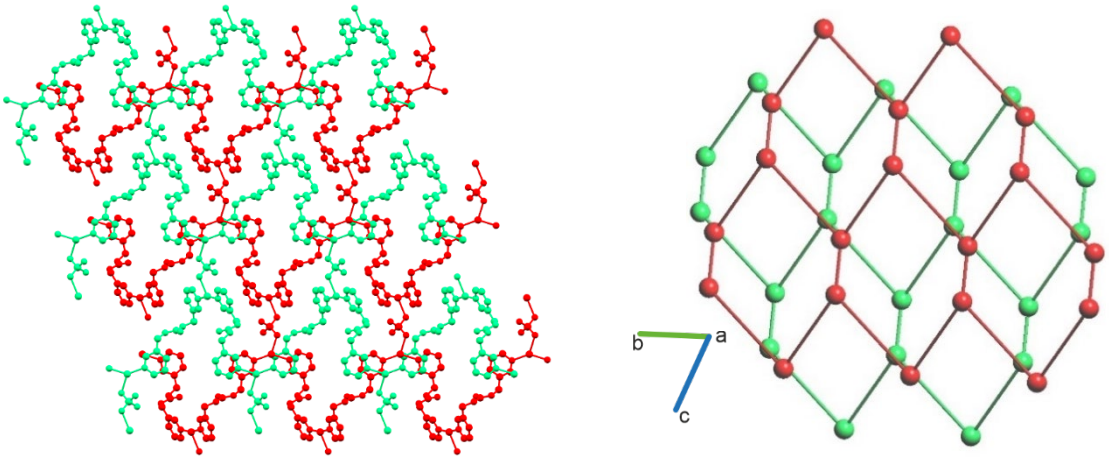

Figure 3.25. Topological analysis of 3-SO_4. ABAB stacking of two-dimensional stacking represented in both structure (left) and net (right) form when viewed down the a axis.

3.3.4 Synthesis and Characterisation of Silver N,N'-bis(4-pyridylmethyl)urea Coordination Polymers

The silver N,N'-bis(4-pyridylmethyl)urea system ([Ag(4-MeUR-N)]) is the final silver system that we explored. In total, we were able to crystallographically solve four coordination polymer structures. Crystals of silver N,N'-bis(4-pyridylmethyl)urea nitrate (**4-NO_3)** were synthesised by combining an aqueous solution of $AgNO_3$ (0.3M) with an ethanolic solution of 4-MeUR-N (0.3M) and leaving the reaction mixture in the dark for five days. Silver N,N'-bis(4-pyridylmethyl)urea (**4-SO_4**) could be synthesised by spiking a silver nitrate solution with an equimolar quantity of bisodium sulphate prior to combining with an ethanolic solution of the organic linker. This resulted in the formation of block crystals of **4-SO_4.** Alternatively, to access suitable quality crystals of both **4-ReO_4** and **4-PF_6,** reagent layering reactions were required. This involved layering 2mL of deionised water on top of a 2 mL aqueous solution of $AgNO_3$ and the appropriate alkali salt (sodium perrhenate or potassium hexafluorophosphate). Followed by careful layering of a 2 mL ethanolic solution of 4-MeUR-N. Crystals of the respective coordination polymers grew over five days at the interface of the solutions. Table 3.7 contains the resulting crystal data and structure refinement details for the [Ag(4-MeUR-N)] coordination polymers discussed above.

Table 3.7. Crystal data and structure refinement for 4-NO_3, 4-SO_4, 4-ReO_4 and 4-PF_6.

Identification code	**4-NO_3**	**4-SO_4**	**4-ReO_4**	**4-PF_6**
Empirical formula	$C_{13}H_{16}AgN_5O_5$	$C_{26}H_{29}Ag_2N_8O_7S$	$C_{15}H_{20}AgN_4O_6Re$	$C_{78}H_{84}Ag_4F_{18}N_{24}O_6P_3$
Formula weight	430.18	813.37	646.42	2320.08
Temperature/K	100.00(10)	100	100.00(10)	104(3)
Crystal system	Monoclinic	monoclinic	orthorhombic	monoclinic
Space group	$P2_1/n$ (14)	$P2_1/n$ (14)	$Pna2_1$ (33)	I2/a (15)
a/Å	7.6582(3)	9.6654(4)	15.8211(6)	28.8092(4)
b/Å	14.9183(5)	20.2499(8)	17.3372(5)	9.04740(10)
c/Å	14.5187(3)	15.6355(7)	6.7850(3)	40.5509(5)
α/°	90	90	90	90
β/°	105.109(3)	103.905(5)	90	104.5530(10)
γ/°	90	90	90	90
Volume/$Å^3$	1601.38(9)	2970.6(2)	1861.08(12)	10230.4(2)
Z	4	4	4	4
$\rho_{calc}g/cm^3$	1.784	1.819	2.307	1.506
μ/mm^{-1}	1.294	1.448	7.591	0.892
F(000)	864.0	1628.0	1232.0	4652.0
Crystal size/mm^3	0.3 x 0.05 x 0.02	0.1 × 0.07 × 0.015	0.13 × 0.08 × 0.02	0.6 × 0.03 × 0.02
Radiation	Mo Kα (λ = 0.71073)	Mo Kα (λ = 0.71073)	Mo Kα (λ = 0.71073)	Mo Kα (λ = 0.71073)
2Θ range for data collection/°	5.812 to 61.386	4.022 to 63.732	6.448 to 57.82	3.986 to 59.14
Reflections collected	11964	38935	6396	62376
Independent reflections	4342 [R_{int} = 0.0483, R_{sigma} = 0.0538]	8229 [R_{int} = 0.0427, R_{sigma} = 0.0382]	3219 [R_{int} = 0.0356, R_{sigma} = 0.0574]	12608 [R_{int} = 0.0394, R_{sigma} = 0.0350]
Final R indexes [I>=2σ (I)]	R_1 = 0.0524, wR_2 = 0.1265	R_1 = 0.0846, wR_2 = 0.2183	R_1 = 0.0604, wR_2 = 0.1310	R_1 = 0.0405, wR_2 = 0.0874
Final R indexes [all data]	R_1 = 0.0721, wR_2 = 0.1426	R_1 = 0.1062, wR_2 = 0.2365	R_1 = 0.0681, wR_2 = 0.1353	R_1 = 0.0522, wR_2 = 0.0917
Flack parameter	-	-	0.51(2)	-

The asymmetric unit of **4-NO$_3$** comprises of one silver centre, one full 4-MeUR-N linker, one water molecule and a nitrate anion (figure 3.26). Both the water molecule and nitrate anion are split across two sites with occupancy ratios of 57:43 (O2:O2A) and 63:37 (B:C) respectively. The silver centre adopts a distorted T-shaped geometry, coordinating to three independent 4-MeUR-N linker molecules. Two of the 4-MeUR-N linkers coordinate through their pyridine nitrogen atoms while the remaining linker coordinates through the urea oxygen.

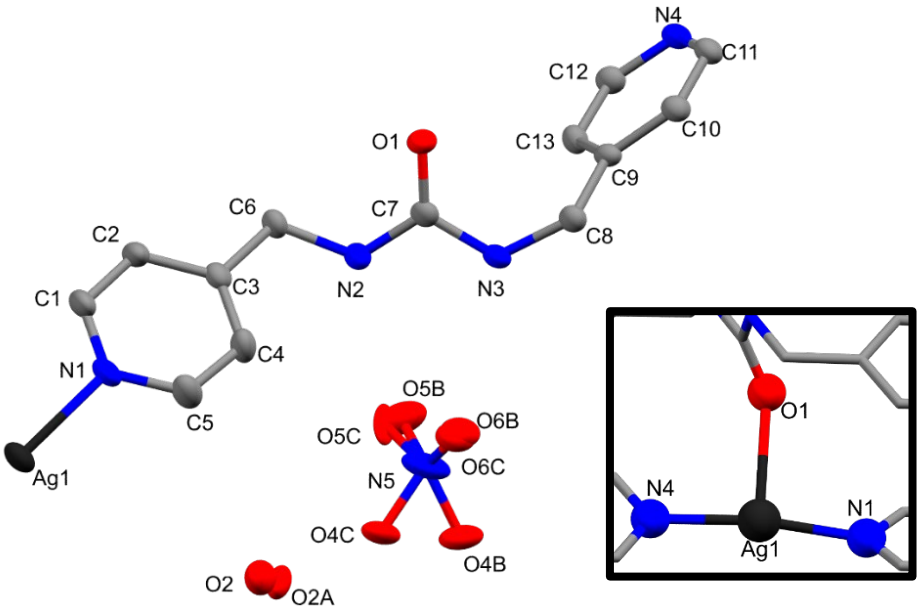

Figure 3.26. Asymmetric unit of 4-NO$_3$ displaying the disorder of both the nitrate anion and oxygen atom of the water molecule across two sites. Thermal ellipsoids are set to 40% probability. (Inset) The silver centre coordination environment within 4-NO$_3$. Hydrogen atoms have been omitted for clarity.

Our findings contradict that presented by Lauher *et al.* whereby they state that the Ag1-O1 bond is too long and the silver (I) centre should adopt a linear geometry.[37] The Ag-O bond length in our structure is 2.679 Å and consistent with the length that they reported. The sum of the atom radii is 3.65 Å and therefore a bond length that falls shorter than this value should be a sensible bond length.[43] Because of this, we have retained the Ag-O bond within our structure.

The three-coordinate silver centres result in a two-dimensional sheet structure that are visible when viewed down the crystallographic c axis (Figure 3.27). Topological analysis of the connectivity in **4-NO$_3$** confirms a **hcb** topology with the Schläfli symbol $\{6^3\}$ (Figure 3.27).

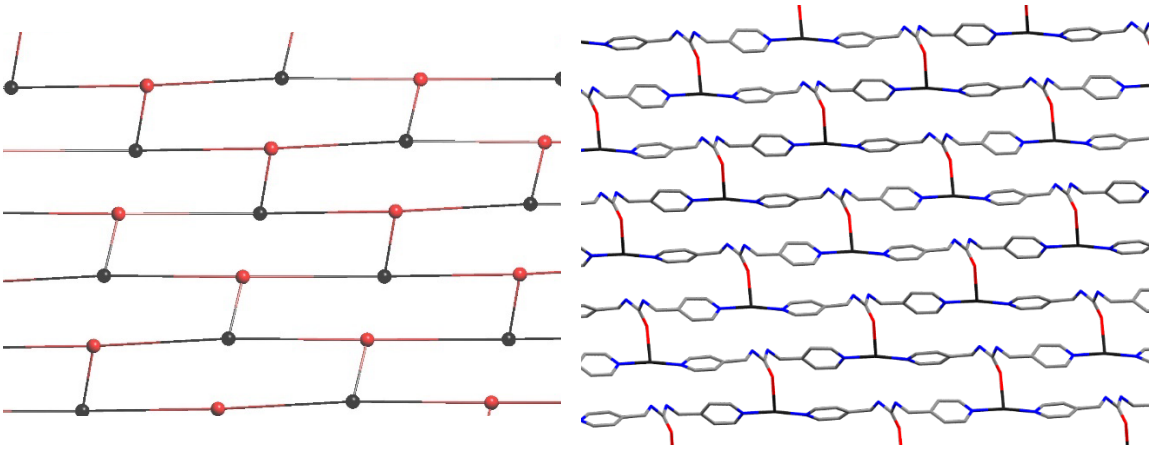

Figure 3.27. (Left) Topological analysis of 4-NO_3 that confirms a hcb topology. (Right) The two-dimensional sheets viewed down the crystallographic c axis within 4-NO_3 as a result of the three-coordinate silver (I) centres and 4-MeUR-N linkers. Red nodes = 4-MeUR-N and black nodes = Ag(I). Nitrate anions and water molecules have been omitted for clarity.

When viewed along the crystallographic a axis we can identify the location of the nitrate anions and water molecules within **4-NO_3** (figure 3.28).

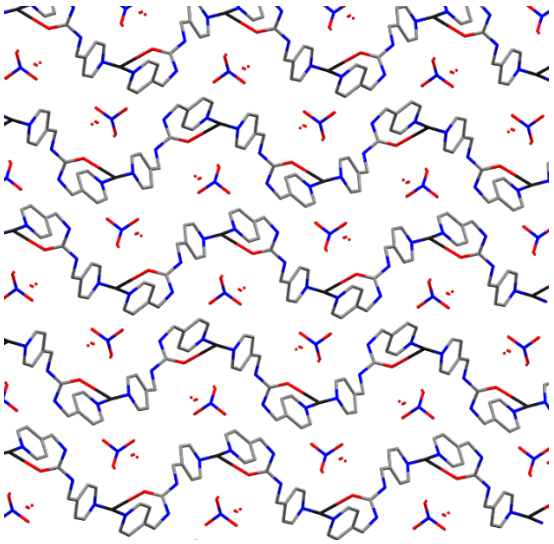

Figure 3.28. Crystal packing viewed down the a axis of 4-NO_3 showing the location of the nitrate anions and water molecules within the structure. Hydrogen atoms have been omitted for clarity.

It is apparent from the anion disorder within **4-NO_3** that the nitrate anion does not sit well within the cavities formed between the coordination polymer chains. Figure 3.29 shows the N-H···O hydrogen bonding between the urea functionality and nitrate anion of **4-NO_3** as well as the anion disorder. The hydrogen bond lengths from the urea groups to the major occupancy atoms of the nitrate anion measure at 2.094 and 2.274 Å for N2-H···O5B and N3-H···O6B respectively. While the location of two of the oxygen atoms of the nitrate anion align well in both occupancies there is a large difference in location of the third oxygen atoms, O4B and O4C. The crystal structure suggests

that the anion sits in a pseudo-tetrahedral cavity and would be better suited for a tetrahedral anion rather than the trigonal planar nitrate.

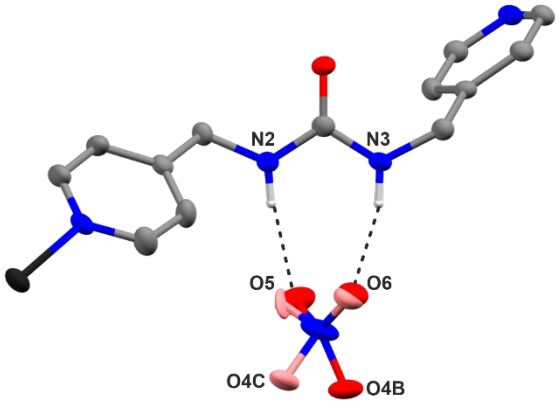

Figure 3.29. N-H···O hydrogen bonding between the urea functionality and nitrate anion of 4-NO_3. Anion disorder is displayed by the different coloured oxygen atoms. Red corresponds to major occupancy positions (O4B) and pink, the minor occupancy (O4C) of the nitrate oxygens.

The asymmetric unit of 4-SO_4 (figure 3.30) is comprised of two silver centres, two 4-MeUR-N linkers, one sulphate anion and one water molecule. The silver centres both adopt distorted T-shaped geometries, each coordinating to two independent 4-MeUR-N linkers as well as an oxygen atom of a bridging sulphate anion. These metal centre environments are near identical to that seen in the structure of 3-SO_4 (section 3.3.3).

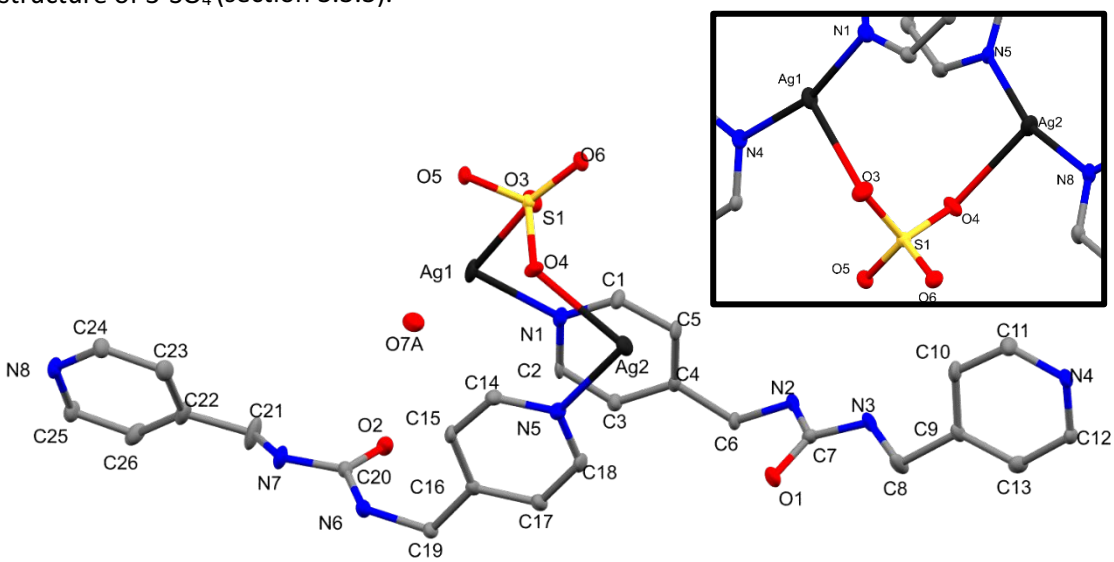

Figure 3.30. Asymmetric unit of 4-SO_4. (Inset) the T-shaped silver centre environments and coordinating sulphate anion. Thermal ellipsoids set to 40% probability. Hydrogen atoms have been omitted for clarity.

4-SO_4 is composed of one-dimensional [Ag(4-MeUR-N)] chains that are coordinated into pairs through sulphates linkages. This is shown in figure 3.31. Topological analysis confirms that 4-SO_4

consists of two-dimensional sheets whereby the short linkages between the longer chains of nodes represent the sulphates. This follows the two-rung laddered topology.

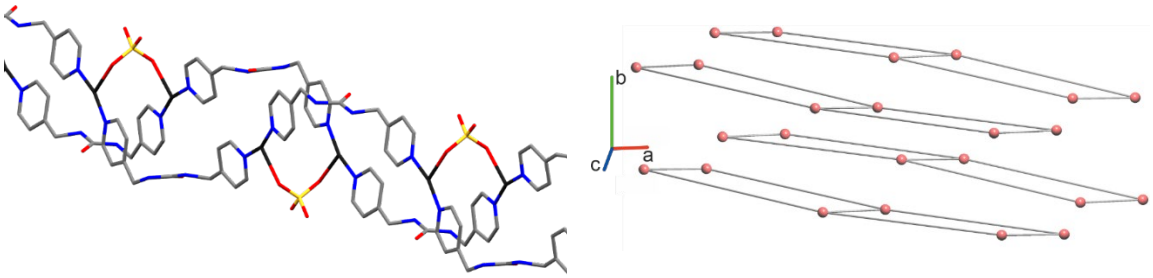

Figure 3.31. (Left) The two-dimensional sheets within 4-SO_4 and (right) topological analysis of 4-SO_4 confirming a two-rung laddered topology.

The packing of these two-dimensional sheets results in a dense crystal packing, with no voids between the layers (figure 3.32).

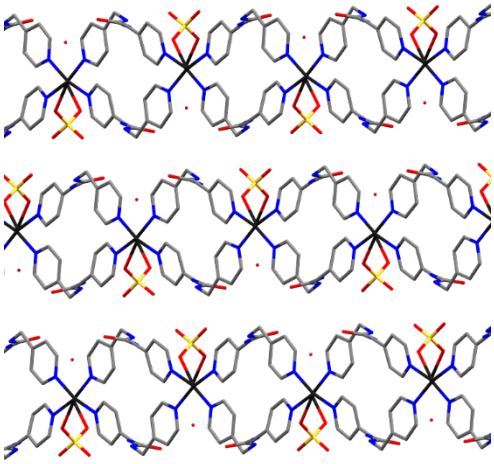

Figure 3.32. Crystal packing of 4-SO_4 viewed along the a axis showing the discrete two-rung laddered chains.

The sulphate anions undergo bridging hydrogen bonding from two urea groups of independent sheets resulting in each sulphate undergoing four hydrogen bond interactions. These occur through the N-H groups of the ureas (figure 3.33). The hydrogen bond lengths (table 3.8) suggest strong interactions between the sheets. A non-coordinated water molecule also acts as a hydrogen bond donor to the carboxyl oxygen of the urea groups.

Table 3.8. Hydrogen bond lengths within 4-SO_4.

Water as hydrogen bond donor (O-H···O)	
Bond	**Distance (Å)**
O7 – O2	1.926

Urea as hydrogen bond donor (N-H···O)	
Bond	**Distance (Å)**
N2 – O5	2.072
N3 – O4	1.957
N6 – O6	2.015
N7 – O3	2.022

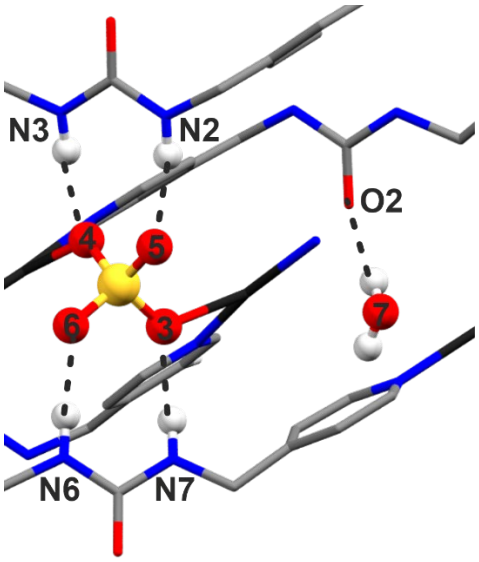

Figure 3.33. Hydrogen bonding between urea groups and water & sulphates within 4-SO_4.

4-ReO_4 crystallises in the space group $Pna2_1$. The asymmetric unit of **4-ReO_4**, shown in figure 3.34, comprises of one silver centre, one 4-MeUR-N linker, one perrhenate anion and one ethanol molecule. EADP restraints were applied judiciously to selected atoms to ensure a sensible convergence. The silver centre adopts a near linear geometry with a N1-Ag1-N4 bond angle of 172.0(6)°.

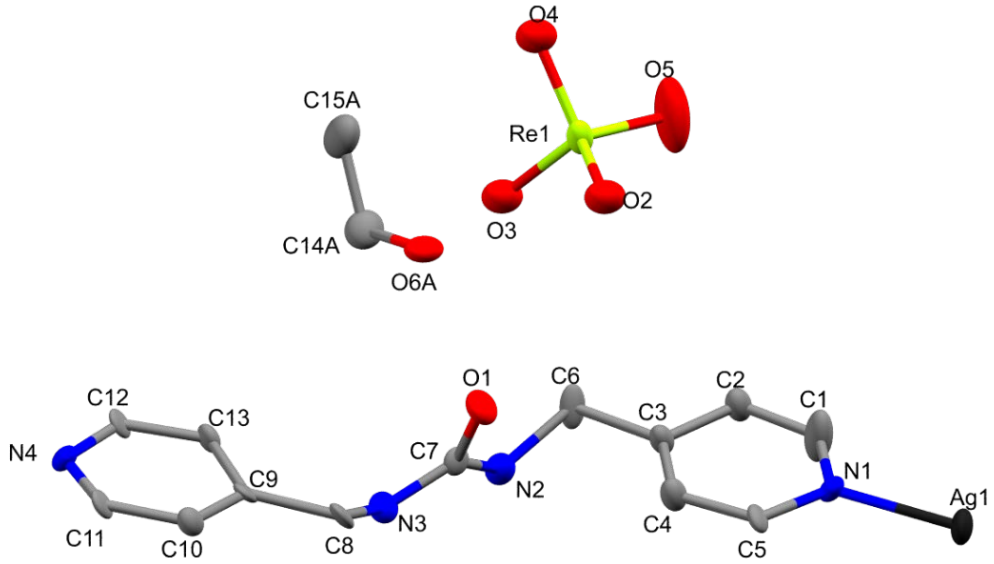

Figure 3.34. Asymmetric unit of 4-ReO_4. Thermal ellipsoids are set to 40% probability. Hydrogen atoms have been omitted for clarity.

4-ReO_4 is the only coordination polymer we have investigated that crystallised with an ethanol solvent molecule within the structure. The hydroxyl group of the alcohol acts as both a strong hydrogen bond donor (O6A-H···O1 = 1.866 Å) and moderate acceptor (N2-H···O6A = 2.411 Å and N3-H···O6A = 2.116 Å) to two independent urea moieties (see figure 3.35). Consequently, the perrhenate anion does not undergo any hydrogen bond interactions with the urea functional

groups. The perrhenate anions and ethanol molecules are positioned between the linear, one-dimensional coordination polymer chains which adopt an ABAB layering. There are no significant interactions between the perrhenate anion and the coordination polymer except that the anion is in close proximity to the silver cations.

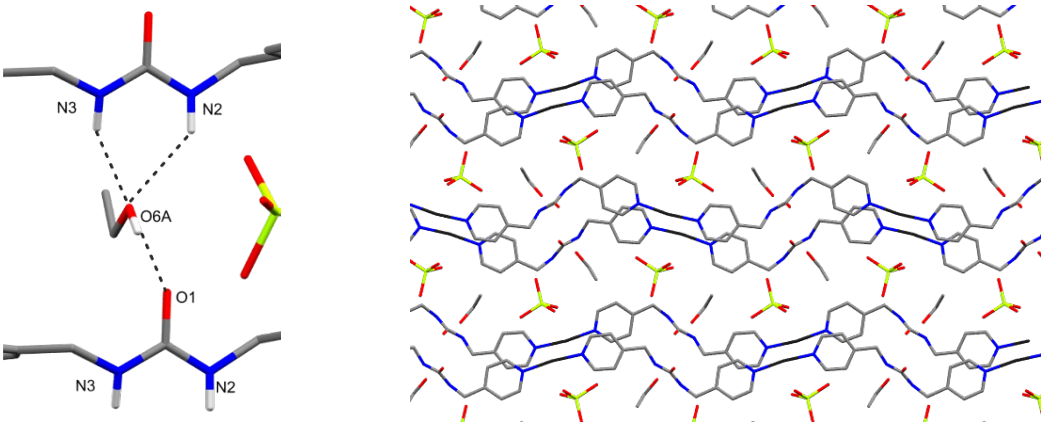

Figure 3.35. (Left) Hydrogen bond interactions between urea functionalities of 4-ReO_4 and sandwiched ethanol molecule. (Right) Crystal packing of 4-ReO_4, viewed down the c axis, showing the location of the perrhenate anion and ethanol guest molecules.

The asymmetric unit of **4-PF_6**, shown in figure 3.36, comprises of two silver centres, three 4-MeUR-N linkers and 1.5 hexafluorophosphate anions. Both silver centres have trigonal planar geometries, coordinating to three independent 4-MeUR-N linkers *via* their pyridine nitrogen atoms. The hexafluorophosphate anion, labelled P1A, sits on a 2-fold rotation axis and thus the remaining half of the anion is generated through the appropriate symmetry operation. We have been unable to locate the remaining 0.5 hexafluorophosphate anion in the asymmetric unit necessary to balance the two Ag (I) cationic centres. A solvent mask was applied to the residual electron density within the crystal structure in Olex 2 and accounted for 80 electrons per ASU. This electron density is present within a void between parallel coordination polymers and thus we believe that a disordered PF_6^- anion is highly likely to be present within these voids.

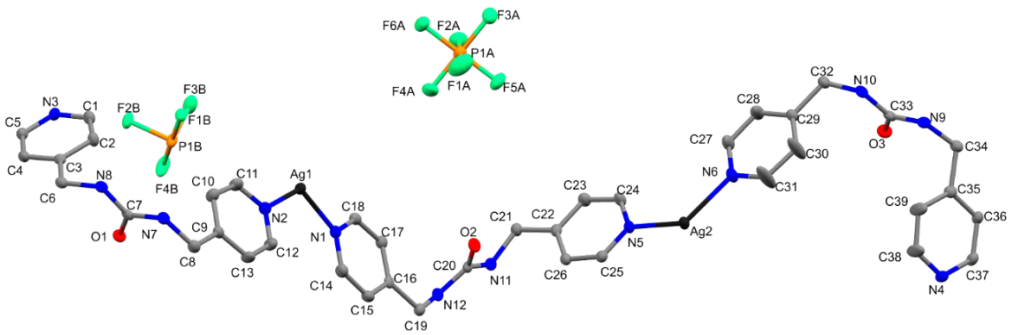

Figure 3.36. Asymmetric unit of 4-PF_6. Thermal ellipsoids are set to 40% probability. Hydrogen atoms have been omitted for clarity. Black = silver, grey = carbon, blue = nitrogen, red = oxygen, green = fluorine and orange = phosphorus.

4-PF_6 consists of one-dimensional chains of [Ag(4-MeUR-N)]. These chains are composed of loops of two 4-MeUR-N linkers coordinated through two silver (I) centres. The loops are linked together through an additional 4-MeUR-N molecule. The coordination polymer chains stack upon one another following AA packing with a separation of between 4.3 – 4.5 Å. The stacking of loops results in the formation of two-dimensional rectangular channels that have cross sections of 9.11 Å (Ag···Ag) and 11.33 Å (urea···urea) in size. These channels are an optimal size for the occupation of PF_6^- (P1B) anions, demonstrated by the partial space filling crystal structure in figure 3.37. The PF_6^- anion has potential to act as a structure determining agent (SDA), directing the formation of the coordination polymer around itself. The hexafluorophosphate anion, labelled P1A in Figure 3.36, sits in the voids between the coordination polymer chains.

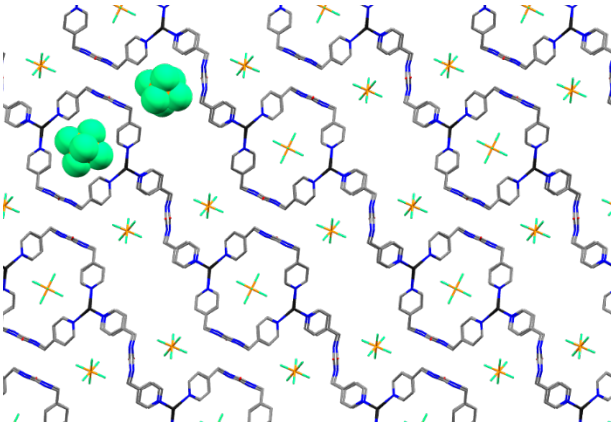

Figure 3.37. Crystal packing of 4-PF_6, down the b axis, showing the location of the hexafluorophosphate anions in between the coordination polymer chains and also within the looped segment of the chains. Hydrogen atoms have been omitted for clarity. Black = silver, grey = carbon, blue = nitrogen, red = oxygen, green = fluorine and orange = phosphorus.

4-PF_6 is the first coordination polymer that we have explored where the organic linker adopts two very distinct conformations (figure 3.38), allowing for the formation of a structure with a more rarely seen loops and chain topology. This is as a result of the sp^3 carbon between the urea and pyridine functionalities which introduces additional degrees of flexibility. 4-MeUR-N adopts the syn conformation to sandwich the hexafluorophosphate anions within the channels whilst the other 4-MeUR-N, which is in a anti conformation, links two adjacent loops through the silver metal centre. This topological type is highly dependent on the system having trigonal planar nodes as well as weakly coordinating anions,[44] in our case these conditions are met by the silver centres and hexafluorophosphate anions respectively in **4-PF_6**. The loops and chains topology has previously been reported by Schröder *et al.* with a rigid 6-bis(pyridin-3-yl)-1,2,4,5-tetrazine (3,3'-pytz) linker as well as by Robson *et al.*[45] and Kim *et al.*[46] in polyrotaxane structures.

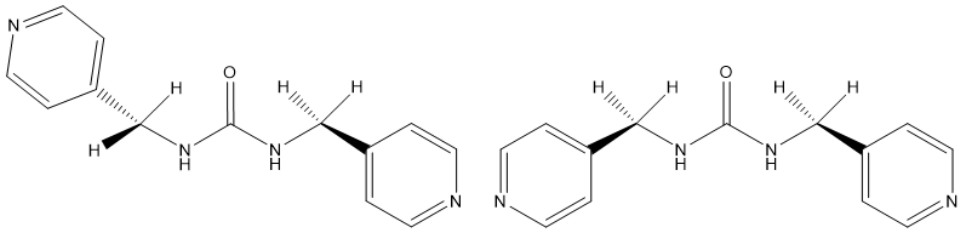

Figure 3.38. (Left) anti and (right) syn conformations of 4-MeUR-N.

All urea functionalities of **4-PF_6** are involved in the formation of urea ladders between layering sheets and thus are not available for urea-anion interactions. The crystal structure in figure 3.39 shows the two different urea ladders in **4-PF_6**. Hydrogen bond interactions, with N-H···O lengths of 2.06 and 2.19 Å, are formed between the urea moieties of the trans 4-MeUR-N linkers (highlighted with blue dashes in figure 3.39). Hydrogen bond interactions that form between the loops of **4-PF_6** vary between 2.04 and 2.17 Å (highlighted in red in figure 3.39).

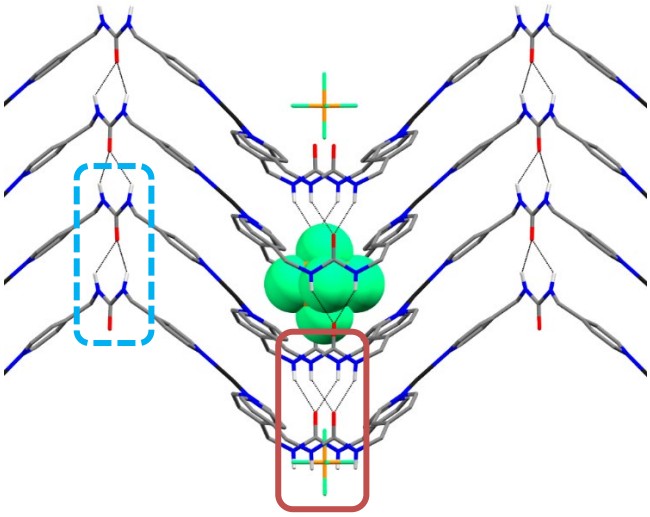

Figure 3.39. The two different urea ladders in 4-PF_6. PF_6^- anions present in the channels of 4-PF_6 have been included.

3.3.5 Discussion

In total, we have synthesised eight new coordination polymers, and produced CIF files for three previously reported coordination polymers that lacked crystal coordinates in the CCDC database. We have summarised these collected structures and their corresponding method of synthesis in Table 3.9. In most cases, we have been able to yield crystal structures of the coordination polymers by combining silver nitrate, the desired organic linker, and an alkali metal salt of the desired anion at room temperature. For selected materials, it was found that undertaking a layered reagent experiment in a test tube resulted in better quality crystals as this method reduces the rate of crystallisation by allowing for the slow diffusion of reagents through the solvent and thus a slower rate of reaction. We also found that the nitrate anion of the silver nitrate can compete with the

crystallisation of different anions into the coordination polymer. We have therefore replaced silver nitrate with the corresponding silver salt in some cases.

Table 3.9. Crystal structures collected of silver coordination polymers. The structures highlighted in bold were collected using crystals synthesised *via* reagent layering experiments. * = The corresponding silver salt was used to synthesise this material rather than a combination of silver nitrate and the corresponding alkali salt.

Anion	Organic Linker		
	2-MeUR-N	**3-MeUR-N**	**4-MeUR-N**
NO_3^-	No crystal growth	White precipitate	**Clear, colourless needles**
SO_4^{2-}	Clear, colourless needles	**White precipitate, needle clusters**	Clear, colourless blocks
ReO_4^-	**Clear, colourless thin needles***	**Clear, colourless blocks***	**Thin, colourless plates***
BF_4^-	Clear, colourless blocks	Clear, colourless needles*	Clusters of thin needles
PF_6^-	Clear colourless blocks	Clear, colourless needles	**Clear, colourless needles**
Cl^-	White precipitate	N/A	N/A
CO_3^{2-}	Yellow precipitate	N/A	N/A

New structure collected

Existing structure

Silver salt formed

No structure collected

The nitrate anion does not crystallise when 2-MeUR-N is used as the organic linker. Silver nitrate therefore can be used as the metal salt precursor, with the nitrate anion playing no effect on the crystallisation of most coordination polymers that we have explored. In the case of **2-ReO_4**, while using silver nitrate and sodium perrhenate does yield **2-ReO_4**, we found that by altering the metal precursor to silver perrhenate, the yielded crystals were larger and therefore more suitable for SCXRD characterisation. During our initial studies of the [Ag(2-MeUR-N)] system we were not able to crystallise sulphate within the coordination polymer. This suggested to us that this system may be suitable for selective crystallisation of perrhenate from solution. Nitrate and sulphate anions are found in high concentration within Sellafield groundwater (table A.1) and therefore are highly competitive anions for adsorbents of pertechnetate/perrhenate. By designing a system with no apparent affinity for sulphate or nitrate, but still able to crystallise perrhenate, we believed that we had overcome this disadvantageous competitiveness. This was however found not to be case for three reasons: **1**) the sulphate anion was eventually, and consistently, crystallised in the [Ag(2-MeUR-N)] system as **2-SO_4**; **2**) the fast precipitation of silver chloride and silver carbonate upon addition of Ag^+ to solutions containing Cl^- or CO_3^{2-} would no doubt preclude the crystallisation of perrhenate and; **3**) we had underestimated the effects that chloride and carbonate would have

on the coordination polymer stability. Upon submersion of 2-BF_4 crystals into an aqueous solution of sodium chloride the crystals degraded into a very fine powder that was not retrievable from solution. The selective crystallisation potential of the [Ag(2-MeUR-N)] system has therefore been shown to not be substantial enough to warrant any further investigation.

The non-suitability of [Ag(3-MeUR-N)] and [Ag(4-MeUR-N)] as systems for selective crystallisation was immediately more apparent than the ortho system because of the facile collection of crystal structures of **3-SO_4, 4-SO_4** and **4-NO_3**. The nitrate anion also yielded a white precipitate when silver nitrate and 3-MeUR-N were reacted, suggesting the formation of a coordination polymer containing nitrate counter anions. A crystal structure was unfortunately not obtainable because the crystals were of inadequate quality for SCXRD characterisation. We did not attempt to crystallise chloride or carbonate within these two systems because we presumed that their respective silver salts would form, as previously seen for the ortho system.

While our efforts to develop a suitable selective crystallisation system for perrhenate have not been successful, we have been able to obtain a series of several interesting and diverse crystal structures of different silver coordination polymers. Hydrogen bonding plays a key role in the stabilisation of these materials with the urea groups of the coordination polymers undergoing interactions with either urea groups of independent coordination polymers, the crystallised anions, or even solvent molecules that have been crystallographically isolated. In particular, the sulphate anions within **2-, 3-,** and **4-SO_4** have crystallised in hydrogen bond rich environments. Water molecules within the structures act as hydrogen bond donors, while the urea groups of the organic linkers also act as hydrogen bond donors towards the sulphate oxygens. The urea groups in **2-** and **4-SO_4** have arranged to form a cavity whereby one urea group is positioned above the sulphate with the N-H bonds pointing downwards, towards the anion, while an independent urea group is positioned below with N-H bonds pointing upwards. This is shown schematically in Figure 3.40. In **3-SO_4**, the urea groups do hydrogen bond to the sulphate anion, but not in a bidentate manner as seen in the other two coordination polymers.

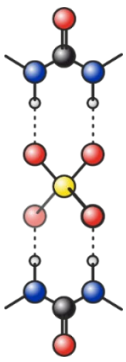

Figure 3.40. Schematic diagram of the hydrogen bond cavity created between two mirrored urea groups within 2-SO_4 and 4-SO_4.

In **4-SO_4**, the hydrogen bonds generated from the urea cavity are the only hydrogen bonds that stabilise the sulphate anion, therefore this is the only system that has fully desolvated the highly chaotropic anion. This is not the case for **2-** or **3-SO_4** however, as additional hydrogen bonding with water solvent molecules is undertaken in these structures. In **2-SO_4**, four water molecules act as hydrogen bond donors each bonding to an individual sulphate oxygen. This totals eight hydrogen bonds to the sulphate anion. Whereas, in **4-SO_4** there are bridging water molecules between sulphate anions, as seen previously in figure 3.24.

The self-associating nature of urea is present in several of our structures, demonstrating the difficulty in controlling this strong interaction. While these strong hydrogen bond interactions aid in stabilisation of the material, they do result in blocking the urea functionality from interacting with oxo-anions, which is the primary reason of incorporating such a functional group in our supramolecular design strategy. In our perrhenate-containing systems only **2-ReO_4** contains hydrogen bond interactions between the anion and coordination polymer through the N-H protons of the urea groups. This is also the case for tetrafluoroborate and hexafluorophosphate anions in the [Ag(2-MeUR-N)] system. The urea groups are blocked in both **3-ReO_4** and **4-ReO_4** by the formation of urea ladders and hydrogen bonding to solvent molecules respectively. In fact, **4-ReO_4** is the only coordination polymer we have studied that contained crystallographically ordered ethanol solvent molecules.

Additional interactions within the sulphate-containing coordination polymers are found within **3-** and **4-SO_4** because the anions covalently bond to two silver centres, bridging between the two primary building units. This is not observed in **2-SO_4**, in which the sulphate is disordered over two crystallographic orientations. Sulphate is the only anion within the systems that we have investigated to undergo covalent bonding with the metal centres and is deemed to be caused by the higher charge density on the anion.

The **sql** net crystal structure of **3-ReO_4** is near identical to that of **3-BF_4** obtained previously by Lauher *et al,* only differing by the counter anion present. This suggests that **3-BF_4** could be an ideal anion exchange material as no single-crystal to single-crystal transformations would be expected to occur when the BF_4^- anions are exchanged for ReO_4^-. The near identical N-Ag bond lengths and N-Ag-N angles within these two structures confirm that the tetrahedral anions explored in our work are well accommodated within the [Ag(3-MeUR-N)] system. In similar fashion, the [Ag(2-MeUR-N)] systems that contain non-coordinating anions (**2-BF_4, -PF_6** and **-ReO_4**) have very similar coordination polymer structures. The coordination polymers all have a two-rung ladder topology, caused by the T-shaped silver centres that coordinate to two 2-MeUR-N linkers *via* the pyridine nitrogen atoms and one 2-MeUR-N linker *via* the carboxyl oxygen of the urea group. The unit cell dimensions of

these three systems are relatively similar but increase based upon the size of the incorporated anion (**2-SO_4** < **2-ReO_4** < **2-PF_6**).

3.4 Results and Discussion of Mixed-Linker Urea-Based Metal-Organic Frameworks and Layered Metal-Organic Frameworks Using Zinc Salts

3.4.1 Zn-MOF-1 ([$Zn_2(OBA)_2$(4-MeUR-N)] 4.5·DMF)

$Zn(NO_3)\cdot 6H_2O$, 4,4'-oxybisbenzoic acid (H_2OBA) and 1,3-bis(pyridin-4-ylmethyl)urea (4-MeUR-N), in equimolar quantities, were dissolved in DMF and heated for 24 hours at 80 ˚C in a sealed autoclave. The reaction yielded orange crystals, hereby referred to as Zn-MOF-1 (figure 3.41). The Zn-MOF-1 crystals were washed by decanting and replacing the solvent with fresh DMF every 24 hours for three days.

Figure 3.41. (Left) Chemical structures of H_2OBA and 4-MeUR-N. (Right) Crystals of Zn-MOF-1 in their mother liquor.

3.4.1.1 Characterisation of Zn-MOF-1 ($Zn_2(OBA)_2$(4-MeUR-N) 4.5·DMF)

A suitable block crystal was selected for SCXRD. The structure refinement and crystal data are presented in table 3.10. The structure was solved using SHELXT structure solution program *via* the intrinsic phasing method in Olex2. Refinements of the structures used SHELXL with least squares minimisation.

Table 3.10. Crystal data and structure refinement for Zn-MOF-1.

Empirical formula	$C_{47}H_{39}N_6O_{13}Zn_2$
Formula weight	1026.58
Temperature/K	100.01(10)
Crystal system	monoclinic
Space group	$P2_1/c$
a/Å	14.6975(3)
b/Å	24.5795(4)
c/Å	15.9812(4)
α/°	90
β/°	105.121(2)
γ/°	90
Volume/Å^3	5573.4(2)
Z	4
ρ_{calc}g/cm^3	1.223
μ/mm^{-1}	0.920
F(000)	2108.0
Crystal size/mm^3	0.4 × 0.15 × 0.07
Radiation	Mo Kα (λ = 0.71073)
2Θ range for data collection/°	5.742 to 61.624
Reflections collected	75987
Independent reflections	16341 [R_{int} = 0.0661, R_{sigma} = 0.0736]
Data/restraints/parameters	16341/0/619
Final R indexes [I>=2σ (I)]	R_1 = 0.0803, wR_2 = 0.1580
Final R indexes [all data]	R_1 = 0.1204, wR_2 = 0.1770

The asymmetric unit (figure 3.42) of Zn-MOF-1 comprises of two zinc centres, one 4-MeUR-N and two OBA linkers. The asymmetric unit also contains two ordered DMF molecules, which have been removed from the majority of the further crystal structure images for clarity. All remaining pore content was diffuse in terms of resolving the electron density and hence was treated with the solvent mask algorithm in Olex-2. This electron density was estimated to be 82 electrons equating to 2.5 additional DMF molecules per asymmetric unit. The complete chemical formula of Zn-MOF-1 from SCXRD characterisation is therefore $[Zn_2(OBA)_2(4\text{-MeUR-N})]$ 4.5·DMF.

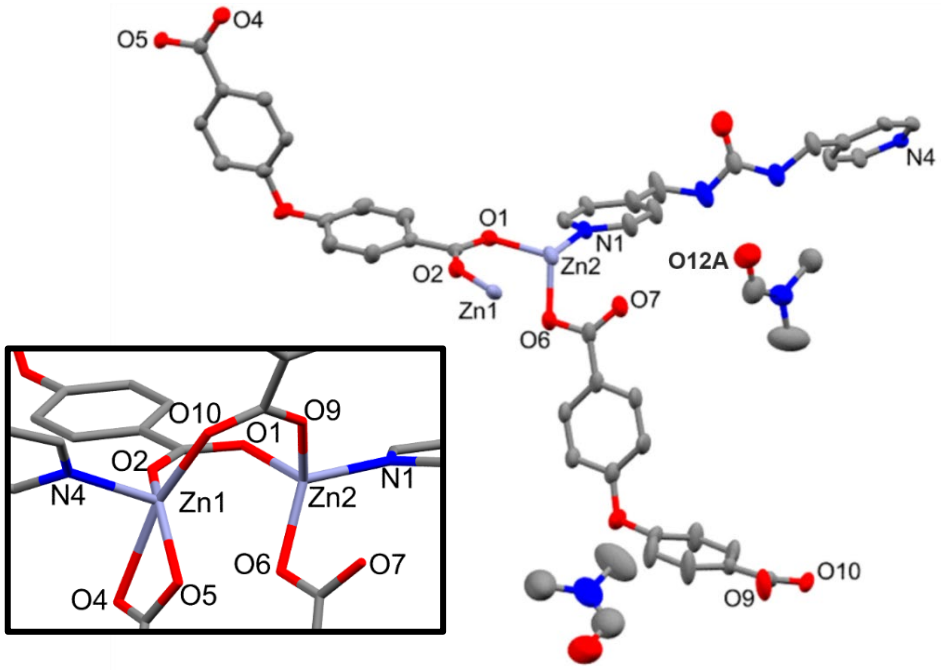

Figure 3.42. Asymmetric Unit of Zn-MOF-1. Thermal Ellipsoids are set to 40% probability. Hydrogen atoms have been removed for clarity. (Inset) The zinc coordination environments in Zn-MOF-1 showing the differing metal geometries. Zinc = purple, grey = carbon, red = oxygen and nitrogen = blue.

The secondary building unit (SBU) of Zn-MOF-1, shown in figure 3.42, consists of two zinc centres, one in a distorted tetrahedral geometry (Zn2) and the other in a distorted square pyramidal geometry (Zn1). Oxygen atoms from bridging carboxylic acid functionalities of two independent OBA linkers occupy two basal positions of the square pyramidal Zn1 centre (O2 and O10) and two of the tetrahedral positions of Zn2 (O1 and O9), analogous to the coordination seen in the paddlewheel SBU of HKUST-1.[47] The remaining two carboxylate groups of the OBA linkers are rotated approximately 90° and only coordinate to one metal centre. Chelating coordination of a carboxylic acid functionality from OBA (O4 and O5) occupies the two remaining basal positions of Zn1. The Zn1-O4 and Zn1-O5 bond lengths differ quite significantly (2.358(2) Å vs 1.993(2) Å respectively). This suggests that the 1- charge of the carboxylate group is not fully delocalised across the two C-O bonds but is concentrated on the Zn1-O5 bond, resulting in a stronger and thus shorter bond. The pyridine nitrogen (N4) from a 4-MeUR-N linker coordinates to Zn1 in the apical position. The remaining vacancies on the Zn2 centre are filled by one pyridine nitrogen (N1) of a 4MeUR-N linker as well as an oxygen atom from an OBA linker (O6).

The coordination of the SBU to independent 4-MeUR-N linkers results in the formation of linear chains that are coordinated to parallel chains in adjacent planes by OBA linkers. This connection by OBA generates hexagonal channels (figure 3.43) due to the bent ether linkage (106.7 - 106.9°) within the linker. Rectangular channels are also present when viewed along the crystallographic a-

axis. Crystallographic analysis, reinforced with topological analysis carried out with ToposPro, confirms a doubly interpenetrated structure that follows the **pcu** topology with the Schläfli symbol $\{4^{12}.6^{3}\}$.

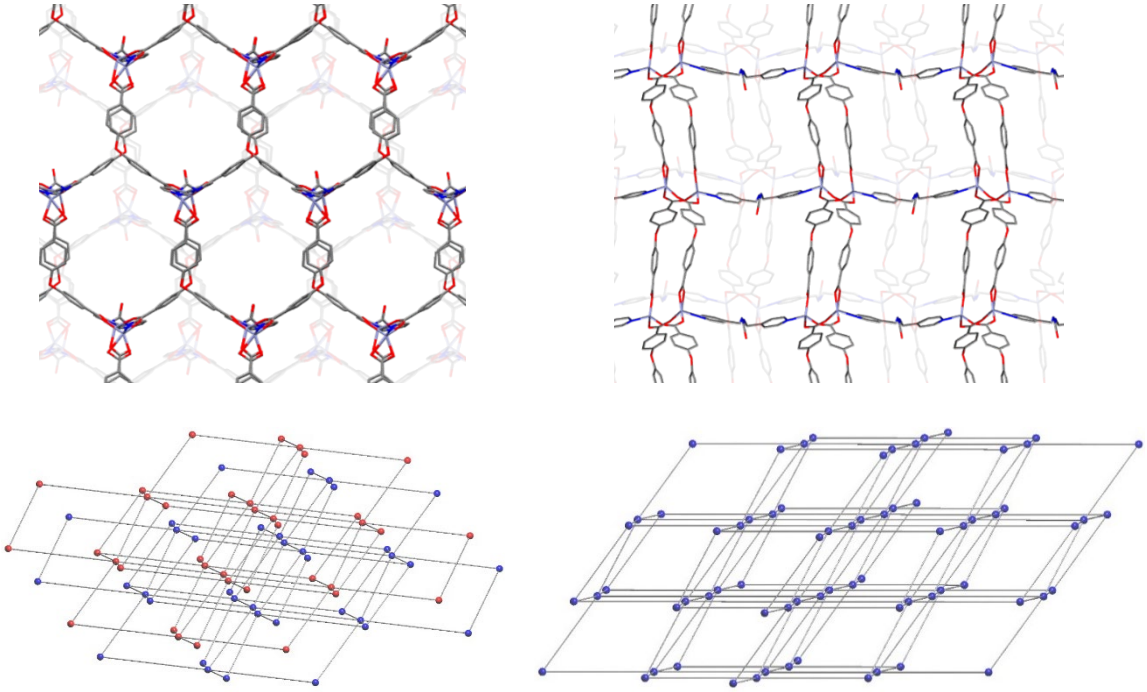

Figure 3.43. (Top row) (left) Hexagonal channels generated by the flexible OBA linker and (right) square channels in Zn-MOF-1. DMF solvent molecules have been omitted and the interpenetrating framework faded out to improve clarity. (Bottom row) (left) two-fold interpenetrated nets of Zn-MOF-1. (Right) single pcu net of Zn-MOF-1.

The close packing of the interpenetrating frameworks allows for the stabilisation, and crystallographic ordering, of two DMF molecules. One DMF molecule undergoes hydrogen bonding to the urea moiety of 4-MeUR-N, shown in figure 3.44. The remaining solvent molecules found within the framework voids lack these stabilising interactions and hence are disordered.

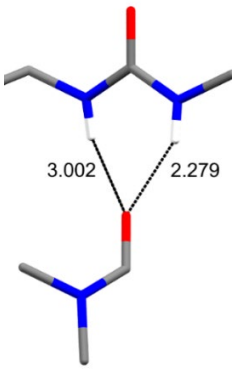

Figure 3.44. Hydrogen bond interaction between aldehyde carbonyl (O12A) of DMF and N-H protons of 4-MeUR-N urea. Non-interacting hydrogens have been omitted for clarity. Grey = Carbon, nitrogen = blue, oxygen = red and white = hydrogen.

A PXRD pattern comparison between the synthesised crystals of Zn-MOF-1 to that of a simulated pattern from the crystal structure is presented in figure 3.45. There is an overall good fit of the experimental pattern to the simulation. We can therefore confirm that the bulk of the synthesised crystals are the expected Zn-MOF-1 structure.

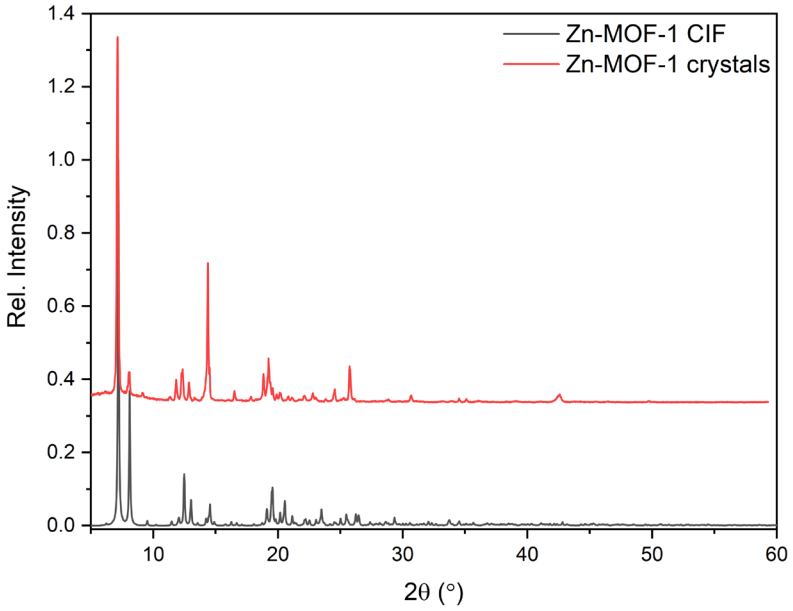

Figure 3.45. PXRD Comparison of synthesised Zn-MOF-1 to a simulated pattern generated from the crystal structure.

The stability of Zn-MOF-1 was also assessed through PXRD (figure 3.46). Approximately 50 mg of MOF was dried on filter paper and ground into a fine powder before being submerged in various solvents over 24 hours. We found that Zn-MOF-1 displays moderate stability in water and Sellafield groundwater simulant, the composition of which are tabulated in table A.1. There is a high degree of peak broadening, suggesting the degradation of Zn-MOF-1 crystals, as well as the loss of the (1,1,-1) peak at 8.1°. When dispersed in alcohols and acetone we found that the MOF degraded into the same, yet unknown, crystalline phase.

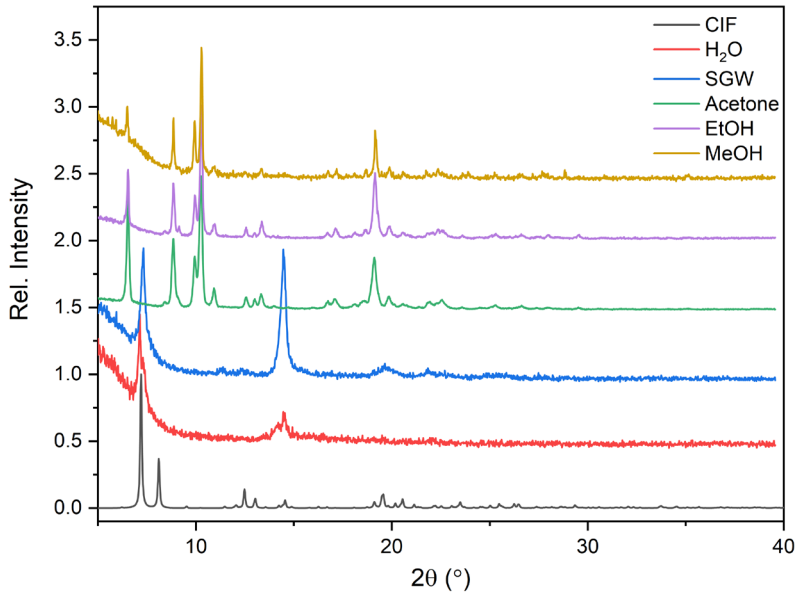

Figure 3.46. PXRD characterisation of Zn-MOF-1 after submersion in various solvents to assess the material's stability.

TGA of Zn-MOF-1 was carried out to assess the thermal stability of the material and to ensure that the composition of the synthesised material is as expected. The TGA plot can be found in figure 3.47 and shows three significant decomposition events. The first is the weight loss between 25 and 200 ˚C corresponding to solvent loss from the surface and pores of the MOF. This weight loss aligns well with the boiling point of DMF at 153 ˚C. The second weight loss occurs at around 300 ˚C and is as a result of the thermal decomposition of the organic components of framework. The last event is the residual mass, composed of zinc oxide, from around 750 ˚C.

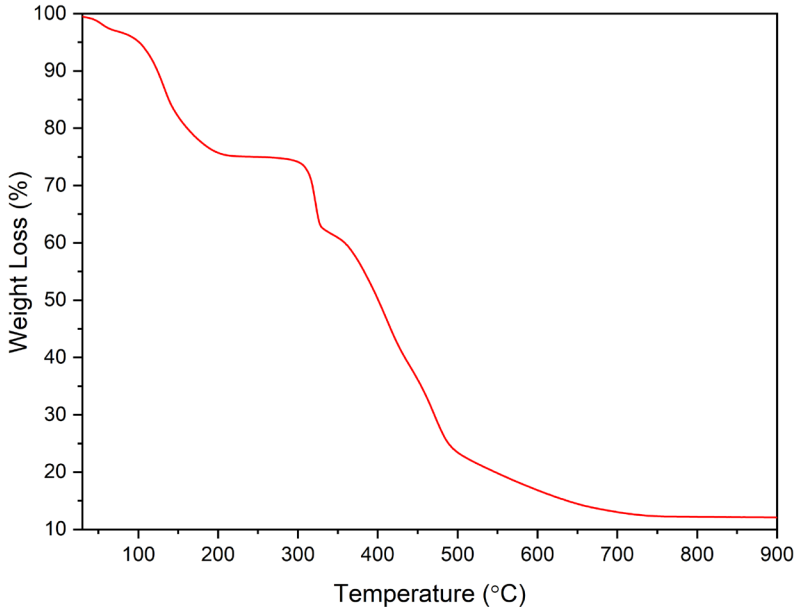

Figure 3.47. TGA of Zn-MOF-1.

Single-crystal characterisation has suggested that each asymmetric unit contains 4.5 DMF molecules and the framework has the composition [$Zn_2(OBA)_2$(4-MeUR-N)]. From these values we can derive theoretical solvent loss, organic loss, and residual mass values for Zn-MOF-1 (table 3.11). The experimental values, calculated from the mass profile in figure 3.47, align reasonably well with the theoretical values and further confirm to us that the material is phase pure and that the bulk composition is as expected from the crystal structure. The residual mass values lie very close to one another confirming the zinc content is correct. We do find a slight deviation from the solvent loss and organic mass loss values, which we attribute to DMF molecules found within the centre of the MOF crystals not being removed below 200 °C. Hence these solvent molecules were lost during the decomposition stage of the experiment at higher temperatures resulting in a lower than expected solvent loss step and a higher organic mass loss. This is quite reasonable due to the high density of Zn-MOF-1, caused by the doubly interpenetrated structure as well as stabilising hydrogen bond interactions between the urea moieties of the framework and DMF molecules that prevents solvent loss at lower temperatures.

Table 3.11. Zn-MOF-1 composition through TGA.

	Composition	Theoretical	Experimental
Solvent Loss (%)	DMF x 4.5	27	24.3
Organic mass loss (%)	(OBA x 2) + 4-MeUR-N – O	60	63.6
Residual mass (%)	(ZnO x2)	13	12.1
Total (%)	$Zn_2(OBA)_2$(4-MeUR-N)·4.5 DMF	100	100

FTIR spectroscopy of Zn-MOF-1 (figure 3.48) confirms the presence of DMF within the structure by the presence of absorbances at 2930, 2860 and 656 cm^{-1} which correspond to the asymmetric CH_3 stretch, symmetric CH_3 stretch and NCO & CN stretches respectively.[48] The C-O stretch of the ether linkage in OBA is present at 1155 cm^{-1}.

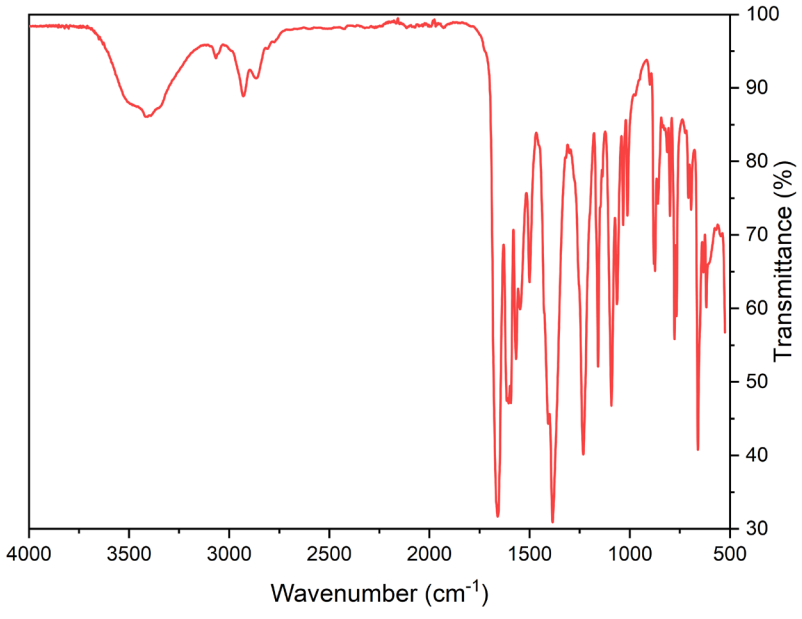

Figure 3.48. FTIR spectrum of Zn-MOF-1.

3.4.2 Zn-LMOF-2 ([Zn(IP)(4-MeUR-N)] 0.7·DMF)

While the flexibility of H_2OBA and 4-MeUR-N allows for the formation of large channels, an ideal characteristic of porous materials, it has resulted in two-fold interpenetration within Zn-MOF-1. This greatly reduces pore volume, increases material density, and makes void space in the material less accessible. We have therefore decided to alter the polycarboxylic acid linker to a less flexible molecule while maintaining the bent structure, in this case H_2IP (1,3-benzenedicarboxylic acid, isophthalic acid). The synthetic procedure was analogous to that of Zn-MOF-1 but H_2OBA was changed for an equimolar quantity of H_2IP. The resulting material was named herein as Zn-LMOF-2.

3.4.2.1 Characterisation of Zn-LMOF-2 ([Zn(IP)(4-MeUR-N)] 0.7·DMF)

The solvothermal reaction yielded orange crystals suitable for SCXRD. Crystal data and structure refinement details are presented in table 3.12. Single-crystal characterisation revealed a layered MOF (LMOF) structure, not the desired MOF material. A unit cell search of the CSD revealed four materials with cell similarities of greater than 95%. All of these materials however did not contain zinc or the organic linkers H_2IP and 4-MeUR-N thus Zn-LMOF-2 is not an already reported structure.

Table 3.12. Crystal data and structure refinement for Zn-LMOF-2

Empirical formula	$C_{21}H_{18}N_4O_5Zn$
Formula weight	471.76
Temperature/K	99.9(3)
Crystal system	monoclinic
Space group	$P2_1/n$
a/Å	14.1036(4)
b/Å	10.1825(2)
c/Å	17.8964(8)
α/°	90
β/°	101.593(4)
γ/°	90
Volume/Å^3	2517.67(15)
Z	4
ρ_{calc}g/cm^3	1.245
μ/mm^{-1}	1.009
F(000)	968.0
Crystal size/mm^3	0.16 × 0.07 × 0.05
Radiation	Mo Kα (λ = 0.71073)
2Θ range for data collection/°	5.898 to 64.646
Reflections collected	41061
Independent reflections	8435 [R_{int} = 0.0479, R_{sigma} = 0.0457]
Data/restraints/parameters	8435/0/280
Final R indexes [I>=2σ (I)]	R_1 = 0.0602, wR_2 = 0.1498
Final R indexes [all data]	R_1 = 0.0852, wR_2 = 0.1617

The asymmetric unit, shown in figure 3.49, of Zn-LMOF-2 consists of one zinc metal centre, an IP linker and a 4-Me-UR-N linker. A solvent mask was applied to the structure in Olex 2 to account for disordered DMF solvent that is present in the voids of the material. 24 electrons are present in the asymmetric unit, corresponding to 0.7 DMF molecules per asymmetric unit. The final chemical formula of Zn-LMOF-2 is therefore [Zn(4-MeUR-N)(IP)]0.7·DMF.

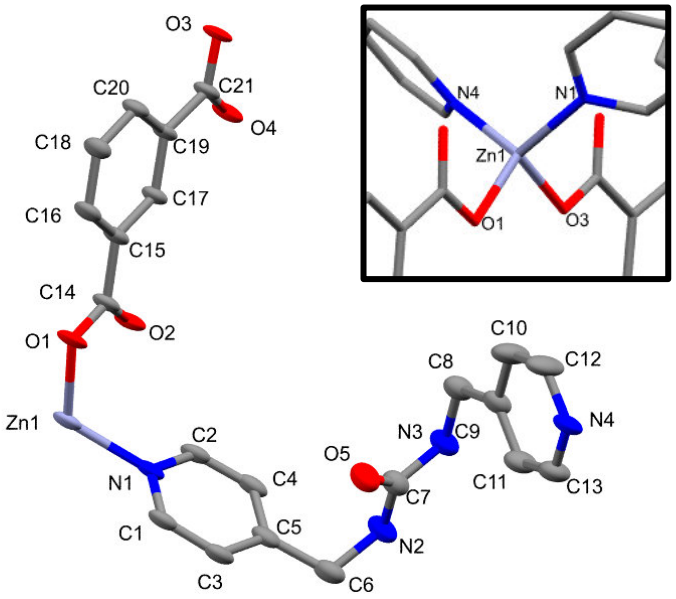

Figure 3.49. Asymmetric unit of Zn-LMOF-2. Thermal ellipsoids are set to 40% probability. (inset) The coordination environment of the tetrahedral zinc metal centre. Purple = zinc, red = oxygen, blue = nitrogen and grey = carbon. Hydrogen atoms have been omitted for clarity.

The zinc centre has a distorted tetrahedral geometry (table 3.13) which is also shown in figure 3.49. Each metal centre coordinates to two independent IP linkers through one oxygen of the carboxylic acid functionality (O1 and O3) as well as two independent 4-MeUR-N linker molecules through the pyridine nitrogen (N1 and N4). The Zn-O and Zn-N bond length pairs are very similar to one another (Zn-O1 = 1.973 Å & Zn-O3 = 1.985 Å, Zn-N1 = 2.031 Å & Zn-N4 = 2.052 Å). Atoms O2 and O4 of the IP linker do not coordinate to a metal centre and therefore are viable hydrogen bond acceptors.

Table 3.13. Bond angles around tetrahedral zinc centre of Zn-LMOF-2.

Atoms	Bond angle (°)	Atoms	Bond angle (°)
O1-Zn-N1	117.28(8)	O3-Zn-N1	108.14(8)
O1-Zn-N4	112.97(9)	O3-Zn-N4	105.28(8)
O1-Zn-O3	99.73(7)	N1-Zn-N4	112.97(9)

The two-dimensional sheets of Zn-LMOF-2 form through the bridging of 4-MeUR-N linkers across parallel one-dimensional chains of IP (figure 3.50). The IP chains have a separation of 12.46 Å. Topological analysis confirms a **sql** topology with the Schläfli symbol $\{4^4.6^2\}$.

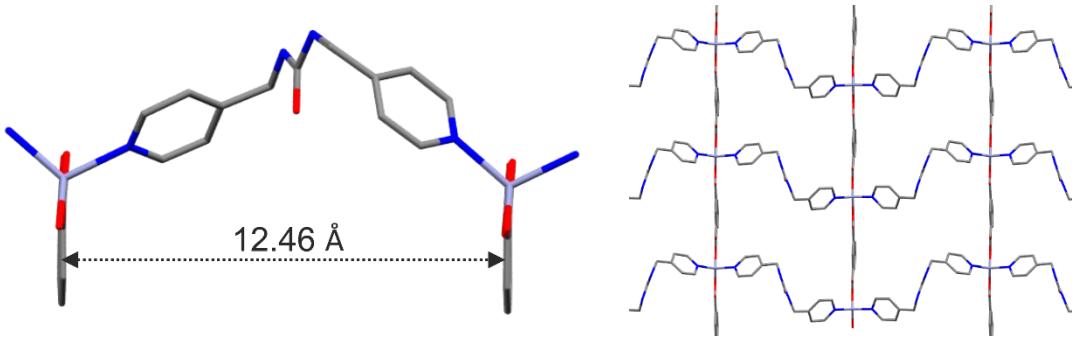

Figure 3.50. 4-MeUR-N linkers bridging one-dimensional IP linker chains in Zn-LMOF-2.

The two-dimensional sheets layer on top of one another in an AB fashion (figure 3.51). The direction of the C=O bond of the urea functionality of 4-MeUR-N is orientated perpendicularly to the sheet direction of Zn-LMOF-2 and alternates between facing up and down. Hydrogen bond interactions occur between the layers and aid in the stabilisation of the structure. These are formed between the N-H donor moiety of the urea and a non-coordinated oxygen from the carboxylic acid functionality of the IP linker. In figure 3.51 we have schematically demonstrated this with the arrows representing the carbonyl group of the urea and the circles representing the IP linkers. Additional stabilisation comes from the offset π-stacking that occurs between the aromatic rings of the IP linkers of layer A and the same moieties of layer B. Both stabilising interactions have been highlighted in figure 3.51.

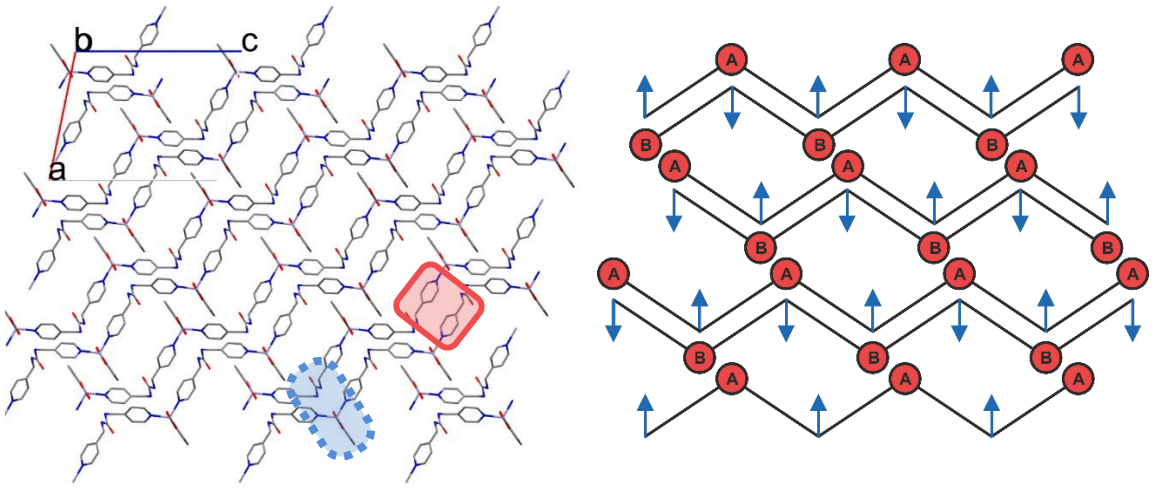

Figure 3.51. (Left) packing of the two-dimensional sheets of Zn-LMOF-2, viewed down the b axis. Hydrogen bond interactions are highlighted in blue (dashed) and offset π stacking in red. (Right) A schematic diagram to show the hydrogen bond and offset π stacking interactions, as well as the ABAB layering, in the overall structure of Zn-LMOF-2. The arrows represent the direction of the C=O bond of the urea group and the circles represent the IP linkers.

Analysis of the crystal structure to validate the offset π-stacking is necessary and was carried out using Mercury. The distance between the planes of adjacent aromatic rings was found to be around 3.6 Å, consistent with the literature reported range of 3.4 – 3.6 Å.[49] The offset angle was found to be 20.5° corresponding to an ring shift of 1.35 Å. This offset distance is almost equal to the length of a C-C bond and confirms that it is chemically sensible to categorise this as an offset π-stacking interaction.

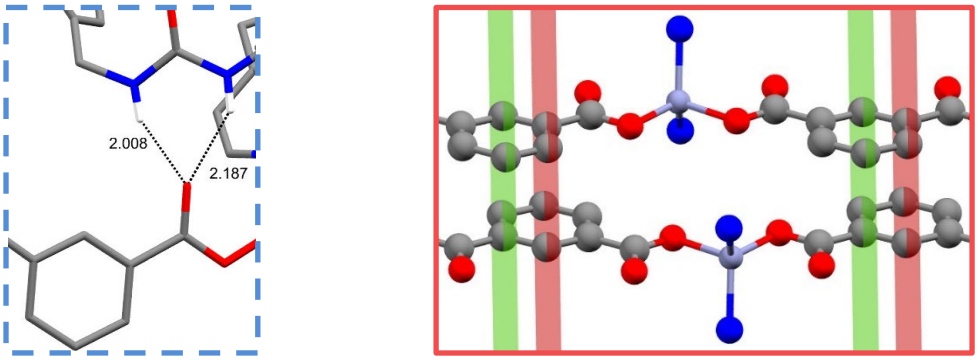

Figure 3.52. (Left) hydrogen bond interaction between urea N-H moieties of 4-MeUR-N and free carboxylate oxygen on IP.(Right) offset π-stacking between aromatic rings of IP linker. Green and red planes help visualise the offset π-stacking of IP linkers.

A portion of Zn-LMOF-2 crystals were dried, ground to a powder, and underwent PXRD characterisation. A comparison of the resulting pattern to the simulated pattern derived from the crystal structure shows good agreement (figure 3.53). It can therefore be confirmed that crystal structure represents the bulk product.

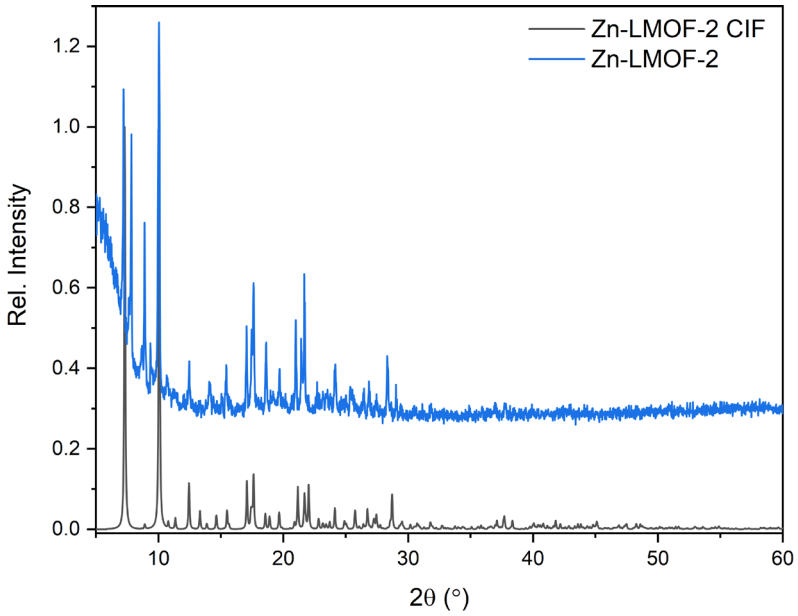

Figure 3.53. PXRD Comparison of synthesised Zn-LMOF-2 to a simulated pattern generated from the crystal structure.

Thermogravimetric analysis (TGA) was carried out on an air-dried portion of Zn-LMOF-2. Figure 3.54 includes the weight loss of Zn-LMOF-2 up to 900 ˚C. This material follows a similar profile to that seen for Zn-MOF-1 in section 3.4.1.1. Solvent is lost from the material up to around 300 ˚C at which temperature the organic components of the material undergo decomposition. At around 600 ˚C all organics have decomposed resulting in a residual mass of 11.8%. Taking into consideration the solvent mass loss step of the system the experimental organic loss and residual mass equate to 85.2% and 14.8% respectively. The expected organic content of Zn-LMOF-2, including the 0.7 DMF molecules per asymmetric unit, is 84.4% and therefore the residual mass should be 15.6%. Our experimental values for the composition of Zn-LMOF-2 align well with the expected values derived from the crystal structure. The TGA data also reveals to us that the disordered DMF molecules found within the voids of Zn-LMOF-2 are not able to escape the structure upon heating and are lost within the organic loss step. This is not surprising because the crystal structure suggests a dense material with small apertures.

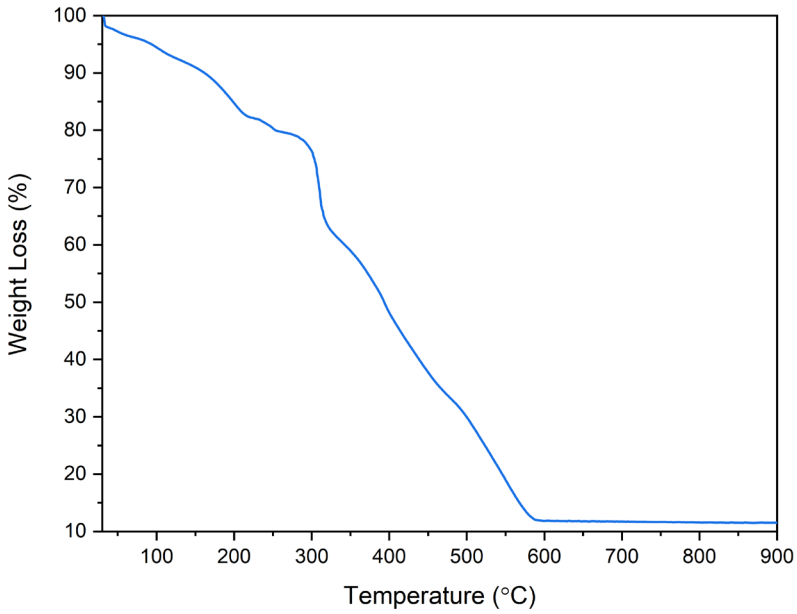

Figure 3.54. TGA of Zn-LMOF-2.

The presence of DMF within the as-made structure of Zn-LMOF-2 is confirmed by the presence of absorbances at 2930, 2863 and 658 cm^{-1} in the FTIR spectrum of a dried portion of the framework (figure 3.55). The strong absorbances at 1661 and 1605 cm^{-1} correspond to the C=O stretch and N-H bend respectively of the urea functionality in the 4-MeUR-N organic linker. In addition, broad absorbances at 3369 and 3318 correspond to the N-H stretch of the urea group.

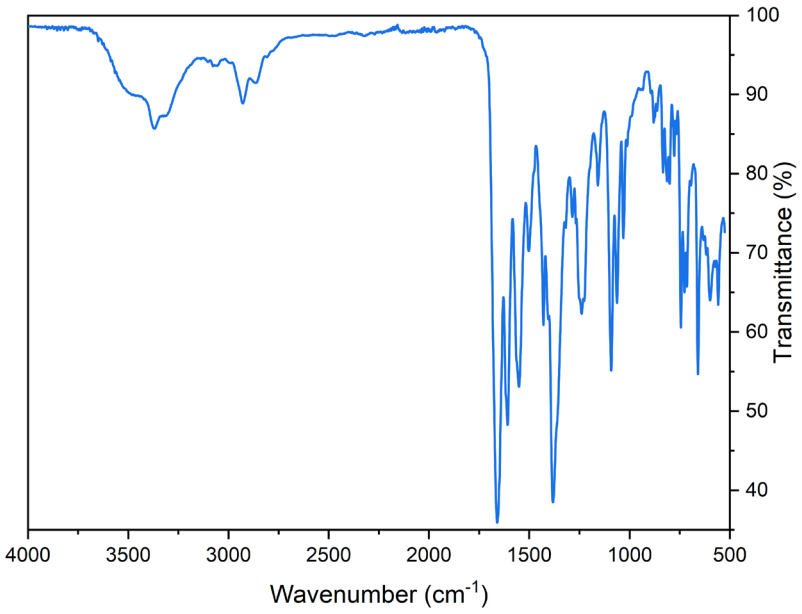

Figure 3.55. FTIR spectrum of Zn-LMOF-2.

3.4.3 Zn-LMOF-3 ([Zn(UR-CO_2H)(H_2O)$_2$])

A zinc-based layered-MOF was synthesised using the dicarboxylic acid organic linker, UR-CO_2H (UR-CO_2H = 4,4'-(carbonylbis(azanediyl)) dibenzoic acid) through a layered solution experiment. $Zn(NO_3)\cdot 6H_2O$ was dissolved in 10 mL of deionised water and added to a test tube. An equal volume of water was carefully added on top of the metal salt solution. This was followed by 10 mL of water containing UR-CO_2H. The test tube was left unagitated for one week resulting in the formation of crystals with the chemical formula [Zn(UR-CO_2H)(H_2O)$_2$], named herein as Zn-LMOF-3, that were suitable for SCXRD experiments. A crystalline powder of Zn-LMOF-3 could be obtained by combining aqueous solutions of the same precursors, under stirring, at room temperature for 24 hours. A white precipitate, indicative of Zn-LMOF-3 formation, formed instantaneously.

3.4.3.1 Characterisation of Zn-LMOF-3 ([Zn(UR-CO_2H)(H_2O)$_2$])

Table 3.14 contains the structure refinement details from a SCXRD experiment performed on a suitable needle crystal of Zn-LMOF-3. The unit cell dimensions were compared to structures in the Cambridge Structural Database (CSD) yielding six results that had matches greater than 95%. None of these structures however contained zinc or the UR-CO_2H linker therefore we can strongly postulate that this is a new structure.

Table 3.14. Crystal data and structure refinement information for Zn-LMOF-3.

Empirical formula	$C_{15}H_{14}N_2O_7Zn$
Formula weight	399.65
Temperature/K	99.97(13)
Crystal system	monoclinic
Space group	$P2_1/c$ (14)
a/Å	16.3672(5)
b/Å	9.2707(3)
c/Å	10.0555(3)
α/°	90
β/°	98.451(3)
γ/°	90
Volume/Å^3	1509.21(8)
Z	4
ρ_{calc}g/cm^3	1.759
μ/mm^{-1}	1.672
F(000)	816.0
Crystal size/mm^3	0.45 × 0.05 × 0.03
Radiation	MoKα (λ = 0.71073)
2Θ range for data collection/°	6.008 to 64.69
Reflections collected	24646
Independent reflections	5127 [R_{int} = 0.0412, R_{sigma} = 0.0371]
Data/restraints/parameters	5127/0/228
Final R indexes [I>=2σ (I)]	R_1 = 0.0383, wR_2 = 0.0833
Final R indexes [all data]	R_1 = 0.0468, wR_2 = 0.0882

The asymmetric unit of Zn-LMOF-3, shown in figure 3.56, comprises of one zinc metal centre, one UR-CO_2H linker and two water molecules coordinated to the metal centre. Each zinc centre has a distorted octahedral geometry (bond angles ranging from 60.23° – 96.49°) and as well as the two water molecules (O6 and O7) is coordinated to three independent URCO_2H linkers through oxygen atoms of the carboxylate functionality (O1, O2, O4 and O5). Two of the equatorial coordination positions on each zinc are occupied by a chelating carboxylic acid functionality (O4 and O5) of UR-CO_2H. Bridging dicarboxylic acid moieties (O1 and O2) between adjacent zinc metal centres results in the formation of an infinite SBU. The remaining axial and equatorial positions are occupied by oxygen atoms of independent water molecules. The overall chemical formula for Zn-LMOF-3 is therefore [Zn(UR-CO_2H)(H_2O)$_2$].

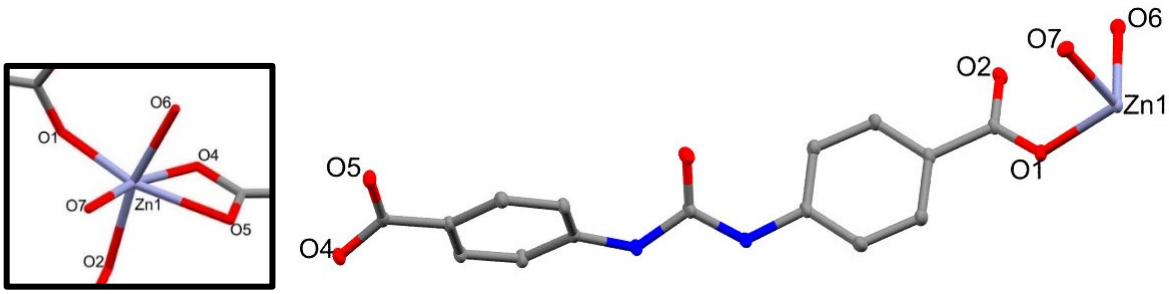

Figure 3.56. (Left) octahedral zinc coordination environment. (Right) Asymmetric unit of Zn-LMOF-3. Thermal ellipsoids are set to 40% probability. Hydrogen atoms have been removed for clarity. Zinc = purple, grey = carbon, red = oxygen and nitrogen = blue.

Figure 3.57. shows the formation of infinite SBUs through the bridging functionality of the carboxylate group of UR-CO_2H (O1 and O2). Here it is clearly visible that this bridging of the metal centres results in the formation of a two-dimensional sheet. The two-dimensional sheets stack in an AA fashion, resulting in a dense structure. Along SBU chains the UR-CO_2H orientate in such a way that the urea C=O bond alternates between pointing up, or downwards to minimise void space.

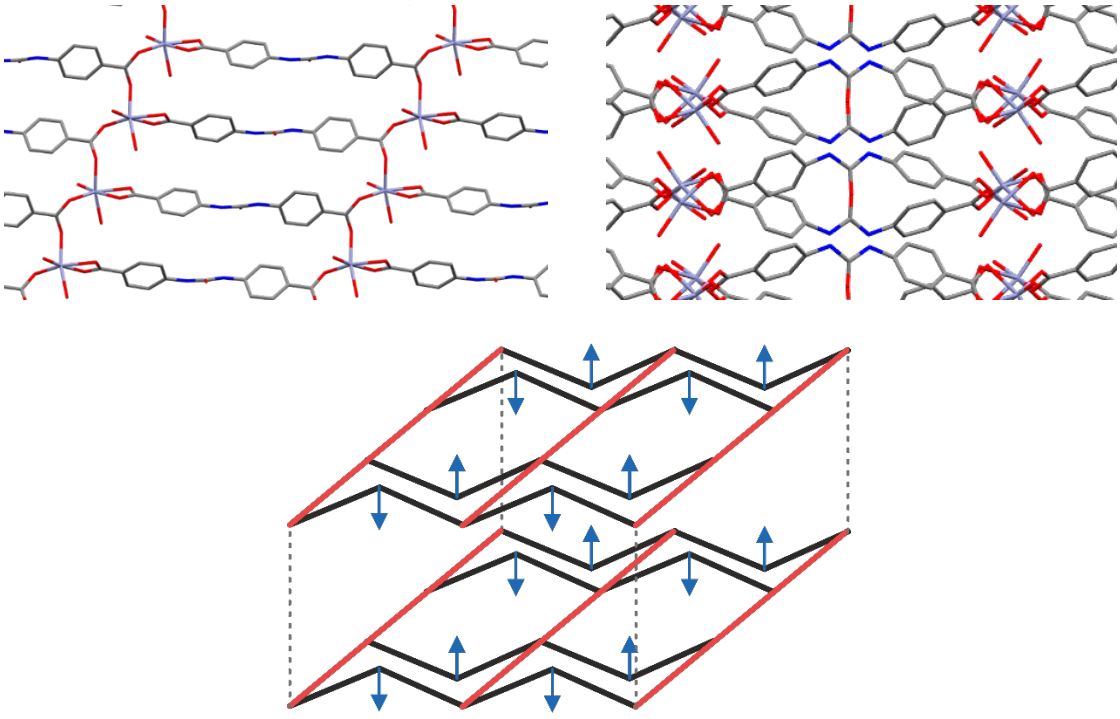

Figure 3.57. (Clockwise from top left) The infinite SBUs of Zn-LMOF-3 and resulting two-dimensional sheets, viewed down the b axis. The layering of sheets within Zn-LMOF-3, viewed down the c axis. Hydrogen atoms have been removed for clarity. A schematic diagram showing the AA layering within Zn-LMOF-3 whereby the arrows show the direction of urea tapes.

Urea's ability to self-associate into α-networks (urea tapes), consequential of the hydrogen bond donor N-H and hydrogen bond acceptor C=O groups found in the functional group, aid in stabilisation of the two-dimensional sheets (figure 3.58).[50] Atom distances in the crystal structure

align with typical values found in the literature for urea tapes. The repeating distance of the α-network in Zn-LMOF-3, measured between the carbonyl carbons of adjacent ureas, is found to be 4.638 Å which is comparable to the literature value of 4.60 Å.[51] The N-H···O hydrogen bond distances between adjacent ureas are also 2.868 Å and 2.821 Å, typical values for hydrogen bonds of this nature.[52] There is also a C_2 point group that runs through the carbonyl bond of the urea, a typical symmetry operation of ureas.[51]

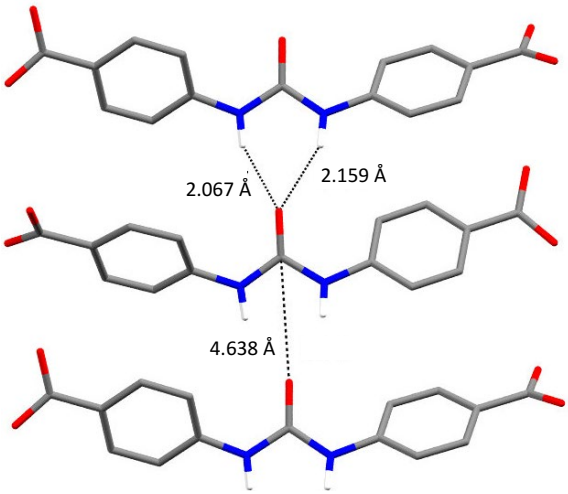

Figure 3.58. Urea tape formation in Zn-LMOF-3. Hydrogen bond interactions are between parallel sheets. Distances measured refer to the N-H···O distances and distance between the carbonyl carbons of parallel layers within Zn-LMOF-3.

Experimental PXRD patterns were obtained of Zn-LMOF-3 from both crystals grown *via* the layering method and the microcrystalline powder formed in the stirring reaction. A portion of the latter material was dried at 50 °C for 24 hours to assess the thermal stability of the material. Comparing these patterns with a simulated pattern derived from the crystal structure of Zn-LMOF-3, in Figure 3.59, confirms that the structure is representative of the bulk sample. An additional peak present at 10° in the stirred product patterns suggests the presence of an impurity that was not removed during washing in water. Portions of the material were further washed with ethanol, methanol, DMF, acetone and DMSO to test both the solvent stability of Zn-LMOF-3 and to see if the peak could be removed. This was carried out by sonicating a portion of Zn-LMOF-3 for one hour at room temperature in each solvent. The resulting PXRD patterns (figure A.29) still contained the additional peak, excluding the DMF and DMSO products which underwent a phase transition and complete degradation respectively. This suggests that this additional peak may not actually come from an impurity but rather is a Bragg reflection that has very low intensity from the single crystal sample. We believe this arises from preferred orientation, further corroborated from SEM which concludes a thin plate crystal morphology, resulting in consistent peak intensities between samples.

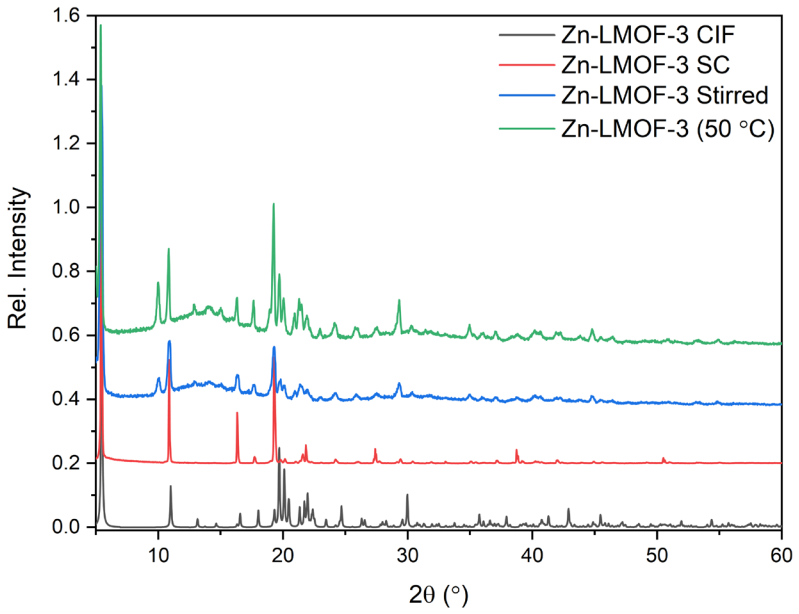

Figure 3.59. PXRD comparison of experimental and simulated patterns of Zn-LMOF-3.

The powder pattern of the DMF product was compared to a series of frameworks reported by Forgan *et al.*[53] These reported MOFs all consist of both zinc, UR-CO_2H, various amounts of DMF, and in some cases contain crystallographically ordered CS_2 guest molecules. There is a good match between our powder pattern and that simulated from CCDC entry 1558149 (figure 3.60). This strongly suggests that Zn-LMOF-3 undergoes a facile transformation to a porous MOF with the chemical formula $[Zn_4O(UR\text{-}CO_2H)_3(DMF)]$.

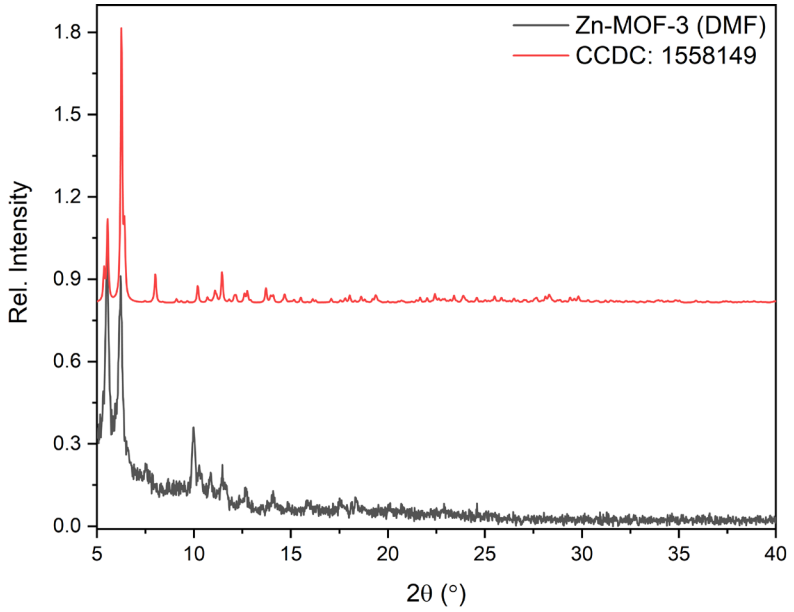

Figure 3.60. PXRD pattern comparison of Zn-LMOF-3 (DMF) to the crystal structure of CCDC entry 1558149.[53]

SEM shows a clear change in crystal morphology upon the submersion of Zn-LMOF-3 in DMF (figure 3.61). As synthesised Zn-LMOF-3 has a plate morphology with the longest length typically being less than 10 µm. Washing in ethanol, methanol, THF and acetone does not change this crystal

morphology however submerging the LMOF in DMF causes the crystal morphology to transform to semi-spherical crystals less than 5 µm in diameter. Submerging the transformed MOF back into water appears to result in the formation of Zn-LMOF-3 plates on the surface of the $Zn_4O(UR\text{-}CO_2H)_3(DMF)$ crystals however PXRD was not convincing for the presence of Zn-LMOF-3. This may have been due to an overlap of peaks from the two materials or the low quantity of Zn-LMOF-3 present.

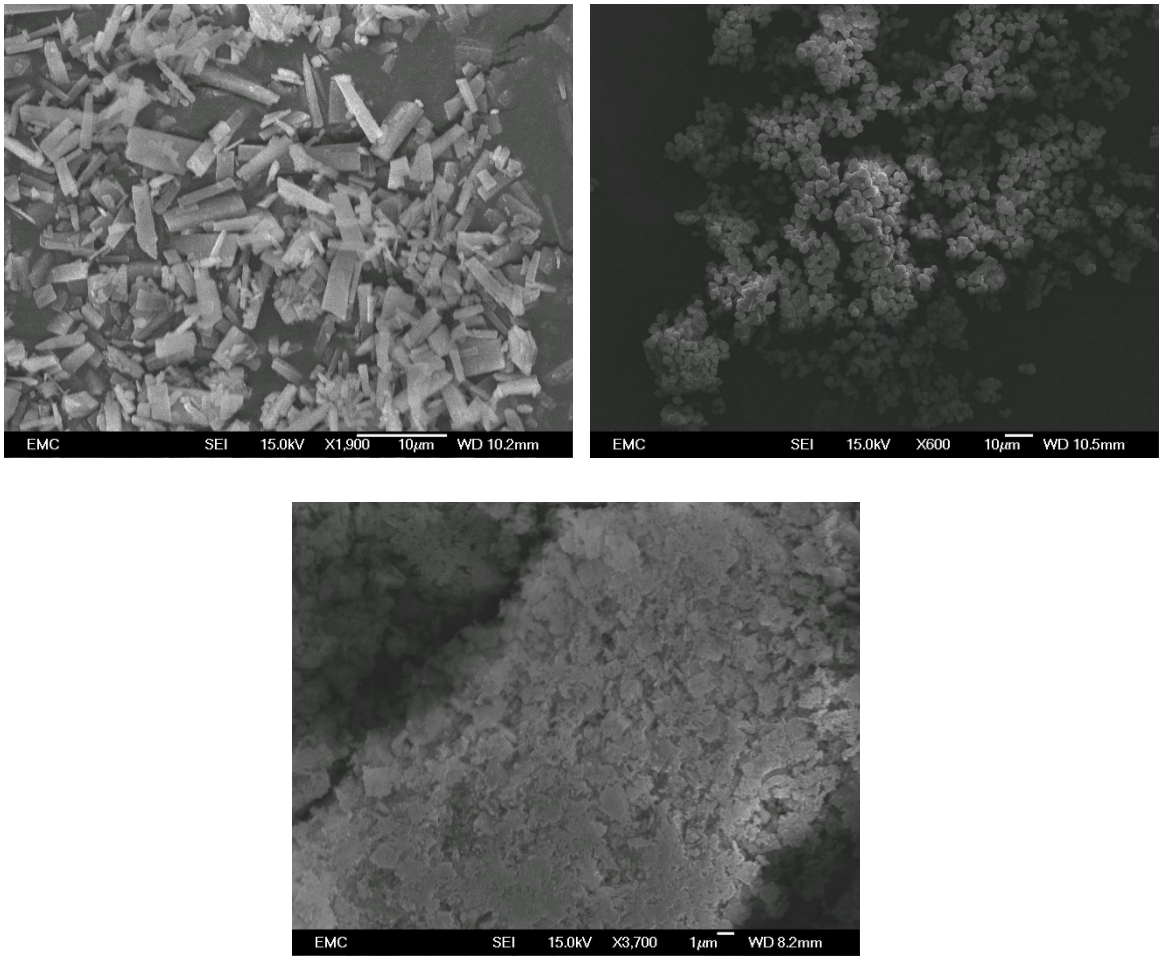

Figure 3.61. (Top) SEM images of (left) Zn-LMOF-3, (right) Zn-LMOF-3 after immersion in DMF (scale bars = 10 µm). (Bottom) SEM image of Zn-LMOF-3-DMF after being immersed back into H_2O (scale bar = 1 µm).

TG analysis of Zn-LMOF-3 is presented in figure 3.62. The decomposition of Zn-LMOF-3 results in two mass loss stages. The first occurs at 150 °C, corresponding to solvent loss and the second, at 300 °C, due to the decomposition of the organic components of the LMOF. The residual mass, consisting of ZnO, is found from 800 °C.

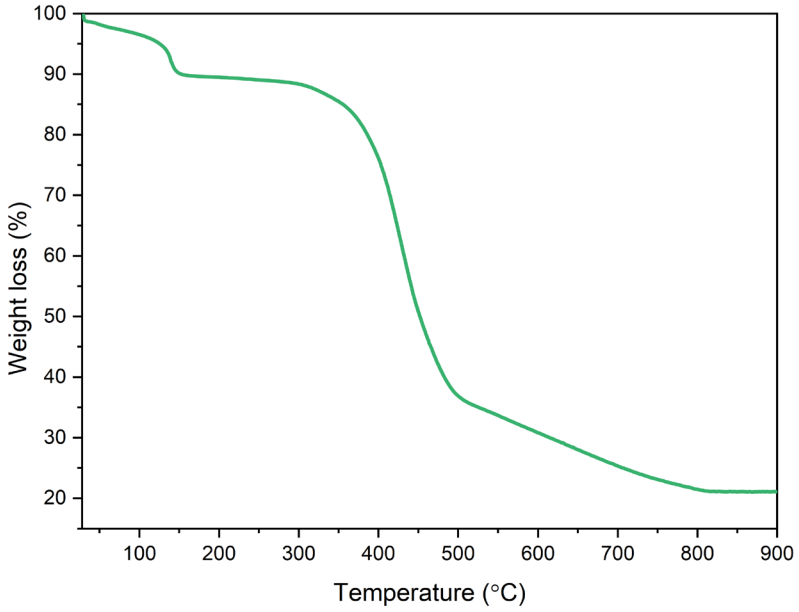

Figure 3.62. TGA of Zn-LMOF-3.

Prior to TGA the sample was heated to 50 °C under an air atmosphere to ensure it was dry. We can therefore presume that any mass loss below 300 °C corresponds to the loss of water molecules coordinated to the zinc centres. Experimentally, this equates to 9.5% of the material. The organic loss experimentally equates to 69.5% and the residual mass is 21.5%. A comparison of the expected, derived from chemical formula obtained through SCXRD, and experimental values for each stage are presented in table 3.15. The values align very well, therefore it can be confirmed that the synthesised material is phase pure, with the expected composition.

Table 3.15. Mass losses found through TGA of Zn-LMOF-3.

	Composition	**Theoretical (%)**	**Experimental (%)**
Solvent Loss (%)	H_2O x 2	9	9.5
Organic Loss (%)	UR-CO_2H – O	71	69.0
Residual Mass (%)	ZnO	20	21.5
Total	Zn(UR-CO_2H)(H_2O)$_2$	100	100

The FTIR spectrum of Zn-LMOF-3 (figure 3.63) confirms the presence of Zn-(OH_2) bonds through the broad, yet weak, absorbance centred at 3220 cm^{-1}. The strong absorbance at 1520 cm^{-1} further confirms the bending mode of water. The urea functionality of UR-CO_2H is present in the spectrum at 1645 and 1605 cm^{-1}, representing the C=O stretch and N-H bend respectively.

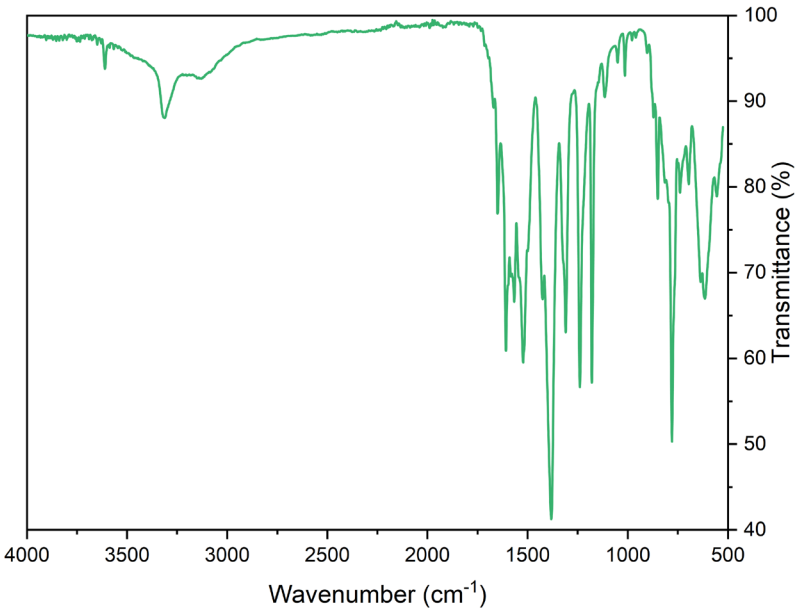

Figure 3.63. FTIR spectrum of Zn-LMOF-3.

3.4.4 Discussion

3.4.4.1 Zn-MOF-1

As a result of the varying bonding modes observed by the carboxylic acid functionalities of the 4,4'-oxybisbenzoic acid (H_2OBA) organic linkers, the zinc centres of Zn-MOF-1 exhibit different distorted geometries, one tetrahedral and the other square pyramidal. It is rare to observe an SBU that is formed by three different carboxylate bonding modes as seen in the resulting SBU of Zn-MOF-1. SCXRD has confirmed that four carboxylic acid groups from independent OBA linkers coordinate to either one or both metal centres through bridging, chelating or monodentate bonding modes, highlighted green, yellow and orange respectively, in Figure 3.64.

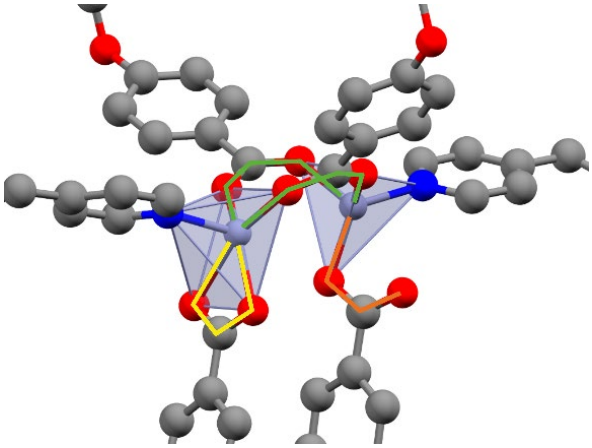

Figure 3.64. The different carboxylate coordination modes present in the SBU of Zn-MOF-1.

Despite the unusual building blocks of the SBU its overall geometry is octahedral and follows the most commonly found unimodal octahedral topology, **pcu**. The hexagonal channels found within

Zn-MOF-1 make the assigned topology appear to be incorrect, because it suggests a honeycomb structure which would not be consistent with the **pcu** topology. The hexagonal channels arise from the flexibility of the OBA^{2-} linker not the MOF topology, however. The C-O-C bonds of the two ether linkages in the OBA^{2-} linkers within the asymmetric unit (Figure 3.42) bend to angles of 116.7(2) and 116.9(3)°. These two bond angles are very close to the internal bond angles of a hexagon (120°) but the connectivity of the SBUs within Zn-MOF-1 maintains a **pcu** net.

The urea functionalities of the 4-MeUR-N linker undergo hydrogen bonding to the carbonyl oxygen of one of the crystallographically ordered DMF molecules. For successful binding of oxo-anions to the urea group these solvent molecules would need to be removed, ideally through a solvent exchange process. Upon submerging a ground powder of Zn-MOF-1 in different solvents we found that the MOF underwent disadvantageous transformations. When submerged in deionised water or Sellafield groundwater simulant the MOF underwent degradation, observed through peak broadening and an overall decrease in crystallinity within the resulting PXRD patterns (figure 3.46). When submerged in organic solvents such as acetonitrile or ethanol, the MOF transformed into a different, unknown, crystalline material. The lack of stability of Zn-MOF-1 within organic solvents makes the process of solvent exchange to remove the hydrogen-bonded DMF molecules more difficult. However, the poor stability within aqueous media suggests that this MOF would not be a suitable pertechnetate adsorbent anyway. We therefore have chosen to not take this framework forward for remediation testing.

3.4.4.2 Zn-LMOF-2 & Zn-LMOF-3

Exchanging the H_2OBA linker in the synthesis of Zn-MOF-1 with H_2IP has a profound effect on the resulting material. Our initial aim of trialling this was to halt the interpenetration observed in Zn-MOF-1 by replacing the flexible dicarboxylic acid linker with a shorter more rigid linker that still observes a bent configuration, due to the meta positioning of the carboxylic acid groups. The resulting material, Zn-LMOF-2, has a layered two-dimensional sheet topology with no covalent bonding in the layer stacking direction aligned along the crystallographic z-axis. Instead, availability of hydrogen bond donor groups (ureas) in 4-MeUR-N and hydrogen bond acceptor groups in IP (oxygen atoms of carboxylates) results in hydrogen bonding between the layers. Similarly, a layered MOF has been formed by reacting zinc nitrate with UR-CO_2H at room temperature to afford Zn-LMOF-3. The urea groups of UR-CO_2H form urea ladders between parallel sheets, forming a robust material. Zn-LMOF-3 is synthesised in deionised water and thus deemed to be water stable.

Most urea moieties found within Zn-LMOF-2 and Zn-LMOF-3 are blocked from interacting with oxo-anions, such as perrhenate and pertechnetate, because of the dense layering within these materials. Our LMOFs could potentially be exfoliated to separate the bulk material into thinner layers exposing the urea moieties (figure 3.65), that were blocked by hydrogen bond interactions with adjacent nanosheets, and thus making them available for hydrogen bonding to anions such as perrhenate and pertechnetate.

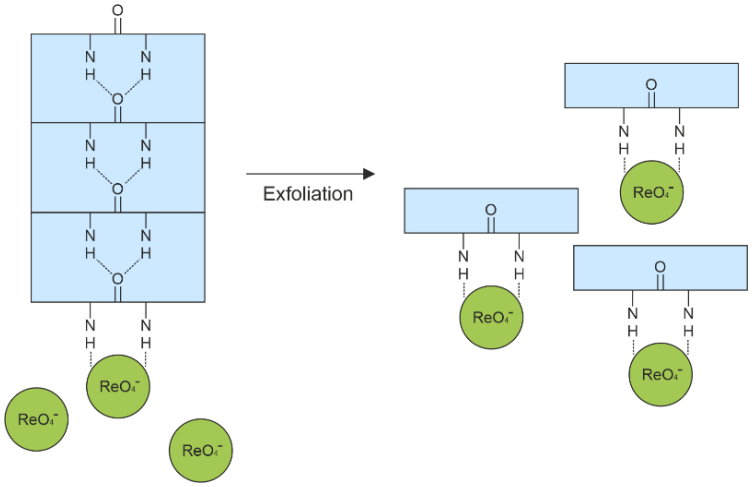

Figure 3.65. Schematic diagram of a proposed exfoliation strategy of LMOFs to increase the number of urea functionalities available to enhance ReO_4^- binding and uptake.

If exfoliation of Zn-LMOF-2 and Zn-LMOF-3 to MONs is possible we would have to carefully consider how the materials are used in our desired application. The nanosheets would no longer be a bulk solid but a suspension in solvent. A key factor in using porous materials in anion remediation from solution is that one can easily recover the solid material from solution by filtration or centrifugation. This advantage is lost if the chosen material is only suitable as a suspension, not an easily retrievable solid. Porphyrin-based nanosheets have been utilised in the nanofiltration of organic dyes from contaminated water.[54] The MONs were formed into membranes through the introduction of polycations, such as polyethylenimine, which cross-linked the periphery carboxylic acid groups of the metal nodes resulting in highly ordered and continuous films.

A different method to mitigate this issue could be to look at encapsulating the MONs in an alginate composite, similar to the systems investigated in our UiO-66-NH_2@alginate work reported in chapter two. Carboxylate tags on the guluronic acid monomers of alginate are essential in the ionotropic gelation of the polymer to form a composite. The carboxylate moieties on the mannuronic acid monomers are not involved in gelation and hence would be available for hydrogen bonding to the urea moieties of Zn-LMOF-3 and Zn-LMOF-2. By controlling the mannuronic acid content of the alginate we could ensure that the majority of urea moieties on the MONs are free to coordinate to oxo-anions, such as perrhenate and pertechnetate, whilst also hopefully stabilising

the MON in the composite through urea-mannuronic carboxylate hydrogen bond interactions. It is recognised however, that the alginate would act as a supporting scaffold and hence we would not be able to class these materials as MON composites.

The pursuit of exfoliation of these two layered MOFs was desired, however due to time constraints could not be further investigated; however, the solvent stability of Zn-LMOF-3 was assessed by submerging the MOF in various solvents and sonicating for one hour. The LMOF was stable in all assessed solvents, excluding DMSO, which degraded the material completely. Sonication of Zn-LMOF-3 in DMF resulted in a transformation to a previously reported MOF (Zn-LMOF-3 (DMF)) by Forgan *et al.*,[53] suggesting a less energy intensive alternative to accessing the Zn-LMOF-3 (DMF) MOF. SEM imaging confirms a change in crystal morphology, from thin sheets to spherical particles upon reaction with DMF. We found that submerging Zn-LMOF-3 (DMF) in water and sonicating did not cause the reverse reaction to occur, as found by PXRD, which suggests that the DMF containing MOF has a higher stability than Zn-LMOF-3. We did however find suggestive evidence, *via* SEM, that Zn-LMOF-3 forms on the surface of the Zn-LMOF-3 (DMF) crystals. This possibly means that the reverse reaction, in water, can occur but is much slower than the forward reaction in DMF.

3.5 Conclusion and Future Work

In this body of work, we have collected 14 crystal structures; 11 silver coordination polymers and three zinc-based MOFs. 11 of these structures are new and have not previously been reported. The aim of this chapter was to explore the crystal engineering of coordination polymers and MOFs that include urea-based organic linkers for the remediation of perrhenate from solution.

Our silver work had the intended application of perrhenate remediation *via* a selective crystallisation mechanism, whereby the anion is removed from contaminated solutions by its crystallisation, and immobilisation, during the formation of a coordination polymer. For this mechanism to be fruitful, the chosen metal and organic linker should only react and form a crystalline coordination polymer with perrhenate and therefore not react with competing anions, such as NO_3^-, SO_4^{2-}, Cl^- or CO_3^{2-}. We explored three organic linkers which are structural isomers of one another; (N,N'-bis(2-pyridylmethyl)urea, N,N'-bis(3-pyridylmethyl)urea and N,N'-bis(4-pyridylmethyl)urea).

To find an optimal system to focus this study on we explored different combinations of urea-based organic linkers and anions with silver (I) sources to crystallise coordination polymers of these starting building blocks. Our aim was to find an organic linker that would form a silver coordination polymer with ReO_4^- counterbalancing anions but not form any crystalline material when the anion is swapped for a different anion. The [Ag(2-MeUR-N)] was initially found to be the best system for selectively crystallising ReO_4^- because Ag^+ and 2-MeUR-N would not react with NO_3^- or SO_4^{2-} to form their corresponding coordination polymers. Unfortunately, sulphate was eventually crystallised in the [Ag(2-MeUR-N)] system. In addition, trialling the reaction of chloride and carbonate anions with Ag (I) and 2-MeUR-N resulted in the precipitation of their respective silver salts. This negatively affects the crystallisation of perrhenate from solution because crystallisation of salts, such as silver nitrate, occur much faster than the crystallisation of 2-ReO_4. Therefore, the silver ions would preferentially react with the chloride or carbonate anions over the perrhenate anion.

The Ag(3-MeUR-N)] and [Ag(4-MeUR-N)] systems also yielded similar results. Sulphate and nitrate both crystallise in these systems and thus they would not show any preference for perrhenate over these anions. Due to the lack of suitability of all three systems, we did not pursue further characterisation or testing.

While these results are disappointing, we recognise that these studies have provided insight into the effect that anions play on the topology and overall structure of silver coordination polymers. The urea group present within the organic linkers have a high affinity to one another, therefore urea ladders are very common within these materials. In some cases, these hydrogen bonds can be

overcome, resulting in the hydrogen bonding of anions, and solvent molecules to these urea groups. We have shown that tetrahedral anions often behave very similarly when incorporated into the same coordination polymer system and that the use of divalent anions can result in direct coordination to the silver centres.

Future work on these systems could involve collecting a full suite of characterisation data including PXRD, TGA and FTIR, to support the crystal structures that we have solved.

Within our zinc work, we have synthesised three new MOFs and LMOFs. Zn-MOF-1 is a doubly interpenetrated, mixed linker framework consisting of 4-MeUR-N and H_2OBA linkers. The MOF has a **pcu** topology, and due to the bent configuration of OBA has hexagonal channels. The SBUs consist of two zinc (II) centres and a partial paddlewheel configuration. Crystallographically isolated DMF molecules have been found within the crystal structure of Zn-MOF-1, one of which undergoes hydrogen bonding to the urea group of 4-MeUR-N. PXRD and TGA confirmed that the material can be synthesised in a phase pure manner. It was however found that the material degrades upon submersion in water or organic solvents, and therefore is not suitable for aqueous applications.

Zn-LMOF-2 is a layered MOF composed of zinc PBUs and 4-MeUR-N & H_2IP linkers. The linkers form a **sql** topology network whereby chains of 4-MeUR-N run across one direction and chains of IP run perpendicular. The sheets of Zn-LMOF-2 layer in an ABAB fashion undergoing stabilising hydrogen bond interactions between the urea groups of 4-MeUR-N and oxygen atom of the carboxylate group of IP. This material was synthesised because we wanted to assess the affect that reducing the length and flexibility of the carboxylic acid linker plays on the structure of Zn-MOF-1. Altering the carboxylic acid linker however, has a dramatic effect on the topology and structure of the resulting material. TGA and PXRD confirms the material can be synthesised solvothermally in DMF and is phase pure.

Zn-LMOF-3 is the final material that we have synthesised. It consists of infinite zinc SBUs and UR-CO_2H linkers. The material is very dense, with no potential void space. Urea ladders form between the urea groups of parallel sheets. The material can be synthesised at room temperature, yielding a microcrystalline, phase pure powder. Sonication in DMF results in a transformation to a different MOF that has previously been reported. This was confirmed *via* PXRD. SEM imaging of the crystals show a change in crystal morphology from thin sheets to spherical particles as a result of this transformation. Submersion of the DMF exchanged Zn-LMOF-3 crystals back into water did not alter these PXRD pattern, but a change to the surface of the Zn-LMOF-3 crystals (DMF) suggests that some transformation of the MOF has been observed. This suggests that the reaction is reversible, but at a much slower rate than the forward transformation in DMF.

The latter two materials are very dense, and most urea groups are blocked by the parallel layering of the two structures. We have proposed that exfoliation may be possible, to free up these urea groups for perrhenate binding. We suggest this to be the next step with this work, particularly with Zn-LMOF-3 because of its stability in aqueous media.

3.6 Experimental

3.6.1 Synthesis of N,N’-bis(2-pyridylmethyl)urea (2-MeUR-N)

Diphenyl carbonate (2.13 g, 0.01 mol) and 2-(aminomethyl)pyridine (2.16 g, 2.2 mL, 0.02 mol) were combined in an argon flushed test tube. The mixture was stirred under an argon atmosphere for two hours at 150 °C. Once above 70 °C, the diphenyl carbonate melted. Upon cooling to room temperature, the resulting solution turned viscous. Ethyl acetate was added on top of the viscous layer. Upon stirring, the product crystallises forming a white solid which was isolated by filtration. The solid was washed further with ethyl acetate and dried overnight.

3.6.2 Synthesis of N,N’-bis(3-pyridylmethyl)urea (3-MeUR-N)

Diphenyl carbonate (2.13 g, 0.01 mol) and 3-(aminomethyl)pyridine (2.16 g, 2.2 mL, 0.02 mol) were combined in an argon flushed test tube. The mixture was stirred under an argon atmosphere for two hours at 150 °C. Once above 70 °C, the diphenyl carbonate melted. Upon cooling to room temperature, the resulting solution turned viscous. Ethyl acetate was added on top of the viscous layer. Upon stirring, the product crystallises forming a white solid which was isolated by filtration. The solid was washed further with ethyl acetate and dried overnight.

3.6.3 Synthesis of N,N’-bis(4-pyridylmethyl)urea (4-MeUR-N)

Diphenyl carbonate (2.13 g, 0.01 mol) and 4-(aminomethyl)pyridine (2.16 g, 2.2 mL, 0.02 mol) were combined in an argon flushed test tube. The mixture was stirred under an argon atmosphere for two hours at 150 °C. Once above 70 °C, the diphenyl carbonate melted. Upon cooling to room temperature, the resulting solution turned viscous. Ethyl acetate was added on top of the viscous layer. Upon stirring, the product crystallises forming a white solid which was isolated by filtration. The solid was washed further with ethyl acetate and dried overnight. Yield = 2.04 g (84% based on diphenyl carbonate for N,N’-bis(4-pyridylmethyl)urea).

3.6.4 Synthesis of 4,4´-(carbonylbis(azanediyl))dibenzoic acid (UR-CO_2H)

Ethyl-4-aminobenzoate (1.67 g, 0.01mol) was dissolved in 25 mL of dry THF. 1,1’-carbonyldiimidazole (0.97 g, 0.006 mol) was added to the solution and refluxed under an argon atmosphere overnight. The reaction was cooled and solvent removed under reduced pressure. The resulting residue was taken up in ethyl acetate and washed with 1M HCl and brine. The organic layer was dried using $MgSO_4$ and concentrated to afford a white powder (1). 1 and NaOH (2.8 g,

0.07 mol) were dissolved in 30 mL methanol and refluxed for 5 hours affording a white powder. The white powder was washed with ethanol and dried at room temperature to afford UR-CO_2H.

3.6.5 Synthesis of Silver N,N'-bis(2-pyridylmethyl)urea tetrafluoroborate (2-BF_4)

Sodium tetrafluoroborate (0.0076 g, 0.07 mmol) was dissolved into 2 mL of an aqueous stock solution of silver nitrate (0.03M) and added to a vial. 2 mL of an ethanolic stock solution of 2-MeUR-N (0.03M) was added to the vial which was capped, shaken briefly, and left in the dark for five days at room temperature. This resulted in the production of large block crystals of **2-BF_4**.

3.6.6 Synthesis of Silver N,N'-bis(2-pyridylmethyl)urea hexafluorophosphate (2-PF_6)

Potassium hexafluorophosphate (0.0110 g, 0.06 mmol) was dissolved into 2 mL of an aqueous stock solution of silver nitrate (0.03M) and added to a vial. 2 mL of an ethanolic stock solution of 2-MeUR-N (0.03M) was added to the vial which was capped, shaken briefly, and left in the dark for five days at room temperature. This resulted in the production of large block crystals of **2-PF_6**.

3.6.7 Synthesis of Silver N,N'-bis(2-pyridylmethyl)urea perrhenate (2-ReO_4)

Silver perrhenate (0.030 g, 0.08 mmol) was dissolved in water (2.5 mL) and added to a test tube.* A blank layer of water (2.5 mL) was carefully layered on top of the silver aqueous solution using a Pasteur pipette. 2-MeUR-N (0.009 g, 0.04 mmol) was dissolved in ethanol (2.5 mL) and carefully layered on top of the aqueous layer, again with a Pasteur pipette. The test tube was covered with parafilm and left in the dark for one week to allow for large crystals to form.

*Alternatively, equimolar quantities of silver nitrate and sodium perrhenate can be dissolved into water.

3.6.8 Synthesis of Silver N,N'-bis(2-pyridylmethyl)urea sulphate (2-SO_4)

Disodium sulphate (g, 0.07 mmol) was dissolved into 2 mL of an aqueous stock solution of silver nitrate (0.03M) and added to a vial. 2 mL of an ethanolic stock solution of 2-MeUR-N (0.03M) was added to the vial which was capped, shaken briefly, and left in the dark for five days at room temperature. This resulted in the production of needle crystals of **2-SO_4**.

3.6.9 Synthesis of Silver N,N'-bis(3-pyridylmethyl)urea tetrafluoroborate (3-BF_4)

Silver tetrafluoroborate (0.016 g, 0.08 mmol) was dissolved in water (2.5 mL) and added to a test tube. A blank layer of water (2.5 mL) was carefully layered on top of the silver aqueous solution using a Pasteur pipette. 2-MeUR-N (0.009 g, 0.04 mmol) was dissolved in ethanol (2.5 mL) and carefully layered on top of the aqueous layer, again with a Pasteur pipette. The test tube was covered with parafilm and left in the dark for one week to allow for large crystals to form.

3.6.10 Synthesis of Silver N,N'-bis(3-pyridylmethyl)urea perrhenate (3-ReO_4)

Silver perrhenate (0.036 g, 0.1 mmol) was dissolved in water (2 mL) and added to a test tube. A layer of water (2 mL) was carefully layered on top of the silver perrhenate solution with a Pasteur pipette. 3-MeUR-N (0.05 g, 0.2 mmol) was dissolved in ethanol (2 mL) and carefully layered on top of the aqueous layer, again with a Pasteur pipette. The test tube was covered with parafilm and left in the dark for one week. A white precipitate formed at the layer interface. When left for one week needle crystals had grown above the precipitate.

3.6.11 Synthesis of Silver N,N'-bis(3-pyridylmethyl)urea sulphate (3-SO_4)

Disodium sulphate (0.0084 g, 0.06 mmol) was dissolved in 2 mL of an aqueous stock solution of silver nitrate (0.03M) and added to a vial. 2 mL of an ethanolic solution of 3-MeUR-N (0.03M) was added to the vial. The vial was capped, shaken briefly and left in the dark for five days producing crystals of 3-SO_4.

3.6.12 Synthesis of Silver N,N'-bis(4-pyridylmethyl)urea nitrate (4-NO_3)

Silver nitrate (0.014 g, 0.08 mmol) was dissolved in water (2.5 mL) and added to a test tube. A blank layer of water (2.5 mL) was carefully layered on top of the silver aqueous solution using a Pasteur pipette. 4-MeUR-N (0.009 g, 0.04 mmol) was dissolved in ethanol (2.5 mL) and carefully layered on top of the aqueous layer, again with a Pasteur pipette. The test tube was covered with parafilm and left in the dark for one week to allow for large crystals to form.

3.6.13 Synthesis of Silver N,N'-bis(4-pyridylmethyl)urea sulphate (4-SO_4)

Disodium sulphate (0.0084 g, 0.06 mmol) was dissolved in 2 mL of an aqueous stock solution of silver nitrate (0.03M) and added to a vial. 2 mL of an ethanolic solution of 4-MeUR-N (0.03M) was added to the vial. The vial was capped, shaken briefly and left in the dark for five days producing crystals of 3-SO_4.

3.6.14 Synthesis of Silver N,N'-bis(4-pyridylmethyl)urea perrhenate (4-ReO_4)

Silver perrhenate (0.107 g, 0.3 mmol) was dissolved in water (10 mL) and added to a test tube. A blank layer of water (10 mL) was carefully layered on top of the silver aqueous solution using a Pasteur pipette. 4-MeUR-N (0.073 g, 0.3 mmol) was dissolved in ethanol (10 mL) and carefully layered on top of the aqueous layer, again with a Pasteur pipette. The test tube was covered with parafilm and left in the dark for one week to allow for large crystals to form.

3.6.15 Synthesis of Silver N,N'-bis(4-pyridylmethyl)urea hexafluorophosphate (4-PF_6)

Silver nitrate (0.051 g, 0.3 mmol) and potassium hexafluorophosphate (0.055 g, 0.3 mmol) was dissolved in water (10 mL) and added to a test tube. A blank layer of water (10 mL) was carefully layered on top of the silver aqueous solution using a Pasteur pipette. 4-MeUR-N (0.073 g, 0.3 mmol) was dissolved in ethanol (10 mL) and carefully layered on top of the aqueous layer, again with a Pasteur pipette. The test tube was covered with parafilm and left in the dark for one week to allow for large crystals to form.

3.6.16 Synthesis of Zn-MOF-1 ($Zn_2(OBA)_2$(4-MeUR-N)$(DMF)_{4.5}$)

Zinc nitrate hexahydrate (0.30 g, 1.5 mmol), 4,4'-oxybis(benzoic acid) (0.39 g, 1.5 mmol) and N,N'-bis(4-pyridylmethyl)urea (0.36 g, 1.5 mmol) were dissolved into DMF (15 mL). The resulting solution was sealed into an autoclave and heated at 80 °C for 24 hours. The orange crystals formed were washed by decanting and replacing the DMF with fresh DMF once every 24 hours for three days.

3.6.17 Synthesis of Zn-LMOF-2 (Zn(IP)(4-MeUR-N)$(DMF)_{0.7}$)

Zinc nitrate hexahydrate (0.30 g, 1.5 mmol), isophthalic acid (0.25 g, 1.5 mmol) and N,N'-bis(4-pyridylmethyl)urea (0.36 g, 1.5 mmol) were dissolved into DMF (15 mL). The resulting solution as sealed into an autoclave and heated at 80 °C for 24 hours. The orange crystals formed were washed by decanting and replacing the DMF with fresh DMF once every 24 hours for three days.

3.6.18 Synthesis of Zn-LMOF-3 (Zn(UR-CO_2H)$(H_2O)_2$)

Zinc nitrate hexahydrate (0.1661 g, 0.75 mmol) was dissolved into 20 mL of deionised water. To this solution UR-CO_2H (0.3725 g, 1.13 mmol) was added. An immediate white precipitate formed. The

mixture was stirred for 24 hours at room temperature. The precipitate was isolated by centrifugation and washed with water and centrifuging (5000 rpm for 15 minutes) three times.

3.6.19 Topological Analysis

Topological analysis of selected materials in this chapter was carried out using ToposPro.[55] All solvent molecules and non-bonded anions were removed from the CIF file prior to analysis. ADS was used to simplify the crystal structure to an array of connected nodes.[56] Nodes that were coordinated to two or fewer nodes were further simplified to links, in all cases these nodes represented organic linkers. Additionally, for the 3-SO_4 and 4-SO_4 structures the sulphate nodes were also simplified to links. The topology of the resulting net was calculated and compared to existing topologies in the TTD database.[55]

3.7 References

1 S. S. Fatima, R. Kumar, M. Iqbal Choudhary and S. Yousuf, *IUCrJ*, 2020, **7**, 105.

2 L. R. Agnew, T. McGlone, H. P. Wheatcroft, A. Robertson, A. R. Parsons and C. C. Wilson, *Cryst. Growth Des.*, 2017, **17**, 2418.

3 C. M. Reddy, *IUCrJ*, 2019, **6**, 505.

4 N. Wang, Y. X. Dai, T. L. Wang, H. Z. Yang and Y. Qi, *IUCrJ*, 2020, **7**, 49.

5 J. D. Rimer, A. Chawla and T. T. Le, *Annu. Rev. Chem. Biomol. Eng.*, 2018, **9**, 283.

6 G. R. Desiraju, *J. Am. Chem. Soc.*, 2013, **135**, 9952.

7 E. Arunan, G. R. Desiraju, R. A. Klein, J. Sadlej, S. Scheiner, I. Alkorta, D. C. Clary, R. H. Crabtree, J. J. Dannenberg, P. Hobza, H. G. Kjaergaard, A. C. Legon, B. Mennucci and D. J. Nesbitt, *Pure Appl. Chem.*, 2011, **83**, 1619.

8 D. Braga and F. Grepioni, in *Making Crystals by Design: Methods, Techniques and Applications*, Wiley-VCH, 2007, pp. 209–240.

9 D. J. Berry and J. W. Steed, *Adv. Drug Deliv. Rev.*, 2017, **117**, 3.

10 O. Ermer and A. Eling, *J. Chem. Soc. Perkin Trans. 2*, 1994, **5**, 925.

11 F. H. Allen, V. J. Hoy, J. A. K. Howard, V. R. Thalladi, G. R. Desiraju, C. C. Wilson and G. J. McIntyre, *J. Am. Chem. Soc.*, 1997, **119**, 3477.

12 IUCr, Polymorphism, https://dictionary.iucr.org/Polymorphism#, (accessed 6 July 2020).

13 M. Eddaoudi, J. Kim, N. Rosi, D. Vodak, J. Wachter, M. O'Keeffe and O. M. Yaghi, *Science (80-.).*, 2002, **295**, 469.

14 A. Laybourn, A. M. López-Fernández, I. Thomas-Hillman, J. Katrib, W. Lewis, C. Dodds, A. P. Harvey and S. W. Kingman, *Chem. Eng. J.*, 2019, **356**, 170.

15 A. V Desai, S. Sharma, A. Roy and S. K. Ghosh, *Cryst. Growth Des.*, 2019, **19**, 7046.

16 Y. Zhang and P. S. Cremer, *Curr. Opin. Chem. Biol.*, 2006, **10**, 658.

17 R. Custelcean, T. J. Haverlock and B. A. Moyer, *Inorg. Chem.*, 2006, **45**, 6446.

18 R. Custelcean and B. A. Moyer, *Eur. J. Inorg. Chem.*, 2007, **2007**, 1321.

19 R. Custelcean, *Chem. Commun.*, 2008, 295.

20 W. Dannecker, J. Kopf and H. Rust, *Crystral Struct. Commun.*, 1979, **8**, 429.

21 F. Lortie, S. Boileau and L. Bouteiller, *Chem. - A Eur. J.*, 2003, **9**, 3008.

22 M. de Loos, A. G. J. Ligtenbarg, J. van Esch, H. Kooijman, A. L. Spek, R. Hage, R. M. Kellogg and B. L. Feringa, *European J. Org. Chem.*, 2000, **22**, 3675.

23 M. C. Etter and T. W. Panunto, *J. Am. Chem. Soc.*, 1988, **110**, 5896.

24 R. Custelcean, B. A. Moyer, V. S. Bryantsev and B. P. Hay, *Cryst. Growth Des.*, 2006, **6**, 555.

25 C. L. Schauer, E. Matwey, F. W. Fowler and J. W. Lauher, *J. Am. Chem. Soc.*, 1997, **119**, 10245.

26 D. K. Kumar, A. Das and P. Dastidar, *CrystEngComm*, 2006, **8**, 805.

27 M. J. Plater, B. M. De Silva, J. M. . Skakle, R. A. Howie, A. Riffat, T. Gelbrich and M. B. Hursthouse, *Inorganica Chim. Acta*, 2001, **325**, 141.

28 D. K. Kumar, D. A. Jose, A. Das and P. Dastidar, *Inorg. Chem.*, 2005, **44**, 6933.

29 D. Krishna Kumar, A. Das and P. Dastidar, *New J. Chem.*, 2006, **30**, 1267.

30 X. Zhang, X.-P. Zhou and D. Li, *Cryst. Growth Des.*, 2006, **6**, 1440.

31 P. F. Shi, G. Xiong, B. Zhao, Z. Y. Zhang and P. Cheng, *Chem. Commun.*, 2013, **49**, 2338.

32 S. Banerjee, N. N. Adarsh and P. Dastidar, *Eur. J. Inorg. Chem.*, 2010, **2010**, 3770.

33 A. Rajbanshi and R. Custelcean, *Supramol. Chem.*, 2012, **24**, 65.

34 R. Custelcean, *Chem. Commun.*, 2013, **49**, 2173.

35 B. C. Tzeng, Y. C. Huang, B. S. Chen, W. M. Wu, S. Y. Lee, G. H. Lee and S. M. Peng, *Inorg. Chem.*, 2007, **46**, 186.

36 S. Banerjee, N. N. Adarsh and P. Dastidar, *Cryst. Growth Des.*, 2012, **12**, 6061.

37 C. L. Schauer, E. Matwey, F. W. Fowler and J. W. Lauher, *Cryst. Eng.*, 1998, **1**, 213.

38 C. P. Li, J. Y. Ai, H. Zhou, Q. Chen, Y. Yang, H. He and M. Du, *Chem. Commun.*, 2019, **55**, 1841.

39 L. Zhu, C. Xiao, X. Dai, J. Li, D. Gui, D. Sheng, L. Chen, R. Zhou, Z. Chai, T. E. Albrecht-Schmitt and S. Wang, *Environ. Sci. Technol. Lett.*, 2017, **4**, 316.

40 H. Fei, M. R. Bresler and S. R. J. Oliver, *J. Am. Chem. Soc.*, 2011, **133**, 11110.

41 D. Sheng, L. Zhu, C. Xu, C. Xiao, Y. Wang, Y. Wang, L. Chen, J. Diwu, J. Chen, Z. Chai, T. E. Albrecht-Schmitt and S. Wang, *Environ. Sci. Technol.*, 2017, **51**, 3471.

42 A. Azhdari Tehrani, L. Esrafili, S. Abedi, A. Morsali, L. Carlucci, D. M. Proserpio, J. Wang, P. C. Junk and T. Liu, *Inorg. Chem.*, 2017, **56**, 1446.

43 S. S. Batsanov, in *Inorganic Materials*, 2001, pp. 871–885.

44 A. N. Khlobystov, A. J. Blake, N. R. Champness, D. A. Lemenovskii, A. G. Majouga, N. V Zyk and M. Schröder, *Coord. Chem. Rev.*, 2001, **222**, 155.

45 B. F. Hoskins, R. Robson and D. A. Slizys, *Angew. Chemie (International Ed. English)*, 1997, **36**, 2336.

46 D. Whang, Y. M. Jeon, J. Heo and K. Kim, *J. Am. Chem. Soc.*, 1996, **118**, 11333.

47 S. S. Y. Chui, S. M. F. Lo, J. P. H. Charmant, A. G. Orpen and I. D. Williams, *Science (80-.).*, 1999, **283**, 1148.

48 A. Shastri, A. K. Das, S. Krishnakumar, P. J. Singh and B. N. Raja Sekhar, *J. Chem. Phys.*, 2017, **147**, 224305.

49 Y. Zhao, J. Li, H. Gu, D. Wei, Y. chang Xu, W. Fu and Z. Yu, *Interdiscip. Sci. Comput. Life Sci.*, 2015, **7**, 211.

50 M. C. Etter, *Acc. Chem. Res.*, 1990, **23**, 120.

51 T. L. Nguyen, F. W. Fowler and J. W. Lauher, *J. Am. Chem. Soc.*, 2001, **123**, 11057.

52 T. Steiner, *Angew. Chemie - Int. Ed.*, 2002, **41**, 48.

53 R. J. Marshall, J. McGuire, C. Wilson and R. S. Forgan, *Supramol. Chem.*, 2018, **30**, 124.

54 H. Ang and L. Hong, *ACS Appl. Mater. Interfaces*, 2017, **9**, 28079.

55 V. A. Blatov, A. P. Shevchenko and D. M. Proserpio, *Cryst. Growth Des.*, 2014, **14**, 3576.

56 E. V Alexandrov, V. A. Blatov, A. V Kochetkov and D. M. Proserpio, *CrystEngComm*, 2011, **13**, 3947.

57 G. R. Desiraju, *IUCrJ*, 2018, **5**, 660.

58 M. E. Light, M. E. Potter, D. Irving, A. E. Oakley, S. Chapman, P. A. Chater, G. L. Cutts, A. Watts, M. T. Wharmby, B. D. Vandegehuchte, M. Schreiber and R. Raja, *Phys. Chem. Chem. Phys*, 2020, **22**, 18860.

59 A. Qiao, H. Tao, M. P. Carson, S. W. Aldrich, L. M. Thirion, T. D. Bennett, J. C. Mauro and Y. Yue, *Opt. Lett.*, 2019, **44**, 1623.

Chapter 4 You Can't Make A MOF Without Breaking Some Eggs – Toward Sustainable Syntheses of Calcium-based Metal-Organic Frameworks

4.1 Introduction

The MOF field is now reaching a level of maturity where industrialisation is coming into focus. Therefore one needs to begin to appreciate the broader aspects of material production, such as scalability, costs, and the environmental impacts of precursors and procedures.[1] Transferring the knowledge gained within the laboratory often proves difficult due to the challenges of scaling up chemical processes and more often than not,[2] environmental hurdles are easily forgotten about at research level. This is often as a result of experimental constraints that necessitate the use of harsh, regularly toxic, and relatively expensive precursors and solvents. Hence these parameters are often lost during the planning stage of a project and never truly considered. The MOF research field is no stranger to this. Expensive metal precursors and organic linkers that in some cases require lengthy synthetic procedures to produce, as well as the use of solvents that are far from environmentally friendly, are all limiting factors in the research area. Additionally, these costly procedures often only yield products in the lower gram scale. There is however a growing desire to turn to friendlier processes that use benign solvents and chemicals, that can be conducted at lower temperatures and that have improved atom economies.

Abundant earth minerals such as metal oxides,[3] hydroxides[4] and carbonates[5] have been shown as attractive metal precursors for MOF synthesis.[6] They are cheap to purchase, readily available, and often result in the release of only benign waste products. An example of this is copper carbonate, which is naturally occurring in the basic carbonate minerals azurite and malachite.[7] Upon reaction with trimesic acid (H_3BTC), copper carbonate forms the MOF HKUST-1 as well as carbon dioxide and water as by-products (equation 4.1).

$$3Cu_2CO_3(OH)_2 + 4(H_3BTC) \rightarrow 2Cu_3(BTC)_2 + 3CO_2 + 9H_2O \qquad \textbf{Equation 4.1}$$

The advantages of using naturally abundant, insoluble metal precursors in MOF synthesis are not just limited to cost and sustainability. Sacrificial metal substrates open the opportunity to synthesise a variety of MOF architectures and hierarchal materials including thin films,[8,9] membranes[9] and patterned MOFs.[10] El-Hankari *et al.* have shown that spherical ZnO particles can be utilised to form well-defined ZnO@ZIF-8 core-shell architectures.[11] These materials in turn can

undergo base-etching to remove the ZnO core affording ZIF-8 yolk-shell structures. Further, Cu_2O nanocubes have been used in the synthesis of HKUST-1 affording hierarchical materials that assemble *via* a domain growth mechanism.[12] The use of carbonate and oxide-based metal sources also avoids the combination of organics and organic solvents with potentially incompatible, and explosive, anions such as nitrates.

Despite their high stabilities, low toxicity & densities, and ease of synthesis, calcium-based MOFs (Ca-MOFs) are vastly overlooked in comparison to their transition metal counterparts. This can appear extremely surprising when one considers that a drawback to many MOFs is their lack of stability when dried in air or dispersed in water. When calcium is utilised in the MOF field the resulting materials have been applied in adsorptions,[13] light molecule storage,[14] separations,[15,16] photoluminescence[17,18] and, given the biocompatibility of the metal ion, in medicinal applications.[19,20]

Calcium is the third most abundant metal found in the Earth's crust (4.1%, see Table A.4) and exists in great quantities as a variety of calcium carbonate polymorphs. The use of calcium carbonate, regularly in its calcite phase, has been explored as a calcium source for MOF synthesis. Sumida *et al.* have elegantly shown the use of natural calcite sources to form Ca-MOF facsimiles of these complex hierarchically structured biominerals.[21] The abundance of marine coral, sea urchin skeletal plates and eggshells offer an extremely cheap resource to synthesise a variety of Ca-MOFs in large quantities. Figure 4.1 shows the coordination replication growth of calcium squarate hydrate ([Ca(SQ)(H_2O)]) (SQ = squarate; H_2SQ = squaric acid) on sea coral by the Kitagawa group.

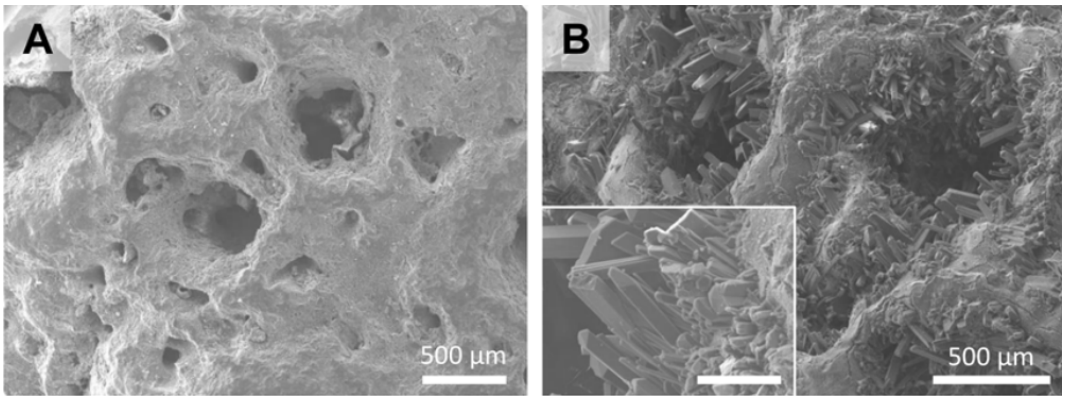

Figure 4.1. SEM images of coral (A) before and (B) after immersion in a solution of squaric acid which results in the formation of [Ca(SQ)(H_2O)] on the biomineralised surface.[21] Scale bar of inset = 100 µm. Copyright 2016 American Chemical Society.

Naturally occurring organic linker molecules are typically limited to cyclodextrins[22] and small biomolecules such as gallic acid.[23] Some basic dicarboxylic acid-based organic linkers do exist naturally such as oxalic acid (H_2OX),[24] maleic acid (H_2MA),[25] and fumaric acid (H_2FU),[26] however

aromatic-based dicarboxylic acids often require manufacturing. Remarkably, the presence of H_2OX in nature has allowed for the natural formation of MOFs outside of the laboratory, an accolade normally reserved for zeolites within the porous material community.[27] In 2016 Huskić *et al.* demonstrated that sometimes nature knows best. SCXRD characterisation of the naturally occurring mineral stepanovite ($NaMgFe(OX)_3 \cdot 8\text{-}9H_2O$) and its aluminium doped analogue, zhemchuzhnikovite ($NaMg(Fe_{0.4}Al_{0.6})(OX)_3 \cdot 8\text{-}9H_2O$), confirmed that they were structurally identical to many proton conducting and magnetic oxalate-based MOFs (figure 4.2).[28] Furthermore they were able to synthetically obtain both minerals through careful control of reagent stoichiometry. This new relationship between rare organic minerals and synthetic MOFs demonstrated for the first time that MOFs were not limited to the laboratory as previously thought.

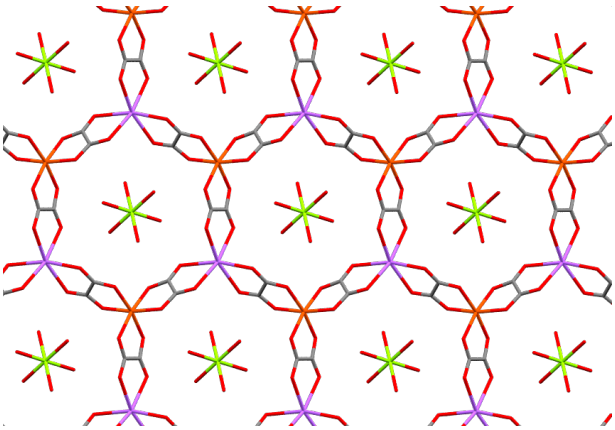

Figure 4.2. Single metal-organic layer in stepanovite by Huskić *et al*, viewed down the c axis.[28] Magnesium = lime, purple = sodium, orange = iron, red = oxygen and grey = carbon.

To overcome the rarity of naturally occurring dicarboxylic acid-based organic linkers, researchers focussed on the sustainable synthesis of MOFs have turned to recycled manmade materials, i.e. plastics, as sustainable and green sources to majorly used organic linkers. PET (polyethylene terephthalate) plastic is one of the most commonly used plastics and hence a major contributor to industrial waste.[29] It finds applications mainly in packaging in pharmaceuticals, food, and beverages.[30] The material is easily malleable due to its low glass transition temperature, is cheap to make, can take the form of many different colours through the addition of dyes and can be processed to yield different levels of transparency. All of these properties make it an ideal material in single use packaging.[31] As of 2014, 60% of household PET plastic is recycled in the UK.[32] The remaining 40% of PET however, is disposed of through mass incineration and landfilling. The former process poses health concerns due to the release of volatiles into the local environment while poor biodegradability of PET makes the latter process a long-term environmental issue. More widely, microplastics are fast becoming one of the largest threats to both wildlife and humans.[33] Improper disposal of plastics result in their presence in waterways and oceans, where sunlight, wind and wave action accelerates the degradation of the plastics into small pieces, i.e. microplastics. While

the recycling of plastics is becoming much more commonplace, there is still a desire to develop and utilise materials that undergo biodegradation much more easily and to find more applications that can benefit from recycled plastics, thus increasing sustainability.

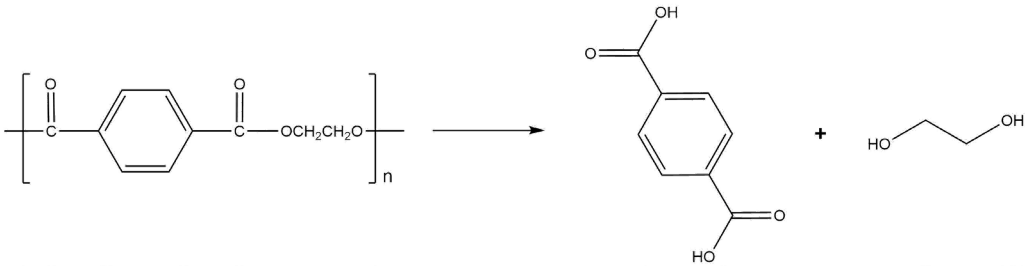

Figure 4.3. Depolymerisation of PET plastic back into its monomers, terephthalic acid (H_2BDC) and ethylene glycol.

Terephthalic acid (H_2BDC), arguably the most common organic linker utilised in MOF synthesis, can be recycled through the depolymerisation of PET (figure 4.3). Work to synthesise nickel[34] and tin-based[35] MOFs from H_2BDC reclaimed from the hydrolysis of PET has been realised, as well as the formation of a thermally robust-water stable **hcp** form of UiO-66.[36] Work by Deleu *et al.*[37] and Ren *et al.*[38] successfully synthesised various MIL (MIL = Matériaux de l'Institut Lavoisier) frameworks from waste PET plastic *via* one pot reactions by matching the temperature necessary for simultaneous plastic depolymerisation and MOF assembly. Very recently, the Szilágyi group have developed a low temperature one-pot synthesis of UiO-66 from PET through the judicious assessment of reaction conditions.[39] Interestingly, they found the use of nitric acid to promote PET depolymerisation caused the resulting H_2BDC to undergo nitration. The nitro groups were ultimately reduced by ethylene glycol, a PET hydrolysis by-product, to yield -NH_2 moieties. Our previous work detailed in chapter two showcases the value of UiO-66-NH_2 with respect to its varied post-synthetic modification chemistry and use in environmentally targeted applications, thus this method to sustainably synthesise the MOF from recycled precursors is very exciting. Ladewig *et al.* have also shown the synthesis of three complex lactate-based MOFs from the combination of calcium acetate with recycled poly(lactic) acid (PLA) cups in a one pot synthesis.[40] The catalogue of organic linkers available for conventional MOF syntheses is extensive. However, their inclusion as monomers in plastics is limited and thus the number of available recyclable organic linker sources are equally low.

The use of green feedstocks for MOF precursors in combination with slow and high temperature reaction conditions only partially solves the question of sustainability of MOF synthesis. Combining green precursors with fast, room temperature techniques would remarkably reduce the energy requirements for MOF synthesis. In 2006, James *et al.* reported the first quantitative mechanochemical synthesis of a robust microporous framework by dry grinding copper acetate

monohydrate and isonicotinic acid (INA) together in a ball-mill for 10 minutes.[41] The synthesis only yields water and acetic acid as by-products and the framework had the same robustness as the identical MOF solvothermally produced over 48 hours at 150 °C.[42] Since then, mechanochemical techniques for MOF synthesise have become very commonplace, and regarded as a superior method for the upscale and commercialisation of the material class.[43] The ability to use minimal quantities of solvent, short reaction times, and relatively low energy inputs make liquid assisted grinding (LAG), twin screw extrusion[44] and, more recently liquid-assisted resonant acoustic mixing,[45] such attractive techniques.

Mechanochemical syntheses have now extended into insoluble metal precursors. Friščić *et al.* have investigated the use of metal oxides in combination with LAG techniques and 2,5-dihydroxyterephtalic acid to yield highly crystalline zinc and copper-based MOFs in as little as 30 minutes.[46] The James group have also used rare-earth carbonates to form several trimesic acid-based MOFs, once again through LAG techniques.[5] From our understanding, this is the only reported attempt to synthesise MOFs, mechanochemically, from metal carbonates.

4.2 Chapter Outlook

Inspired by the previous work presented above, this chapter explores the use of recycled waste calcium carbonate and terephthalic acid sources, chicken eggshells and PET plastic bottles respectively, for the synthesis of various calcium-based MOFs (Ca-MOFs). We also employ mechanochemistry, in the form of ball-milling, to synthesise these MOFs *via* a sustainable and low-cost method in combination with our green precursors.

The urea-based organic linker 4,4´-(carbonylbis(azanediyl))dibenzoic acid (UR-CO_2H) is once again utilised to produce a new MOF (Ca(UR-CO_2H)(H_2O)$_4$) (Ca-MOF-1). We will investigate the effects of dehydrating this MOF and the resulting porosity the transformation creates. To expand on the strong foundation we developed of using naturally occurring calcium precursors for MOF synthesis, we attempt to use UR-CO_2H and calcium carbonate to synthesis Ca-MOF-1 with the intention of replacing calcium carbonate with recycled eggshells to form a sustainable synthesis of this MOF.

4.3 Results and Discussion

4.3.1 Characterisation of Recycled Precursors

4.3.1.1 Eggshells

Characterisation of chicken eggshells prior to any attempt of MOF synthesis is important to establish the similarities between the biomineralized precursor and commercially sought, reagent quality, calcium carbonate. Firstly, the organic membrane that is present on the inner surface of eggshells was removed by soaking the eggshells in deionised water. This softens any dried membrane and allows for its removal *via* gentle exfoliation with gloved fingers. The eggshells were then dried at 70 °C overnight followed by grinding in a pestle and mortar to a coarse powder. SEM imaging of the ground eggshells confirmed that they had an irregular particle size and morphology (figure 4.4).

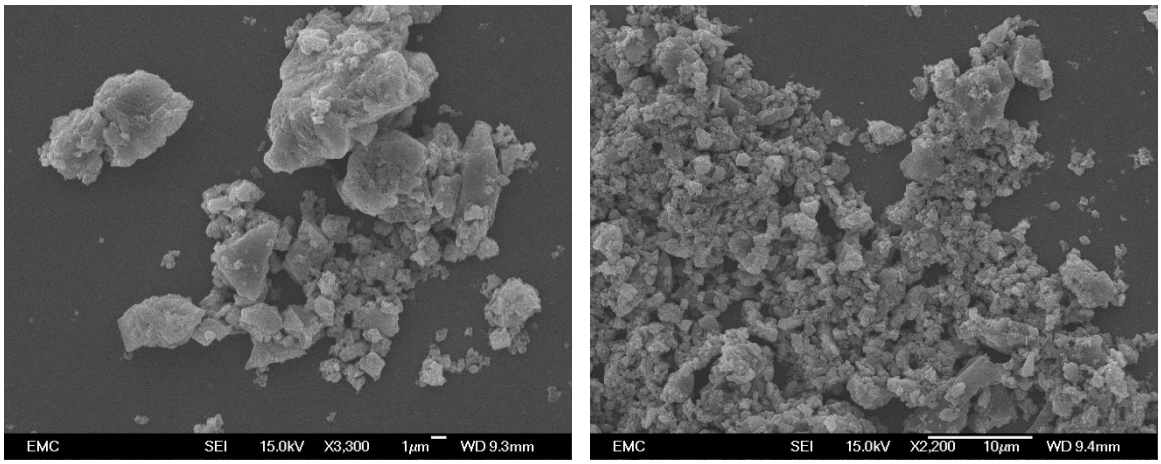

Figure 4.4. SEM images of ground eggshells with their internal membrane removed. Scale bars = (left) 1 µm and (right) 10 µm.

PXRD of the ground eggshells compared to commercially sought $CaCO_3$ confirms that both materials consist wholly of the calcium carbonate polymorph, calcite (figure 4.5).

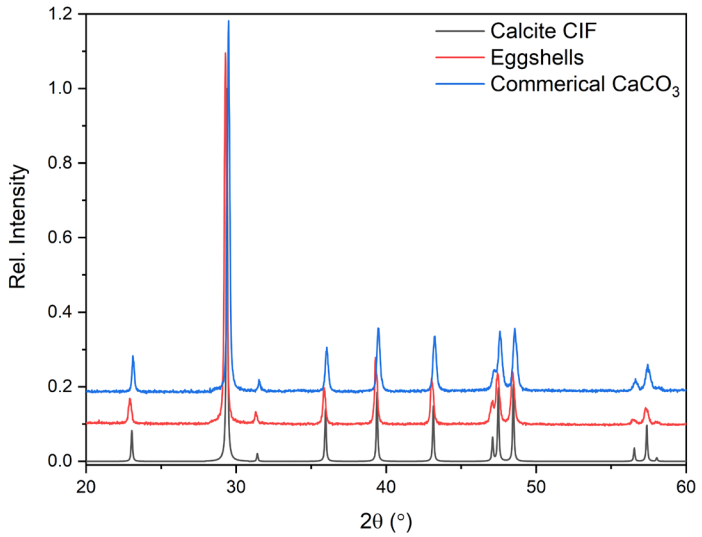

Figure 4.5. PXRD comparison of eggshells and commercial $CaCO_3$ to a calcite CIF.[47] The membrane has been removed from the eggshells.

Further proof of the polymorph of the calcium carbonate precursors is available from FTIR (figure A.32). The FTIR spectra of ground eggshells and commercial $CaCO_3$ aligns very well with a reported calcite spectrum whereby all three spectra display absorptions corresponding to the asymmetric stretch (ν_3 – 1395 cm^{-1}), the asymmetric deformation (ν_2 – 807 cm^{-1}) and the symmetric deformation (ν_4 – 709cm^{-1}) of the carbonate anion.

To assess how effective our mechanical exfoliation method is at removing the inner organic membrane of the eggshells, TGA was used and the results compared to commercial $CaCO_3$ (figure 4.6). The thermal decomposition of $CaCO_3$ in air is expected to form CaO with the release of CO_2 gas from 600 °C. Indeed, both eggshell with and without the internal membrane undergo a large mass loss between 600 to 800 °C corresponding to the thermal decomposition of calcite, as well as an additional mass loss due to surface organics between 300-550 °C.

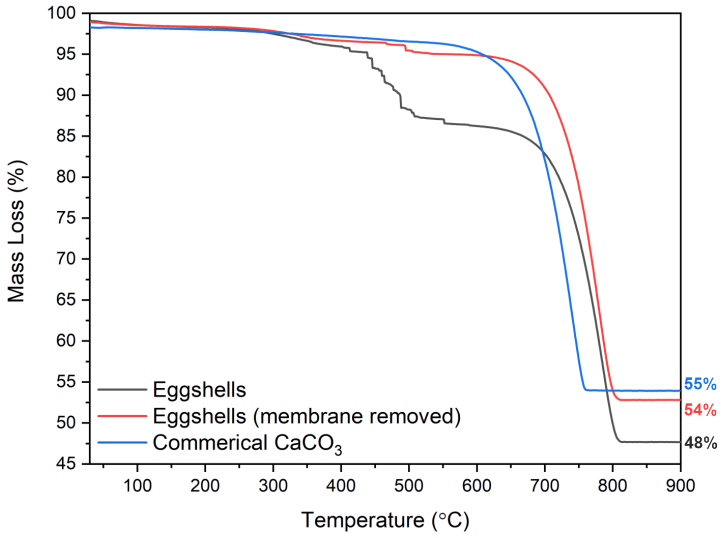

Figure 4.6. TGA of eggshells with both membrane and no membrane compared to commercial $CaCO_3$. Conducted under an air atmosphere. Residual masses are found to the right of the graph.

The theoretical residual mass for calcite is 56% which agrees well to commercial $CaCO_3$ (55%) and membrane removed eggshells (54%). The slightly lower than expected residual mass does however suggest the presence of some persistent organics on the latter material, which is further corroborated by the small mass loss (3%) prior to thermal decomposition. Removal of this small quantity of organic matter could possibly be achieved with thorough washing in organic solvents, such as hexane, using a Soxhlet extractor. This is a commonly used step by the zeolite community to aid in the removal of organic-based structure-determining agents (SDAs) post-material synthesis.[48] To keep to the sustainable and green theme of this body of work we have however opted to not follow such a process due to the large energy input and use of organic solvents for removal of such a minimal amount of organic material. We also believe that it could be possible for these organics to impregnate the calcite layer and become a key part of the shell itself, thus making the removal of these organics even more difficult.

4.3.1.2 Hydrolysis of Poly(ethylene terephthalate)

Onyango *et al.* have shown that PET plastic can be used as a sustainable source of terephthalic acid upon depolymerisation for MOF synthesis.[38] We used a slightly modified procedure to hydrolyse recycled PET plastic bottles. Labels and caps were removed prior to thorough washing of the bottles with water and subsequent drying. The PET bottles were cut into small squares, roughly 0.25 cm^2 in size, and added to a 100 mL Teflon-lined steel autoclave. A solvent mixture of H_2O and ethylene glycol (EG) (10:1) was added and the reaction sealed prior to heating at 210 °C for 8 hours. After cooling to room temperature colourless crystals had grown on the sides and bottom of the liner. These crystals were collected by centrifugation and washed with ethanol twice, before being dried at 100 °C overnight. No further purification of the resulting H_2BDC was performed prior to MOF synthesis.

^1H NMR spectroscopy was conducted on a portion of the material dissolved in d_6-DMSO (figure A.34). The resulting spectrum contained three peaks at 8.00, 2.48 and 3.35 ppm. These peaks correspond to the four equivalent aromatic protons of terephthalic acid, DMSO solvent and residual water respectively. Reverse phase ultra-high-performance liquid chromatography mass spectrometry (RP UHPLC-MS) was performed on a basic aqueous solution of hydrolysed PET (figure A.35). An m/z peak at 165.42 confirmed the presence of $HBDC^-$ anions. FTIR peaks in the reclaimed H_2BDC spectrum were observed at 1280, 1412, 1674, 2541 and 2657 cm^{-1} (figure A.33). These values correspond to the C-O, C-C, C=C and C=O bond stretches respectively, which are consistent with terephthalic acid.

When viewed under a light microscope it was clear that single-crystal quality crystals of terephthalic acid have been formed by the hydrolysis of PET plastic. To demonstrate this, a crystal was selected

and mounted in fomblin oil and single-crystal data was collected. The asymmetric unit of the resulting structure is found in figure 4.7, which consists of one half of a terephthalic acid molecule. The full molecule is generated through a centre of inversion present in the middle of the aromatic ring of terephthalic acid, consequential of the P-1 space group. A comparison between the unit cell parameters of the collected crystal data and an already reported structure shows good agreement (table A.6 & A.7). PXRD characterisation was performed on the hydrolysed PET and the resulting pattern compared to a simulated one, derived from the crystal structure. The two patterns showed good agreement therefore the crystal structure can be considered as representative of the bulk material (figure A.30).

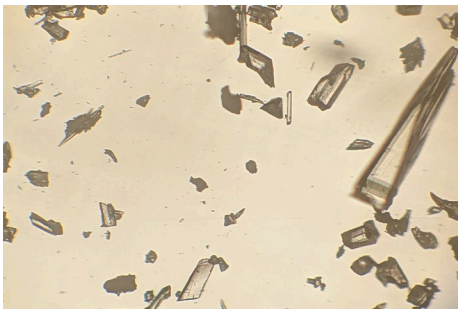

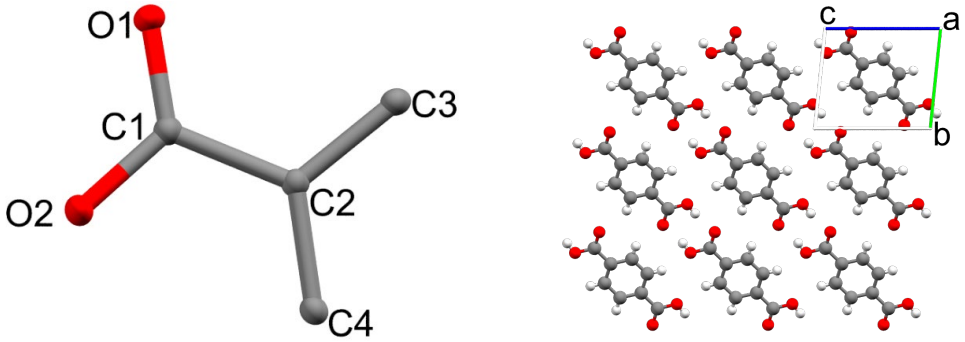

Figure 4.7. (Top) Optical microscope image of H_2BDC crystals synthesised from the hydrolysis of PET plastic. Magnification x56. (Left) Asymmetric unit of H_2BDC from hydrolysed PET plastic. Thermal ellipsoids are set to 40% probability. (Right) Molecule packing of H_2BDC.

4.3.2 Calcium Squarate Hydrate ([Ca(SQ)(H_2O)])

Squaric acid (3,4-dihydroxy-3-cyclobutene-1,2-dione) (SQ) is a tetradentate ligand which upon coordination to calcium ions affords a three-dimensional cubic MOF ([Ca(SQ)(H_2O)]), as shown in figure 4.8. The MOF contains microporous channels with an accessible diameter of 3.4 Å and face-to-face plane distance of 6.94 Å, therefore [Ca(SQ)(H_2O)] holds great potential in gas separations.[49] The small access diameter of this MOF falls precisely in between the molecular kinetic diameters of CO_2 (3.3 Å) and N_2 (3.65 Å), and thus [Ca(SQ)(H_2O)] has shown high selectivity in molecular sieving of CO_2 from flue gas.[50] The MOF has additionally been tested and proven to be superior in capturing trace propyne and propadiene from propylene during its purification.[51]

[Ca(SQ)(H$_2$O)] was first isolated by Weiss *et al.* in 1987.[52] The asymmetric unit consists of two halves of independent squarate linkers and one calcium centre (figure 4.8). The calcium centre is eight-coordinate and holds a bicapped trigonal prismatic geometry.

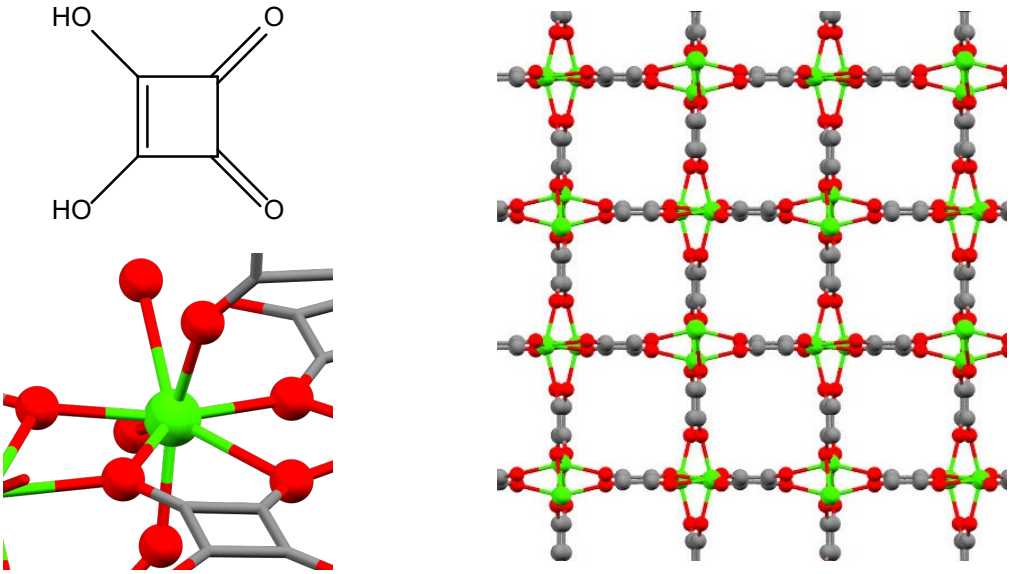

Figure 4.8. (Top left) Chemical structure of 3,4-dihydroxy-3-cyclobutene-1,2-dione (squaric acid). (Bottom left) Calcium centre coordination in [Ca(SQ)(H$_2$O)]. (Right) Crystal structure of Ca(SQ)(H$_2$O) viewed down the c axis.[52]

[Ca(SQ)(H$_2$O)] can be synthesised through various means. Weiss *et al.* first synthesised [Ca(SQ)(H$_2$O)] by a layering method.[52] An aqueous solution of sodium squarate was layered above a solution containing Ca(NO$_3$)$_2$, ethanoic acid and sodium ethanoate. This resulted in the growth of crystals after several days. The CH$_3$COOH/CH$_3$COO$^-$ buffer was found to be essential for the growth of large crystals otherwise thin needles were obtained. Bao *et al.* prepared [Ca(SQ)(H$_2$O)] *via* a hydrothermal method, again dissolving the acid in water and adding CaCO$_3$ before heating to 120 °C for 24 hours.[49] They found that adjusting the post-synthesis cooling rate from 1 to 0.1 °C min^{-1}, resulted in the formation of single crystals. Sumida *et al.* synthesised the MOF by dissolving the acid in water and adding CaCO$_3$ prior to heating in a microwave reactor at 100 °C for 10 minutes.[21] This convenient microwave procedure has been used to synthesise a reference sample of the MOF which we herein refer to as 'bulk [Ca(SQ)(H$_2$O)]'.

4.3.2.1 Aqueous Syntheses of [Ca(SQ)(H$_2$O)]

Initial work in our group established that [Ca(SQ)(H$_2$O)] could be synthesised from CaCO$_3$ in an aqueous, room temperature synthesis. Albeit over 24 hours rather than the short microwave synthesis used for bulk [Ca(SQ)(H$_2$O)]. CaCO$_3$ was suspended in an aqueous solution of squaric acid, the vial was covered with pierced parafilm to account for the evolution of CO_2 and the contents was stirred gently. Over 24 hours the solution turned a deep purple colour, and the formation of a white

powder was evident. PXRD confirmed the formation of [Ca(SQ)(H_2O)] in a quantitative yield, as no calcite peaks were present in the powder pattern (figure 4.9).

We furthered this work by replacing $CaCO_3$ with ball-milled eggshells and repeating the experiment. This indeed resulted in the formation of the MOF with no presence of persistent precursor eggshells (figure 4.9). This initial study confirms that replacement of commercially sought calcium precursors with biomineralised calcite has no effect on the resulting reactions and thus eggshells can be expected to behave similarly to calcium carbonate in bulk MOF syntheses.

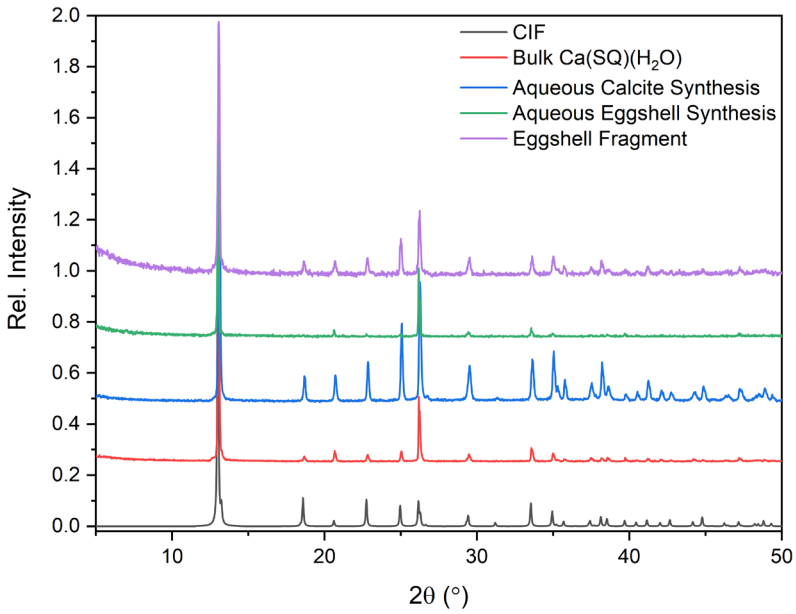

Figure 4.9. PXRD pattern comparison of [Ca(SQ)(H_2O)] (bottom to top) CIF; [Ca(SQ)(H_2O)] bulk; [Ca(SQ)(H_2O)] synthesised aqueously from calcite; [Ca(SQ)(H_2O)] synthesised aqueously from ball-milled eggshells; [Ca(SQ)(H_2O)] synthesised from an eggshell fragment.

TG analysis of bulk [Ca(SQ)(H_2O)] and [Ca(SQ)(H_2O)] synthesised aqueously from eggshells (figure 4.10) show the same decomposition profiles. Water loss from [Ca(SQ)(H_2O)] occurs at 100 °C, followed by the decomposition of the organic components between 200-850 °C to form the residual mass consisting of CaO. While we find that for both samples the solvent losses are well aligned with the expected mass loss value (table 4.1) there are deviations from the organic mass losses and residual masses. Both samples have higher than expected organic contents and thus lower residual masses. While we cannot account for the deviation of the bulk synthesis values, we find that persistent amorphous organics, found on the eggshell surfaces, may have transferred onto the MOF crystals during synthesis. This would account for the larger than expected organic content of this sample and is consistent with the 3-4% deviation that is observed from the TG analysis of just eggshells. We can see from the mass loss profile that after desolvation the material remains stable up to 250 °C, which is also found to be the case in previously reported work.[49,50] [Ca(SQ)(H_2O)] synthesised from both methods therefore have the expected thermal stabilities.

Table 4.1. Mass losses of [Ca(SQ)(H_2O)] found through TGA.

	Composition	Theoretical (%)	Bulk synthesis (%)	Aqueous synthesis (%)
Solvent Loss	H_2O	11	11.0	10.1
Organic Loss	SQ^{2-} - O	56	59.0	60.3
Residual Mass	CaO	33	30.0	26.9
Total	Ca(SQ)(H_2O)	100	100	100

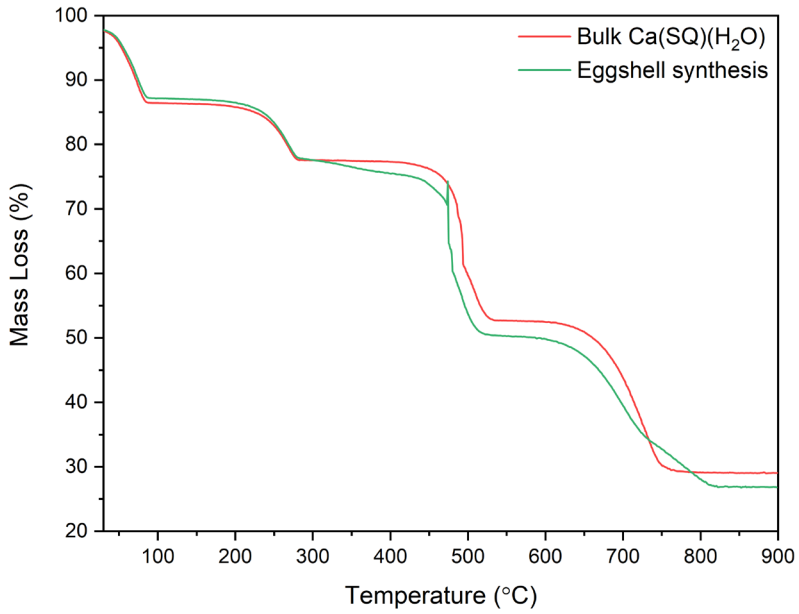

Figure 4.10. TGA of bulk [Ca(SQ)(H_2O)] and [Ca(SQ)(H_2O)] synthesised aqueously with eggshells.

SEM imaging of the MOF synthesised from calcite and eggshells shows a rod-like crystal morphology with crystal sizes ranging from 1-20 µm (figure 4.11). We do not notice any presence of unreacted metal precursor (calcite) which would be visible as irregularly shaped and sized particles.

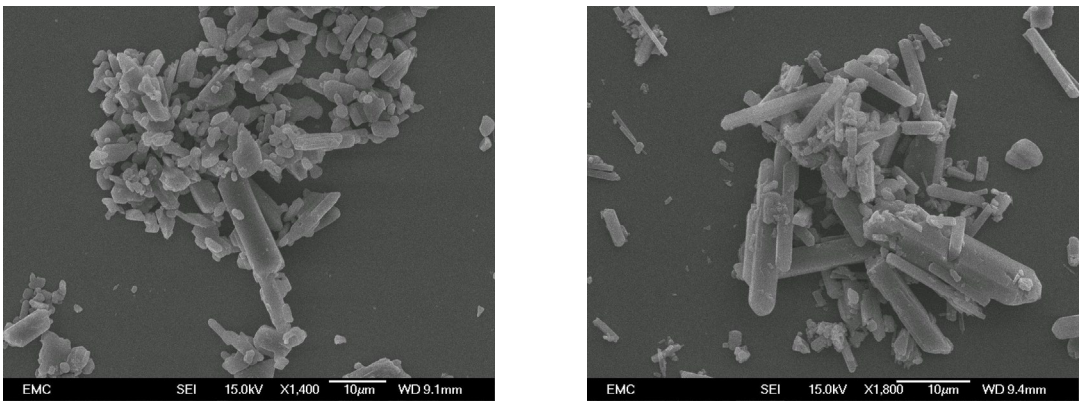

Figure 4.11. SEM images of [Ca(SQ)(H_2O)] synthesised aqueously from (left) calcite and (right) ground eggshells. Scale bars = 10 µm.

The membrane of an eggshell fragment was removed and the biomineralised calcite source was immersed in an aqueous solution of squaric acid for one week, resulting in the growth of large colourless needle crystals on both the interior and exterior surfaces of the eggshell (figure 4.12).

This initial crystal growth is reminiscent of the coordination replication work carried out by the Kitagawa group.[21]

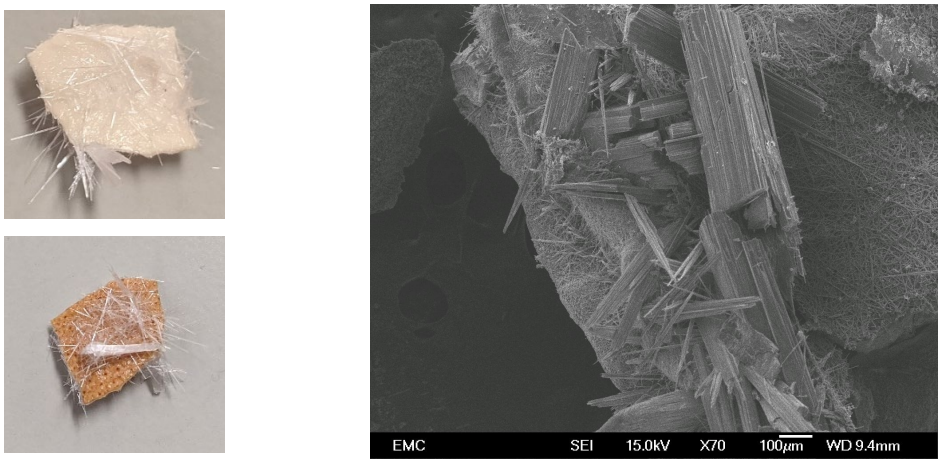

Figure 4.12. (Left) [Ca(SQ)(H_2O)] grown on the inner (top) and outer (bottom) surfaces of an eggshell. (Right) SEM image of [Ca(SQ)(H_2O)] grown from eggshell fragment (scale bar = 100 µm).

A portion of these crystals were carefully removed and subjected to PXRD characterisation which confirmed the formation of phase pure [Ca(SQ)(H_2O)]. The quality of these crystals was proven by selecting a suitable crystal and characterising it by SCXRD. The resulting unit cell parameters were compared to a known structure of [Ca(SQ)(H_2O)] and found to agree very well. The eggshell fragment was returned to the mother liquor for a further week. Following this, the eggshell was once again removed, dried, and ground into a powder with a pestle and mortar. PXRD prior to washing the powder revealed that the material wholly consisted of [Ca(SQ)(H_2O)], with no remaining calcite peaks (figure 4.9). The MOF was then washed with water to remove any residual squaric acid on the crystal surface as well as within its channels.

4.3.2.2 Mechanochemical Synthesis of [Ca(SQ)(H_2O)]

To reduce the quantity of solvent required for synthesising [Ca(SQ)(H_2O)] through the reported 'bulk' synthesis and our room temperature aqueous syntheses, we opted to attempt mechanochemical routes for this MOF. Rather than using 10-20 mL of water, ball-milling only requires 10-50 µL. Achieving this would improve the sustainability of the synthesis of this MOF. We do recognise that the use of benign water is far better than organic solvents commonly used in the MOF field, however reducing water usage, especially that which requires processing into deionised water, is still very beneficial.

Commercially sought calcite was combined with squaric acid in a ball-mill vessel along with several ZrO_2 milling balls. The vessel was sealed and shaken at 50Hz for five minutes to allow for sufficient mixing of the solid precursors. It was then opened, and deionised water (50 µL) was added. The addition of water caused effervescence and the vessel contents turned purple. These observations

are very characteristic of the reaction of calcium carbonate with squaric acid. The vessel was promptly resealed and shaken once more at 50Hz for a further 20 minutes, yielding a white powder. We know from our initial experiments that water promotes the reaction of squaric acid and eggshells to form [Ca(SQ)(H_2O)]. It is therefore important to ensure that MOF formation has occurred prior to washing, not doing so would make it ambiguous over whether the MOF formed during the mechanochemical step or potentially the washing step of this experiment.

Once we had confirmed through PXRD that the MOF had formed successfully, the material underwent washing with water and centrifugation cycles followed by drying at room temperature. The resulting PXRD patterns of the unwashed and washed products show good alignment to the simulated CIF pattern and there is no presence of calcite peaks in the unwashed pattern (figure 4.13). We can therefore presume that there has been a quantitative conversion in the mechanochemical synthesis step of the experiment.

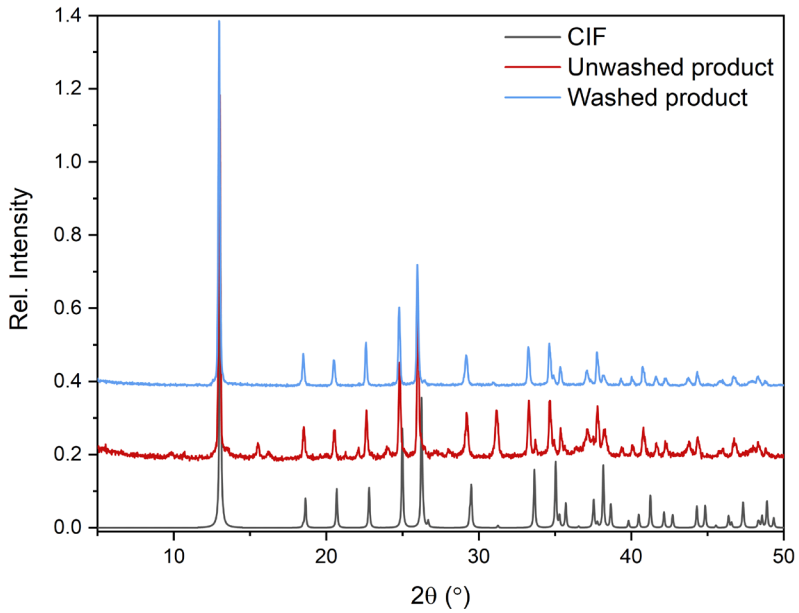

Figure 4.13. PXRD pattern comparison of unwashed and washed [Ca(SQ)(H_2O)] synthesised from calcite mechanochemically to the CIF.

Attempts to synthesise [Ca(SQ)(H_2O)] mechanochemically with ball-milled eggshells proved more challenging than with commercial calcite. We found that replacing calcite with eggshells and repeating the reaction indeed did form the MOF but also resulted in the formation of an unknown crystalline phase. In addition, PXRD confirmed the presence of unreacted eggshells in the unwashed product amongst the [Ca(SQ)(H_2O)] and unknown phase. Figure 4.14 shows the PXRD pattern of the unwashed product of this reaction, the product after one water wash, and the product after full washing. Washing the ball-milled product results in the removal of the unknown phase and unreacted precursors. This is shown by the removal of the corresponding peaks in the washed product pattern and indicates to us that the unknown phase is water soluble. The removal of

unreacted, and insoluble, eggshells from the product can only occur through the reaction of the metal source with H_2SQ during washing. This demonstrates what we have previously hypothesised, confirming that the washing stage of this MOF synthesis can further promote MOF formation. We therefore cannot state that [Ca(SQ)(H_2O)] can be quantitatively synthesised mechanochemically from eggshells.

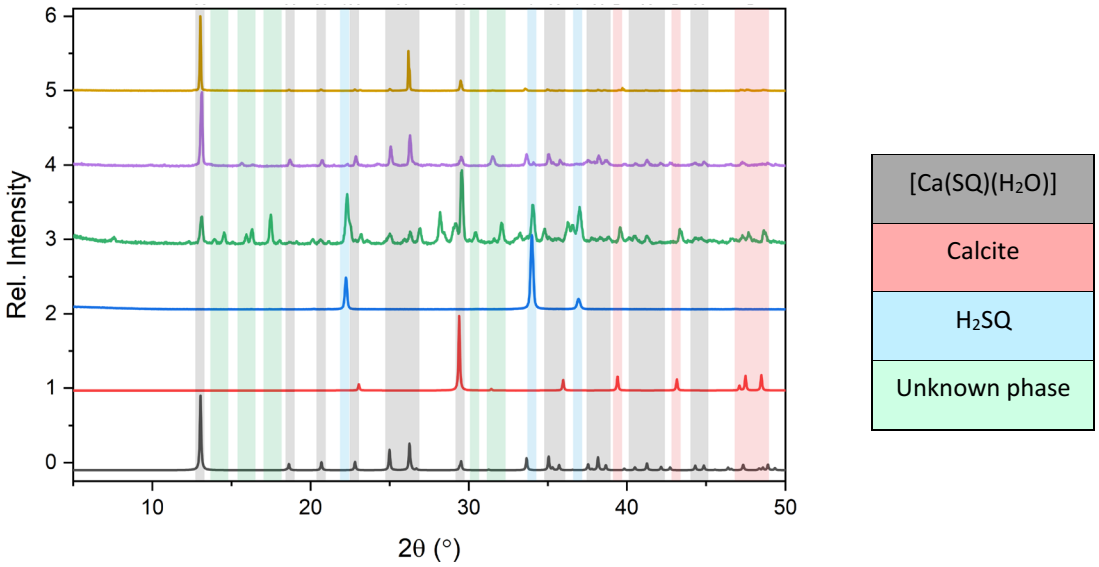

Figure 4.14. PXRD comparison of mechanochemically synthesised [Ca(SQ)(H_2O)] against its precursors. (Bottom to top) [Ca(SQ)(H_2O)] CIF; calcite CIF; H_2SQ; Unwashed BM MOF; Partially washed BM MOF; Fully washed BM MOF.

TG analysis of mechanochemically synthesised [Ca(SQ)(H_2O)] from calcite (figure 4.15) shows a mass loss profile consistent with those produced *via* the bulk and aqueous syntheses (figure 4.10). The water loss step at 100 °C matches well to the theoretical value in table 4.1 however we again find that the organic loss is larger than expected (+5%) and the residual mass lower than expected (-8%). We cannot rationalise this in the same way as the aqueous eggshell synthesis because commercial calcite was used at the metal precursor in this reaction. We do believe however that this deviation may have occurred as a result of defects within the MOF structure, i.e. missing calcium centres within the linear SBUs. Although we cannot prove this to be the case without further probing. This is a sensible deduction however because rapidly synthesised materials are known to contain defects due to the fast rate of crystallisation. This was found to be the case by Chaemchuen *et al.* whereby ZIF-8 samples with more defects had improved catalytic properties, due to the increase in catalytic sites.[53] Our material, once again, shows good thermal stability, well in line with reported values despite the likely presence of defects.

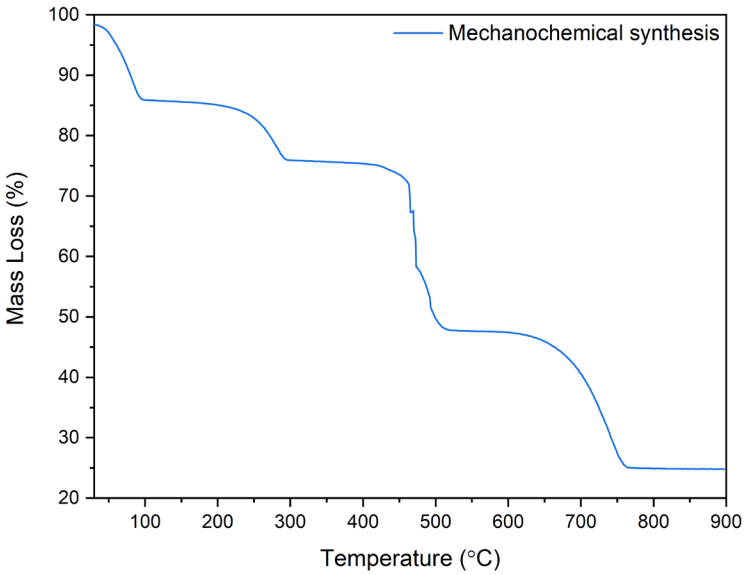

Figure 4.15. TGA of [Ca(SQ)(H$_2$O)] synthesised mechanochemically from calcite.

SEM imaging of the mechanochemically synthesised MOF show crystals with a cubic morphology in the size range of approximately 0.75-2 µm (figure 4.16). Some crystals exhibit a smooth and almost spherical shape which is likely due to the kinetic bombardment of the crystals against the milling balls, other crystals, and collisions with the walls of the reaction vessel. Similar mechanochemical erosion has previously been observed by Pichon *et al.*, who found that solvent-free grinding for five minutes resulted in smaller, and less well defined crystals of [Cu(INA)$_2$], when compared to crystals prepared in one minute.[41]

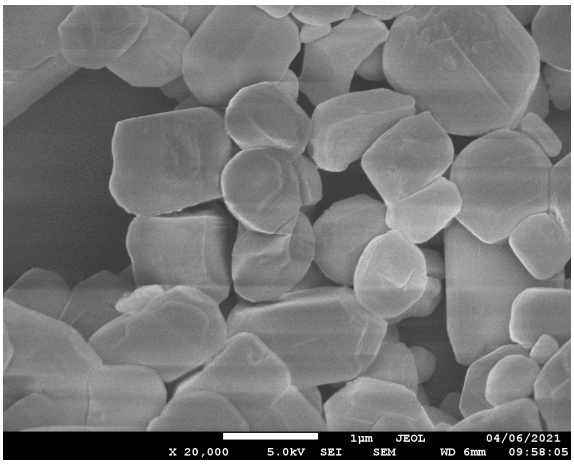

Figure 4.16. SEM image of [Ca(SQ)(H$_2$O)] synthesised mechanochemically from calcite. Scale bar = 1 µm.

4.3.2.3 CO_2 Adsorption of [Ca(SQ)(H$_2$O)]

The porosity of [Ca(SQ)(H$_2$O)] can be probed with CO_2 adsorption. Nitrogen gas is typically used to gain insight into a material's surface area, however in the case of this MOF the channel width of 3.4 Å is too small to allow for N_2 adsorption. Measuring the CO_2 capacity of our materials and comparing the values at one bar pressure to a reference sample of [Ca(SQ)(H$_2$O)] however allows

for a more than adequate assessment of porosity. The samples were degassed at 100 °C overnight and the CO_2 capacity was measured up to 1 bar at 298 K (figure 4.17). The reference MOF was synthesised following a procedure described by Tu and Zhang *et al*.[50] whereby a calcium salt as the metal precursor is used rather than an insoluble carbonate. This ensures that the reference material is pure [Ca(SQ)(H_2O)] because all unreacted precursors are soluble and can be removed with adequate washing prior to characterisation, ensuring a representative CO_2 capacity.

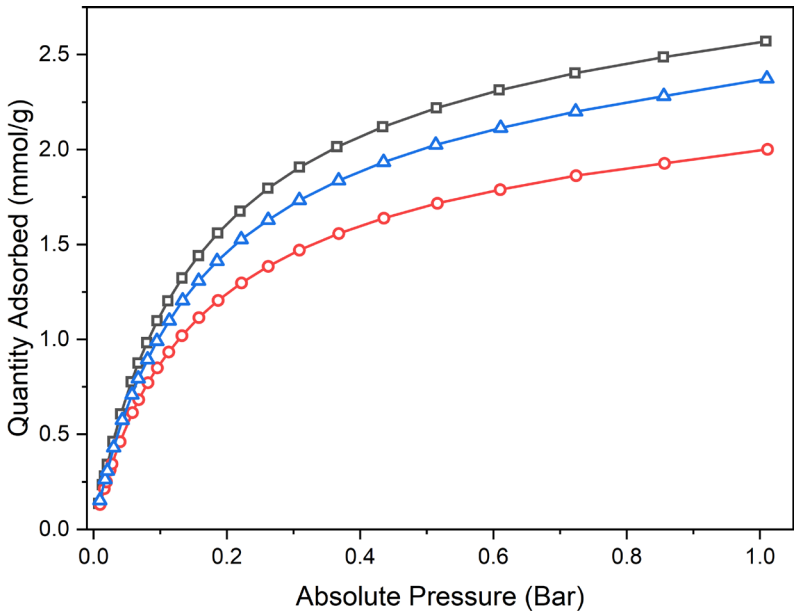

Figure 4.17. CO_2 adsorption isotherms at 298 K for [Ca(SQ)(H_2O)] synthesised by; (black squares) a reference procedure with $Ca(NO_3)_2{\cdot}4H_2O$; (red circles) eggshells in aqueous conditions; (blue triangles) mechanochemical means with calcite.

The CO_2 adsorption at one bar for the reference MOF, [Ca(SQ)(H_2O)] synthesised from eggshells, mechanochemically produced [Ca(SQ)(H_2O)] and the reported literature value for this MOF are 2.57, 2.00, 2.37 and 2.65[(50)] mmol/g respectively. This firstly confirms that [Ca(SQ)(H_2O)] synthesised from calcite, regardless of composition, retains porosity and does not undergo detrimental channel blockage from the precursor. The capacity of the MOF synthesised mechanochemically aligns well with both the reference value and the reported value by Tu and Zhang *et al*. This suggests that mechanochemical techniques do not cause channel collapse in [Ca(SQ)(H_2O)]. The CO_2 capacity for [Ca(SQ)(H_2O)] synthesised from an eggshell fragment shows porosity, albeit 25% lower than expected (when compared to the literature value). This reduction in porosity can further corroborate our theory, gained from TG analysis, that amorphous organics from the eggshells have transferred to, or encapsulated within, the MOF crystals. This is a sensible resolution as our preliminary work on precursors concluded, through TGA, that mechanical removal of the eggshells internal organic membrane was not 100% and that a small and persistent quantity will remain.

4.3.3 Calcium Fumarate Trihydrate ([Ca(FU)(H$_2$O)$_3$])

Calcium fumarate trihydrate ([Ca(FU)(H$_2$O)$_3$]) is a one-dimensional MOF consisting of infinite calcium-based SBUs and fumaric acid (H$_2$FU) organic linkers (figure 4.18). The linker only coordinates to an SBU through one of its two carboxylate groups, leaving the remaining group dangling between two other SBUs where it undergoes substantial hydrogen bonding. [Ca(FU)(H$_2$O)$_3$] has been reported for the use of fluoride removal from brick tea[54] as well as the removal of pesticides and cadmium from wastewater.[55]

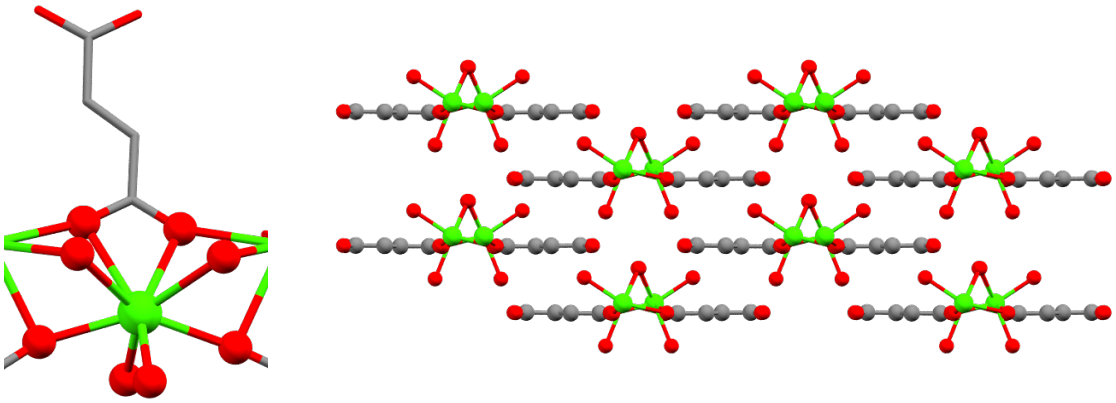

Figure 4.18. (Left) Coordination environment of calcium centres in [Ca(FU)(H$_2$O)$_3$]. (Right) Crystal packing of [Ca(FU)(H$_2$O)$_3$] viewed down the a axis.

Previously reported syntheses of [Ca(FU)(H$_2$O)$_3$] involve dissolving fumaric acid and calcium nitrate in methanol followed by prolonged heating at high temperature (130 °C), then cooling to low temperature for a period of two weeks for crystallisation to occur.[55] Alternatively, dissolution of fumaric acid with calcium acetate in water can yield the MOF after 16 hours of heating at 65 °C.[54] The former method requires a large energy input and both utilise calcium-based salts which could be readily replaced by a calcite source, including eggshells.

We started by synthesising [Ca(FU)(H$_2$O)$_3$] through a hydrothermal route, where H$_2$FU was partially dissolved in deionised water by sonication followed by the addition of calcium carbonate in a scintillation vial. The mixture was stirred briefly and only when effervescence ceased was it capped and heated to 100 °C for 24 hours. Upon initial cooling it was evident that no crystallisation of product had occurred, but heating had allowed for complete dissolution of the insoluble precursors. The solution was left to sit for a further 24 hours which allowed for the growth of large colourless crystals. These crystals underwent both single-crystal (table A.8) and powder -XRD (figure 4.19) characterisation to confirm the material composition was in fact the expected MOF. Comparison of the simulated powder pattern to the hydrothermally synthesised crystals from calcite showed excellent agreement.

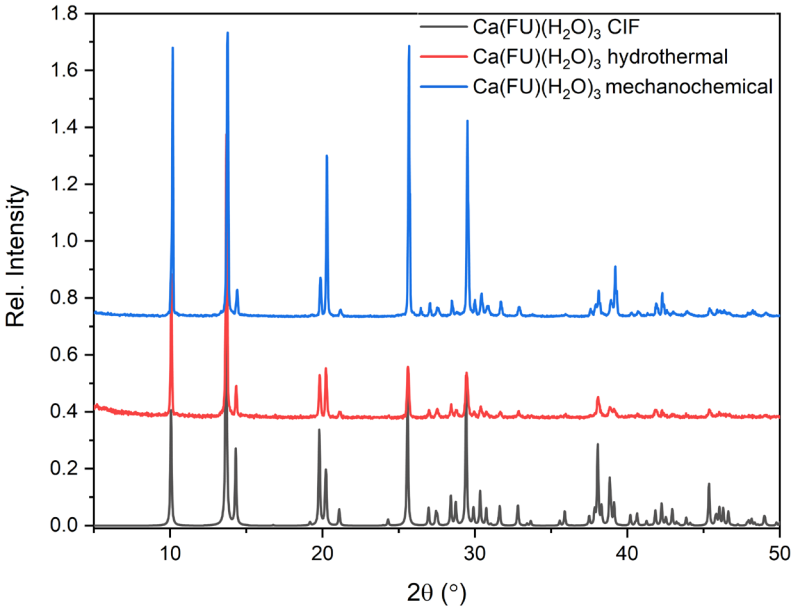

Figure 4.19. PXRD comparison of (bottom to top) [Ca(FU)(H$_2$O)$_3$] CIF; [Ca(FU(H$_2$O)$_3$] synthesised hydrothermally from calcite; [Ca(FU)(H$_2$O)$_3$] mechanochemically from eggshells.

Replacing calcium carbonate with ball-milled eggshells and repeating the hydrothermal experiment did not result in complete dissolution of the metal precursor. Upon cooling some eggshell particles remained and ultimately acted as nucleation sites for the growth of [Ca(FU)(H$_2$O)$_3$] over the subsequent 24 hours.

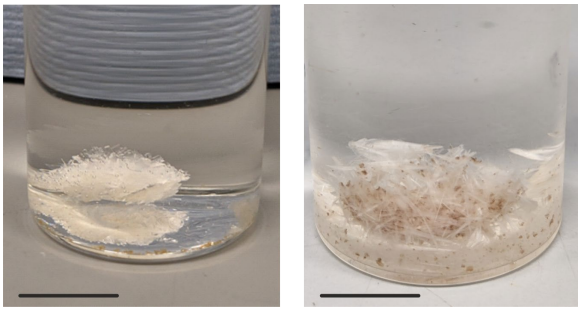

Figure 4.20. Crystals of [Ca(FU)(H$_2$O)$_3$] hydrothermally from (left) calcite and (right) ball-milled eggshells. Scale bar = 1 cm.

Further pursuit of optimising the hydrothermal route of this MOF with eggshells was not taken because of the opportunity to use mechanochemical techniques. Synthesising [Ca(FU)(H$_2$O)$_3$] *via* ball-milling with eggshells proved trouble-free. The calcium source was loaded into a ball-mill vessel with an equimolar quantity of H$_2$FU. The vessel was sealed and shaken at 50Hz for five minutes to allow for sufficient mixing of the precursors. The vessel was then opened, deionised water added, resealed, and shaken for 20 minutes at 50Hz. The resulting white powder underwent PXRD characterisation (figure 4.19) and found to match very well with the simulated powder pattern of [Ca(FU)(H$_2$O)$_3$]. We found that replacing H$_2$FU with its disodium salt, disodium fumarate, in this

reaction did not yield the MOF (figure A.31). We attribute this finding to the necessity of reacting stable precursors with acidic organic linkers under ball-milling conditions.

TG analysis of $[Ca(FU)(H_2O)_3]$ reveals very similar weight loss profiles for the material synthesised *via* both hydrothermal and mechanochemical methods (figure 4.21). It is expected for the MOF to exhibit two explicit weight losses; water loss at 100 °C (19%) and organic loss from 300-750 °C (55%) as well as a residual mass (27%) consisting of CaO. Indeed, $[Ca(FU)(H_2O)_3]$ synthesised through both methods followed this mass loss profile. The sudden mass loss experienced between 30-50 °C for the mechanochemical product is presumed to be residual solvent on the surface of the Al_2O_3 crucible from washing. The mass loss values of the two $[Ca(FU)(H_2O)_3]$ samples align very well with the theoretical composition of the MOF (table 4.2). This confirms that both methods form phase pure $[Ca(FU)(H_2O)_3]$ with no residual calcium metal precursor.

Table 4.2. Mass losses found through TGA of $[Ca(FU)(H_2O)_3]$ synthesised hydrothermally and mechanochemically.

	Composition	Theoretical (%)	Hydrothermal (%)	Mechanochemical (%)
Solvent Loss	3 x H_2O	27	25.5	27.4
Organic Loss	FU^{2-} - O	48	49	48.4
Residual Mass	CaO	26	25.5	24.2
Total	$[Ca(FU)(H_2O)_3]$	100	100	100

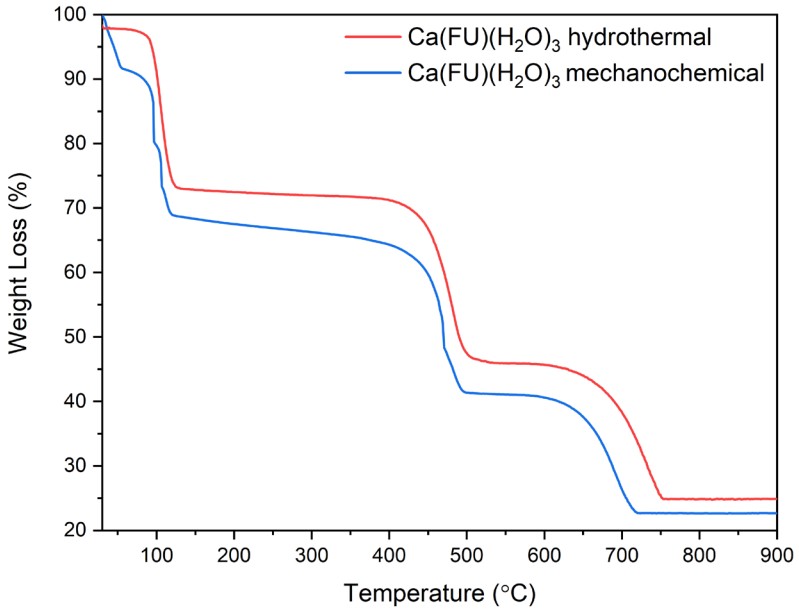

Figure 4.21. TGA of $[Ca(FU)(H_2O)_3]$ synthesised hydrothermally from calcite and ball-milled from eggshells. Conducted under an air atmosphere.

SEM imaging of the ball-milled product revealed rod-like crystals with longest dimensions of between 1-6 µm (figure 4.22). Sub-micron particles are also visible in the SEM which we believe to be fragments of $[Ca(FU)(H_2O)_3]$ and not unreacted eggshells, which would have a much more

uneven particle shape and also would be visible in the PXRD pattern through the presence of calcite peaks.

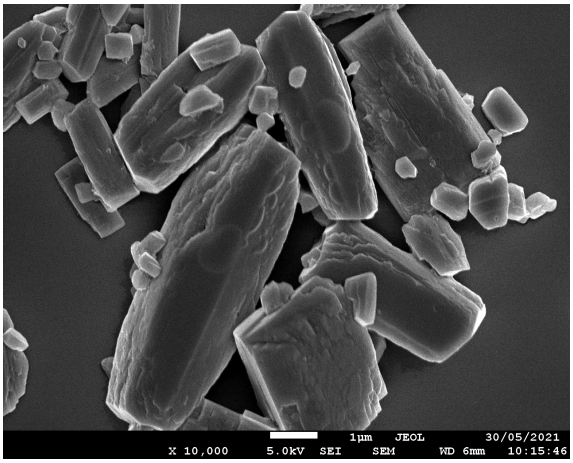

Figure 4.22 SEM image of [Ca(FU)(H_2O)$_3$] synthesised mechanochemically from eggshells.

4.3.4 Calcium Terephthalate Trihydrate ([Ca(BDC)(H_2O)$_3$])

The structure of [Ca(BDC)(H_2O)$_3$] was first solved through SCXRD in 1972,[56] 16 years before the first MOF structure by Robson *et al.* was ever reported.[57] The asymmetric unit (figure 4.23) of the MOF comprises of one calcium (II) centre, three water molecules and one whole terephthalate linker. Each calcium centre coordinates to four oxygen atoms from independent water molecules and four oxygen atoms from the carboxylate functionalities of three BDC linkers; totalling an eightfold coordination. Bridging water and BDC linkers results in the formation of infinite SBUs that are packed parallel to one another in the c direction (figure 4.23). This structure is isoreticular to that of [Ca(FU)(H_2O)$_3$].

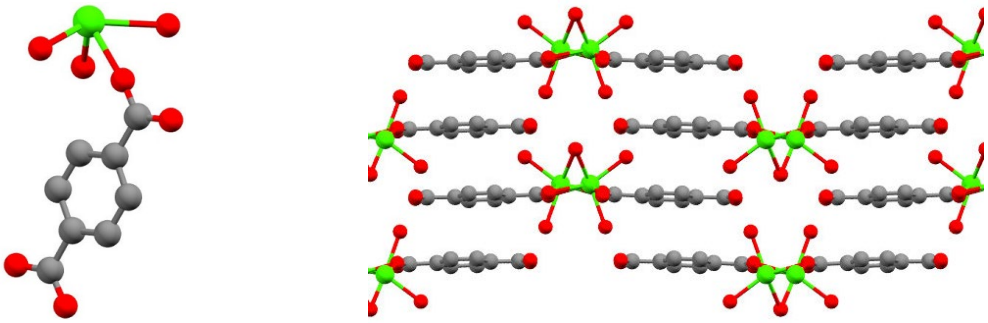

Figure 4.23. (Left) Asymmetric unit of [Ca(BDC)(H_2O)$_3$]. (Right) Crystal packing of [Ca(BDC)(H_2O)$_3$] viewed down the c axis.[56]

Matsuzaki and Iitaka formed crystals of the MOF by layering an aqueous solution of calcium acetate on top of an aqueous solution of potassium hydroxide and H_2BDC resulting in the formation of crystals within 24 hours.[56] More recently Sumida *et al.* synthesised the MOF by forming a

suspension of $CaCO_3$ and H_2BDC in a 50:50 mixture of H_2O and methanol followed by microwave heating at 120 °C for 10 minutes.[21]

4.3.4.1 Solvothermal Synthesis of [Ca(BDC)(H$_2$O)$_3$]

A one-pot fully sustainable synthesis of [Ca(BDC)(H_2O)$_3$] from eggshells and PET will require *in-situ* hydrolysis of the PET, to generate terephthalate anions that can be further reacted with the $CaCO_3$ from the eggshells to form the framework. The necessary high temperatures required for the depolymerisation of PET means that the use of Teflon-lined steel autoclaves is essential to avoid solvent evaporation and maintain high pressure. PET has been successfully depolymerised, as previously discussed, at 210 °C in a H_2O/EG solvent mixture.[38] (Cr)MIL-101 has also been successfully synthesised in a one-pot synthesis at the same temperature in H_2O and formic acid by the same researchers. It is therefore essential that [Ca(BDC)(H_2O)$_3$] can be synthesised and remain stable at the high temperatures and in the solvent mixture necessary to hydrolyse PET.

Our initial reaction in this study therefore is to react $CaCO_3$ and H_2BDC at 210 °C in H_2O/EG (10:1) overnight (**1**). This reaction was then modified twice by replacing the H_2BDC with PET (**2**) and replacing both $CaCO_3$ and H_2BDC with eggshells and PET, respectively (**3**). The PET was sourced from recycled bottles that were washed thoroughly in deionised water prior to being cut into small pieces, roughly 0.25 cm^2 in size. The terephthalate content of PET is approximately 85%. The mass of PET used was therefore adjusted to ensure that an equimolar quantity of terephthalate was present in all three reactions. After heating, the solid contents of all three reactions were collected by centrifugation and washed with DMF and methanol three times each before being dried at room temperature for 24 hours. We have summarised the reagent sources of each reaction in table 4.3.

Table 4.3. Ca^{2+} and BDC^{2-} sources for experiments 1-4 to synthesise [Ca(BDC)(H_2O)$_3$]. Additional information on experimental conditions is presented in table A.5.

Experiment	Ca^{2+} Source	BDC^{2-} Source
1	Commercial $CaCO_3$	Commercial H_2BDC
2	Commercial $CaCO_3$	PET
3	Eggshells	PET
4	Ball-milled eggshells	PET

Figure 4.24 contains the PXRD patterns of the resulting solids after washing and drying compared to a simulated pattern derived from the crystal structure of [Ca(BDC)(H_2O)$_3$]. It is apparent that the MOF has formed in all three cases and has reached a high level of crystallinity. Upon closer inspection of experiment **3** which utilised eggshells and PET as MOF precursors, there is a high

intensity peak at 29.5° corresponding to calcite. This suggests that the eggshells have not completely reacted with the terephthalate derived from the added PET. Experiment **3** was further modified by ball-milling the eggshells prior to carrying out the MOF synthesis (now denoted as experiment **4**). PXRD confirmed that this additional treatment yielded $[Ca(BDC)(H_2O)_3]$ with no residual calcite (figure 4.24). We attributed this finding to the increase in surface area that ball-milling introduces through particle size reduction of the metal precursor. $[Ca(BDC)(H_2O)_3]$ is non-porous and thus formation of the MOF on the surface of the eggshell fragments will inhibit further growth, due to limited opportunity for both further leaching of Ca(II) or impregnation of BDC^{2-} through the deposited MOF layer.

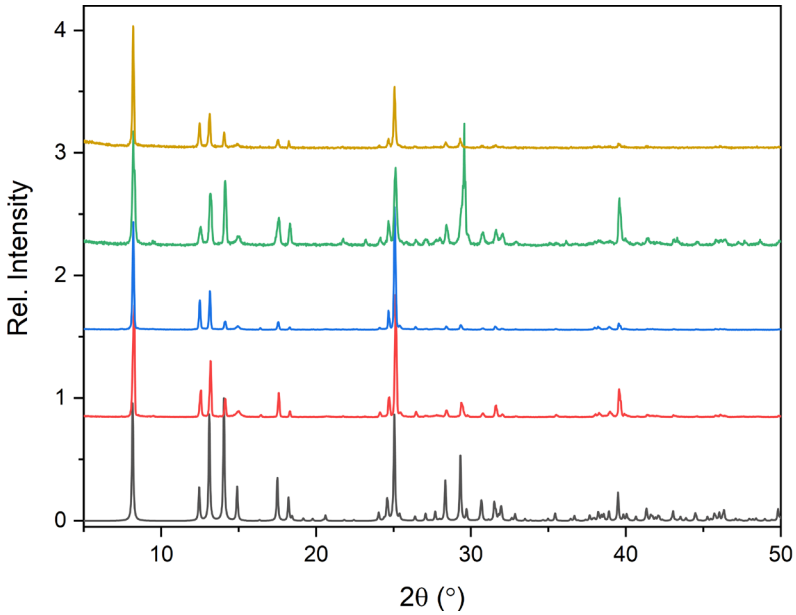

Figure 4.24. PXRD patterns of $[Ca(BDC)(H_2O)_3]$ (bottom to top); CIF; synthesised from $CaCO_3$ and H_2BDC (1); $CaCO_3$ and PET (2); eggshells and PET (3); ball-milled eggshells and PET (4).

TG analysis of all four products further confirms the presence of residual calcite in the reaction product of experiment **3** and its absence in products **1**, **2** and **4** (figure 4.25). The much higher than expected residual mass, after 800 °C, is caused by additional calcium oxide from the thermal decomposition of calcium carbonate.

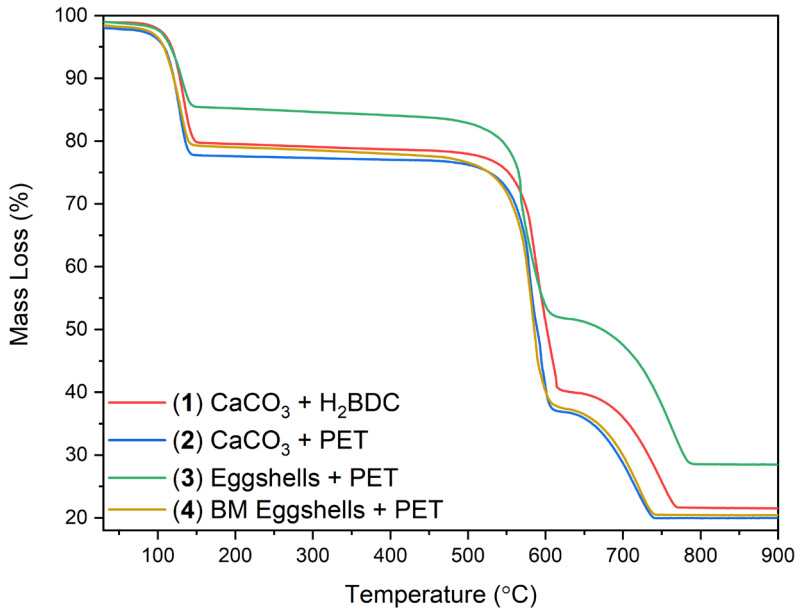

Figure 4.25. TGA of $[Ca(BDC)(H_2O)_3]$; synthesised from $CaCO_3$ and H_2BDC (1); $CaCO_3$ and PET (2); eggshells and PET (3); ball-milled eggshells and PET (4). Conducted under an air atmosphere.

Further analysis of the mass loss profiles from figure 4.25 shows that $[Ca(BDC)(H_2O)_3]$ in experiments **1**, **2** and **4** align very well with the theoretical water loss, organic loss and residual mass of the MOF, confirming that the materials are phase pure. The additional residual mass of 7% in experiment **3** corresponds to 2.46 mg of remaining $CaCO_3$ in the TGA sample, which equates to a residual $CaCO_3$ amount of 12% in the product of experiment **3** (calculation found in section A.4.7).

Table 4.4. Mass losses found through TGA of $[Ca(BDC)(H_2O)_3]$ in experiments 1-4.

	Composition	Theoretical (%)	Experimental (%)			
			1	**2**	**3**	**4**
Solvent Loss	3 x H_2O	21	21	22	15	21
Organic Loss	BDC^{2-} - O	57	57	58	56	58
Residual Mass	CaO	22	22	20	29	21
Total	$[Ca(BDC)(H_2O)_3]$	100	100	100	100	100

SEM imaging of $[Ca(BDC)(H_2O)_3]$ bulk and that synthesised from PET and ball-milled eggshells (experiment **4**) (figure 4.26) show a very different crystal morphology. The former material has an irregular shape and size distribution while the MOF synthesised from sustainable precursors has a more regular plate like crystal morphology with the longest dimension measuring ≈1 µm in length and very closely resemble the biomineralised structure of aragonite nacre platelets (figure 4.26). We believe that $[Ca(BDC)(H_2O)_3]$ crystallises much more slowly in experiment **4** due to the required depolymerisation of PET to yield H_2BDC prior to MOF formation. Sumida *et al.* reported microwave procedure yields crystalline $[Ca(BDC)(H_2O)_3]$ within 15 minutes, we therefore believe that the bulk synthesis procedure results in much faster crystallisation of the MOF. This promotes a much more irregular crystal morphology.

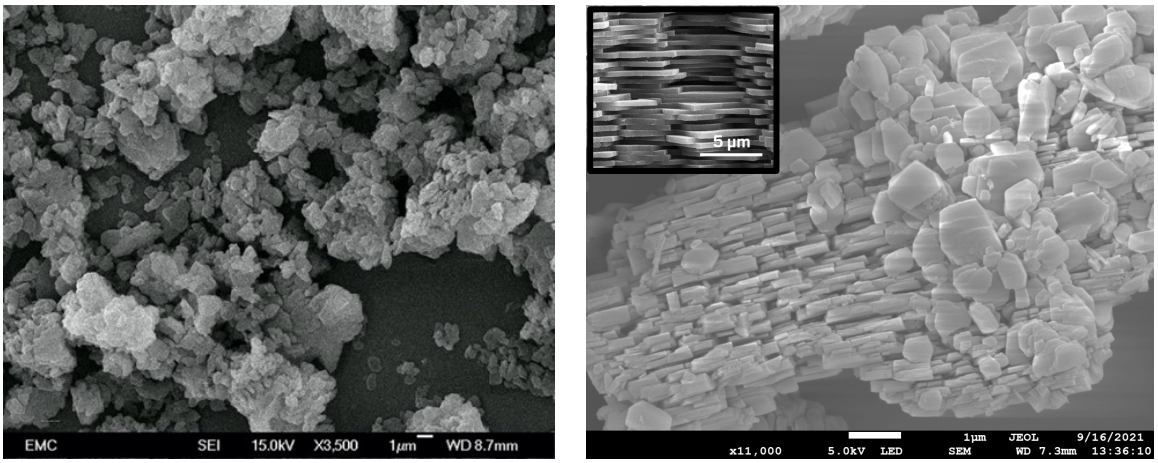

Figure 4.26. SEM images of (left) [Ca(BDC)(H_2O)$_3$] synthesised in bulk from calcite and (right) [Ca(BDC)(H_2O)$_3$] synthesised from eggshells and PET. (Inset) Nacre platelets.[58]

4.3.4.2 Mechanochemical Synthesis of [Ca(BDC)(H_2O)$_3$]

Mechanochemical syntheses of the previous two MOFs *via* ball-milling proved very fruitful and thus the same was repeated for [Ca(BDC)(H_2O)$_3$]. An initial experiment using calcium carbonate and commercially sought H_2BDC as precursors was carried out to ensure viability, before optimising the reaction with their recycled counterparts; chicken eggshells and reclaimed H_2BDC from PET plastic bottles. The reclaimed H_2BDC was obtained following the procedure discussed in section 4.3.1.2 and did not undergo any further purification prior to reaction.

H_2BDC and calcite were combined in a Teflon ball-mill vessel along with seven ZrO_2 balls, one drop of methanol and one drop of deionised water. We estimate that each drop measured 100 µL in volume. The vessel was sealed and shaken at 50Hz for 20 minutes. Following this the resulting white powder was removed and characterised by PXRD (figure 4.27). This confirmed the successful formation of [Ca(BDC)(H_2O)$_3$] with no apparent presence of either unreacted H_2BDC or calcite. We found that the addition of solvent to this reaction was essential to form the MOF. A control experiment conducted without the water/methanol mixture yielded no product and the resulting PXRD pattern was an overlap of the two crystalline precursors. This is not surprising when it is considered that LAG is very commonplace in the formation of MOFs through mechanochemical means. In this case the MOF structure contains coordinated water molecules and thus the solvent acts as both reaction medium and reagent.

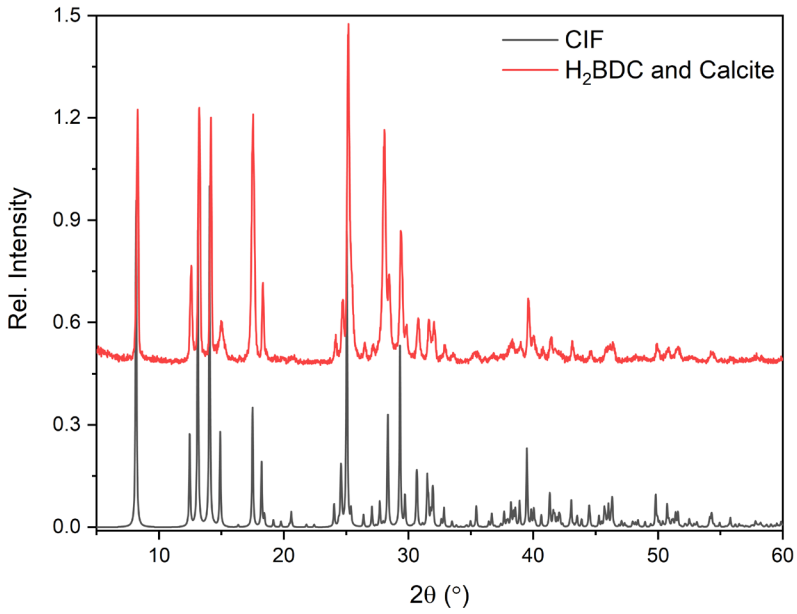

Figure 4.27. PXRD pattern comparison of (bottom to top) [Ca(BDC)(H₂O)₃] CIF; [Ca(BDC)(H₂O)₃] synthesised mechanochemically with H₂BDC and calcite; [Ca(BDC)(H₂O)₃] synthesised mechanochemically with reclaimed H₂BDC and eggshells.

Once we had established the feasibility of forming [Ca(BDC)(H$_2$O)$_3$] mechanochemically, we exchanged the reagents for their sustainable counterparts and took this as an opportunity to optimise the necessary solvent quantities. To limit the number of variable parameters in this set of experiments we did not alter the vibration frequency or reaction time, thus all reactions were shaken at a frequency of 50Hz for 20 minutes. Reclaimed H$_2$BDC and ball-milled eggshells were combined within the reaction vessel, along with a defined quantity of deionised water or deionised water/methanol mixture (50:50) and then shaken. If insufficient water, below that observed in the MOF stoichiometry of 1:3 (Ca^{2+}:H$_2$O), is added to the reaction vessel then a large quantity of eggshells would remain unreacted, indicated by the presence of sharp calcite peaks in the PXRD pattern. When an excess quantity of water was applied, the reaction went to completion with no unreacted eggshells remaining, as confirmed via PXRD. This reaction would proceed quantitatively regardless of whether reclaimed H$_2$BDC was added in excess (experiment **5**) or equimolar quantities (experiment **6**) in comparison to the eggshells, as well as whether a solvent mixture (**5**) or solely water (**6**) was used. We therefore believe that the optimised reaction conditions for the mechanochemical synthesis of [Ca(BDC)(H$_2$O)$_3$] from eggshells and reclaimed H$_2$BDC, for a 10 mL reaction vessel containing seven ZrO$_2$ milling balls, are those stated for experiment **6** in table 4.5. This set of conditions ensure the least amount of reagent waste because the eggshells and reclaimed H$_2$BDC are in the same stoichiometry as the MOF formula. In addition, the use of methanol is avoided and replaced by benign water, marking an improvement to this reaction based upon chemical safety.

Table 4.5. Reagent ratios and solvent quantities for selected mechanochemical syntheses of [Ca(BDC)(H$_2$O)$_3$] from eggshells and reclaimed H$_2$BDC.

	Moles of reagents (mmol)			Solvent quantities (µL)	
	Ca^{2+}	BDC^{2-}	H_2O	H_2O	Methanol
5	0.3	0.6	1.1	20	20
6	0.6	0.6	2.2	40	0

The PXRD patterns of the resulting MOFs from experiments **5** and **6** are presented in figure 4.28 and clearly show crystalline [Ca(BDC)(H$_2$O)$_3$]. The presence of unreacted calcite is also not present in either of these samples.

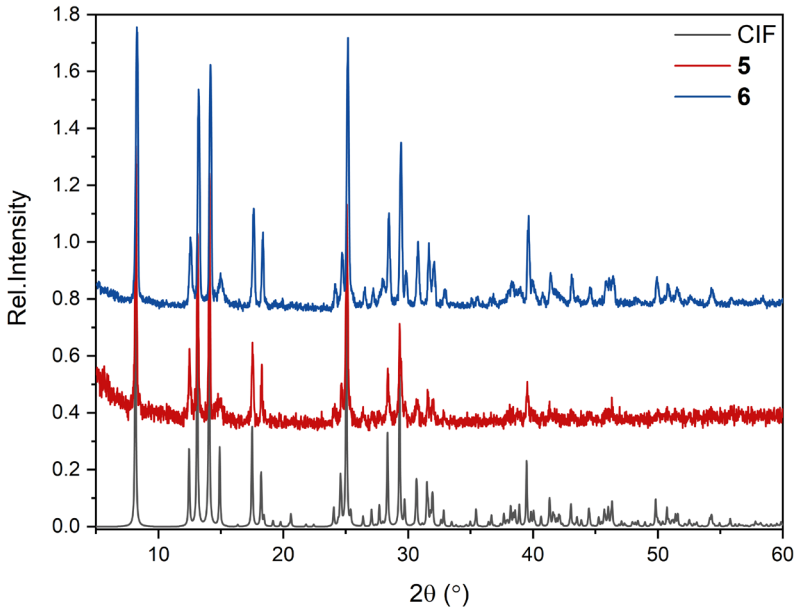

Figure 4.28. PXRD comparison of [Ca(BDC)(H$_2$O)$_3$] CIF; [Ca(BDC)(H$_2$O)$_3$] synthesised from reclaimed H$_2$BDC and eggshells in a 2:1 ratio (5) and in equimolar quantities (6).

TG analysis of [Ca(BDC)(H$_2$O)$_3$] synthesised through experiment **6** is presented in figure 4.29. As expected, we find two mass loss events that correspond to water loss and organic decomposition, as well as a residual mass from 750 °C.

We have found that the composition of [Ca(BDC)(H$_2$O)$_3$] synthesised in experiment **6** aligns well with the predicted composition. There is a slightly higher than expected (2.5%) organic content of the sample and consequently a lower-than-expected residual mass (2.5%). We attribute this very small deviation to persistent organics within the eggshells that have not be removed during the washing stage of synthesis. Again, this deviation is consistent with the deviation found of the TG analysis of eggshells, and also the MOFs synthesised from eggshells that have been described above.

Table 4.6. Mass losses found through TGA of mechanochemically synthesised [Ca(BDC)(H$_2$O)$_3$] from eggshells and reclaimed H$_2$BDC.

	Composition	Theoretical (%)	6 (%)
Solvent Loss	3 x H_2O	21	21.0
Organic Loss	BDC^{2-} - O	57	59.5
Residual Mass	CaO	22	19.5
Total	[Ca(BDC)(H$_2$O)$_3$]	100	100

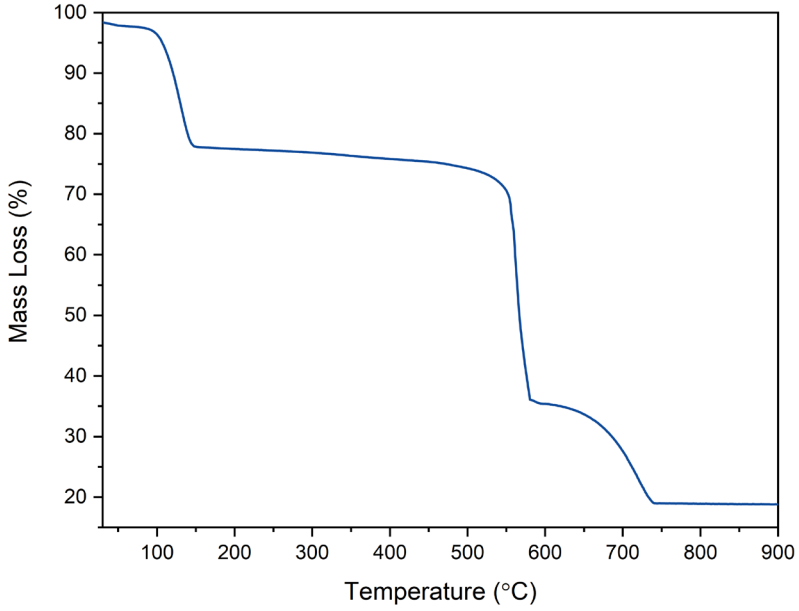

Figure 4.29. TGA of [Ca(BDC)(H$_2$O)$_3$] synthesised from reclaimed H$_2$BDC & eggshells (experiment 6).

SEM imaging of our mechanochemically synthesised [Ca(BDC)(H$_2$O)$_3$] samples show similar crystal size and morphology (figure 4.30) to one another. Interestingly, the mechanochemically synthesised [Ca(BDC)(H$_2$O)$_3$] has a similar crystal size of ≈1 µm as the solvothermally synthesised MOF from PET and eggshells (figure 4.26). We would expect a much smaller crystal size from mechanochemically syntheses because of the physical bombardment of the material with the milling balls.

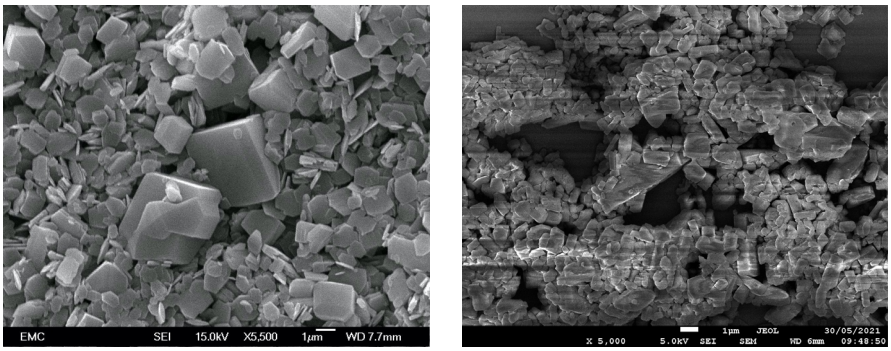

Figure 4.30. SEM images of [Ca(BDC)(H$_2$O)$_3$] synthesised mechanochemically from (left) H$_2$BDC & calcite and (right) reclaimed H$_2$BDC and eggshells. Scale bars = 1 µm.

4.3.5 Ca-MOF-1 (Ca(UR-CO_2H)(H_2O)$_4$)

Following the success of synthesising the three previously reported calcium-based MOFs from recycled precursors we have endeavoured to expand this work into synthesising a new MOF. We opted for utilising the organic linker UR-CO_2H (4,4´ (carbonylbis(azanediyl))dibenzoic acid) for two reasons: a calcium MOF based on the same organic linker has been previously reported by Forgan *et al.* albeit it using a DMF/H_2O solvent mixture and a calcium salt, [59] and because UR-CO_2H had been successfully used in chapter three to form a range of zinc-based materials.

Prior to attempting to synthesise a new MOF using a source of calcium carbonate, our first step was to combine a calcium salt, in this case calcium chloride, with UR-CO_2H in deionised water and characterise the resulting material, which from herein we refer to as Ca-MOF-1. This provides a baseline set of characterisation information we can use as a comparison for later synthesis attempts utilising calcium carbonate. The crystal structure of the calcium-based material described by Forgan *et al.* contains coordinated DMF molecules, therefore we can say with confidence that any resulting material from our initial experiment would differ to their reported structure.

Crystals of Ca-MOF-1 were grown *via* a layering method where $CaCl_2$ and UR-CO_2H were separately dissolved in deionised water and carefully layered on top of one another, with a blank H_2O layer separating the two reagents. We found that reagent concentrations of 0.05M were too high for this system as they resulted in the precipitation of, what we assume to be, microcrystalline Ca-MOF-1 within minutes of the addition of the UR-CO_2H layer. While single-crystal quality crystals were eventually obtained after leaving the reaction for 24 hours, severe twinning was experienced. Even halving the reagent concentrations to 0.025 M to slow crystallisation still resulted in thin and brittle plate crystals that could not allow for good quality SC data to be collected. We were however able to obtain a crystal structure which was chemically sensible and topologically similar to previously reported calcium-carboxylate based MOFs.

Table 4.7. Crystal data and structural refinement information for Ca-MOF-1.

Empirical formula	$C_{15}H_{16}CaN_2O_9$
Formula weight	408.38
Temperature/K	100
Crystal system	Monoclinic
Space group	Ia (9)
a/Å	7.0678(4)
b/Å	37.207(2)
c/Å	6.5007(3)
α/°	90
β/°	90
γ/°	90
Volume/Å^3	1709.50(16)
Z	4
ρ_{calc}g/cm^3	1.587
μ/mm^{-1}	0.422
F(000)	848
Crystal size/mm^3	0.3 x 0.1 x 0.02
Radiation	Mo Kα (λ = 0.71073)
2Θ range for data collection/°	4.378 to 69.736
Reflections collected	20292
Independent reflections	4969 [R_{int} = 0.1434, R_{sigma} = 0.1302]
Final R indexes [I>=2σ (I)]	R_1 = 0.1169, wR_2 = 0.2977
Final R indexes [all data]	R_1 = 0.1345, wR_2 = 0.3079

The asymmetric unit of Ca-MOF-1 is shown in figure 4.31 and comprises of one full UR-CO_2H linker, one calcium centre and four water molecules. Three water molecules (O7A, O7B and O7C) are coordinated to the calcium centres while one is non-coordinated but in good crystallographic order (O6A). The thermal ellipsoids of carbon atoms C1 and C2 are flat and do not exhibit a sensible ellipsoidal shape. The calcium centre has eight-fold coordination, adopted a bicapped trigonal prismatic geometry (Figure 4.31). It coordinates to four water molecules and four oxygen atoms from the carboxylate groups of UR-CO_2H.

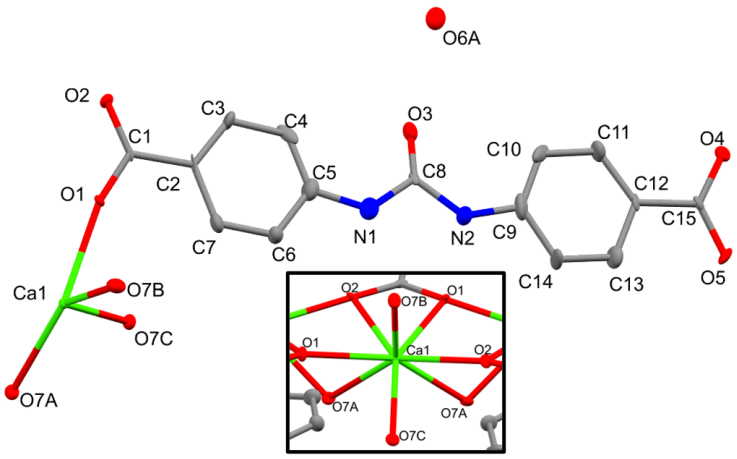

Figure 4.31. Asymmetric unit of Ca-MOF-1. Thermal ellipsoids are set to 40% probability. (Inset) Coordination environment of the calcium metal centre.

Ca-MOF-1 adopts the same one-dimensional chain topology as other calcium-based MOFs with linear dicarboxylic acid linkers such as [Ca(FU)(H_2O)$_3$] and [Ca(BDC)(H_2O)$_3$] . The UR-CO_2H linker coordinates to linear calcium SBUs through only one of its carboxylate groups, leaving the other group dangling with no formal coordination. The carboxylate that does coordinate to the SBU does so through a bidentate coordination to a central calcium centre as well as bridging to the calcium centres either side of this central metal (figure 4.32), affording the infinite linear SBU. The chemical structure in Figure 4.32 clarifies the bicapped trigonal prismatic geometry of the calcium centres.

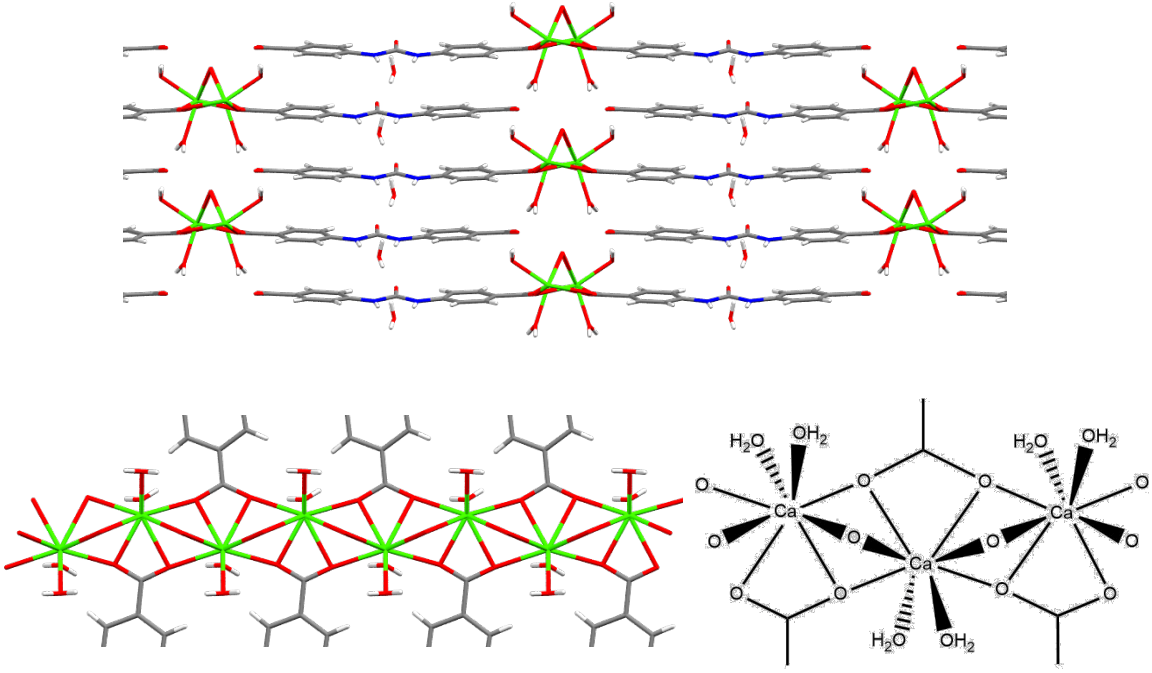

Figure 4.32. (Top) Crystal packing of Ca-MOF-1 viewed down the a axis. (Bottom) Linear SBU of Ca-MOF-1, viewed down the c axis, and the chemical structure of the SBU.

The dangling carboxylate group of the UR-CO_2H linker undergoes a substantial level of hydrogen bond stabilisation from the coordinated water molecules of adjacent SBUs above and below the COO^- group (figure 4.33). The hydrogen bond lengths range from 1.9 to 2.2 Å, signifying strong interactions between the water molecules and organic linker.

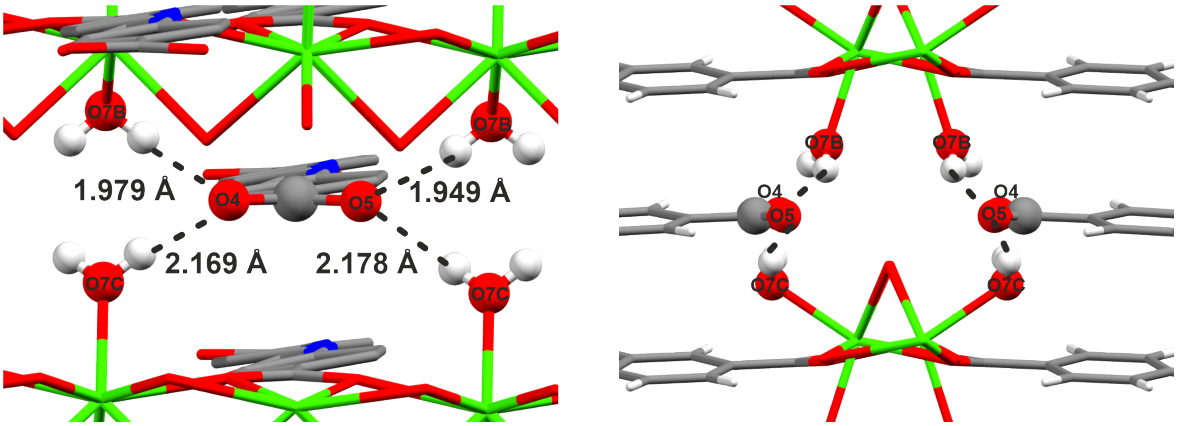

Figure 4.33. Hydrogen bond environment of the dangling carboxylate group in Ca-MOF-1.

The non-coordinated water molecule in Ca-MOF-1 also undergoes substantial hydrogen bonding to the urea group of three independent UR-CO_2H linkers. The water molecule acts as a hydrogen bond acceptor to both amine groups of a urea moiety located above, as well as acting as a hydrogen bond donor to two independent carboxylate groups of urea moieties below (figure 4.34). Both [Ca(BDC)$(H_2O)_3$] and [Ca(FU)$(H_2O)_3$] do not contain non-coordinated solvent molecules within their structures, despite being isoreticular to Ca-MOF-1. We postulate that this difference arises from the presence of hydrogen bond rich functional groups such as urea and the non-linear nature of UR-CO_2H, which reduces the ability for close structural packing within Ca-MOF-1, and thus promotes the inclusion of water within its structure to avoid void space.

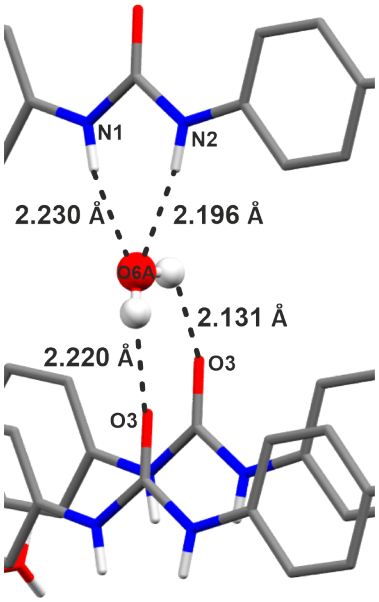

Figure 4.34. Hydrogen bond environment of the free water molecule within Ca-MOF-1.

Ca-MOF-1 could also be synthesised by simply combining equimolar aqueous solutions of $CaCl_2$ and UR-CO_2H followed by gentle stirring overnight. The material was collected by centrifugation and washed with water to remove unreacted precursors followed by drying at room temperature. PXRD confirms that the material consists of the same phase as the Ca-MOF-1 crystals grown *via* the layering reagents method (figure 4.35). A comparison of the two patterns to a simulated pattern from the obtained crystal structure shows good agreement. We can expect, and do see, some deviations from the simulated pattern that we can attribute to the non-optimised crystal structure.

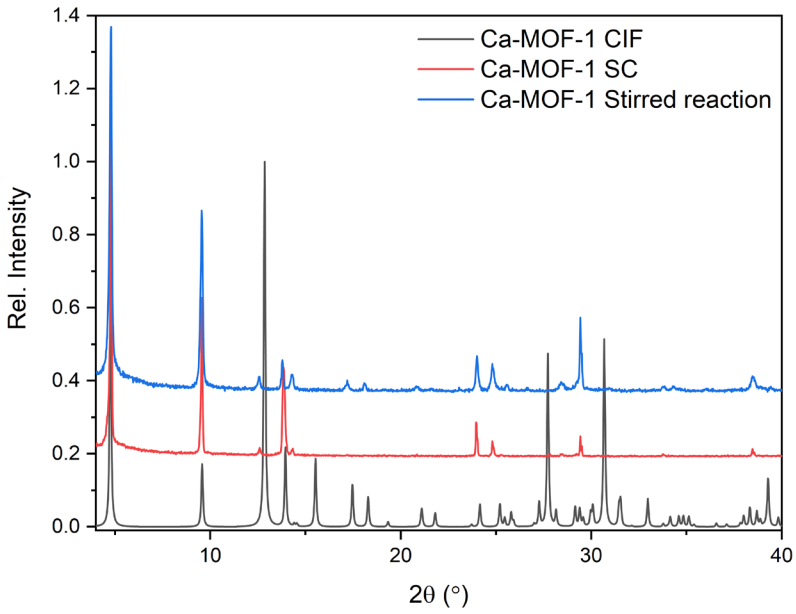

Figure 4.35. PXRD pattern comparison of single crystal and bulk Ca-MOF-1 to a simulated pattern derived from our crystal structure.

SEM imaging of Ca-MOF-1 synthesised *via* our stirred method confirms a thin plate crystal morphology (figure 4.36), identical to our understanding from the reagent layered method. Crystal size varies quite considerably but we suggest this to be caused by large, brittle, crystals (≤ 10 µm) breaking down into smaller sub-micron crystals.

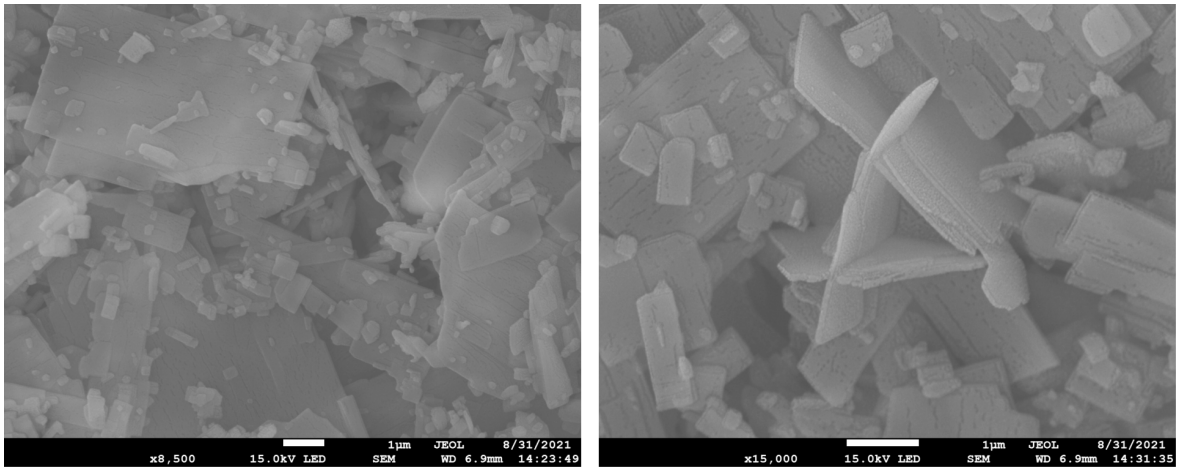

Figure 4.36. SEM image of Ca-MOF-1 crystals prepared from a stirred reaction. Scale bars = 1 µm.

TG analysis of Ca-MOF-1 was conducted on a portion of Ca-MOF-1 which was air dried on filter paper. The resulting TG plot, in figure 4.37, unambiguously shows a solvent loss step, organic loss step and residual mass at 100, 409 and 712 °C respectively.

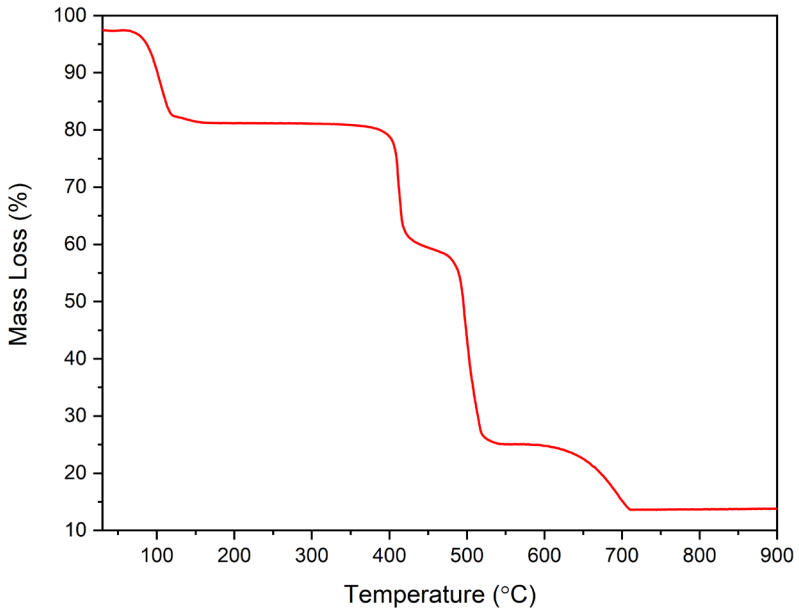

Figure 4.37. TGA of Ca-MOF-1 conducted in an air atmosphere.

Our solved crystal structure reveals that the ratio of calcium centres, UR-CO_2H linkers and water molecules is 1:1:4, thus our theoretical chemical formula of Ca-MOF-1 is [Ca(UR-CO_2H)(H_2O)$_4$]. The experimental values, derived from TGA, align very well with the theoretical values of our presumed formula, as shown in table 4.8. Analysis of the mass loss profile of Ca-MOF-1 can unequivocally confirm that this chemical formula is correct and that our material is phase pure.

Table 4.8. Comparison of theoretical and experimental composition of Ca-MOF-1.

	Composition	**Theoretical (%)**	**Experimental (%)**
Solvent Loss	4 x H_2O	17	17
Organic Loss	$(UR\text{-}CO_2)^{2-}$ - O	70	69
Residual Mass	CaO	13	14
Total	Ca(UR-CO_2H)(H_2O)$_4$	100	100

TGA shows that after solvent removal at 100 °C, Ca-MOF-1 is stable up to around 400 °C, at which point the organic components of the material begin decomposition. We can apply isoreticular chemistry in this instance and propose that Ca-MOF-1 undergoes the same transformation upon heating as seen by Mazaj *et al*. with [Ca(BDC)(H_2O)$_3$].[60] They found that desolvating [Ca(BDC)(H_2O)$_3$] caused a phase change which yielded a microporous MOF. It is likely that removing water from the hydrated phase results in undercoordinated calcium centres. To avoid this the dangling carboxylate group of BDC undergoes coordination to compensate.

To investigate whether Ca-MOF-1 behaves similarly to [Ca(BDC)(H_2O)$_3$], a portion of Ca-MOF-1 was heated to 100 °C for 24 hours (now denoted as Ca-MOF-Anh) and then subjected to PXRD, TGA and N_2 gas adsorption characterisation. We expect to see a change in lattice parameters due to structural rearrangements and thus a change in powder pattern, the removal of water resulting in

the absence of a mass loss at 100 °C in TGA, and finally, the material will display some porosity towards N_2.

The PXRD pattern in figure 4.38 confirms that the removal of water molecules upon heating results in a change in the lattice parameters of the material because of the difference in patterns of Ca-MOF-1 and Ca-MOF-Anh. Similarly, dehydrating [Ca(BDC)(H_2O)$_3$] results in peak shift at low angle which is also observed for (020) peak of Ca-MOF-1 at 4.8°.

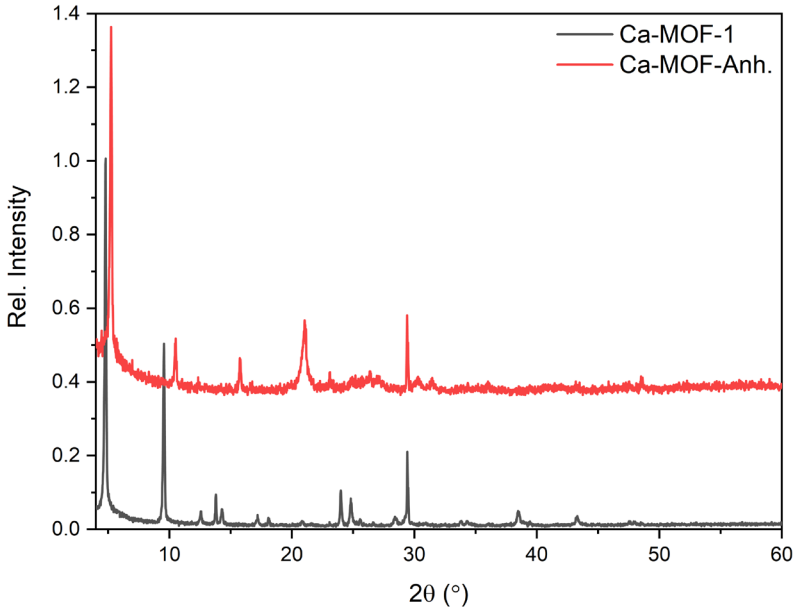

Figure 4.38. PXRD comparison of Ca-MOF-1 and Ca-MOF-Anh.

Figure 4.39 shows the difference in mass loss over increasing temperature between Ca-MOF-1 and Ca-MOF-Anh. The heat treatment of the latter material has clearly removed all water molecules from the structure due to the lack of a mass loss step at 100 °C. Organic decomposition occurs at 409 °C as also seen for the hydrated sample and a residual mass is present from 700 °C. From the mass loss profile of Ca-MOF-Anh we can derive a chemical formula for the material. The organic content and residual mass are 85% and 15% respectively. This aligns very well to a calcium:UR-CO_2H ratio of 1:1 (table 4.9). The chemical formula for Ca-MOF-Anh is therefore [Ca(UR-CO_2H)].

Table 4.9. Comparison of theoretical and experimental composition of Ca-MOF-Anh.

	Composition	**Theoretical (%)**	**Experimental (%)**
Organic Loss	$(UR\text{-}CO_2)^{2-}$ - O	84	85
Residual Mass	CaO	16	15
Total	Ca(UR-CO_2H)	100	100

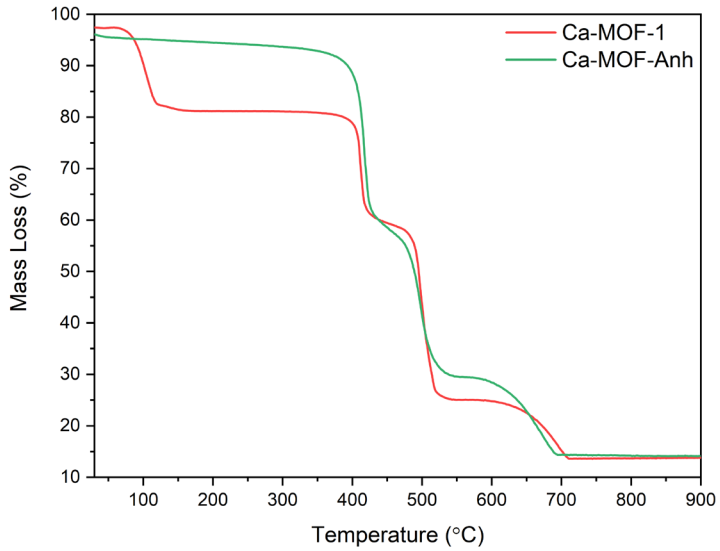

Figure 4.39. TGA comparison of Ca-MOF-1 and Ca-MOF-Anh.

Further proof of the removal of water molecules from Ca-MOF-1 upon heating can be found through a comparison of FTIR spectra between the hydrated MOF and Ca-MOF-Anh (figure 4.40). The loss of strong absorbances centred at 3278 and 1535 cm-1, which corresponds to the O-H stretch and bend of water respectively, confirms solvent loss.

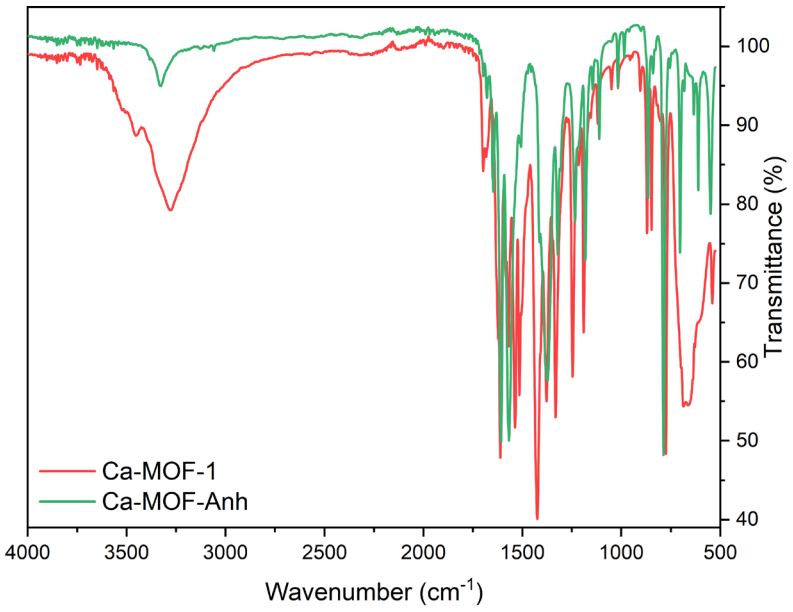

Figure 4.40. FTIR spectra of Ca-MOF-1 and Ca-MOF-Anh.

The linear N_2 adsorption isotherm plot is presented in figure 4.41 and resembles a type II isotherm. This isotherm is characteristic of non-porous or microporous materials. The BET surface area was calculated and found to be 420 m^2/g however we must treat this value with scepticism due to its isotherm type. We believe that probing with a more appropriate molecule, such as krypton or CO_2, would be a more suitable next step.

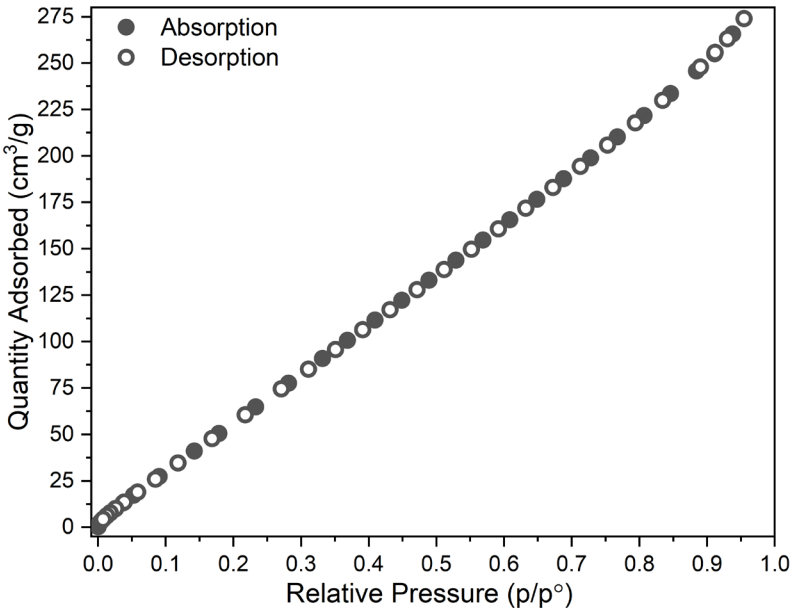

Figure 4.41. N_2 gas adsorption isotherm of Ca-MOF-Anh.

The removal of water from Ca-MOF-1 causes drastic changes to the crystal morphology. SEM imaging of the anhydrous MOF shows a thin petal-like crystal morphology (figure 4.42) in comparison to the plate morphology of Ca-MOF-1, previously shown in figure 4.36. Structural characterisation of this material through typical single-crystal routes is very unlikely due to the crystal size and habit. The growth of Ca-MOF-Anh would be extremely difficult to achieve and therefore would only be accessed through dehydration of Ca-MOF-1. Figure 4.38 confirms that Ca-MOF-Anh has a good degree of crystallinity therefore it is foreseeable that structure solution from PXRD and/or synchrotron techniques would be possible.

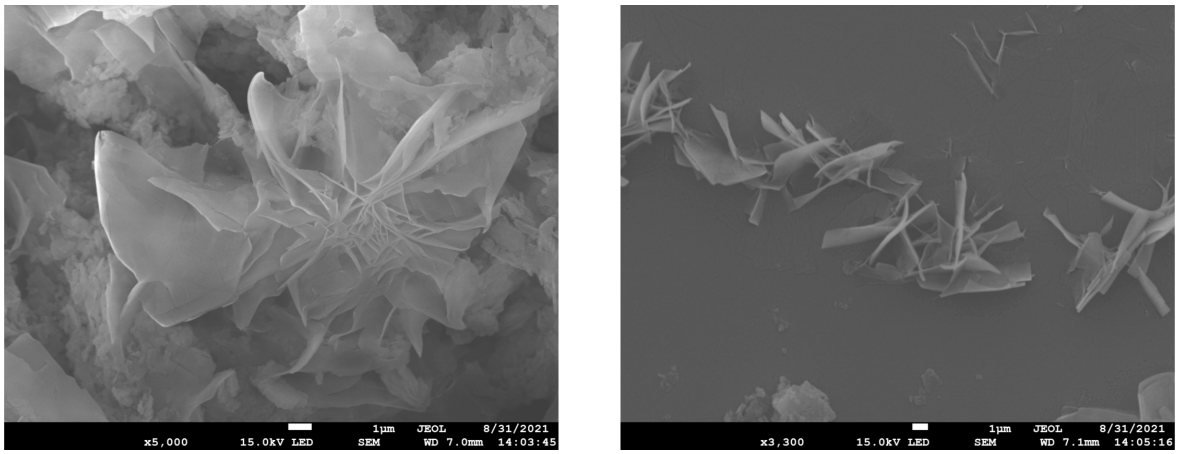

Figure 4.42. SEM images of Ca-MOF-Anh. Scale bar = 1 µm.

4.3.5.1 Ca-MOF-1 Synthesis Attempts Using Calcium Carbonate

Two attempts we made to synthesise Ca-MOF-1 from recycled chicken eggshells. Unfortunately, due to time constraints more thorough trials were not able to be made. We found that in both instances, the reactions did not yield Ca-MOF-1.

In experiment **1** we trialled reacting UR-CO_2H and ball-milled eggshells in water at room temperature. We did so by simply dissolving the organic linker in deionised water and adding the metal precursor. No effervescence occurred doing so which, when compared to our procedures for the three previously discussed MOFs, suggests that the no reaction takes place at room temperature. We found that only squaric acid has a pKa low enough to react with the biomineralised calcium carbonate source while terephthalic acid and fumaric acid required further energy input. The reaction mixture of experiment **1** was therefore transferred to a microwave vial and heated to 120 °C for 10 minutes. The solids within the vial were separated from its supernatant *via* centrifugation and then dried overnight. No washing of the material was undertaken.

For experiment **2**, we altered the mechanochemical synthesis of [Ca(BDC)(H_2O)$_3$] to include UR-CO_2H rather than terephthalic acid. UR-CO_2H and eggshells were combined in a Teflon ball-mill vessel with several ZrO_2 milling balls and a small quantity of water. The vessel was then sealed and shaken at 50Hz for 20 minutes. The resulting powder was not washed. We have summarised the two experimental conditions in table 4.10.

Table 4.10. Reaction conditions for the synthesis of Ca-MOF-1 from recycled eggshells and UR-CO_2H.

Experiment	Heating method	Conditions	Solvent	Reagents
1	1) RT. 2) Microwave	1) RT 2) 120 °C, 10 min	H_2O	Eggshells + UR-CO_2H
2	Ball-mill	RT, 50Hz, 20 min	H_2O	Eggshells + UR-CO_2H

To judge the success of experiments **1** and **2**, the resulting powders underwent PXRD characterisation. The results of which are presented in figure 4.43 ,alongside the precursor and the intended product patterns.

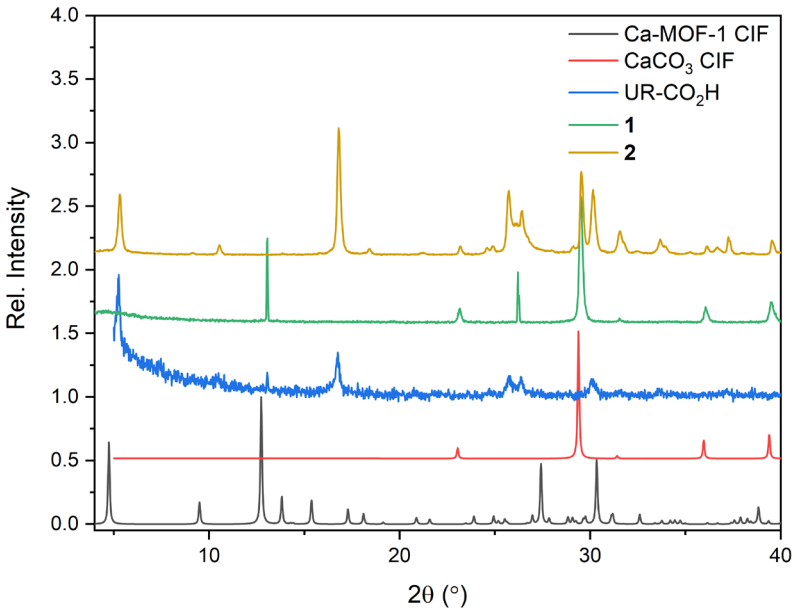

Figure 4.43. PXRD pattern comparison of (bottom to top); Ca-MOF-1 CIF; $CaCO_3$ CIF; UR-CO_2H; product from attempt one; and product from attempt two.

The powder pattern of the product from experiment **1** closely resembles that of the powder pattern of calcite (calcium carbonate). This suggests that the metal source has not reacted with the dissolved UR-CO_2H to any extent during either the room temperature or heating stage of the reaction. The lack of UR-CO_2H peaks is not surprising because we would expect the organic linker to be removed upon decanting of the reaction solvent. We cannot identify the peak found at 13° in the powder pattern of **1**. For the powder pattern of product **2** we can see that there is an overlap of powder patterns of the two starting materials, with no presence of Ca-MOF-1.

4.4 Conclusion and Further Work

We have successfully developed green and largely sustainable routes to the production of [Ca(SQ)(H_2O)], [Ca(BDC)(H_2O)$_3$] and [Ca(FU)(H_2O)$_3$]. Recycled precursors, such as chicken eggshells and PET bottles, have been used as feedstocks for these MOFs in mechanochemical, aqueous, room temperature, and solvothermal procedures. Remarkably, the terephthalate MOF could be formed, in high yield, *via* a one-pot solvothermal synthesis, whereby ball-milled eggshells and intact PET plastic were combined and simply heated in a water/ethylene glycol solvent mixture. Ball-milling has proven to be a very fruitful and low solvent mechanochemical technique for the formation of all three MOFs. Hydrolysis of PET to reclaim highly crystalline terephthalic acid allowed for a sustainable mechanochemical route to [Ca(BDC)(H_2O)$_3$] to be established in combination with previously ball-milled eggshells. The use of eggshells to form [Ca(SQ)(H_2O)] *via* ball-milling proved difficult. It was found that washing the product was essential in removing an unknown, but water-soluble phase. Unreacted eggshells were present in the unwashed material which could be removed through thorough washing. Due to their insolubility, the removal off eggshells during the washing step must occur through their reaction with residual squaric acid, resulting in further MOF formation.

Recent work to denature PET through mechanochemistry, in combination with either precursor aging[61] or enzyme inclusion,[62] suggests that a one-pot mechanochemical synthesis of [Ca(BDC)(H_2O)$_3$] from eggshells and PET has viability, but also highlights the requirements for specifically tailored conditions to promote PET hydrolysis. As the MOF field reaches a level of maturity where upscale and industrialisation comes into focus, we hope that sustainable and green syntheses become commonplace. To further expand on the catalogue of MOFs we have sustainably synthesised, future work would look into incorporating organic linkers from various recycled plastics, such as lactic acid from poly(lactic) acid. We also appreciate that the washing of [Ca(BDC)(H_2O)$_3$] requires the use of DMF and methanol. This is not ideal due to the associated toxicities and high flammability; therefore, further efforts should be taken to find alternative solvents for this step.

We have formed a calcium-based MOF (Ca-MOF-1) using the urea linker 4,4´-(carbonylbis(azanediyl))dibenzoic acid in water and solved its structure *via* SCXRD. Thin plate crystals made doing so difficult however a sensible structure was deduced. Heating this material at a modest temperature resulted in the removal of water molecules from the structure and a change in crystal parameters, confirmed by TGA and PXRD respectively. N_2 gas adsorption of the heated material (Ca-MOF-Anh) confirmed porosity which must correspond to a substantial crystallographic phase change as it is highly unlikely that the dense Ca-MOF-1 would show any adsorption capability.

The lazy S shape of the Ca-MOF-Anh isotherm does however suggest that Ca-MOF-Anh is highly microporous and thus to confirm porosity we would require the use of a smaller probe molecule, such as CO_2. Additional crystallographic characterisation of Ca-MOF-Anh would be beneficial but would require solving from powder, and possibly with a synchrotron source.

Synthesis attempts of Ca-MOF-1 from eggshells have been made but in both cases were unsuccessful. We have found that the MOF will not form at room temperature when using this precursor or after applying energy *via* microwave or mechanochemical means. We however did not attempt a solvothermal synthesis, which may be beneficial due to the longer reaction time as well as a slower rate of crystallisation.

4.5 Experimental

Bulk [Ca(SQ)(H_2O)] and [Ca(BDC)(H_2O)$_3$] were synthesised via procedures described by Sumida *et al.*[21]

4.5.1 Poly(ethylene terephthalate) Hydrolysis

The following synthesis was modified from Onyango *et al.*[38] Recycled PET plastic (3.5014 g, approximately 0.018 mol of terephthalate) was cut up into roughly 5 mm x 5mm squares and added to a 100 mL Teflon liner. 70 mL deionised water and 7 mL ethylene glycol were added to the liner and sealed in a steel autoclave. The reaction mixture was heated to 210 °C for 8 hours. Terephthalic acid crystals grew on the walls and bottom of the liner and were collected by centrifugation (5000 rpm for 15 minutes). The crystals were then washed with ethanol and further centrifugation twice. The crystals were dried in an oven at 100 °C overnight prior to characterisation. (Yield = 2.4747 g, 83%).

4.5.2 Room temperature synthesis of calcium squarate hydrate ([Ca(SQ)(H_2O)])

H_2SQ (0.172 g, 1.52 mmol) was dissolved in deionised water (20 mL). Commercially bought $CaCO_3$ (0.152 g, 1.52 mmol) was added to the solution and stirred at room temperature for 24 hours. Pierced parafilm covered the reaction vessel to stop pressurisation from occurring due to gas evolution. The resulting white precipitate was washed with water and centrifugation cycles thrice. The white powder was left to air dry at room temperature. Yield = 0.1522 g (61%).

4.5.3 Synthesis of calcium squarate hydrate ([Ca(SQ)(H_2O)]) from Eggshell

An eggshell piece (0.0685 g) was submerged in deionised water for 15 minutes. The shell was removed from the water and gently exfoliated to remove the thin organic membrane on the interior of the shell. The shell was added to an aqueous solution of H_2SQ (0.043 g, 0.38 mmol) and the vial covered with pierced parafilm. The mixture was left undisturbed. Crystals of Ca(SQ)(H_2O) on the shell were visible after one week. The crystals were collected by agitating the MOF composite to dislodge the crystals from the eggshell and filtering the solution. Yield = 0.117 g (50%)

4.5.4 Hydrothermal synthesis of calcium fumarate trihydrate ([Ca(FU)(H_2O)$_3$])

H_2FU (0.381 g, 3 mmol) was partially dissolved in deionised water (15 mL) by sonicating for 15 minutes. Commercially bought calcium carbonate (0.276 g, 2.8 mmol) was added to the mixture and sealed in a scintillation vial before being heated to 100 °C for 24 hours. The resulting clear

solution was left at room temperature overnight resulting in the formation of large, clear crystals. Yield = 0.3052 g (52%).

4.5.5 Mechanochemical synthesis of calcium fumarate trihydrate ([Ca(FU)(H_2O)$_3$])

Eggshells or calcium carbonate (0.0600 g, 0.6 mmol) and H_2FU (0.0700g, 0.6 mmol) were loaded into a 10 mL Teflon ball-mill vessel with several ZrO2 balls. The vessel was sealed and shaken for 5 minutes at 50Hz. The vessel was open, 40 µL deionised water added and resealed. The vessel was shaken again at 50Hz for 20 minutes. Yield = 0.0923 g (75%).

4.5.6 Solvothermal synthesis of calcium terephthalate trihydrate ([Ca(BDC)(H_2O)$_3$])

$CaCO_3$ (0.2470 g, 2.47 mmol) and H_2BDC (0.4198 g, mmol) were added to a mixture of deionised water (15 mL) and ethylene glycol (1.5 mL) in a Teflon liner and sealed in a steel autoclave. The reaction was heated to 210 °C overnight. After cooling to room temperature, the resulting white precipitate was washed in DMF three times with centrifuging between each wash (5000 rpm for 15 minutes) and then repeated with methanol. $CaCO_3$ and H_2BDC can be replaced with ground eggshells or reclaimed H_2BDC (0.42 g)/PET (0.50 g) respectively.

4.5.7 Solvothermal synthesis of calcium terephthalate trihydrate ([Ca(BDC)(H_2O)$_3$]) from egg shells and PET plastic

Ball-milled eggshells (0.244 g, 2.4 mmol) and PET plastic pieces (0.503 g, approximate terephthalate content of 2.6 mmol) were combined in a Teflon-lined steel autoclave with deionised water (15 mL) and ethylene glycol (1.5 mL), sealed and heated to 210 °C for 15 hours. The resulting material was washed with DMF and centrifugation cycles thrice followed by methanol and centrifugation cycled twice. The powder was dried at room temperature overnight. Yield = 0.330 g (55%).

4.5.8 Mechanochemical synthesis of calcium terephthalate trihydrate ([Ca(BDC)(H_2O)$_3$])

Eggshells (0.0623 g, 0.60 mmol) were soaked in deionised water for 15 minutes. The shell was removed from the water and gently exfoliated to remove the thin organic membrane on the interior of the shell. The eggshell was dried and ground into a fine powder and added to the ball miller reaction vessel. H_2BDC (0.1940 g, 0.60 mmol) was added to the vessel along with seven zirconia milling balls and in a 50:50 solvent mixture of deionised water and methanol (20 µL). The vessel was capped and shaken at 50 Hz for 20 minutes. The resulting white powder was washed in DMF

three times with centrifuging between each wash (5000 rpm for 15 minutes) and then repeated with methanol. The white powder was allowed to dry at room temperature for 24 hours. Yield = 0.130 g (83%).

4.5.9 Layering synthesis of Ca(UR-CO_2H)(H_2O)$_4$ (Ca-MOF-1)

$CaCl_2$ (0.028 g, 0.25 mmol) was dissolved in deionised water (10 mL) and added to a test tube. A blank layer of deionised water (10 mL) was carefully added on top of the layer with a Pasteur pipette. UR-CO_2H (0.075 g, 0.25 mmol) was dissolved in deionised water (10 mL) and carefully added on top of the blank layer with a Pasteur pipette. The test tube was sealed with parafilm and left unagitated for 24 hours. Clear, colourless crystals grew on the test tube walls within this time.

4.5.10 Stirring synthesis of Ca(UR-CO_2H)(H_2O)$_4$ (Ca-MOF-1)

$CaCl_2$ (0.028 g, 0.25 mmol) was dissolved in deionised water (10 mL) and combined with an aqueous solution (10 mL) of UR-CO_2H (0.075 g, 0.25 mmol). The solution was stirred overnight at room temperature. A white precipitate formed which was isolated and washed with water via centrifugation.

4.6 References

1 M. I. Severino Neves, E. Gkaniatsou, F. Nouar, M. L. Pinto and C. Serre, *Faraday Discuss.*, 2021, **231**, 326.

2 G. Shaw, *Drug Discov. Dev.*, 2007, 1–8.

3 S. M. Meckler, C. Li, W. L. Queen, T. E. Williams, J. R. Long, R. Buonsanti, D. J. Milliron and B. A. Helms, *Chem. Mater.*, 2015, **27**, 7673.

4 G. Majano, O. Ingold, M. Yulikov, G. Jeschke and J. Pérez-Ramírez, *CrystEngComm*, 2013, **15**, 9885.

5 W. Yuan, J. O'Connor and S. L. James, *CrystEngComm*, 2010, **12**, 3515.

6 G. Zhan and H. C. Zeng, *Chem. Commun.*, 2017, **53**, 72.

7 R. Riccò, O. Linder-Patton, K. Sumida, M. J. Styles, K. Liang, H. Amenitsch, C. J. Doonan and P. Falcaro, *Chem. Mater.*, 2018, **30**, 5630.

8 Y. Abdollahian, J. L. Hauser, I. R. Colinas, C. Agustin, A. S. Ichimura and S. R. J. Oliver, *Cryst. Growth Des.*, 2014, **14**, 1506.

9 I. Stassen, M. Styles, G. Grenci, H. Van Gorp, W. Vanderlinden, S. De Feyter, P. Falcaro, D. De Vos, P. Vereecken and R. Ameloot, *Nat. Mater.*, 2016, **15**, 304.

10 K. Okada, R. Ricco, Y. Tokudome, M. J. Styles, A. J. Hill, M. Takahashi and P. Falcaro, *Adv. Funct. Mater.*, 2014, **24**, 1969.

11 S. El-Hankari, J. Aguilera-Sigalat and D. Bradshaw, *J. Mater. Chem. A*, 2016, **4**, 13509.

12 G. Zhan and H. C. Zeng, *Chem. Commun.*, 2016, **52**, 8432.

13 R. K. Alavijeh, K. Akhbari and J. White, *Cryst. Growth Des.*, 2019, **19**, 7290.

14 D. Ozer, N. A. Oztas, D. A. Köse and O. Şahin, *J. Mol. Struct.*, 2018, **1156**, 353.

15 X. Chen, A. M. Plonka, D. Banerjee, R. Krishna, H. T. Schaef, S. Ghose, P. K. Thallapally and J. B. Parise, *J. Am. Chem. Soc.*, 2015, **137**, 7007.

16 A. M. Plonka, X. Chen, H. Wang, R. Krishna, X. Dong, D. Banerjee, W. R. Woerner, Y. Han, J. Li and J. B. Parise, *Chem. Mater.*, 2016, **28**, 1636.

17 Balendra and A. Ramanan, *J. Mol. Struct.*, 2017, **1131**, 171.

18 P. Suresh, C. Naga Babu, N. Sampath and G. Prabusankar, *Dalt. Trans.*, 2015, **44**, 7338.

19 S. R. Miller, E. Alvarez, L. Fradcourt, T. Devic, S. Wuttke, P. S. Wheatley, N. Steunou, C. Bonhomme, C. Gervais, D. Laurencin, R. E. Morris, A. Vimont, M. Daturi, P. Horcajada and C. Serre, *Chem. Commun.*, 2013, **49**, 7773.

20 D. J. Levine, M. I. Gonzalez, C. M. Legendre, T. Runčevski, J. Oktawiec, K. A. Colwell and J. R. Long, *ChemMedChem*, 2017, **12**, 1739.

21 K. Sumida, M. Hu, S. Furukawa and S. Kitagawa, *Inorg. Chem.*, 2016, **55**, 3700.

22 D. P. Ferris, C. L. Stern, J. F. Stoddart, M. S. Nassar, Y. Y. Botros, J. M. Holcroft, K. J. Hartlieb and I. Kandela, *Mol. Pharm.*, 2017, **14**, 1831.

23 M. Ismail, M. A. Bustam and Y. F. Yeong, *Crystals*, 2020, **10**, 1006.

24 S. E. Keates, N. M. Tarlyn, F. A. Loewus and V. R. Franceschi, *Phytochemistry*, 2000, **53**, 433.

25 I. Goldberg and J. S. Rokem, in *Encyclopedia of Microbiology*, Elsevier Inc., 2009, p. 421.

26 P. Yadav, A. K. Chauhan, R. B. Singh, S. Khan and G. Halabi, in *Functional Foods and Nutraceuticals in Metabolic and Non-Communicable Diseases*, Elsevier, 2022, p. 325.

27 P. Misaelides, *Microporous Mesoporous Mater.*, 2011, **144**, 15.

28 I. Huskić, I. V Pekov, S. V Krivovichev and T. Friščić, *Sci. Adv.*, 2016, **2**, 1600621.

29 N. Malik, P. Kumar, S. Shrivastava and S. B. Ghosh, *Int. J. Plast. Technol.*, 2017, **21**, 1.

30 J. Miltz, A. Ram and M. M. Nir, *Food Addit. Contam.*, 1997, **14**, 649.

31 S. Ko, Y. J. Kwon, J. U. Lee and Y. P. Jeon, *J. Ind. Eng. Chem.*, 2020, **83**, 449.

32 BSDA, *PET Plastic Bottles - Facts Not Myths*, 2009.

33 S. D'Angelo and R. Meccariello, *Int. J. Environ. Res. Public Heal.*, 2021, **18**, 2392.

34 K. Song, X. Qiu, B. Han, S. Liang and Z. Lin, *Environ. Sci. Nano*, 2021, **8**, 390.

35 A. Ghosh and G. Das, *J. Environ. Chem. Eng.*, 2021, **9**, 105288.

36 L. Zhou, S. Wang, Y. Chen and C. Serre, *Microporous Mesoporous Mater.*, 2019, **290**, 109674.

37 W. P. R. Deleu, I. Stassen, D. Jonckheere, R. Ameloot and D. E. De Vos, *J. Mater. Chem. A*, 2016, **4**, 9519.

38 J. Ren, X. Dyosiba, N. M. Musyoka, H. W. Langmi, B. C. North, M. Mathe and M. S. Onyango, *Int. J. Hydrogen Energy*, 2016, **41**, 18141.

39 M. Crespo-Ribadeneyra, J. King, M. Titirici and P. A. Szilagyi, *Chem. Commun.*, 2022, **58**, 1330.

40 B. Slater, S. O. Wong, A. Duckworth, A. J. P. White, M. R. Hill and B. P. Ladewig, *Chem. Commun.*, 2019, **55**, 7319.

41 A. Pichon, A. Lazuen-Garay and S. L. James, *CrystEngComm*, 2006, **8**, 211.

42 Y. H. Liu, Y. L. Lu, H. L. Tsai, J. C. Wang and K. L. Lu, *J. Solid State Chem.*, 2001, **158**, 315.

43 D. Chen, J. Zhao, P. Zhang and S. Dai, *Polyhedron*, 2019, **162**, 59.

44 D. Crawford, J. Casaban, R. Haydon, N. Giri, T. McNally and S. L. James, *Chem. Sci.*, 2015, **6**, 1645.

45 H. M. Titi, J. L. Do, A. J. Howarth, K. Nagapudi and T. Friščić, *Chem. Sci.*, 2020, **11**, 7578.

46 T. Stolar, A. Prašnikar, V. Martinez, B. Karadeniz, A. Bjelić, G. Mali, T. Friščić, B. Likozar and K. Užarević, *ACS Appl. Mater. Interfaces*, 2021, **13**, 3070.

47 E. Zolotoyabko, E. N. Caspi, J. S. Fieramosca, R. B. Von Dreele, F. Marin, G. Mor, L. Addadi, S. Weiner and Y. Politi, *Cryst. Growth Des.*, 2010, **10**, 1207.

48 S. J. Sedlmaier, M. Döblinger, O. Oeckler, J. Weber, J. Schmedt Auf Der Günne and W. Schnick, *J. Am. Chem. Soc.*, 2011, **133**, 12069.

49 L. Li, L. Guo, S. Pu, J. Wang, Q. Yang, Z. Zhang, Y. Yang, Q. Ren, S. Alnemrat and Z. Bao, *Chem. Eng. J.*, 2019, **358**, 446.

50 R. Tu, W. Zhang, J. Zhang, M. Wang, F. Zhang, K. Yang, J. Li, H. Pan, M. T. Bernards, P. Xie, Y. He and Y. Shi, *Energy & Fuels*, 2021, **35**, 13900.

51 L. Li, L. Guo, F. Zheng, Z. Zhang, Q. Yang, Y. Yang, Q. Ren and Z. Bao, *ACS Appl. Mater. Interfaces*, 2020, **12**, 17147.

52 C. Robl and A. Weiss, *Mater. Res. Bull.*, 1987, **22**, 373.

53 S. Chaemchuen, Z. Luo, K. Zhou, B. Mousavi, S. Phatanasri, M. Jaroniec and F. Verpoort, *J. Catal.*, 2017, **354**, 84.

54 F. Ke, C. Peng, T. Zhang, M. Zhang, C. Zhou, H. Cai, J. Zhu and X. Wan, *Sci. Rep.*, 2018, **8**, 939.

55 S. Singh, S. Kaushal, J. Kaur, G. Kaur, S. K. Mittal and P. P. Singh, *Chemosphere*, 2021, **272**, 129648.

56 T. Matsuzaki and Y. Iitaka, *Acta Cryst.*, 1972, **8**, 1977.

57 B. F. Hoskin and R. Robson, *J. Am. Chem. Soc.*, 1989, **111**, 5962.

58 J. Peng, C. Huang, C. Cao, E. Saiz, Y. Du, S. Dou, A. P. Tomsia, H. D. Wagner, L. Jiang and Q. Cheng, *Matter*, 2020, **2**, 220.

59 R. J. Marshall, J. McGuire, C. Wilson and R. S. Forgan, *Supramol. Chem.*, 2018, **30**, 124.

60 M. Mazaj and N. Zabukovec Logar, *Cryst. Growth Des.*, 2015, **15**, 617.

61 V. Štrukil, *ChemSusChem*, 2021, **14**, 330.

62 S. Kaabel, J. P. D. Therien, C. Deschenes, D. Duncan, T. Friscic and K. Auclair, *Proc. Natl. Acad. Sci.*, 2020, **118**, e2026452118.

Chapter 5 Conclusion and Future Work

This body of work has focused on two popular areas of research within the MOF community. We have explored the use of crystalline porous materials in the remediation of a key environmental contaminant, pertechnetate, as well as sustainable syntheses that use recycled reagents.

We have taken the MOF UiO-66-NH_2, in chapter two, and performed a covalent PSM reaction to graft ethyl urea groups onto the framework. When the daughter MOF was acidified with HCl, its perrhenate uptake improved in comparison to its acidified parent MOF. This demonstrates the use of urea groups as binding sites for oxo-anions such as perrhenate and pertechnetate in MOFs. UiO-66-NH_2 has been immobilised into two application-specific bio-composites, and again tested for its perrhenate uptake capabilities. We have shown that doing so does not harm its uptake of the anion, and in fact improves the separation of adsorbent from solution. With this section of work, we wanted to explore a well understood MOF rather than synthesise a novel MOF which may have expensive precursors or require organic linkers synthesised *via* multistep chemical reactions. We appreciate that UiO-66-NH_2 has only modest perrhenate uptakes in comparison to other reported MOFs, however we are much more interested in its processability into composites and its use in PSM reactions. Pertechnetate is found in very low concentrations within contaminated groundwater and therefore designing materials with ultra-high capacities may appear impressive, but it is questionable whether they are actually worth their synthesis costs, time, or resulting configuration.

To further this segment of work we would continue with the material testing that has already been initiated to fully assess the ability of the material's synthesised in chapter two to remediate perrhenate in the presence of competing anions such as sulphate and nitrate. We would also like to trial the remediation of pertechnetate from solution with these materials.

The use of selective crystallisation as a remediation mechanism was explored in chapter three. Silver coordination polymers which utilised urea-based linkers were synthesised, with their crystal structures deduced where possible. In this case, we were unable to find a system that could crystallise only perrhenate, and thus be regarded as highly selective for this anion. We were, however, able to synthesise 8 new coordination polymers and show how the anion choice and structural isomer of the linker plays a role in the resulting materials topologies and structures. In addition to this, we have synthesised three new zinc-based materials. Two of these materials are layered-MOFs and therefore have the potential to be exfoliated into metal-organic nanosheets.

To fully complete this work, we would like to carry out a fully suite of characterisation on our synthesised silver-based materials. This would include PXRD, TGA, and FTIR. In regards to the zinc material's we have produced, the trialling of exfoliation into MONs would be interesting and should be pursued.

We have established sustainable, and largely solventless, syntheses for three calcium-based MOFs in chapter four. We utilised chicken eggshells and recycled PET plastic bottles as precursors, and where possible have exploited mechanochemical techniques to reduce the energy demand of our reactions. The work reported in chapter four explores an important area of concern for the MOF community. As the research area reaches a level of maturity where industrialisation and upscale of our materials comes into focus, we hope that recycled precursors become more commonplace and that solvent-minimised procedures continue to be favoured over slow, intensive, and expensive batch processes. As existing industrial processes undergo retrofitting to reduce their environmental impact, the MOF field has an opportunity to start as it means to go on; focussing on responsible chemistry to produce materials that are as sustainable as the applications they are often intended for.

The potential that we have shown through the syntheses could be carried forward into new systems by turning our attention to different polymers, such as PLA (polylactic acid), or even using natural sources of different metals.

The UK nuclear energy sector is facing a resurgence of both interest and funding, with the construction of the UK's first nuclear power station in over 27 years underway, and with two more progressing positively through their planning and public consultation phases. What remains however is the need for a permanent solution to the country's legacy nuclear waste. Novel techniques and materials, such as MOFs, are essential in resolving some of the most unique and challenging problems that the sector will ever face.

Chapter 6 Appendix

A.1 Chapter One

Table A.1 Anion Concentrations of Sellafield and Hanford Groundwater.

Anion	Sellafield Simulant		Hanford Simulant[1]	
	Concentration (mol dm^{-3})	Anion:TcO_4^- mole ratio	Concentration (mol dm^{-3})	Anion:TcO_4^- mole ratio
TcO_4^-	1.4×10^{-6} [2]	1.0	1.94×10^{-4}	1.0
SO_4^{2-}	2.00×10^{-4}	143	6.64×10^{-6}	0.0343
NO_3^-	2.87×10^{-4}	205	6.07×10^{-2}	314
CO_3^{2-}	8.00×10^{-4}	571	4.30×10^{-5}	0.222
Cl^-	8.35×10^{-4}	596	6.39×10^{-2}	330
NO_2^-	-	-	1.69×10^{-1}	873

A.2 Chapter Two

A.2.1 Powder X-Ray Diffraction

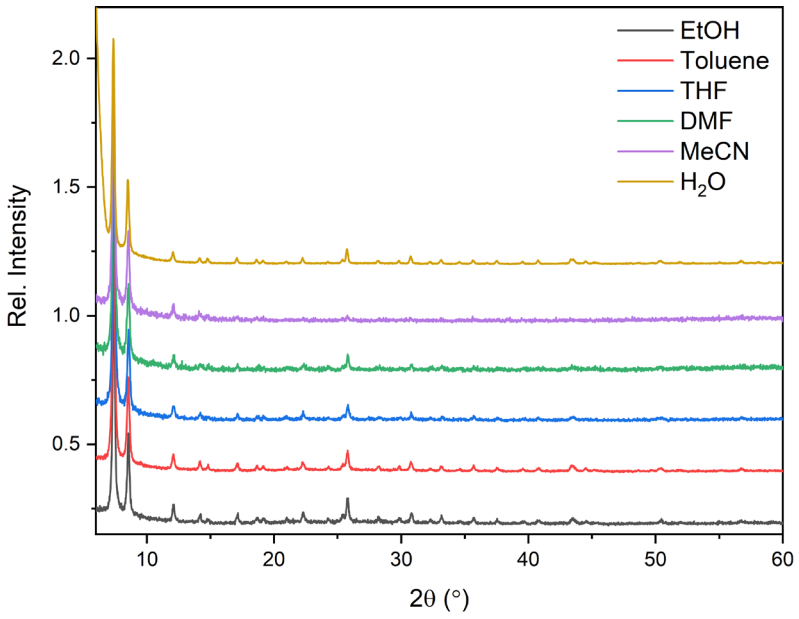

Figure A.1. PXRD pattern comparison of products from UiO-66-NH_2 PSM reactions under different solvents. No effect on crystallinity is observed.

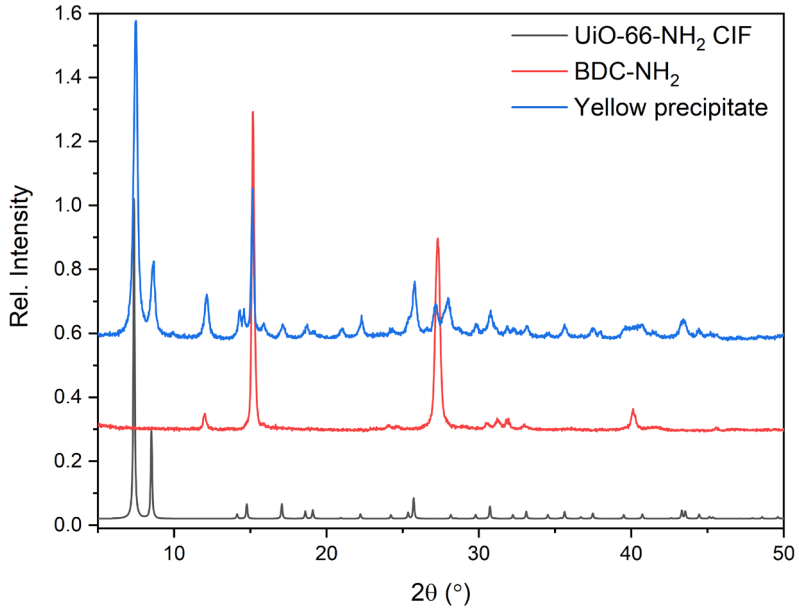

Figure A.2. PXRD comparison of the yellow precipitate formed on the surface of FFP during the dip coat synthesis of UiO-66-NH_2@FFP.

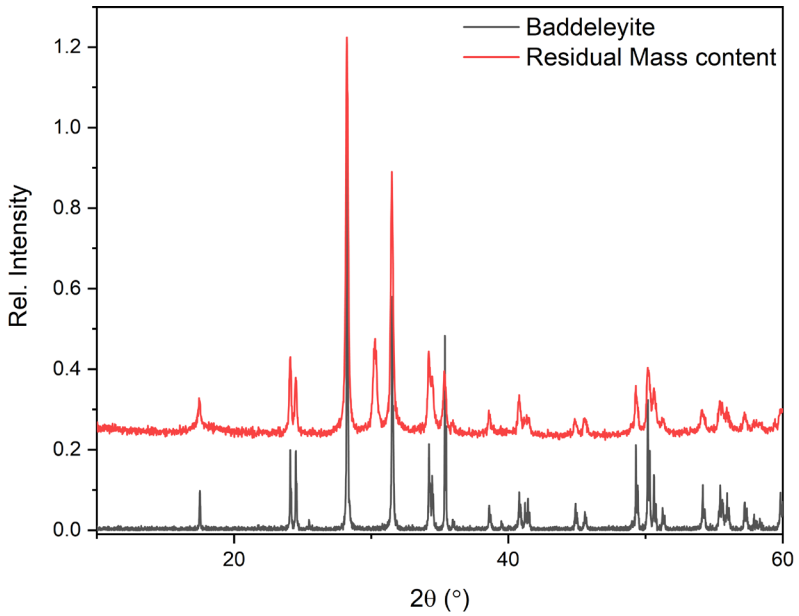

Figure A.3. PXRD comparison of residual mass contents from UiO-66-NH_2@FFP to baddeleyite. Baddeleyite RRUFF ID: R060016.1.

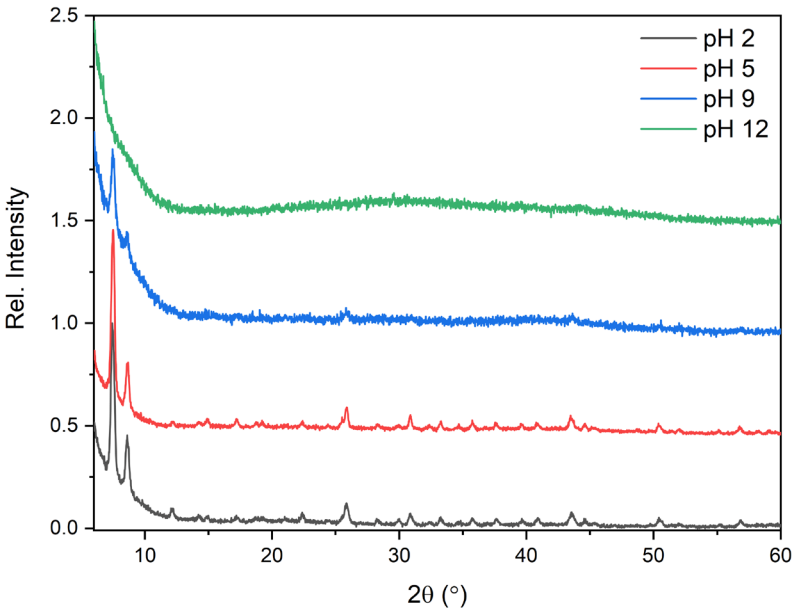

Figure A.4. PXRD comparison of UiO-66-NH_2@alg composites after exposure to solutions of varying pH.

A.2.2 Nuclear Magnetic Resonance Spectroscopy

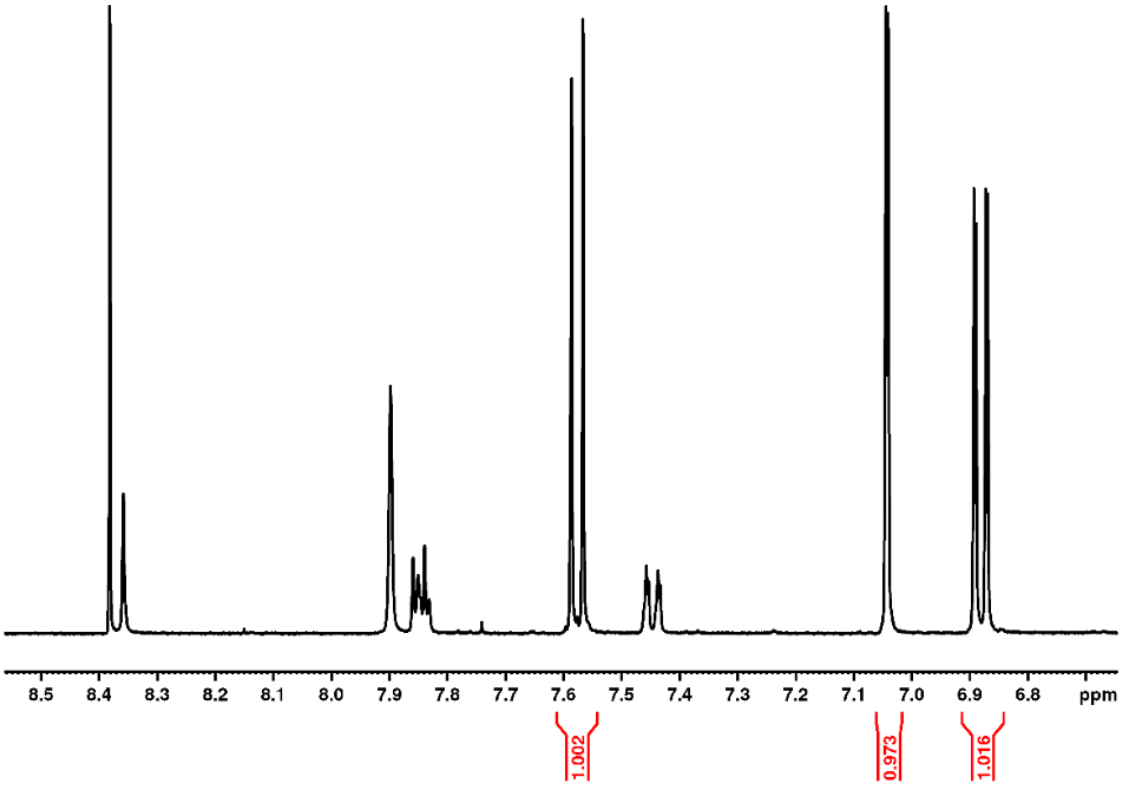

Figure A.5. ^{1}H NMR spectrum of UiO-66-NH_2 digested with NH_4F. Integrated peaks correspond to the aromatic protons of BDC-NH_2.

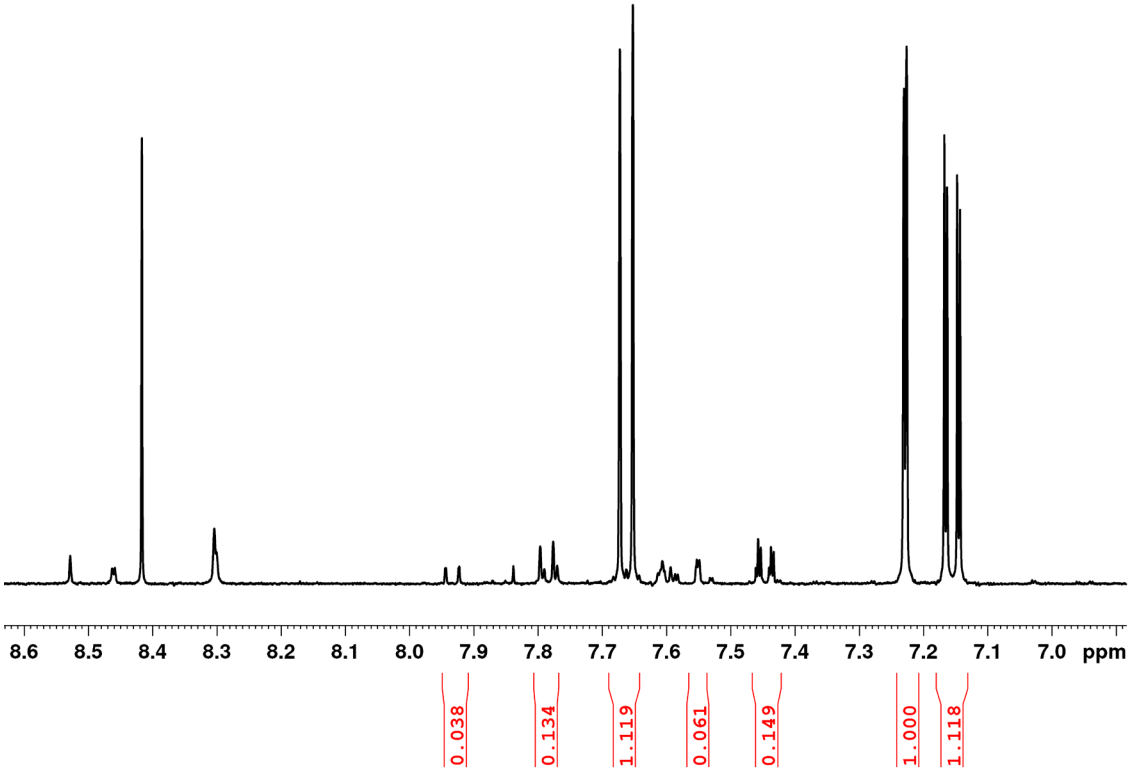

Figure A.6. H^1 NMR spectrum of PSM product. Solvent = DMF. Digested in NaOD/D_2O.

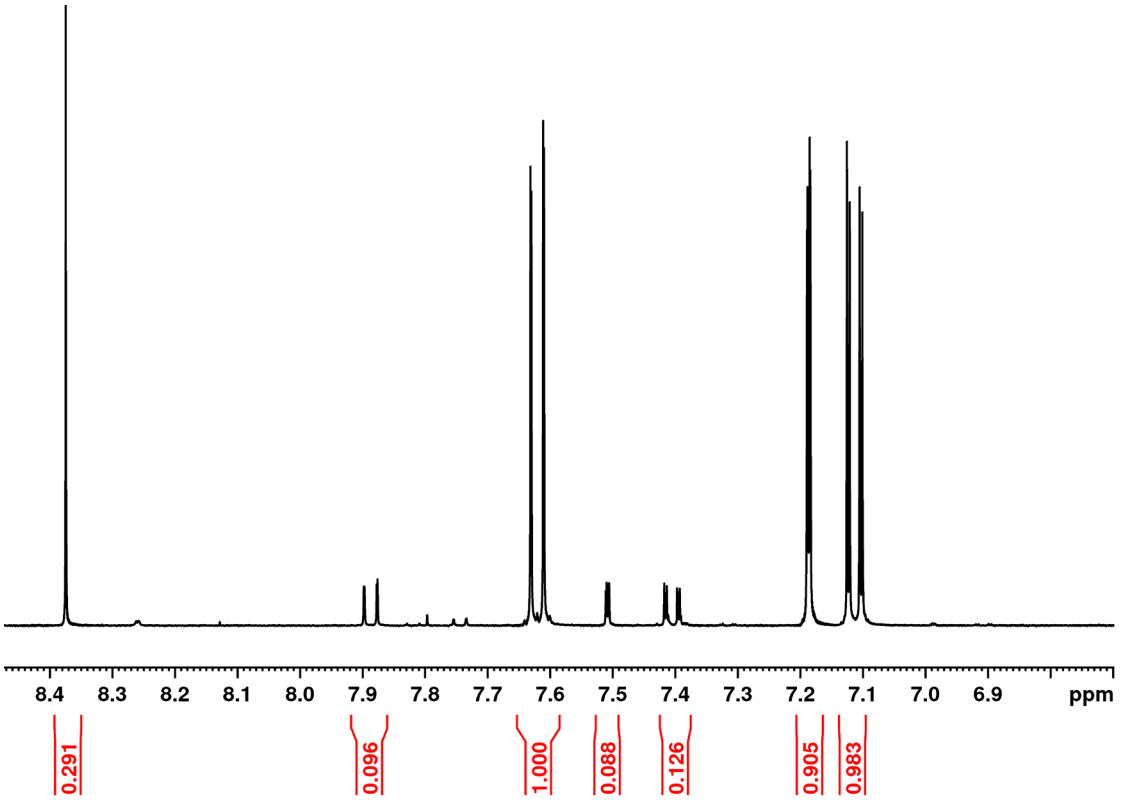

Figure A.7. H^1 NMR spectrum of PSM product. Solvent = ethanol. Digested in NaOD/D_2O.

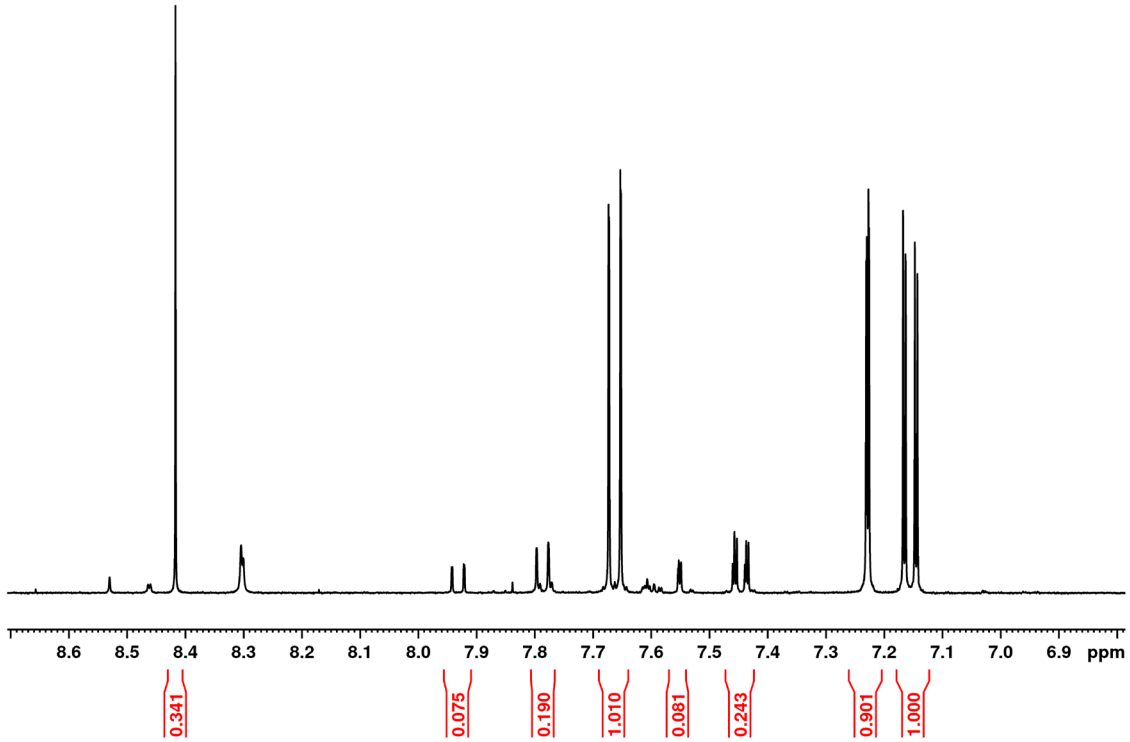

Figure A.8. H^1 NMR spectrum of PSM product. Solvent = THF. Digested in $NaOD/D_2O$.

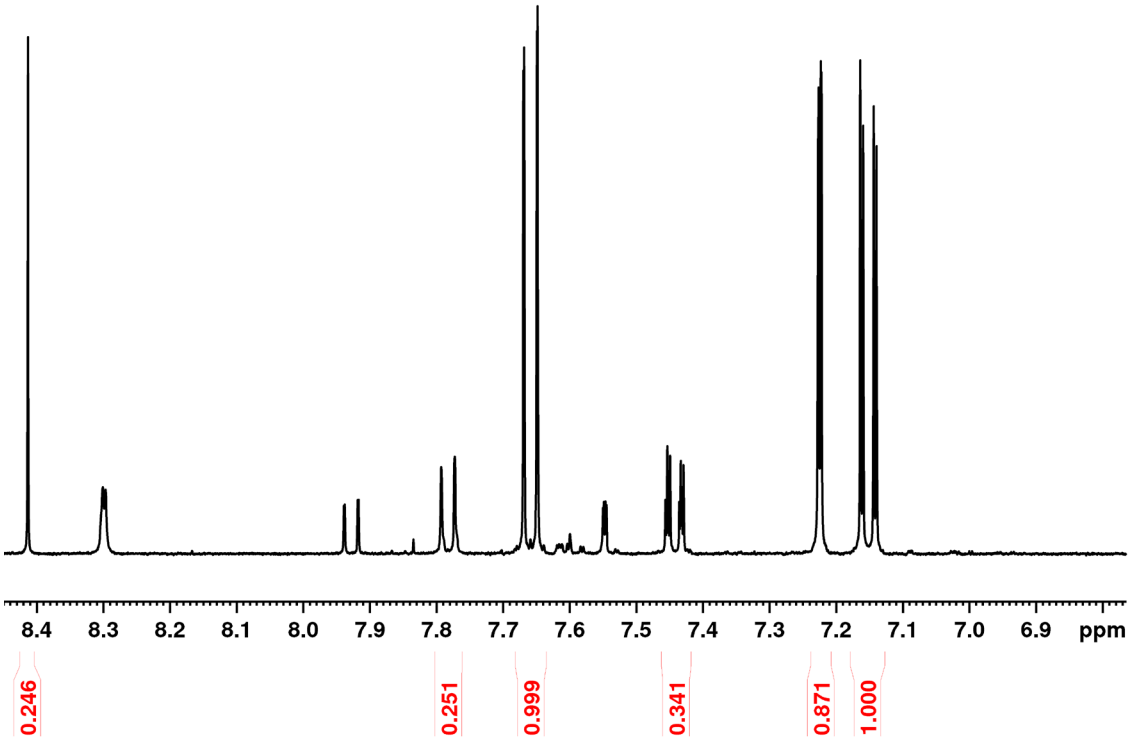

Figure A.9. H^1 NMR spectrum of PSM product. Solvent = toluene. Digested in $NaOD/D_2O$.

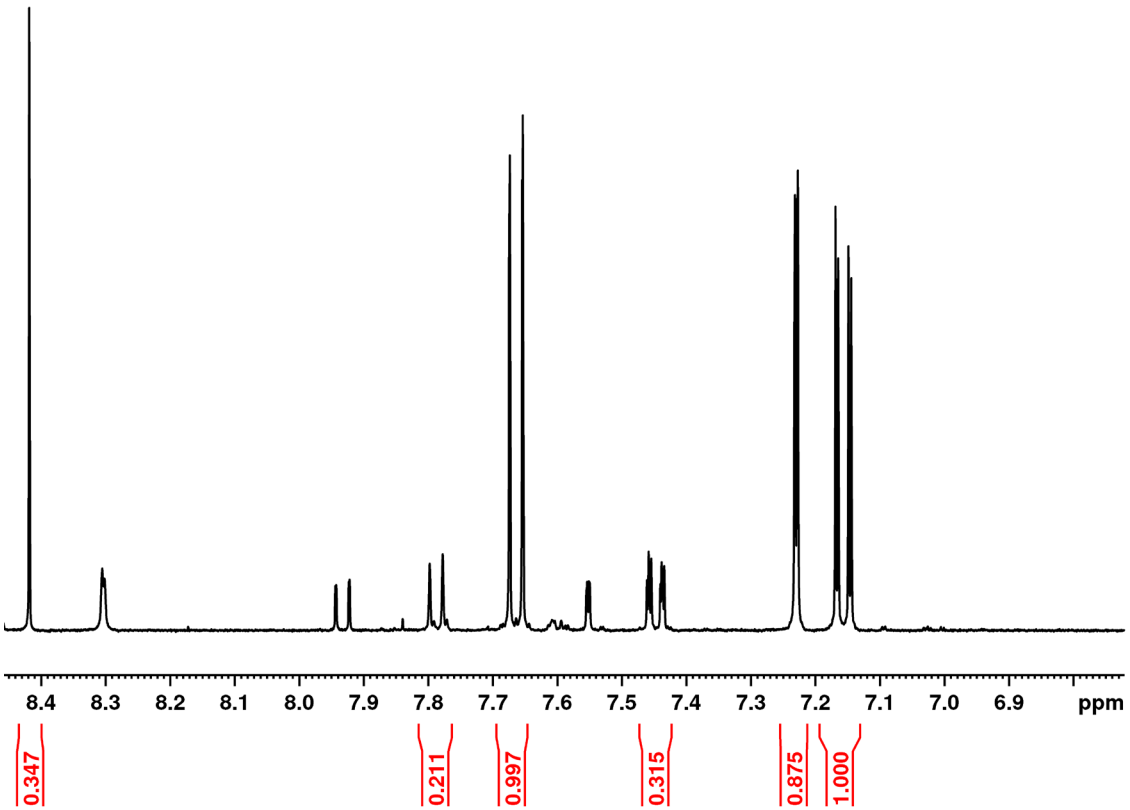

Figure A.10. H^1 NMR spectrum of PSM product. Solvent = acetonitrile. Digested in $NaOD/D_2O$.

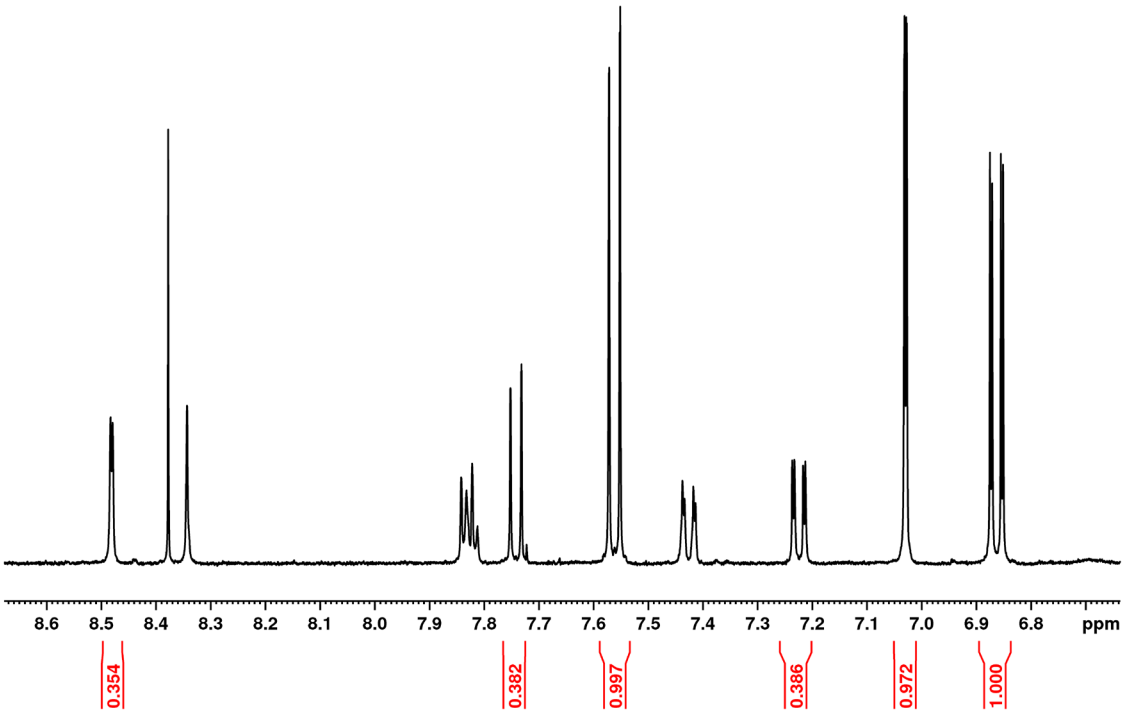

Figure A.11. H^1 NMR spectrum of PSM product. Solvent = acetontrile. Digested in NH_4F.

A.2.3 Thermogravimetric Analysis

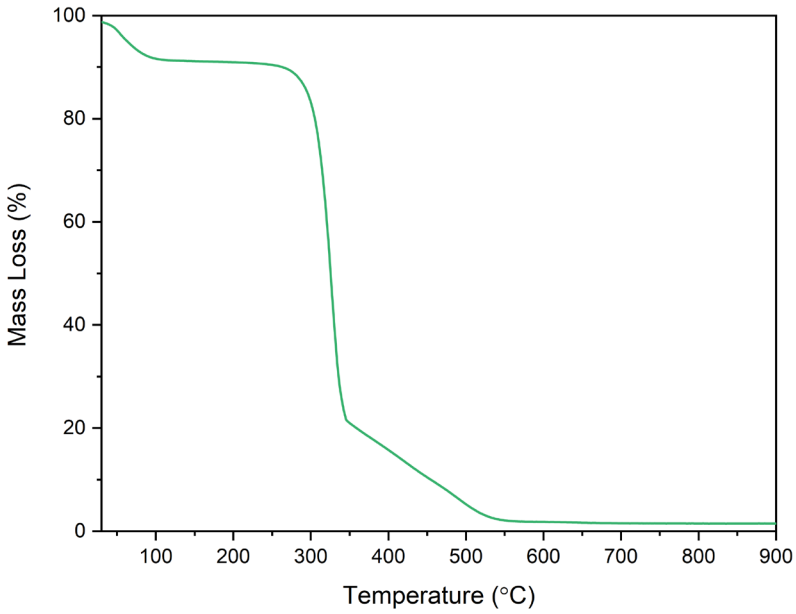

Figure A.12. TG analysis of [UiO-66-NH_3][Cl]$_6$@FFP.

Table A.2. MOF loadings of UiO-66-NH_2@FFP after n number of cycles, derived from TGA.

Cycles	Starting mass of composite (mg)	Mass of residual mass (mg)	Mass of MOF (mg)	MOF loading (wt%)	MOF mass per cm^2 (mg/cm^2)
5	12.22	0.48	1.15	9.4	1.0
10	9.54	0.54	1.29	13.5	1.5
15	10.10	0.68	1.62	16.1	1.9
20	14.34	1.15	2.75	19.2	2.3
NH_3	16.08	0.49	1.17	7.4	0.8

A.2.4 Perrhenate Uptake

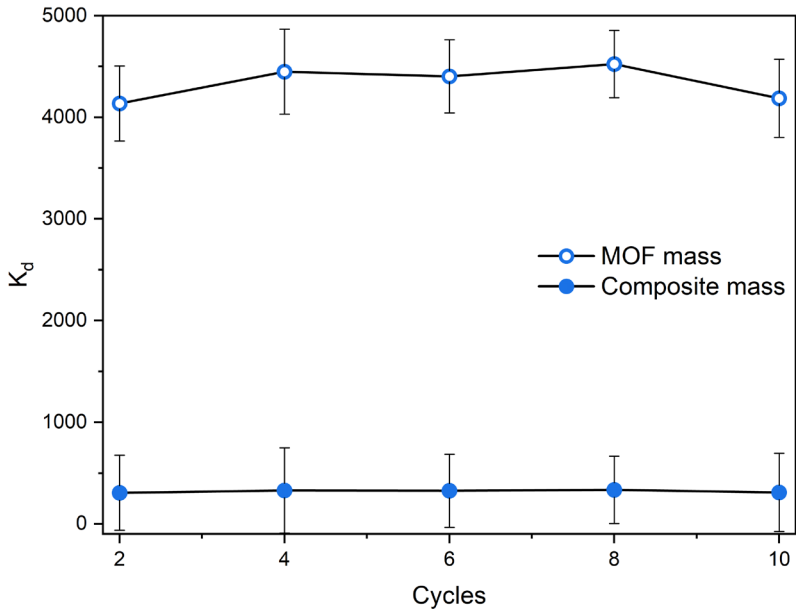

Figure A.13. Partition coefficients for [UiO-66-NH_3][Cl]@FFP over 10 filtration cycles. Combined method uncertainty given as standard error ($2\sigma K_d$).

A.2.5 Additional Images

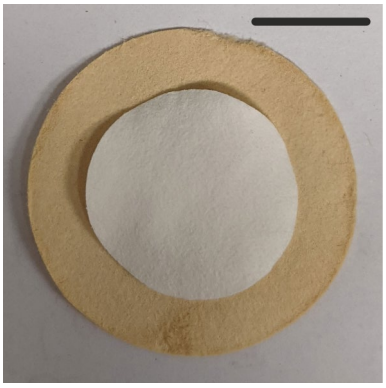

Figure A.14. Size comparison of UiO-66-NH_2@FFP (behind) and mercerised FP. Scale bar = 1 cm.

A.3 Chapter Three

A.3.1 ^{1}H Nuclear Magnetic Spectroscopy

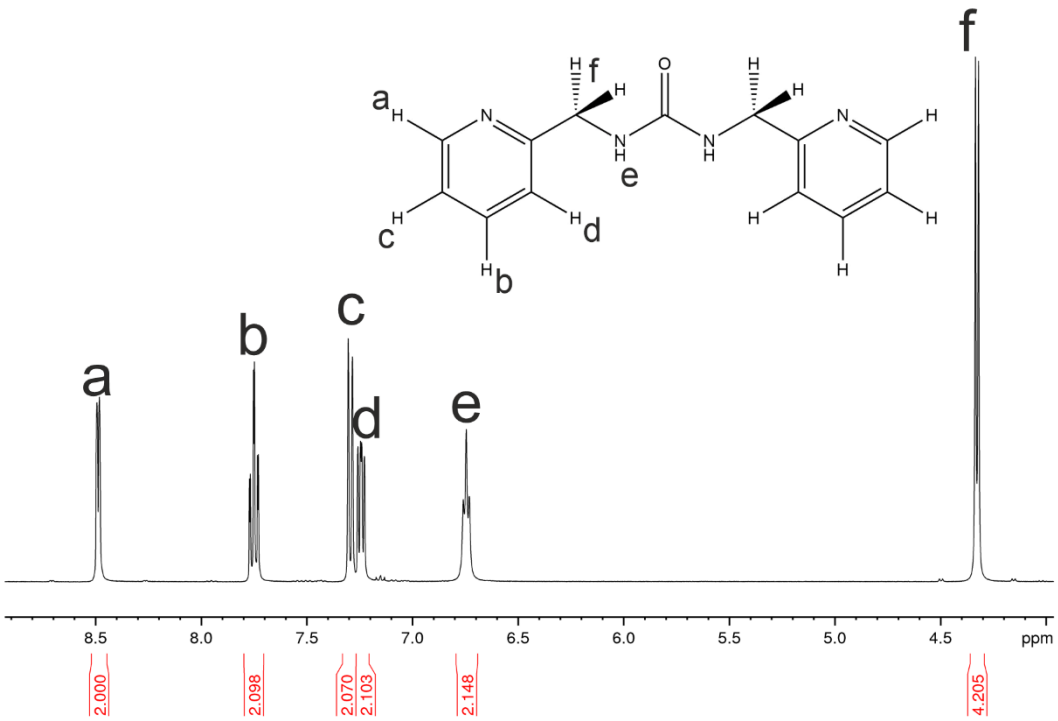

Figure A.15. ^{1}H NMR spectrum of 2-MeUR-N. DMSO-d_6 solvent.

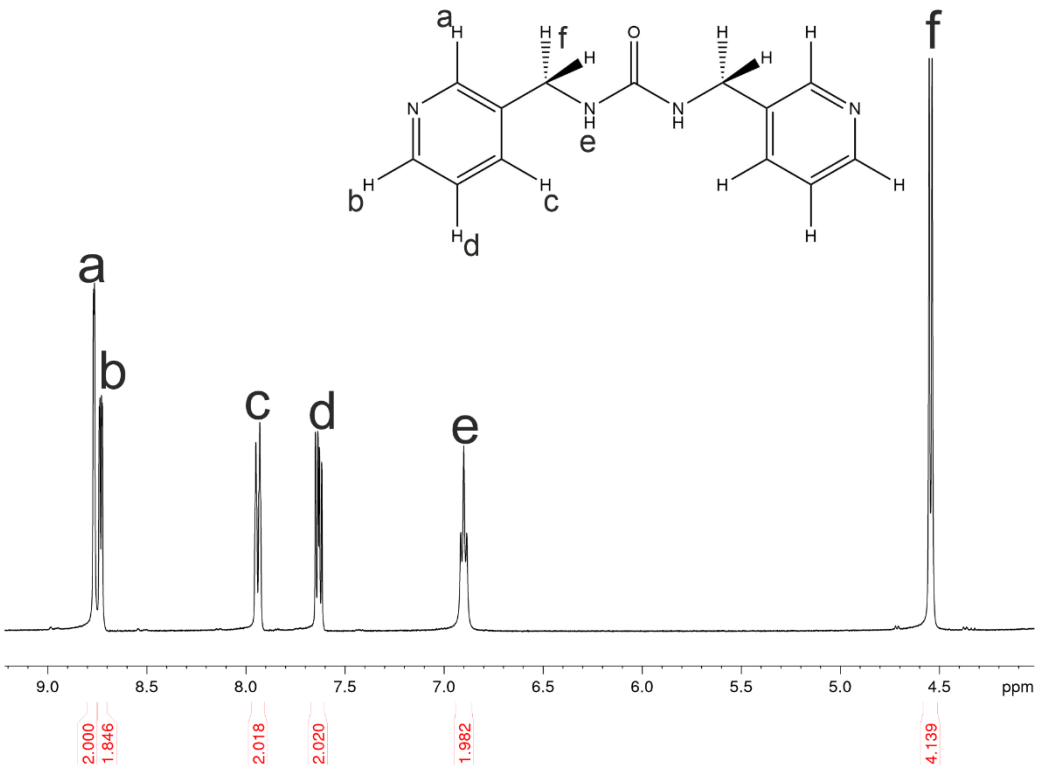

Figure A.16. ^{1}H NMR spectrum of 3-MeUR-N. DMSO-d_6 solvent.

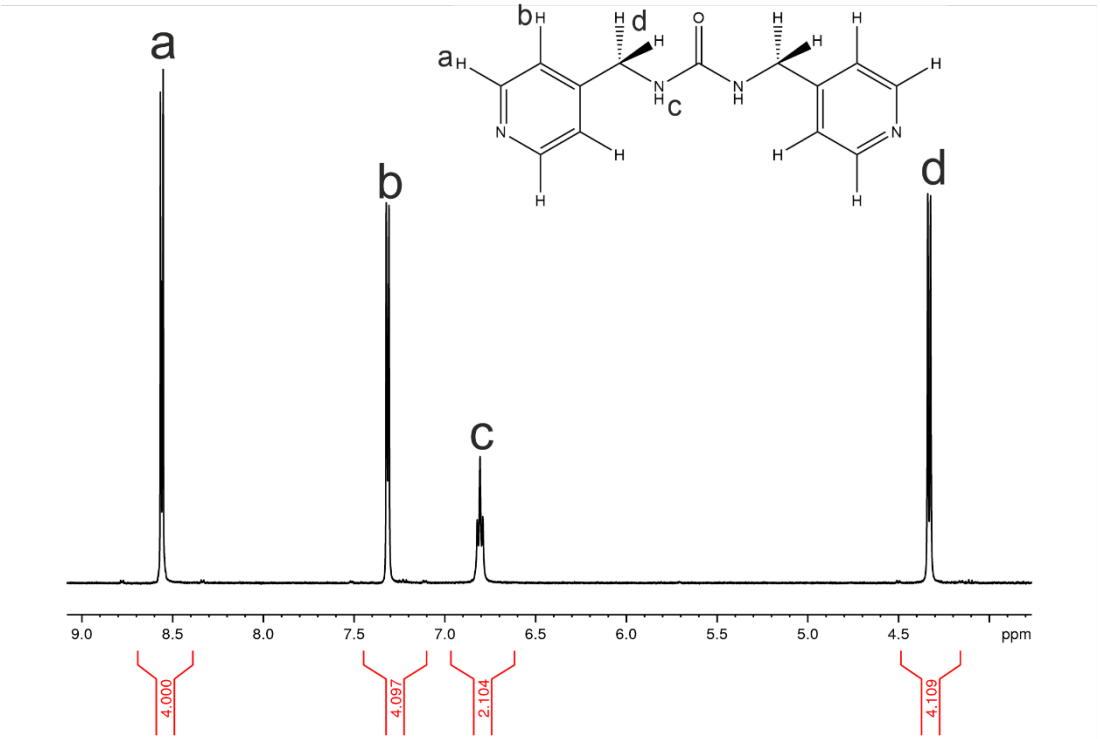

Figure A.17. ^{1}H NMR spectrum of 4-MeUR-N. DMSO-d_6 solvent.

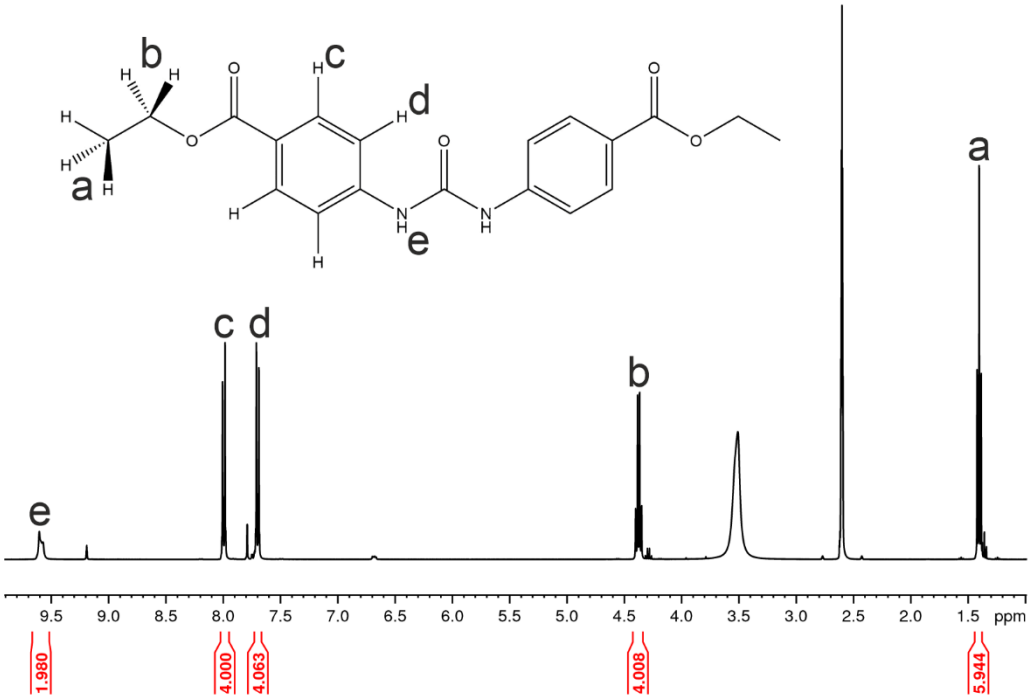

Figure A.18. ^{1}H NMR spectrum of UR-CO_2Et. DMSO-d_6 solvent. Residual water peak from washing visible at 3.5 ppm.

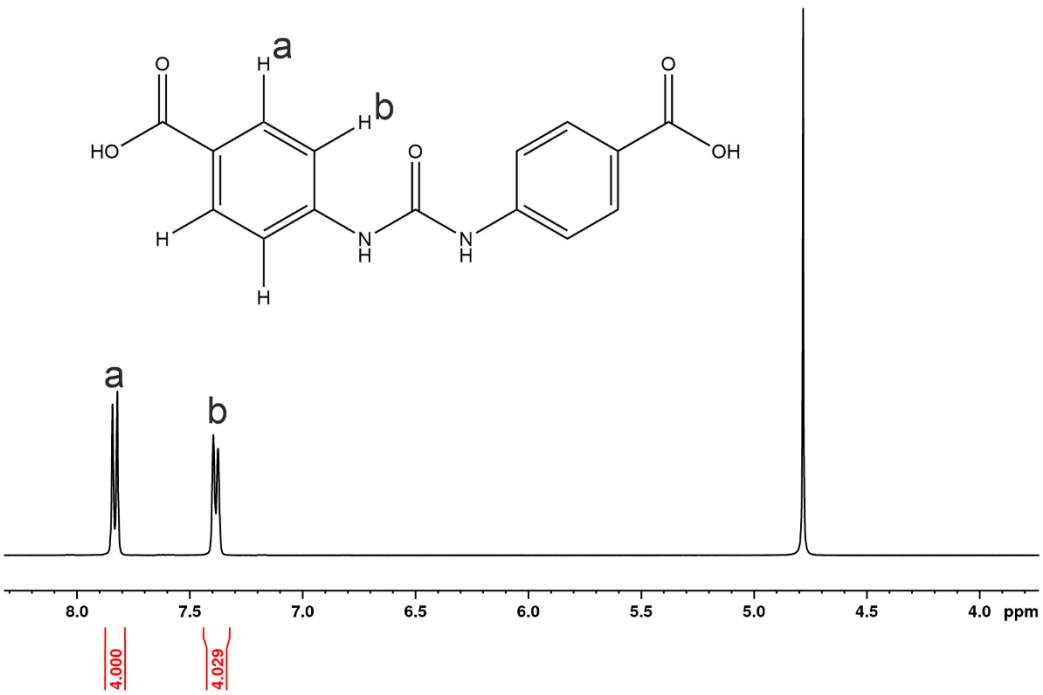

Figure A.19. ^{1}H NMR spectrum of UR-CO_2H. D_2O-d_2 solvent.

A.3.2 Fourier Transform Infrared Spectroscopy

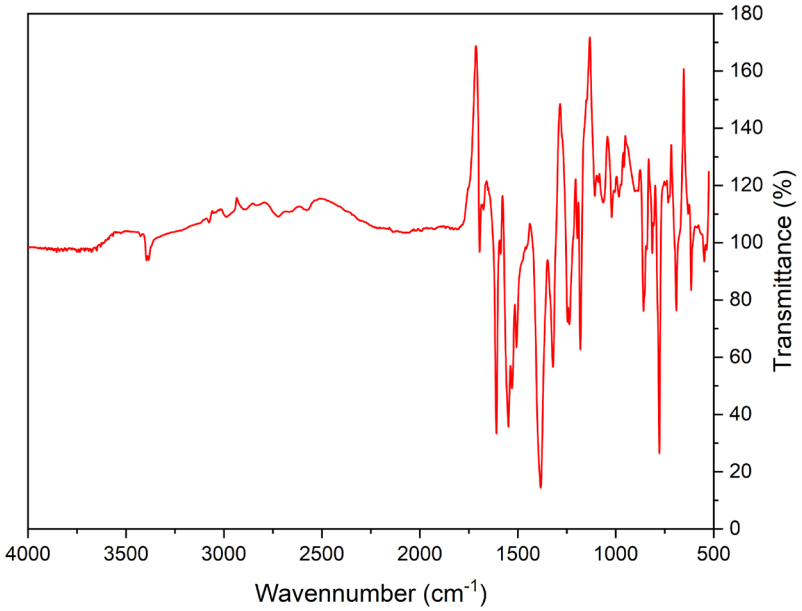

Figure A.20. FTIR of UR-CO_2H.

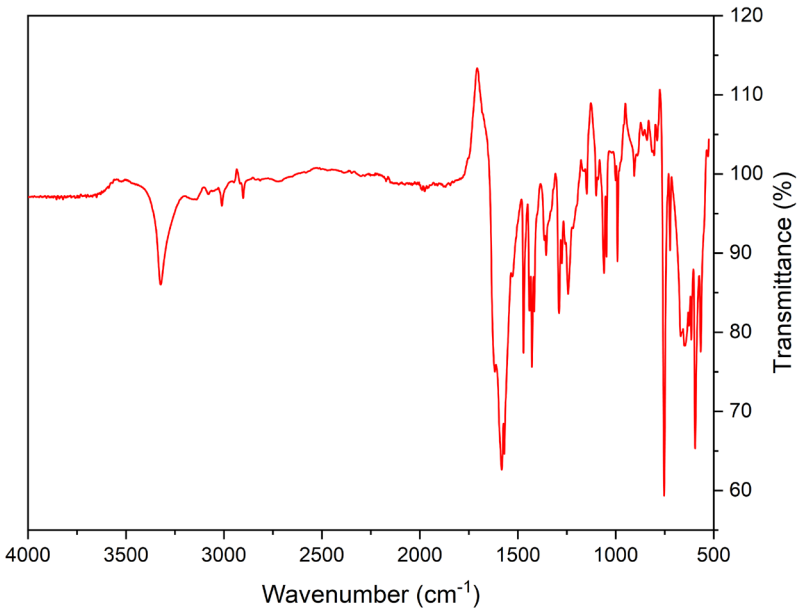

Figure A.21. FTIR of 2-MeUR-N.

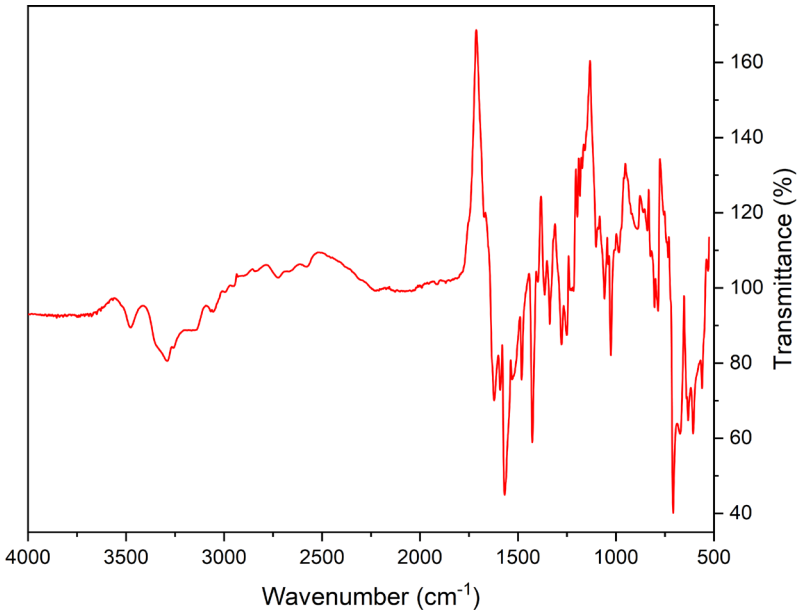

Figure A.22. FTIR of 3-MeUR-N.

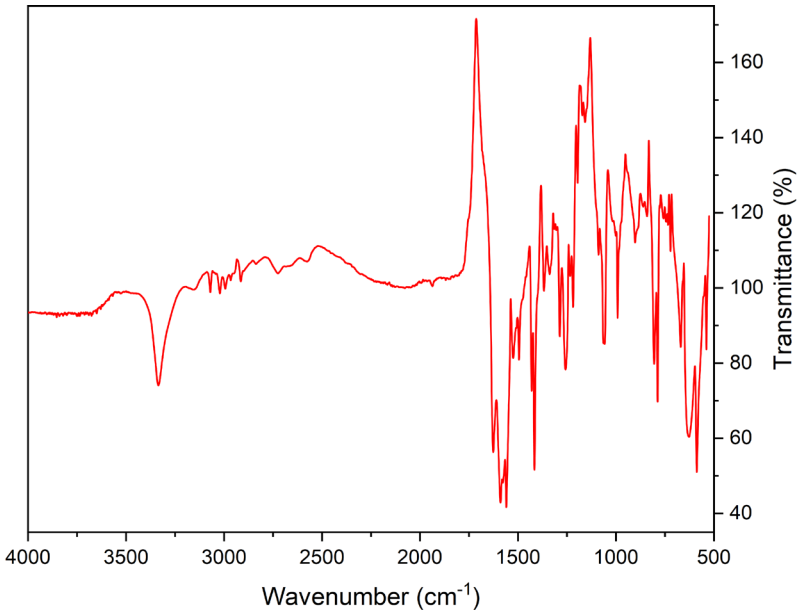

Figure A.23. FTIR of 4-MeUR-N.

A.3.3 Mass Spectrometry

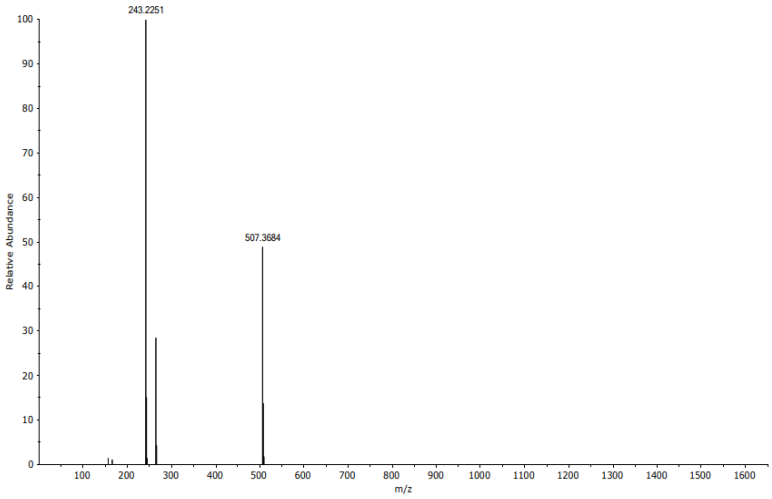

Figure A.24. RP UHPLC-MS of 2-MeUR-N. Peak at 243 m/z = 2-Me-UR-N$^+$.

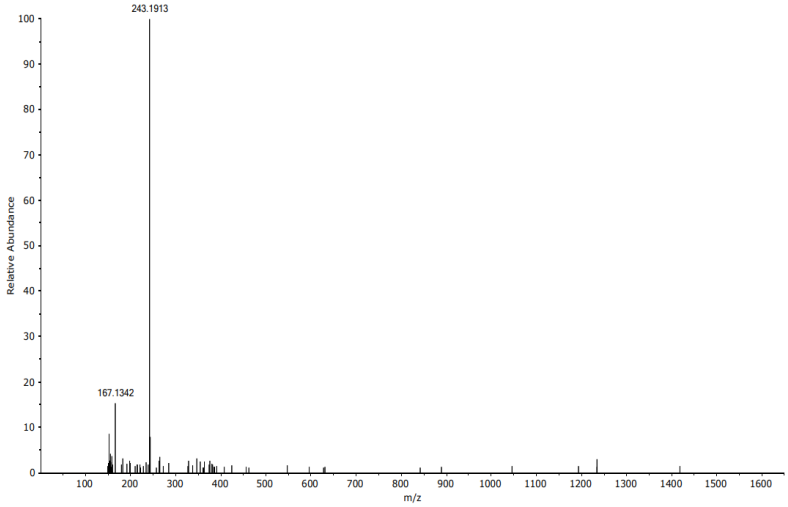

Figure A.25. RP UHPLC-MS of 4-MeUR-N. Peak at 243 m/z = 4-Me-UR-N$^+$.

A.3.4 Powder X-Ray Diffraction

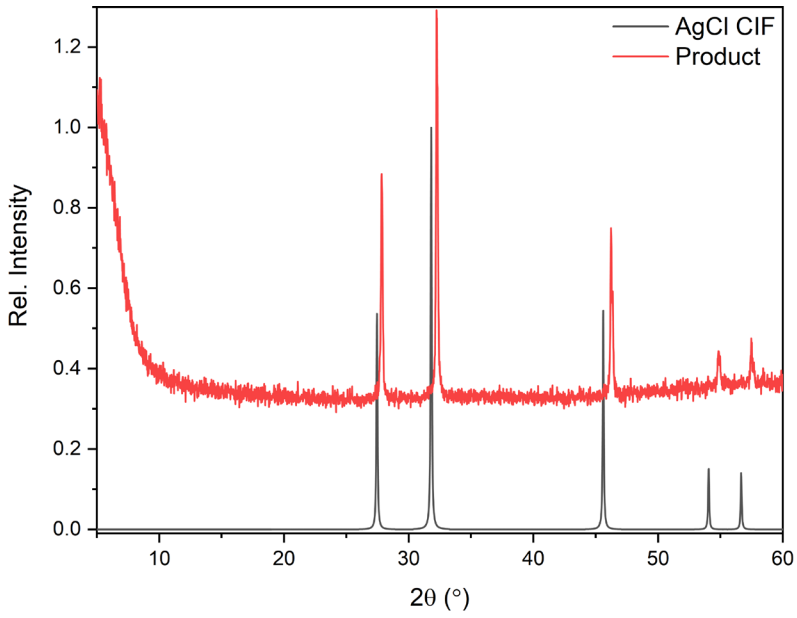

Figure A.26. PXRD pattern comparison of AgCl CIF to the precipitation formed from the reaction of $AgNO_3$, 2-MeUR-N and NaCl in water.

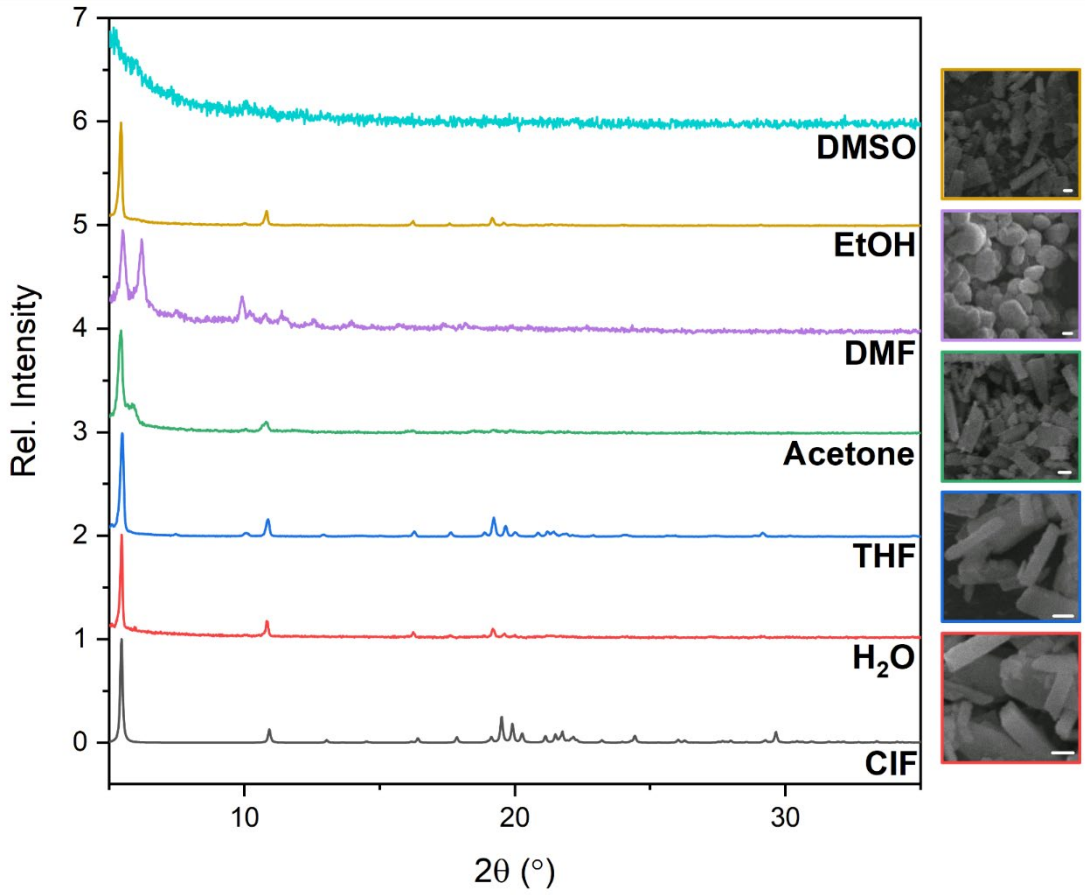

Figure A.27. PXRD pattern and SEM comparison of Zn-LMOF-3 after sonication for one hour in various solvents. Inset scale bars = 1 µm.

A.4 Chapter Four

Table A.3. Abundance of elements in the Earth's crust.[3]

Rank	Element	Contribution to Earth's crust (%)
1	Oxygen	46.1
2	Silicon	28.2
3	Aluminium	8.2
4	Iron	5.6
5	**Calcium**	**4.1**
6	Sodium	2.3
7	Magnesium	2.3
8	Potassium	2.0
9	Titanium	0.5
10	Hydrogen	0.1
Other	Remaining elements	0.5

A.4.1 Reaction Conditions

Table A.4. Solvothermal reaction conditions to synthesise $Ca(BDC)(H_2O)_3$. EG = ethylene glycol.

	Ca^{2+} source	Ca^{2+} source mass (g)	$(BDC)^{2-}$ source	$(BDC)^{2-}$ source mass (g)	Solvent (mL)	Temperature (°C)	Duration (hours)	Product yield (g)
1	$CaCO_3$	0.2470 (2.5 mmol)	H_2BDC	0.4198 (2.5 mmol)	H_2O = 15 EG = 1.5	210	16	0.4717
2	$CaCO_3$	0.2584 (2.6 mmol)	PET	0.5116 (2.5 mmol)	H_2O = 15 EG = 1.5	210	16	0.4760
3	Eggshells	0.2659 (2.7 mmol)	PET	0.4852 (2.5 mmol)	H_2O = 15 EG = 1.5	210	16	0.3269

A.4.2 Powder X-Ray Diffraction

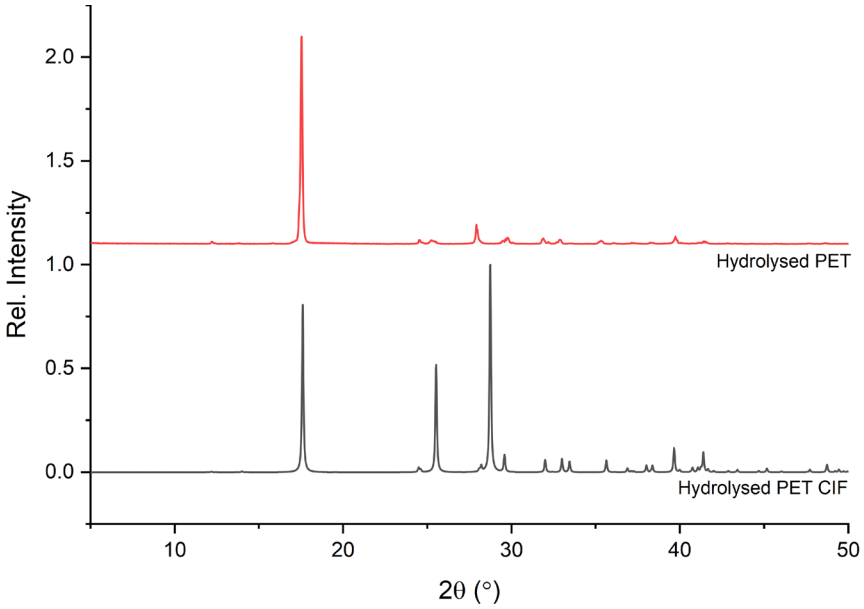

Figure A.28. PXRD comparison of hydrolysed PET to a simulated pattern generated from the crystal structure of H_2BDC synthesised from PET hydrolysis.

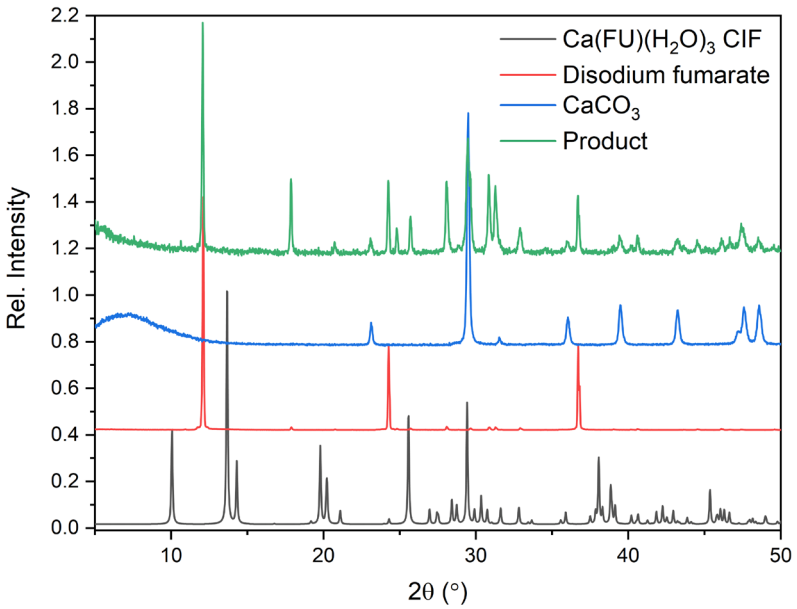

Figure A.29. PXRD comparison of product from the attempted mechanochemical synthesis of $Ca(FU)(H_2O)_3$ from the disodium linker salt to its precursors. The product pattern consists of overlapping $CaCO_3$ and Na_2FU peaks.

A.4.3 Single-Crystal X-Ray Diffraction

Table A.5. Crystal data and structure refinement for terephthalic acid from hydrolysed PET plastic.

Empirical Formula	$C_4H_3O_2$
Formula Weight	83.06
Temperature/K	100
Crystal System	triclinic
Space Group	P-1 (2)
a/Å	3.6762(4)
b/Å	6.3654(8)
c/Å	7.4242(11)
α/°	83.688(11)
β/°	79.779(12)
γ/°	87.413(10)
Volume/Å^3	169.88(4)
Z	2
ρ_{calc}g/cm3	1.624
μ/mm^{-1}	0.133
Crystal size/mm^3	0.20×0.02×0.02
Radiation	Mo Kα (λ = 0.71073)
2Θ range for data collection/°	2.803 to 31.988
Reflections collected	1891
Independent reflections	969 [R_{int}=0.0298]
Data/restraints/parameters	969/0/59
Final R indexes [all data]	R_1= 0.0677, wR_2=0.1474
Final R indexes [I>=2σ (I)]	R_1= 0.0537, wR_2 = 0.1477

Table A.6. Unit cell parameter comparison between the collected and reported H_2BDC crystal structure.

	H_2BDC from hydrolysed PET	**H_2BDC from CCDC deposition 2042484**
Space group	P-1 (2)	P-1 (2)
a / Å	3.6762(4)	3.744(2)
b / Å	6.3654(8)	6.441(4)
c / Å	7.4242(11)	7.398(5)
α / °	83.688(11)	83.214(17)
β / °	79.779(12)	80.642(17)
γ / °	87.413(10)	88.464(15)

Table A.7. Crystal data and structure refinement for $Ca(FU)(H_2O)_3$ synthesised hydrothermally from calcite.

Empirical Formula	$C_4H_6CaO_7$
Formula Weight	206.17
Temperature/K	100
Crystal System	orthorhombic
Space Group	$Pna2_1$
a/Å	6.6116(2)
b/Å	17.5832(5)
c/Å	6.8874(2)
α/°	90
β/°	90
γ/°	90
Volume/Å^3	800.68(4)
Z	4
ρ_{calc}g/cm3	1.710
μ/mm^{-1}	0.783
Crystal size/mm^3	0.3 × 0.2 × 0.08
Radiation	Mo Kα (λ = 0.71073)
2Θ range for data collection/°	6.354 to 63.99
Reflections collected	6060
Independent reflections	2236 [R_{int} = 0.0171, R_{sigma} = 0.0177]
Data/restraints/parameters	2236/2/113
Goodness-of-fit on F^2	1.116
Final R indexes [all data]	R_1 = 0.0267, wR_2 = 0.0712
Final R indexes [I>=2σ (I)]	R_1 = 0.0271, wR_2 = 0.0714
Largest diff. peak/hole / e Å^{-3}	1.13/-0.41
Flack parameter	0.253(11)

A.4.4 Fourier Transform Infrared Spectroscopy

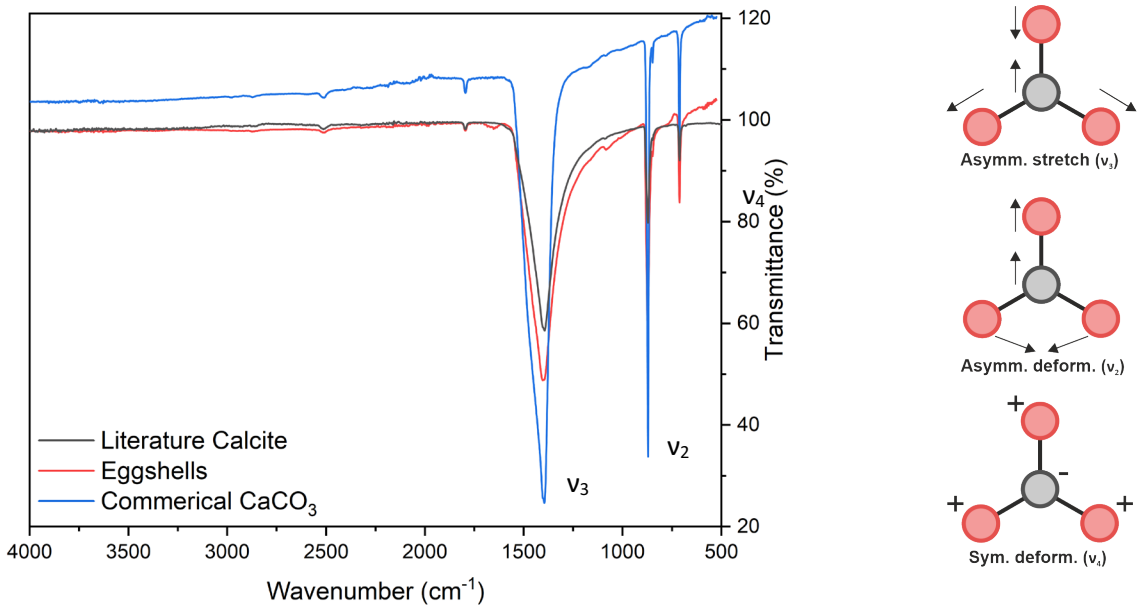

Figure A.30. FTIR spectra of eggshells and commercial $CaCO_3$ compared to a reported spectrum of calcite (RRUFF ID = R040070.1). The membrane has been removed from the eggshells.

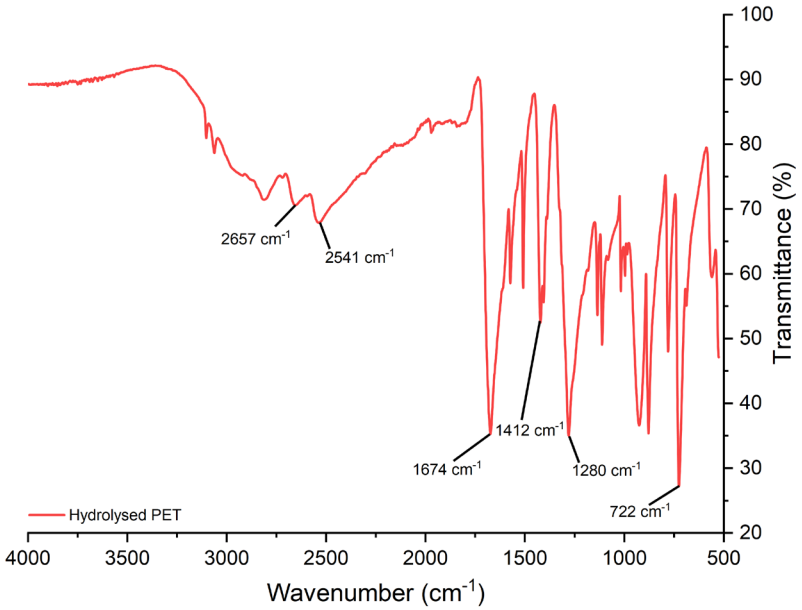

Figure A.31. FTIR of hydrolysed PET.

A.4.5 ^{1}H Nuclear Magnetic Resonance

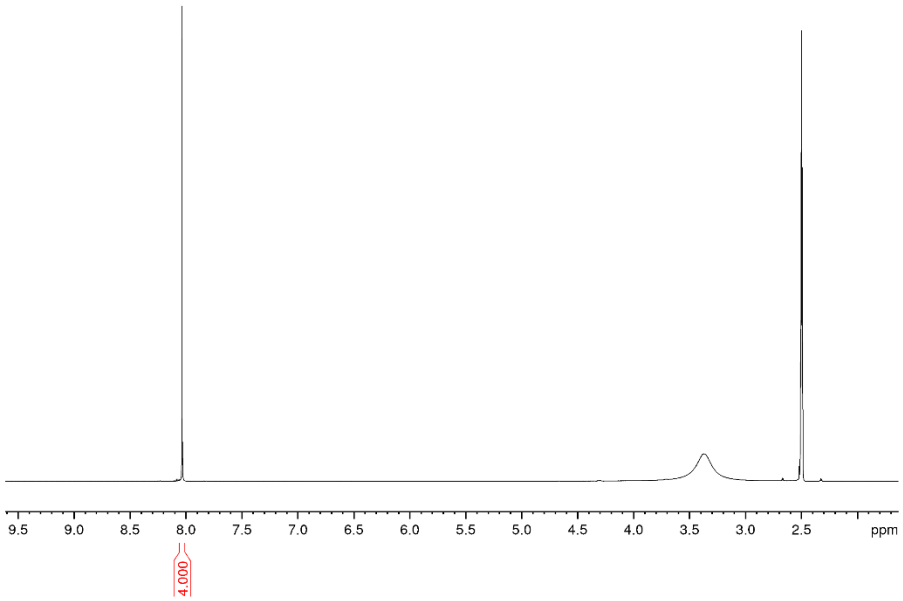

Figure A.32. ^{1}H NMR spectrum of H_2BDC from hydrolysed PET.

A.4.6 Mass Spectrometry

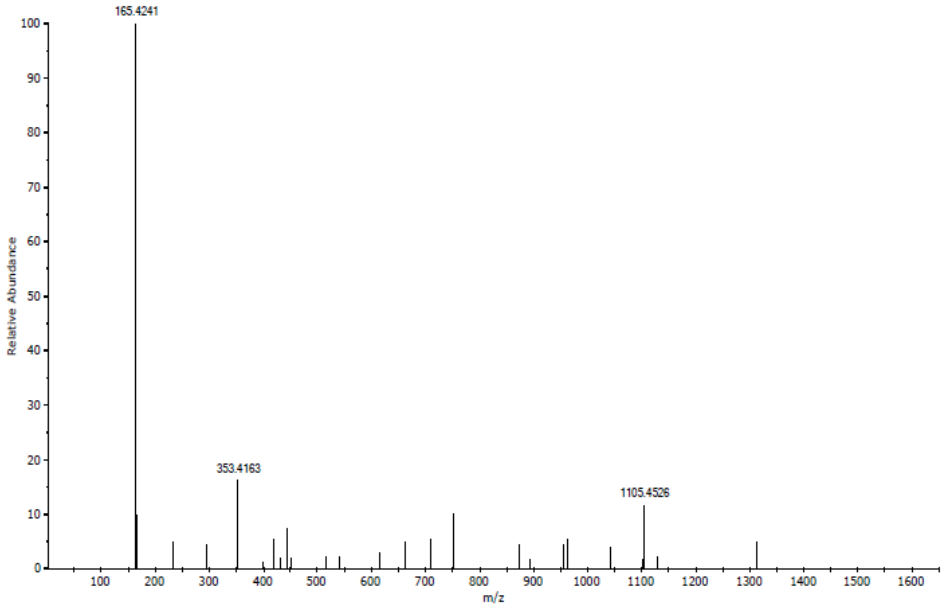

Figure A.33. RP UHPLC-MS of hydrolysed PET in a basic aqueous solution. The high abundance peak at 165.42 m/z corresponds to the $HBDC^-$ anion.

A.4.7 Calculations

Calcium Carbonate Content in [Ca(BDC)(H_2O)$_3$]

Additional residual mass from TGA = **7%**

The sample mass for TGA experiment = **19.78 mg**

$19.78 \times 0.07 = \mathbf{1.38}\ \boldsymbol{mg}\ of\ CaO = \mathbf{0.025}\ \boldsymbol{moles}\ of\ CaO$

0.025 moles of $CaCO_3$ = **2.46 mg** of $CaCO_3$

$\left(\frac{2.46}{19.78}\right) \times 100 = \mathbf{12}\%$

A.4.8 BET of Ca-MOF-Anh

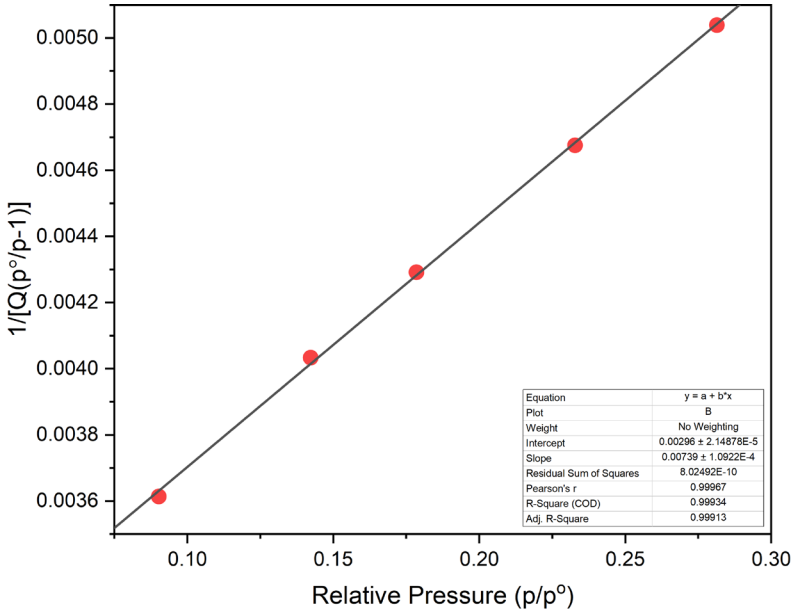

Figure A.34. BET Plot derived from N_2 gas adsorption data of Ca-MOF-Anh.

A.5 References

1 S. Wang, P. Yu, B. A. Purse, M. J. Orta, J. Diwu, W. H. Casey, B. L. Phillips, E. V Alekseev, W. Depmeier, D. T. Hobbs and T. E. Albrecht-Schmitt, *Adv. Funct. Mater.*, 2012, **22**, 2241.

2 J. H. P. Watson and D. C. Ellwood, *Nucl. Eng. Des.*, 2003, **226**, 375.

3 B. Venditti and N. LePan, Visualizing the abundance of elements in the Earth's crust, https://elements.visualcapitalist.com/elements-in-the-earths-crust-abundance/, (accessed 2 June 2022).